NUREG/CR–4667, Vol. 34
ANL–05/17

Environmentally Assisted Cracking in Light Water Reactors

Annual Report
January—December 2003

Manuscript Completed: May 2005
Date Published: 2005

Prepared by
B. Alexandreanu, O. K. Chopra, H. M. Chung,
E. E. Gruber, and W. J. Shack

Argonne National Laboratory
9700 South Cass Avenue
Argonne, IL 60439

W. H. Cullen, Jr., and C. E. Moyer, NRC Project Managers

Prepared for
Division of Engineering Technology
Office of Nuclear Regulatory Research
U.S. Nuclear Regulatory Commission
Washington, DC 20555–0001
NRC Job Code Y6388

Previous Documents in Series

Environmentally Assisted Cracking in Light Water Reactors Semiannual Report
April—September 1985, NUREG/CR–4667 Vol. I, ANL–86–31 (June 1986).
October 1985—March 1986, NUREG/CR–4667 Vol. II, ANL–86–37 (September 1987).
April—September 1986, NUREG/CR–4667 Vol. III, ANL–87–37 (September 1987).
October 1986—March 1987, NUREG/CR–4667 Vol. IV, ANL–87–41 (December 1987).
April—September 1987, NUREG/CR–4667 Vol. V, ANL–88–32 (June 1988).
October 1987—March 1988, NUREG/CR–4667 Vol. 6, ANL–89/10 (August 1989).
April—September 1988, NUREG/CR–4667 Vol. 7, ANL–89/40 (March 1990).
October 1988—March 1989, NUREG/CR–4667 Vol. 8, ANL–90/4 (June 1990).
April—September 1989, NUREG/CR–4667 Vol. 9, ANL–90/48 (March 1991).
October 1989—March 1990, NUREG/CR–4667 Vol. 10, ANL–91/5 (March 1991).
April—September 1990, NUREG/CR–4667 Vol. 11, ANL–91/9 (May 1991).
October 1990—March 1991, NUREG/CR–4667 Vol. 12, ANL–91/24 (August 1991).
April—September 1991, NUREG/CR–4667 Vol. 13, ANL–92/6 (March 1992).
October 1991—March 1992, NUREG/CR–4667 Vol. 14, ANL–92/30 (August 1992).
April—September 1992, NUREG/CR–4667 Vol. 15, ANL–93/2 (June 1993).
October 1992—March 1993, NUREG/CR–4667 Vol. 16, ANL–93/27 (September 1993).
April—September 1993, NUREG/CR–4667 Vol. 17, ANL–94/26 (June 1994).
October 1993—March 1994, NUREG/CR–4667 Vol. 18, ANL–95/2 (March 1995).
April—September 1994, NUREG/CR–4667 Vol. 19, ANL–95/25 (September 1995).
October 1994—March 1995, NUREG/CR–4667 Vol. 20, ANL–95/41 (January 1996).
April—December 1995, NUREG/CR–4667 Vol. 21, ANL–96/1 (July 1996).
January 1996—June 1996, NUREG/CR–4667 Vol. 22, ANL–97/9 (June 1997).
July 1996—December 1996, NUREG/CR–4667 Vol. 23, ANL–97/10 (October 1997).
January 1997—June 1997, NUREG/CR–4667 Vol. 24, ANL–98/6 (April 1998).
July 1997—December 1997, NUREG/CR–4667 Vol. 25, ANL–98/18 (September 1998).
January 1998—June 1998, NUREG/CR–4667 Vol. 26, ANL–98/30 (December 1998).
July 1998—December 1998, NUREG/CR–4667 Vol. 27, ANL–99/11 (October 1999).
January 1999—June 1999, NUREG/CR–4667 Vol. 28, ANL–00/7 (July 2000).
July 1999—December 1999, NUREG/CR–4667 Vol. 29, ANL–00/23 (November 2000).
January 2000—June 2000, NUREG/CR–4667 Vol. 30, ANL–01/08 (June 2001).
July 200—December 2000, NUREG/CR–4667 Vol. 31, ANL–01/09 (April 2002).

Environmentally Assisted Cracking in Light Water Reactors Annual Report
January—December 2001, NUREG/CR–4667 Vol. 32, ANL–02/33 (June 2003).
January—December 2002, NUREG/CR–4667 Vol. 33, ANL–03/36 ().

Abstract

This report summarizes work performed by Argonne National Laboratory on fatigue and environmentally assisted cracking (EAC) in light water reactors (LWRs) from January to December 2003. Topics that have been investigated include: (a) environmental effects on fatigue crack initiation in carbon and low–alloy steels and austenitic stainless steels (SSs), (b) irradiation–assisted stress corrosion cracking (IASCC) of austenitic SSs in boiling water reactors (BWRs), (c) evaluation of causes and mechanisms of irradiation-assisted cracking of austenitic SS in pressurized water reactors (PWRs), and (d) cracking in Ni alloys and welds.

Fatigue tests have been conducted on two heats of Type 304 stainless steel (SS) under various material conditions to determine the effect of heat treatment on fatigue crack initiation in these steels in air and LWR environments. Heat treatment has little or no effect on the fatigue life in air and low dissolved oxygen (DO) environment, whereas in a high–DO environment, fatigue life is lower for sensitized SSs.

Crack growth rate (CGR) data were obtained on Type 304L SS (Heat C3) irradiated to 0.3×10^{21} n/cm^2, nonirradiated Type 304 L SS weld heat affected zone (HAZ) specimens from the Grand Gulf (GG) reactor core shroud, and a Type 304 SS laboratory–prepared weld. The irradiated specimen of Heat C3 showed very little enhancement of CGRs in high–DO water. The results for the weld HAZ material indicate that under predominantly mechanical fatigue conditions, the CGRs for the GG Type 304L weld HAZ are lower than those for shielded metal arc (SMA) weld HAZ prepared in the laboratory with Type 304 SS.

Slow-strain-rate tensile (SSRT) tests have been completed in high-purity 289°C water on steels irradiated to ≈3 dpa. The bulk S content correlated well with the susceptibility to intergranular stress corrosion cracking (IGSCC) in 289°C water. The irradiation-assisted stress corrosion cracking (IASCC) susceptibility of SSs that contain >0.003 wt.% S increased drastically. These results and a review of other data in the literature indicate that IASCC in 289°C water is dominated by a crack-tip grain-boundary process that involves S. The IASCC–resistant or –susceptible behavior of austenitic SSs in BWR-like oxidizing environment is described in terms of a two–dimensional map of bulk S and C contents of the steels.

Crack growth tests were completed on a Alloy 600 round robin specimen and a Alloy 182 weld specimen in simulated PWR water at 320°C. Under cyclic loading, the CGRs for the weld specimen were a factor of ≈5 higher than those for Alloy 600 under the same loading conditions; little or no environmental enhancement was observed. The CGRs obtained with a trapezoidal waveform (i.e., a constant load with periodic unload/reload) were comparable to the average behavior of Alloy 600 in a PWR environment. The cyclic CGRs for the Alloy 600 round-robin specimen were a factor of ≈2 lower than those predicted in air. However, the crack front was U-shaped, indicating that the growth rates were significantly higher near the edge of the specimen than the center.

Foreword

Contents

Abstract iii

Foreword v

Contents vii

Executive Summary xvii

Acknowledgments xx

Abbreviations xxi

1 Introduction 1

2 Environmental Effects on Fatigue Crack Initiation in Carbon and Low–Alloy Steels and Austenitic Stainless Steels 3

2.1 Introduction 3

2.2 Experimental 4

2.3 Results – Effect of Heat Treatment on Fatigue Life 7

2.3.1 Fatigue ε–N Behavior 7

2.3.2 Fatigue Crack and Fracture Surface Morphology 10

3 Irradiation–Assisted Stress Corrosion Cracking of Austenitic Stainless Steel in BWRs 23

3.1 Slow-Strain-Rate-Tensile Test of Model Austenitic Stainless Steels Irradiated in the Halden Reactor 23

3.1.1 Introduction 23

3.1.2 Representation of IASCC-Resistant or –Susceptible Behavior of 304- and 316-Type Steels in Sulfur-Carbon Map 24

3.1.3 Grain-Boundary Segregation of Sulfur and Carbon 26

3.1.4 Analysis of Solubility of Carbon in Sulfides 30

3.2 Crack Growth Rate Test of Austenitic Stainless Steels Irradiated in the Halden Reactor 32

3.2.1 Introduction 32

3.2.2 Experimental 33

3.2.2.1 Specimen Geometry and Materials 33

3.2.2.2 Test Procedure 38

3.2.3 Crack Growth Rates of Irradiated Stainless Steels in BWR Environments 41

3.2.3.1 Specimen C3–A of Type 304L SS, Test CGRI-12 41

3.2.3.2 Irradiated Austenitic SSs under Continuous Cycling 44

3.2.3.3 CGRs of Irradiated Austenitic SSs under Trapezoidal Waveform with Long Hold Periods 45

3.2.4 Crack Growth Tests on Nonirradiated Stainless Steel Weld HAZ Specimens 46

3.2.4.1 Specimen GG5B–A of the HAZ from Grand Gulf Core Shroud H5 SA Weld, Test CGR–10 46

3.2.4.2 Specimen 85–3A–TT of the HAZ from Laboratory–Prepared SMA Weld, Test CGR-11 49

3.2.4.3 Specimen GG3B–A–TT of the HAZ from Grand Gulf Core Shroud H5 SA Weld, Test CGR-14 56

3.2.4.4 Austenitic SS Weld HAZ under Continuous Cycling 59

3.2.4.5 Austenitic SS Weld HAZ under Constant Load or Cycling with Long Hold Periods 61

4 Evaluation of Causes and Mechanisms of Irradiation-Assisted Cracking of Austenitic Stainless Steel in PWRs 63

4.1 Introduction 63

4.2 Irradiation of Austenitic Stainless Steels in the BOR-60 Reactor 63

4.3 Representation of IASCC–Ressistant or –Susceptible Behavior of Types 304 and 316 Stainless Steel in Sulfur–Carbon Map 63

5 Cracking of Nickel Alloys and Welds 67

5.1 Introduction 67

5.2 Experimental 68

5.2.1 Material and Specimen Design 68

5.2.2 Test Facility 70

5.2.3 Test Procedure 70

5.2.4 Material Characterization 71

5.2.4.1 Alloy 600 for the Round Robin Specimen 71

5.2.4.2 Double–J Weld 74
5.3 Results 87
5.3.1 Alloy 600 Round Robin Specimen 87
5.3.2 Alloy 182 Double–J Weld Specimen 92
6 Summary 101
6.1 Environmental Effects on Fatigue ε–N Behavior 101
6.2 Irradiation–Assisted Stress Corrosion Cracking of Austenitic Stainless Steel in BWRs 101
6.3 Irradiation–Assisted Cracking of Austenitic Stainless Steel in PWRs 102
6.4 Cracking of Nickel Alloys and Welds 103
References 105

Figures

1. Typical microstructures observed by SEM, showing degree of sensitization for alloys used in this study: low magnification; high magnification. 5

2. Configuration of fatigue test specimen 6

3. Schematic diagram of electron–beam–welded bar for machining A302–Gr B fatigue test specimens. 6

4. Effect of material heat treatment on fatigue life of Type 304 stainless steel in air, BWR, and PWR environments at 289°C, ≈0.38% strain amplitude, sawtooth waveform, and 0.004%/s tensile strain rate. 8

5. Effect of sensitization annealing on fatigue life of Type 304 and 316 stainless steel in low–DO water at 325°C. 8

6. Effect of sensitization anneal on the fatigue lives of Type 304 and 316NG stainless steel in high–DO water. 9

7. Cyclic stress response of Heat 30956: MA, MA + 0.67 h at 700°C, and MA + 24 h at 700°C; and Heat 10285, MA + 24 h at 600°C, in air, BWR, and PWR environments at 289°C. 9

8. Photomicrographs showing sites of crack initiation on fracture surfaces of Type 304 SS specimens tested in air: low magnification; high magnification. 11

9. Photomicrographs showing sites of crack initiation on fracture surfaces of Type 304 SS specimens tested in simulated BWR environment: low magnification; high magnification. 13

10. Photomicrographs showing the sites of crack initiation on the fracture surfaces of Type 304 SS specimen tested in simulated PWR environment: low magnification; high magnification. 14

11. Photomicrographs showing striations at select locations on fracture surfaces of MA specimen of Heat 30956 in simulated BWR environment: low magnification; high magnification 14

12. Photomicrographs showing striations at select locations on fracture surfaces of MA specimens of Heat 30956 heat–treated for 0.67 h at 700°C in air, BWR, and PWR environments: low magnification; high magnification 15

13. Photomicrographs showing striations at select locations on fracture surfaces of MA specimens of Heat 10285 heat–treated for 24 h at 600°C in air, BWR, and PWR environments: low magnification; high magnification 16

14. Photomicrographs showing striations at select locations on fracture surfaces of MA specimens of Heat 30956 heat–treated for 24 h at 700°C in air, BWR, and PWR environments: low magnification; high magnification 17

15. Photomicrographs of the crack morphology of Type 304 SS under all test and environmental conditions. 18

16. Photomicrographs showing crack initiation site at low and high magnification, and striations at select locations in Type 316NG SS tested in air. 19

17. Photomicrographs showing crack initiation site and striations at select locations in Type 316NG SS tested in BWR and PWR environment. 20

18. Photomicrographs showing the morphology of lateral cracks formed in Type 316NG SS in three test environments. 21

19. Range of bulk S and C contents in which 304- or 316-type steels are resistant or susceptible to IASCC in BWR-like oxidizing water. 25

20. Expanded view of low-S portion of Fig. 19 showing data in detail. 25

21. Range of bulk S and C contents in which 304– or 316–type steels are resistant or susceptible to IASCC, including four susceptible heats tested at 1.3 dpa in this study. 26

22. High-magnification fractograph of H-charged BWR neutron absorber tube, 304 SS, Heat B, ≈3 dpa; fracture was produced at 23°C in ultra-high vacuum environment in a scanning Auger electron microscope 27

23. Summary of AES analysis of grain-boundary segregation of S and C in BWR neutron absorber tube fabricated from Type 304 SS Heat A and irradiated to 3 dpa: S and C peak heights from ductile and IG fracture surfaces are compared. 28

24. Summary of AES analysis of grain-boundary segregation of S and C in BWR neutron absorber tube fabricated from Type 304 SS Heat B and irradiated to 3 dpa: S and C peak heights from ductile and IG fracture surfaces are compared. 28

25. Result of AES depth-profiling analysis of grain-boundary segregation of S and C in BWR neutron absorber tubes fabricated from Type 304 SS Heats A and B and irradiated to ≈3 dpa. 29

26. AES signal showing high concentrations of Cu, S, and C in CuS-type precipitate denoted with number “6” in Fig. 22 30

27. AES signal showing a high concentration of C in CuS-type precipitate in BWR neutron absorber tube, 304 SS, Heat B, ≈3 dpa. 31

28. AES signal showing a high concentration of C in another CuS-type precipitate in BWR neutron absorber tube, 304 SS, Heat B, ≈3 dpa. 31

29. Configuration of compact–tension specimen for this study 33

30. Orientation of the 1/4–T CT specimens from the Grand Gulf H5 SA weld HAZ and laboratory–prepared SMA weld HAZ. 34

31. Low- and high–magnification photomicrographs of the structure of the Type 304L base metal from the top shell of the H5 weld of the Grand Gulf core shroud. 35

32. Micrographs of the interface between the weld metal and top shell of the H5 weld of the Grand Gulf core shroud. 35

33. Low- and high–magnification photomicrographs of the structure of the Type 304L base metal from the bottom shell of the H5 weld of the Grand Gulf core shroud. 36

34. Micrographs of the interface between the weld metal and bottom shell of the H5 weld of the Grand Gulf core shroud. 36

35. Low- and high–magnification photomicrographs of the structure of Heat 10285 of the Type 304 base metal from the top shell of the H5 weld of the Grand Gulf core shroud. 37

36. Micrographs of the interface between the weld metal and base metal. 37

37. Plot of CGR in water vs. the CGR in air showing environmental enhancement of growth rates in high purity water at 289°C 40

38. Crack length vs. time plots for irradiated Type 316 SS in high–purity water at 289°C during test periods 1–2, 3–5, 6–7, 8–10, and 11–12. 42

39. Photomicrograph of the fracture surface of Specimen C3–A 44

40. CGR data for irradiated austenitic SSs under continuous cycling at 289°C in high–purity water with ≈300 ppb and <30 ppb dissolved oxygen. 44

41. CGR data under constant load with periodic partial unloads for irradiated austenitic SSs in high–purity water at 289°C 45

42. Crack length vs. time plots for nonirradiated Grand Gulf Type 304L bottom shell H5 weld HAZ in high–purity water at 289°C during test periods precracking–3, 4-6, and 7–8. 47

43. Photomicrograph of the fracture surface of Specimen GG5B–A 48

44. Micrograph of the fracture surface of Specimen GG5B–A tested in high–DO water at 289°C. 48

45. Micrographs showing slice of the entire length of fracture surface, and high magnification micrographs of the fracture surface at locations 1, 2, and 3, respectively. 49

46. Change in crack length and ECP of Pt and SS electrodes during test periods 5–6 and the intermediate transition period 50

47. Photomicrographs of the fracture surfaces of the two halves of Specimen 85–3A-TT. 51

48. Micrograph of the cross section of Specimen 85-3A-TT showing the fracture plane profile. 51

49. Crack length vs. time for nonirradiated HAZ soecimen of Grand Gulf Type 304L bottom shell H5 weld in high–purity water at 289°C during test periods 1–3, 4-6, 7–8, and 9. 52

50. Micrograph of the fracture surface of Specimen 85-3A-TT tested in high–DO water at 289°C. 53

51. Micrograph showing slice of the fracture surface that was perpendicular to the stress axis, and high magnification micrographs of the fracture surface at locations 1, 2, and 3, respectively. 54

52. Typical fracture morphologies along the change in the fracture plane direction and before and after the change in direction. 55

53. Micrograph of the cross section of Specimen GG3B-A-TT showing the fracture plane profile 57

54. Micrograph of the fracture surface of Specimen GG3B-A-TT tested in high–DO water at 289°C 57

55. Crack length vs. time plots for nonirradiated thermally treated Type 304L bottom shell HAZ from the Grand Gulf H5 SA weld in high–purity water at 289°C during test periods precracking, 1-5, and 5–7. 58

56. Micrographs showing slice of the entire length of the fracture surface and high magnification micrographs of the fracture surface at locations 1, 2, and 3, respectively. 59

57. CGR data for nonirradiated specimens of laboratory–prepared Type 304 SS SMA weld HAZ and Type 304L SA weld HAZ from the Grand Gulf core shroud under continuous cycling at 289°C in high–purity water with 300–500 ppb dissolved oxygen 60

58. CGR data under constant load with or without periodic partial unloads for nonirradiated SS weld HAZ specimens in high–purity water at 289°C 61

59. Representation of IASCC resistance or susceptibility of austenitic stainless steels as function of bulk S and C contents 64

60. Configuration of compact-tension specimen used for this study 69

61. Schematic of the weld joint design and weld passes 69

62. Orientation of the CT specimen from the Alloy 182 SMA weld 70

63. Microstructure of the round robin Alloy 600 etched with nital and phosphoric acid solution 72

64. Microstructure of the round robin alloy in the plane of the crack at two magnifications. 73

65. Microstructure of the round robin alloy in the plane of the crack at two magnifications and that of a different heat of Alloy 600 used previously in our experiments. 73

66. Schematic showing the locations of the three samples cut from the weld. 74

67. Weld microstructure from Sample 1; transition area between the weld and Alloy 600; and dendritic microstructure in the weld. 75

68. Large grain microstructure in the HAZ, pictures at two opposite positions. 76

69. Dendritic microstructure on sample 3A, and at a weld pass. 76

70. Examples of dendritic microstructure at a weld passes on sample 3B and high magnification micrographs at the respective locations. 77

71. Dendritic mictostructure on sample 3B and at high magnification of a region. 77

72. Dendritic microstructure observed on the surface of sample 3A at 200×, 200×, and 800× magnifications. 78

73. Micrograph showing one of the matrix precipitates observed on the surface of sample 3A and EDX spectra resulting from the bulk and the precipitate. 79

74. Micrographs showing the microstructure on plane 3A, and both matrix and grain boundary precipitates, and EDX spectra resulting from the bulk and from the grain boundary precipitate. 80

75. Dendritic microstructure observed on the surface of sample 3A at magnification 300×, 500×, 800×, and 9,000×. 81

76. Micrographs showing Ti-rich precipitates in the weld material, and maps showing the topography at the locations where the high magnification micrographs were taken. 82

77. Micrographs showing the heat affected zone, and high magnification micrographs showing precipitates in the heat affected zone. 83

78. OIM map of the weld, on plane "B", sample 3B; the same OIM map showing the orientation of each grain; and legends for crystal directions and the resulting grain boundary character distribution. 84

79. OIM map on the surface of sample 3B and the resulting grain boundary character distribution.. 85

80. The same OIM map as in Fig. 79a showing crystal directions and SEM micrograph illustrating the dendritic microstructure of the weld. 86

81. Crack length vs. time plot for Alloy 600 round robin specimen RR-1 in simulated PWR environment at 320°C during periods 1-5, 3B-5C, 6-7, and 6C-7C. 88

82. CGR data for specimen RR-1 of the Alloy 600 round robin test in simulated PWR environment at 320°C. 89

83. Entire crack surface of Alloy 600 round-robin specimen RR-1 tested in PWR water at 320°C. 90

84. Entire crack surface of Alloy 600 round robin specimen RR-3 tested in PWR water at 320°C 90

85. Selected portion of the crack surface of Alloy 600 round robin specimen RR-1 tested in PWR water at 320°C showing the changes in fracture morphology, and micrographs taken at the boxed positions 1 and 2, respectively 91

86. Crack length vs. time plot for Alloy 182 SMA weld–metal specimen in simulated PWR environment at 320°C during test periods 1–4a, 4b-5, 6–8, 9, and 10. 93

87. Photomicrograph of the fracture surface of specimen CT31-W01 94

88. A higher magnification photomicrograph showing entire crack extension in a region in the center of the specimen 95

89. Transition from TG to IG fracture and higher magnification micrograph of the boxed area showing the tip of a few cracks. 96

90. Mixed TG and IG fracture modes, high magnification micrograph of the boxed area, and micrographs showing the crack tips at locations “1” and “2.” 97

91. Photomicrographs detailing the fracture in a region during test periods with a hold time and/or a high rise time, and high magnification micrographs of positions indicated by arrows. 98

92. Photomicrographs detailing the fracture in a region during test periods with a hold time and/or a high rise time, and high magnification micrographs 98

93. CGR data for Alloy 182 SMA weld–metal specimen in simulated PWR environment at 320°C. 99

94. Comparison of the SCC growth rate for the Argonne Alloy 182 weld with the available data for Alloy 182 and 82 welds in simulated PWR environment. 100

Tables

1. Composition of austenitic stainless steels for fatigue tests 4

2. Fatigue test results for Type 304 stainless steel in air and simulated BWR and PWR environments at 289°C 7

3. Composition of Heat C3 of Type 304L stainless steel irradiated in the Halden reactor 33

4. Tensile properties of irradiated Heat C3 of Type 304L stainless steel at 288°C 33

5. Composition of Type 304 stainless steels investigated 34

6. Tensile properties of the austenitic stainless steels irradiated in the Halden reactor 38

7. Crack growth results for Specimen C3–A of Type 304 SS in high–purity water at 289°C 41

8. Crack growth results for Specimen GG5B–A of Type 304L HAZ in high–purity water at 289°C 46

9. Crack growth results for Specimen 85–3A–TT of nonirradiated Type 304 SS SMA weld HAZ in high–purity water at 289°C 50

10. Crack growth results for Specimen GG3B–A–TT of Type 304L HAZ in high–purity water at 289°C 56

11. Chemical composition of Alloy 600 base metal and Inconel 182 and 82 weld metals 69

12. Welding process and conditions for various weld passes 69

13. Chemical compositions of the bulk material and matrix precipitate resulting from EDX analysis. 79

14. Chemical compositions of the bulk material and grain boundary precipitate resulting from EDX analysis. 80

15. Loading conditions for the Alloy 600 round-robin test 87

16. Crack growth results for Alloy 600 round-robin specimen RR-1 in PWR water at 320°C 87

17. Crack growth data for specimen CT31-W01 of Alloy 182 SMA weld in PWR water at 320°C 92

Executive Summary

The existing fatigue strain vs. life (ε–N) data indicate potentially significant effects of light water reactor (LWR) coolant environments on the fatigue resistance of carbon and low–alloy steels, as well as of austenitic stainless steels (SSs). In LWR environments, the fatigue lives of austenitic SSs depend on applied strain amplitude, strain rate, temperature, and dissolved oxygen (DO) in water. A minimum threshold strain is required to cause an environmentally assisted decrease in the fatigue life. Strain rate and temperature have a strong effect on fatigue life in LWR environments. Fatigue life decreases logarithmically with decreasing strain rate below 0.4%/s; this effect stops at 0.0004%/s. Similarly, the fatigue ε–N data suggest a threshold temperature of 150°C; in the range of 150–325°C, the logarithm of life decreases linearly with temperature. The effect of DO on fatigue life may depend on the composition and heat treatment of the steel. Limited data indicate that, in high–DO water, the environmental effects are influenced by the material heat treatment. In low–DO water, the material heat treatment seems to have little or no effect on the fatigue life of austenitic SSs.

Fatigue tests have been conducted on two heats of Type 304 SS under various material conditions to determine the effect of heat treatment on fatigue crack initiation in these steels in air and LWR environments. The results indicate that heat treatment has little or no effect on the fatigue life of Type 304 SS in air and low–DO pressurized water reactor (PWR) environment. In a high–DO boiling water reactor (BWR) environment, fatigue life is lower for sensitized SSs; life continues to decrease as the degree of sensitization is increased. The cyclic strain–hardening behavior of Type 304 SS under various heat treatment conditions is identical; only the fatigue life varies in different environments.

In air, irrespective of the degree of sensitization, the fracture mode for crack initiation (crack lengths up to ≈200 μm) and crack propagation (crack lengths >200 μm) is transgranular (TG), most likely along crystallographic planes, leaving behind relatively smooth facets. With increasing degree of sensitization, cleavage–like or stepped TG fracture and, occasionally, ridge structures were observed on the smooth surfaces. In the BWR environment, the initial crack appeared intergranular (IG) for all heat–treatment conditions, implying a weakening of the grain boundaries. For all conditions tested, the initial IG mode transformed within 200 μm into a TG mode with cleavage–like features. However, the size of the IG portion of the crack surface increased with the degree of sensitization. By contrast, for all of the samples tested in PWR environments, the cracks initiated and propagated in a TG mode irrespective of the degree of sensitization. The fracture surfaces in the PWR case were highly angular, cleavage–like facets that exhibited well–defined "river" patterns. Intergranular facets were rarely observed. Those that did appear were found mostly in the more heavily sensitized alloys.

The susceptibility of austenitic SSs and their welds to irradiation-assisted stress corrosion cracking (IASCC) as a function of the fluence level, water chemistry, material chemistry, welding process, and fabrication history is being evaluated. Crack growth rate (CGR) tests and slow strain rate tests (SSRTs) are being conducted on model SSs, irradiated at ≈288°C in a helium environment in the Halden boiling heavy water reactor, to investigate the effects of material chemistry and irradiation level on the susceptibility of SSs to IASCC. Crack growth tests are also being conducted on irradiated specimens of Type 304 and 304L SS weld heat-affected zone (HAZ) to establish the effects of fluence level on IASCC of these materials.

Slow-strain-rate tensile tests have been completed in high-purity 289°C water on steels irradiated to ≈0.43, 1.3, and 3.0 dpa in helium in the Halden Reactor. The bulk S content provided the only good correlation with the susceptibility to IG SCC in 289°C water. Good resistance to IASCC was observed in

Type 304 and 316 steels that contain very low sulphur concentrations of ≈0.002 wt.% or less. The IASCC susceptibility of Type 304, 304L, 316, and 316L steels that contain >0.003 wt.% S increased drastically. Steels containing ≥0.008 wt.% were very susceptible at high fluence. A comparison of the results with data available in the literature is presented. The IASCC–resistant or –susceptible behavior of austenitic SSs in BWR-like oxidizing environment is represented in terms of a two–dimensional map of bulk S and C contents of the steels. To investigate the importance of the roles of S and C on IASCC, evidence of grain-boundary segregation was characterized by Auger electron spectroscopy on BWR neutron absorber tubes fabricated from two heats of Type 304 SS.

Also, CGR data were obtained on Type 304L SS (Heat C3) irradiated to 0.3×10^{21} n/cm^2, nonirradiated Type 304L SS weld HAZ specimens from the Grand Gulf (GG) reactor core shroud and a Type 304 SS laboratory–prepared weld. The irradiated specimen of Heat C3 showed very little enhancement of CGRs in high–DO water. Under cyclic loading, the CGRs may be represented by the Shack/Kassner model for nonirradiated austenitic SSs in high–purity water with 0.2 ppm DO. Under constant load, the CGRs were below the NUREG–0313 disposition curve for sensitized SSs in water with 8 ppm DO.

The results for the weld HAZ material indicate that, under cyclic loading conditions that resulted in predominantly mechanical fatigue (i.e., no environmental enhancement), experimental CGRs for the GG Type 304L weld HAZ are lower than those for the Type 304 SMA weld HAZ. The CGRs for the Type 304 weld HAZ are consistent, and those for the Type 304 L weld HAZ are a factor of ≈2 lower than those predicted for austenitic SSs in air. In the high–DO BWR environment (i.e., with environmental enhancement), the cyclic CGRs of Type 304 SS SMA weld HAZ are comparable to those of the GG Type 304L SA weld HAZ. For either the GG or the laboratory–prepared weld HAZ, the growth rates of the thermally treated condition are marginally higher than those of the as–welded condition.

Under constant load, the CGRs of as–welded and as–welded plus thermally treated GG weld HAZ are comparable. For both conditions, the CGRs are a factor of ≈2 lower than the NUREG–0313 curve for sensitized SSs in water with 8 ppm DO. For the thermally treated condition, the CGR of the Type 304 SS HAZ weld is a factor of ≈10 higher than that for the Type 304L weld HAZ.

A comprehensive irradiation experiment in the BOR-60 Reactor is in progress to obtain a large number of tensile and disk specimens irradiated under PWR-like conditions at ≈325°C to 5, 10, and 40 dpa. Irradiation to ≈5 and ≈10 dpa has been completed; the specimens are expected in August 2004.

Tests performed on the materials irradiated in the Halden BWR reactor may, however, give some insight into potential mechanisms for IASCC that is also relevant to PWRs. On the basis of these results, and studies on binary Ni–S and crack-tip microstructural characteristics of LWR core internal components reported in the literature, an initial IASCC model based on a crack-tip grain-boundary process that involves S has been proposed. In this model, the following processes play key roles: grain-boundary segregation of Ni and S, formation of grain-boundary oxide in front of crack tip, formation of Ni– and S–rich thin films, and islands between the oxide and metal matrix, and disorder–induced melting or amorphization of the Ni–S thin films and islands at sufficiently high concentration of S.

The resistance of Ni alloys to environmentally assisted cracking (EAC) in simulated LWR environments is being evaluated. Crack growth tests are being conducted to establish the effects of alloy chemistry, material heat treatment, cold work, temperature, load ratio, stress intensity, and DO level on the CGRs of Ni alloys. A CGR test was conducted on an Alloy 182 SMA weld specimen in the TS orientation in simulated PWR water at 320°C. The experimental CGRs obtained under cyclic loading

were a factor of ≈5 higher than those for Alloy 600 under the same loading conditions. However, for the Alloy 182 weld metal, little or no environmental enhancement in PWR environment occurred. The experimental CGRs obtained with a trapezoidal waveform (essentially a constant load with periodic unload/reload) were compared with the available CGR data from the literature and with the CGR curve based on the Scott model, proposed in PWRMRP–21 for Alloy 182. The growth rate for the specimen tested at ANL compared well with the available data for Alloy 182 welds, and was close to the average behavior of Alloy 600. The CGR test was complemented by an extensive examination of the fracture surface conducted with the objective of correlating the test parameters to the resultant fracture modes. The analysis has found that cracking initiated in a transgranular mode and transitioned to an intergranular mode during long rise-time testing periods. This testing approach also resulted in a uniform, straight crack front. Another potentially important observation was that the fracture mode was affected by grain orientation. Specifically, intergranular cracking initiated more readily along grains having the dendrites parallel to the crack front than on grains having the dendrites perpendicular to the crack front. This orientation-dependent crack growth was also the cause of the unbroken ligaments left behind, which in turn caused the DC potential technique to underestimate the crack length.

A CGR test was conducted on an Alloy 600 round–robin specimen in a simulated PWR environment at 320°C according to the testing protocol agreed upon by the Cooperative IASCC Research (CIR) group. The resultant CGR data under cyclic loading indicate that for high growth rates, the rates measured for the round robin specimen are a factor of ≈2 lower than those predicted in air. The difference, most likely, is due to the material condition; the round-robin specimen was 30% cold worked, whereas the data for the alloy in air are for annealed material. For low growth rates, the measured CGRs were higher than those for the alloy in air. The examination of the fracture surface revealed that the fracture mode was transgranular near the machine notch, followed by a transition region of highly angular, cleavage–like facets with "river" patterns, which changed to completely intergranular fracture mode for the remainder of the test. Also, the appearance of the crack front was U-shaped, implicating that the crack growth rates were significantly higher near the edge of the specimen than the center. This last observation is consistent with those made by other round-robin participants from France and Switzerland, and seems to suggest that the distribution of cold work was not uniform across the specimen thickness.

During the reporting period, orientation imaging microscopy (OIM) of the weld microstructure was also begun. These initial results indicate that weld alloys contain relatively high proportions of cracking-susceptible random boundaries. In addition, OIM imaging revealed that the weld microstructure consists of clusters of grains sharing similar orientations. The possible implication of this finding is that weld alloys may contain a class of random boundaries that are more resistant to cracking when separating grains of similar orientations than different orientations.

Acknowledgments

The authors thank E. Listwan, T. M. Galvin, R. W. Clark, and J. Tezak for their contributions to the experimental effort. This work is sponsored by the Office of Nuclear Regulatory Research, U.S. Nuclear Regulatory Commission, under Job Code Y6388; Program Manager: William H. Cullen, Jr.; Tasks 2 and 3 Manager: Carol E. Moyer.

Abbreviations

AAEM	Advanced Analytical Electron Microscopy
AES	Auger Electron Spectroscopy
ANL	Argonne National Laboratory
ASME	American Society of Mechanical Engineers
ASTM	American Society for Testing and materials
BWR	Boiling Water Reactor
CGR	Crack Growth Rate
CIR	Cooperative IASCC Research
CSLB	Coincident Site Lattice Boundary
CT	Compact Tension
CUF	Cumulative Usage Factor
CW	Cold Worked
DO	Dissolved Oxygen
EAC	Environmentally Assisted Cracking
ECP	Electrochemical Potential
FEG	field-emission-gun
GBE	Grain Boundary Engineered
GBO	Grain Boundary Optimized
GG	Grand Gulf
GTA	Gas Tungsten Arc
HAB	High Angle Boundary
HAZ	Heat Affected Zone
HWC	Hydrogen Water Chemistry
IAC	Irradiation Assisted Cracking
IASCC	Irradiation Assisted Stress Corrosion Cracking
IG	Intergranular
IHI	Ishikawajima–Harima Heavy Industries Co.
JoBB	Joint Owners Baffle Bolt
LAB	Low Angle Boundary
LWR	Light Water Reactor
MC	Metal Carbide
MHI	Mitsubishi Heavy Industries, Ltd.

MRP	Materials Reliability Program
NRC	Nuclear Regulatory Commission
NRR	Nuclear Reactor Regulation
NWC	Normal Water Chemistry
OIM	Orientation Imaging Microscopy
PWR	Pressurized Water Reactor
SA	Submerged Arc
SEM	Scanning Electron Microscopy
SCC	Stress Corrosion Cracking
SMA	Shielded Metal Arc
SS	Stainless Steel
SSRT	Slow Strain Rate Tensile
TG	Transgranular

1 Introduction

Since 1967, the Nuclear Regulatory Commission (NRC) and its predecessor the Atomic Energy Commission (AEC) have conducted research programs that address aging of reactor components. The results of this research have been used to evaluate and establish regulatory guidelines to ensure acceptable levels of reliability for light water reactor (LWR) components. The products of this program, i.e., technical reports, methodologies for evaluating licensee submittals, and other inputs to the regulatory process, have led to the resolution of regulatory issues, as well as the development, validation, and improvement of regulations and regulatory guides. The research on the effects of the environment on component cracking was initiated in response to the determination that environmental effects were critical to several important cracking phenomena in LWR components. A major research program at Argonne National Laboratory (ANL) was initiated in 1979 to address pipe–cracking problems in boiling water reactors (BWRs). Since that time, in response to needs for additional research to support the Office of Nuclear Reactor Regulation (NRR) in assessing developing cracking problems in aging reactors, the focus of the project has shifted to address other problems in environmental cracking of LWR components. In recent years this activity has been supplemented by NRC participation in the Cooperative Irradiation Assisted Stress Corrosion Cracking Research (CIR) Program, a proprietary activity in which groups in several countries contribute money that is used to support research on irradiation–assisted stress corrosion cracking (IASCC) problems of common interest.

This project consists of several tasks with differing objectives; so the objectives are best described on a task–by–task basis:

Task 1: Environmental Effects on Fatigue Crack Initiation.

The objective of this task is to provide information on such topics as fatigue crack initiation in stainless steel (SS), and the synergistic effects of surface finish or loading sequence and environment on fatigue life. A comprehensive evaluation of SS fatigue test specimens will be performed to explain why environmental effects are more pronounced in low–dissolved oxygen (DO) than high–DO water. The contractor will review and evaluate issues related to environmental effects on fatigue as required by the NRC, and will participate in ASME Code committees to incorporate the effects of LWR environments in fatigue life analyses.

Task 2: Evaluation of the Causes and Mechanisms of IASCC in BWRs.

This task will evaluate the susceptibility of austenitic SSs and their welds to IASCC as a function of fluence level, water chemistry, material chemistry, welding process, and fabrication history. It will provide data and technical support required for determination of inspection intervals. The purpose is to help NRC address various issues that arise in license renewal or other licensee submittals. Crack growth rate (CGR) tests and slow strain rate tests (SSRTs) will be conducted on high–fluence model SSs from Halden Phase–I irradiations (carried out under NRC FIN W6610) to investigate the effects of material chemistry and irradiation level on the susceptibility of SSs to IASCC. CGR tests will be conducted on submerged arc (SA) and shielded metal arc (SMA) welds of Type 304 and 304L steels irradiated to 1.2 x 10^{21} n/cm^2 in the Halden reactor to establish the effects of fluence level, material chemistry, and welding process on IASCC. Also, SSRTs and CGR tests will be carried out on grain boundary optimized (GBO) model SS alloys to study the effect of grain boundary geometry on IASCC and assess the

prospect of using GBO as a mitigative measure. Models and codes developed under CIR and from industry sources will be benchmarked and used in conjunction with this work.

Industry-developed crack growth models will be analyzed and assessed. Also, the effectiveness of mitigative water chemistry measures, e.g., hydrogen water chemistry or noble metal additions, will be assessed. Much of this assessment will depend on data provided by industry, data available in the literature, and developed as part of this task. However, for CGR models for irradiated materials, it is anticipated that relatively few data will be available because of the expense and difficulty of testing. Additional testing on nonirradiated materials will be performed to provide "limiting cases" against which the models can be tested. These tests will seek to determine the effects of Cr level in the steel and cold work on CGRs in austenitic SSs in LWR environments. This will be accomplished by procuring material and fabricating and testing compact–tension (CT) specimens from model SS alloys with low Cr content and cold–worked (CW) Type 304L and 304 SS.

Task 3: Evaluation of Causes and Mechanisms of IASCC of Austenitic SS in PWRs.

The task will evaluate (a) the effects of very high fluence on CGRs, (b) neutron irradiation embrittlement, e.g., loss of fracture toughness, and (c) void swelling behavior in austenitic SSs. Tests will be conducted on material procured from the EBR–II reactor hexagonal fuel channels or irradiated in the BOR–60 reactor in Russia and shipped to Argonne.

Task 4: Cracking of Nickel Alloys and Weldments.

The objective of this task is to provide the NRC with technical data on the implications of cracks in Ni–alloy components and weldments for residual life, inspection, and repair. Many reactor vessel internal components and their attachment welds, vessel penetrations, and piping butt welds are made of alloys such as Alloy 600, Alloy X750, and Alloy 182, which are susceptible to intergranular stress corrosion cracking (IGSCC). The causes and mechanisms of this cracking and the implications of microstructure, microchemistry, and surface finish for component life are also not well understood, and thus lead to greater uncertainty in licensee submissions that address issues such as damage accumulation and inspection intervals. The NRC research program will address these issues and provide data required to support staff assessment of industry CGR models, and potential crack detection and mitigation measures.

Task 5: Investigation of Other Modes of Degradation in High–Fluence Materials in PWR Environments.

Research at Saclay, France, has shown that gas generation in high fluence materials can produce unexpected changes in material behavior. Because studies on materials at high fluences and at temperatures of interest to LWRs are relatively limited, additional degradation phenomena beyond those studied in detail in the other tasks are possible. The work in this task would seek to study, in cooperation with staff at Saclay and others in the CIR, the potential for other degradation phenomena.

2 Environmental Effects on Fatigue Crack Initiation in Carbon and Low–Alloy Steels and Austenitic Stainless Steels (O. K. Chopra and B. Alexandreanu)

2.1 Introduction

Cyclic loadings on a structural component occur because of changes in mechanical and thermal loadings as the system goes from one load set (e.g., pressure, temperature, moment, and force loading) to any other load set. For each load set, an individual fatigue usage factor is determined by the ratio of the number of cycles anticipated during the lifetime of the component to the allowable cycles. Figures I–9.1 through I–9.6 of Appendix I to Section III of the ASME Boiler and Pressure Vessel Code specify fatigue design curves that define the allowable number of cycles as a function of applied stress amplitude. The cumulative usage factor (CUF) is the sum of the individual usage factors, and the ASME Code Section III requires that the CUF at each location must not exceed 1.

The ASME Code fatigue design curves, given in Appendix I of Section III, are based on strain–controlled tests of small polished specimens at room temperature in air. The design curves have been developed from the best–fit curves to the experimental fatigue–strain–vs.–life (ε–N) data that are expressed in terms of the Langer equation[1] of the form

$$\varepsilon_a = A1(N)^{-n1} + A2, \quad (1)$$

where ε_a is the applied strain amplitude, N is the fatigue life, and A1, A2, and n1 are coefficients of the model. Equation 1 may be written in terms of stress amplitude S_a instead of ε_a, in which case stress amplitude is the product of ε_a and elastic modulus E, i.e., $S_a = E\,\varepsilon_a$. The fatigue design curves were obtained from the best–fit curves by first adjusting for the effects of mean stress on fatigue life and then reducing the fatigue life at each point on the adjusted curve by a factor of 2 on strain (or stress) or 20 on cycles, whichever is more conservative.

The factors of 2 and 20 are not safety margins but rather conversion factors that must be applied to the experimental data to obtain reasonable estimates of the lives of actual reactor components. Although the Section III criteria document[2] states that these factors were intended to cover such effects as environment, size, and scatter of data, Subsection NB–3121 of Section III of the Code explicitly notes that the data used to develop the fatigue design curves (Figs. I–9.1 through I–9.6 of Appendix I to Section III) did not include tests in the presence of corrosive environments that might accelerate fatigue failure. Article B–2131 in Appendix B to Section III states that the owner's design specifications should provide information about any reduction to fatigue design curves that has been necessitated by environmental conditions.

The existing fatigue ε–N data illustrate potentially significant effects of light water reactor (LWR) coolant environments on the fatigue resistance of carbon and low–alloy steels,[3–5] as well as austenitic stainless steels (SSs).[4–7] Under certain environmental and loading conditions, fatigue lives of austenitic SSs can be a factor of 20 lower in water than in air.[6]

In LWR environments, the fatigue lives of austenitic SSs depend on applied strain amplitude, strain rate, temperature, and dissolved oxygen (DO) in water. A minimum threshold strain is required for inducing an environmentally assisted decrease in the fatigue life.[7] Environmental effects on life occur primarily during the tensile–loading cycle and at strain levels greater than the threshold value. Strain rate

and temperature have a strong effect on fatigue life in LWR environments.[6,7] Fatigue life decreases logarithmically with decreasing strain rate below 0.4%/s; this effect vanishes at 0.0004%/s. In addition, the fatigue ε–N data suggest a threshold temperature of 150°C; in the range of 150–325°C, the logarithm of life decreases linearly with temperature. The effect of DO on fatigue life may depend on the composition and heat treatment of the steel. Limited data indicate that, in high–DO water, the environmental effects are influenced by the material heat treatment.[7] In low–DO water, the material heat treatment seems to have little or no effect on the fatigue life of austenitic SSs.

This section presents experimental data on the effect of heat treatment on fatigue crack initiation in austenitic SS in LWR coolant environments. Fatigue tests have been conducted on two heats of Type 304 SS under various conditions to determine the effect of heat treatment on fatigue crack initiation in these steels in air and LWR environments. A detailed metallographic examination of the fatigue test specimens was performed to characterize the crack morphology and fracture morphology in austenitic SSs in air, as well as BWR and PWR environments.

2.2 Experimental

Fatigue tests have been conducted on two heats of Type 304 SS in the mill–annealed (MA) as well as MA plus additional heat treatment conditions. The chemical compositions of the heats are given in Table 1. Heat 10285 was heat treated at 600°C for 24 h whereas two heat treatments were used for Heat 30956: 0.67 h at 700°C and 24 h at 700°C. These heat treatments correspond to EPR (electrochemical potentiodynamic reactivation) values of ≈16 C/cm^2 for Heat 10285,[8] and ≈8 and 30 C/cm^2, respectively, for Heat 30956.[9]

Table 1. Composition (wt.%) of austenitic stainless steels for fatigue tests

Material	Source	C	P	S	Si	Cr	Ni	Mn	Mo
Type 304[a]	Supplier	0.060	0.019	0.007	0.48	18.99	8.00	1.54	0.44
Type 304[b]	Supplier	0.060	0.025	0.011	0.59	18.31	8.51	1.58	0.38

[a]76 x 25 mm bar stock, Heat 30956. Solution annealed at 1050°C for 0.5 h.
[b]25–mm–thick plate, Heat 10285. Solution annealed at 1050°C for 0.5 h.

The metallographic examination of the sensitized alloys was carried out on 10 x 10 x 10–mm specimens that were ground and polished with SiC paper by successively increasing the grade of the paper up to #4000, then finishing with 1–μm diamond paste. Next, the samples were electrochemically etched in a solution of HNO_3 (10%) and distilled water at 8 V for ≈15 s. The microstructure was examined by scanning electron microscopy (SEM) in a JEOL JSM–6400 microscope.

Typical photomicrographs obtained from the sensitized alloys are shown in Fig. 1. Etching revealed a partially sensitized microstructure for the MA Heat 30956 that was heat treated for 0.67 h at 700°C. This is most evident in the higher–magnification photomicrograph (Fig. 1b) showing that sensitization occurred selectively, most likely at curved, high–energy boundaries. A somewhat more uniform degree of sensitization was observed in MA Heat 10285 (heat–treated for 24 h at 600°C), where almost all non-twin boundaries were sensitized. Stringers, also observed in this heat, most likely were parts of the microstructure before the sensitization treatment. Sensitization of Heat 30956 for 24 h at 700°C affected all of the boundaries, especially the curved, high–energy ones; also, it appears that some incoherent twin boundaries were also affected (Fig. 1f).

Heat 30956, mill annealed plus heat treated 0.67 h at 700°C

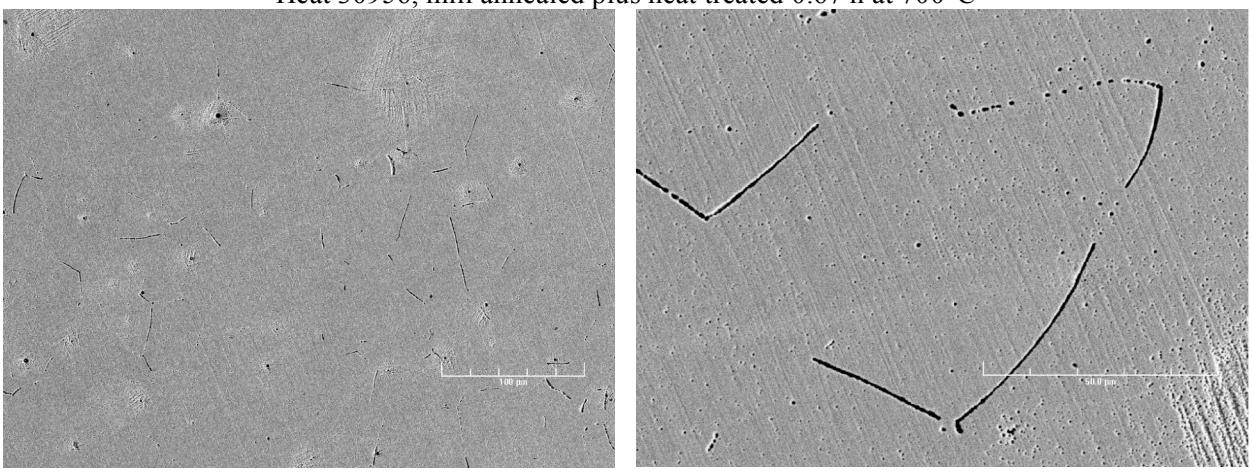

(a) (b)

Heat 10285, mill annealed plus heat treated 24 h at 600°C

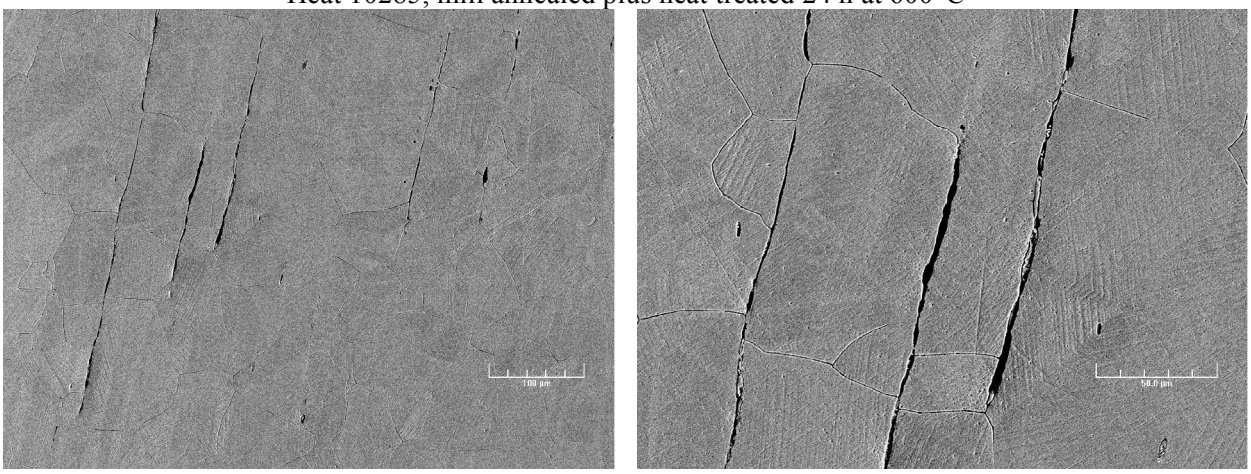

(c) (d)

Heat 30956, mill annealed plus heat treated 24 h at 700°C

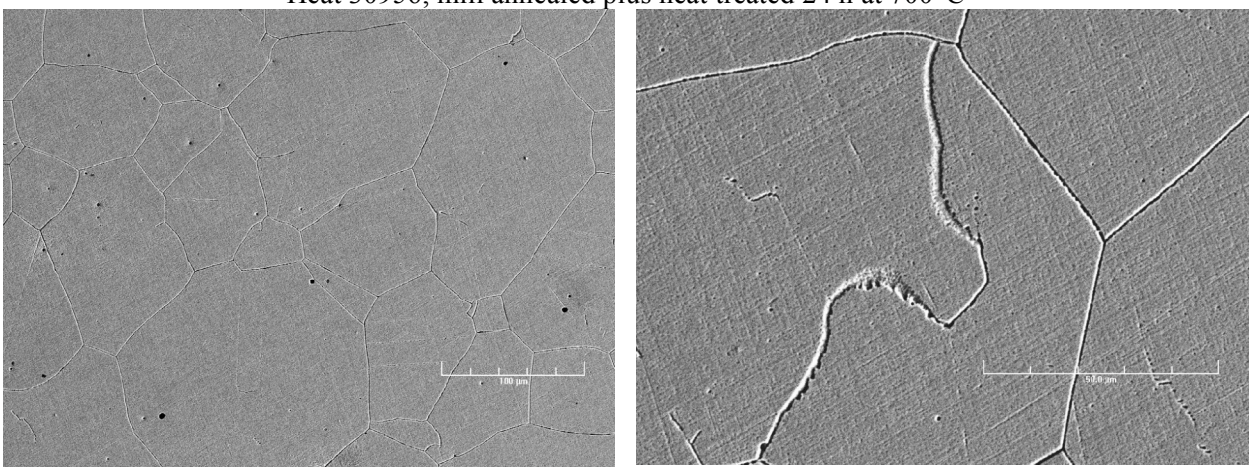

(e) (f)

Figure 1. Typical microstructures observed by SEM, showing degree of sensitization for alloys used in this study: (a), (c), (e), low magnification; (b), (d), (f), high magnification.

Smooth cylindrical specimens, with a 9.5–mm diameter and a 19–mm gauge length, were used for the fatigue tests (Fig. 2). The test specimens were machined from a composite bar fabricated by electron–beam welding of two 19.8–mm–diameter, 137–mm–long pieces of Type 304 SS bar stock on to each side of an 18.8–mm–diameter, 56–mm–long section of the test material, Fig. 3. The gauge section of the specimens was oriented along the rolling direction for the bar and plate stock. The gauge length of all specimens was given a 1–μm surface finish in the axial direction to prevent circumferential scratches that might act as sites for crack initiation.

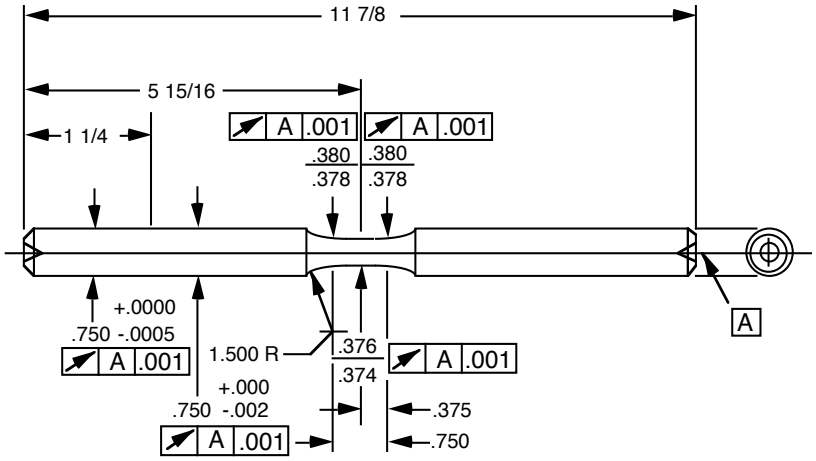

Figure 2. Configuration of fatigue test specimen (all dimensions in inches).

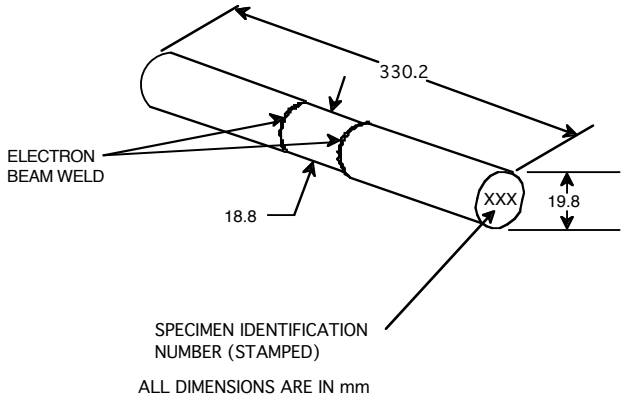

Figure 3. Schematic diagram of electron–beam–welded bar for machining A302–Gr B fatigue test specimens.

Tests in water were conducted in a 12–mL autoclave equipped with a recirculating water system. All tests were conducted at 288°C, with fully reversed axial loading and a triangular or sawtooth waveform. A detailed description of the test facility and test procedures has been presented earlier.[6]

Following testing, ≈10–mm–long sections that contained the fracture surface were cut from the gauge length. These were further stripped of oxides by boiling in a 20 wt.% NaOH and 3 wt.% $KMnO_4$ solution, followed by boiling in a 20 wt.% $(NH_4)_2C_6H_6O_7$ solution. The samples were examined by SEM. Special attention has been paid to crack morphology at the sites of initiation on the fracture surface, and the occurrence of striations. Also, lateral surfaces were inspected to determine the morphology of lateral cracks.

2.3 Results – Effect of Heat Treatment on Fatigue Life

2.3.1 Fatigue ε–N Behavior

Several fatigue tests have been completed on two heats of Type 304 SS under various heat–treatment conditions. These specimens were tested in air and simulated BWR and PWR environments at 289°C. The results from these tests and data obtained earlier on MA Heat 30956 are given in Table 2.

Table 2. Fatigue test results for Type 304 stainless steel in air and simulated BWR and PWR environments at 289°C

Test No.	Spec. No.	Environ-ment[a]	Dis. Oxygen[b] (ppb)	pH at RT[c]	Conduct-ivity[b] (μS/cm)	ECP Pt[b] mV (SHE)	ECP SS[b] mV (SHE)	Ten. Rate (%/s)	Comp. Rate (%/s)	Stress Amp. (MPa)	Strain Amp. (%)	Life N_{25} (Cycles)
	Heat 30956 MA											
1805	309-03	Air	–	–	–	–	–	4.0E-3	4.0E-1	234.0	0.38	14,410
1853	309-22	BWR	880	6.0	0.06	248	155	4.0E-3	4.0E-1	233.3	0.38	12,300
1856	309-24	BWR	870	6.2	0.07	272	163	4.0E-3	4.0E-1	236.8	0.38	10,450
1808	309-06	PWR	4	6.4	18.87	-693	-690	4.0E-3	4.0E-1	234.2	0.39	2,850
1821	309-09	PWR	2	6.5	22.22	-700	-697	4.0E-3	4.0E-1	237.2	0.38	2,420
1859	309-28	PWR	2	6.5	18.69	-699	-696	4.0E-3	4.0E-1	235.9	0.38	2,420
Heat 30956 MA plus 0.67 h at 700°C												
1893	309-43	Air	–	–	–	–	–	4.0E-3	4.0E-1	236.9	0.38	17,000
1894	309-44	BWR	800	6.7	0.07	263	158	4.0E-3	4.0E-1	239.1	0.38	3,920
1899	309-46	BWR	800	6.2	0.06	285	126	4.0E-3	4.0E-1	241.4	0.38	3,740
1898	309-45	PWR	6	6.3	17.24	-677	-467	4.0E-3	4.0E-1	241.2	0.38	2,530
Heat 30956 MA plus 24 h at 700°C												
1891	309-47	Air	–	–	–	–	–	4.0E-3	4.0E-1	235.8	0.38	16,680
1892	309-48	BWR	860	–	0.06	257	119	4.0E-3	4.0E-1	237.3	0.39	2,790
1897	309-50	PWR	6	6.3	16.67	-629	-543	4.0E-3	4.0E-1	234.1	0.39	2,380
Heat 10285 MA plus 24 h at 600°C												
1895	102-07	Air	–	–	–	–	–	4.0E-3	4.0E-1	222.4	0.38	19,300
1896	102-09	BWR	800	–	0.1	265	206	4.0E-3	4.0E-1	222.2	0.39	1,665
1900	102-08	PWR	7	6.2	16.95	-522	-527	4.0E-3	4.0E-1	228.0	0.37	2,840

[a]PWR = simulated PWR water with 2 ppm Li, 1000 ppm B, and ≈2 ppm dissolved H_2 (or ≈23 cc/kg) in the feedwater; BWR = high-purity deionized water.
[b]Measured in effluent.
[c]RT = room temperature.

The effect of heat treatment on the fatigue life of Type 304 SS in air, BWR, and PWR environments is shown in Fig. 4. Fatigue life is plotted as a function of the EPR value for the various material conditions. The results indicate that heat treatment has little or no effect on the fatigue life of Type 304 SS in air and PWR environments. In a BWR environment, fatigue life is lower for the sensitized SSs. The decrease in life seems to increase with increasing EPR value.

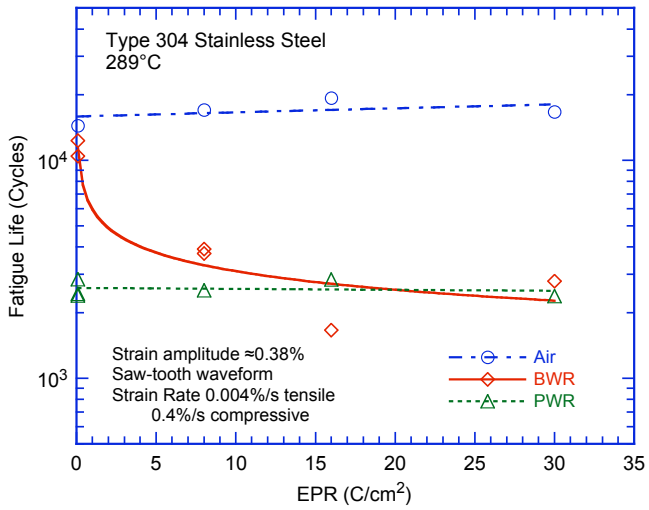

Figure 4.
Effect of material heat treatment on fatigue life of Type 304 stainless steel in air, BWR, and PWR environments at 289°C, ≈0.38% strain amplitude, sawtooth waveform, and 0.004%/s tensile strain rate.

These results are consistent with the data obtained at Mitsubishi Heavy Industries, Ltd. (MHI)[10–12] and Ishikawajima–Harima Heavy Industries Co. (IHI)[13] on solution–annealed and sensitized Type 304, 316, and 316NG SS (Figs. 5 and 6). For example, in low–DO (<0.005 ppm) water, environmental effects on the fatigue life of Type 304 and 316 SS are significant irrespective of material heat treatment (Fig. 5). In high–DO (8 ppm) water, the fatigue life of solution–annealed Type 304 SS is a factor of ≈2 longer than that of the sensitized steel (Fig 6a). A sensitization anneal appears to have little or no effect on the fatigue life of Type 316NG SS in high–DO water at 288°C (Fig. 6b). Fatigue lives of solution–annealed and sensitized Type 316NG SS are comparable.

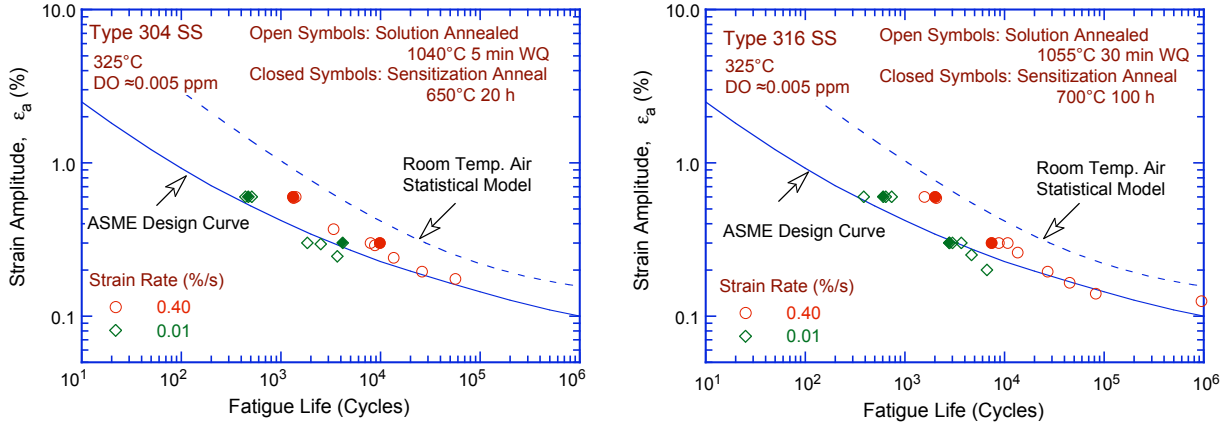

(a) (b)

Figure 5. Effect of sensitization annealing on fatigue life of Type (a) 304 and (b) 316 stainless steel in low–DO water at 325°C (Refs. 10,11). WQ = water quenched.

The cyclic stress response of the various materials in air, BWR, and PWR environments at 289°C is shown in Fig. 7. As expected, the cyclic strain–hardening behavior of Type 304 SS under various heat treatment conditions is identical; only the fatigue life varies in the environments.

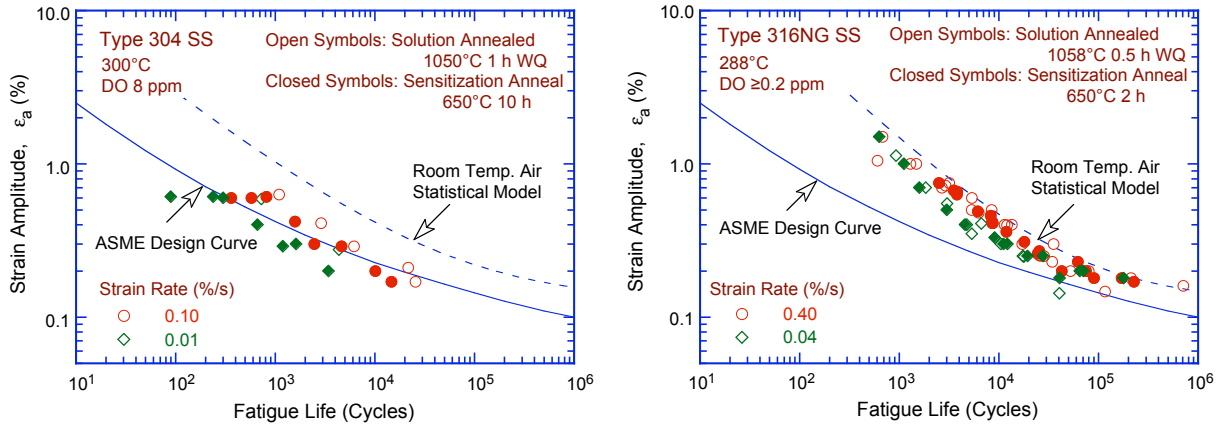

Figure 6. Effect of sensitization anneal on the fatigue lives of Type (a) 304 and (b) 316NG stainless steel in high–DO water (Refs. 12,13). WQ = water quenched.

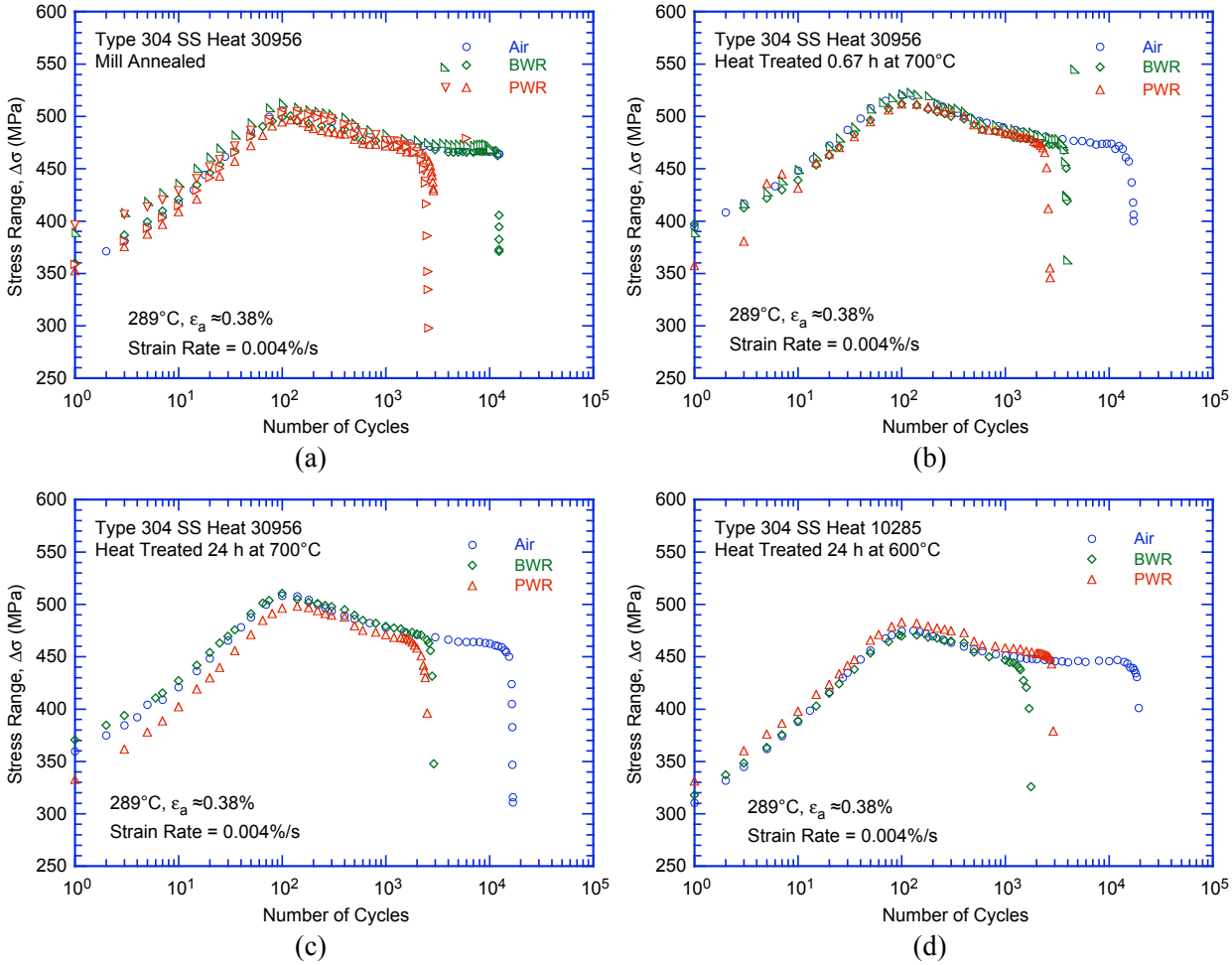

Figure 7. Cyclic stress response of Heat 30956: (a) MA, (b) MA + 0.67 h at 700°C, and (c) MA + 24 h at 700°C; and Heat 10285, (d) MA + 24 h at 600°C in air, BWR, and PWR environments at 289°C.

2.3.2 Fatigue Crack and Fracture Surface Morphology

A detailed metallographic evaluation of the fatigue test specimens was performed to characterize the crack and fracture morphology of the various heats under different heat treatment conditions. Figure 8 shows low– and high–magnification crack initiation sites on the fracture surfaces of the sensitized Type 304 SS tested in air. Apparently, irrespective of the degree of sensitization, the fracture mode for crack initiation (i.e., crack lengths up to ≈200 μm) and crack propagation (i.e., crack lengths >200 μm) is transgranular (TG), most likely along crystallographic planes, leaving behind relatively smooth facets. With increasing degree of sensitization, cleavage–like or stepped TG fracture (e.g., Figs. 8 c and d), and occasionally ridge structures were observed on the smooth surfaces (e.g., Figs. 8e and f).

The effect of a simulated normal–water chemistry BWR environment, Fig. 9, was to cause intergranular (IG) crack initiation, implying a weakening of the grain boundaries. In the BWR environment, the initial crack appeared IG under all heat–treated conditions. Photomicrographs of the fracture surface of the more heavily sensitized steel, e.g., Heat 30956 MA + 24 h at 700°C (Figs. 9g and h) and especially Heat 10285 MA + 24 h at 600°C (Figs. 9e and f), are good examples of smooth IG fracture. Furthermore, comparison of the four material conditions indicates that the extent of IG fracture increases with the degree of sensitization, at least through the MA + 24 h at 600°C condition, whereas MA + 24 h at 700°C appears to have a somewhat more mixed IG and TG morphology. Also, one effect of the BWR environment (Figs. 9a–h) was to cause IG crack initiation, implying a weakening of the grain boundaries. Nevertheless, for all four conditions tested, the initial IG mode transformed within <200 μm into a TG mode with cleavage–like features. By contrast, for all samples of Type 304 SS tested in PWR environments (Fig. 10), cracks initiated and propagated in a TG mode irrespective of the degree of sensitization. Prominent features of all fracture surfaces are highly angular, cleavage–like facets that exhibit well–defined "river" patterns. Intergranular facets were rare, mostly in the more heavily sensitized alloys. These observations suggest brittle behavior throughout the testing period.

Fatigue striations normal to the crack advance direction were clearly visible beyond ≈200 μm on the fracture surfaces of all materials under all environmental conditions, as documented in Figs. 11–14. For example, for the MA Heat 30956 samples tested in BWR water (Fig. 11), striations were easily discernible on the facets irrespective of the steps, cleavage–like features, or river patterns. Similar striations were also observed on the fracture surface of MA Heat 30956 heat–treated 0.67 h at 700°C irrespective of the testing environment (Fig. 12). Striations were found on both the TG and IG facets of the samples tested under BWR conditions, or co-existing with the "river" patterns specific to the samples tested in the PWR environment. Evidence of extensive rubbing due to repeated contact between the two mating surfaces (Figs. 12a and b) was also found.

Figure 13 shows fatigue striations observed on the fracture surface of MA Heat 10285 heat–treated 24 h at 600°C. In spite of the wide coverage with rubbing and fretting marks, striations are clearly observed on some facets. Figures 13e and f show striations on one IG facet in a sample tested in PWR conditions. The fracture surfaces of MA Heat 30956 heat–treated 24 h at 700°C are presented in Fig. 14. Low– and high–magnification photomicrographs are presented of fatigue striations on faceted, stepped TG, and cleavage–like fracture surfaces.

Air Environment

Heat 30956 mill annealed plus heat treated 0.67 h at 700°C

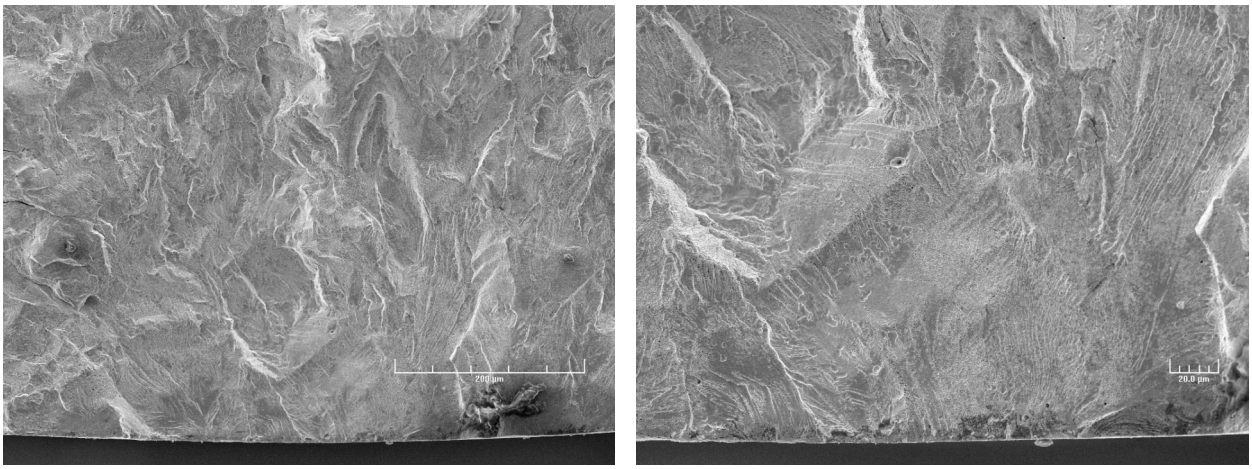

(a) (b)

Heat 10285 mill annealed plus heat treated 24 h at 600°C

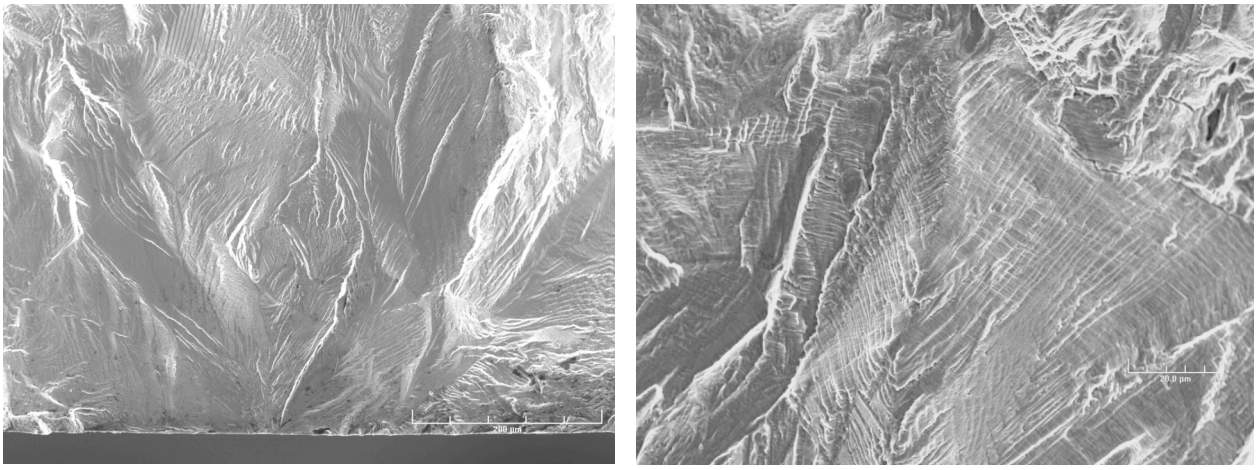

(c) (d)

Heat 30956 mill annealed plus heat treated 24 h at 700°C

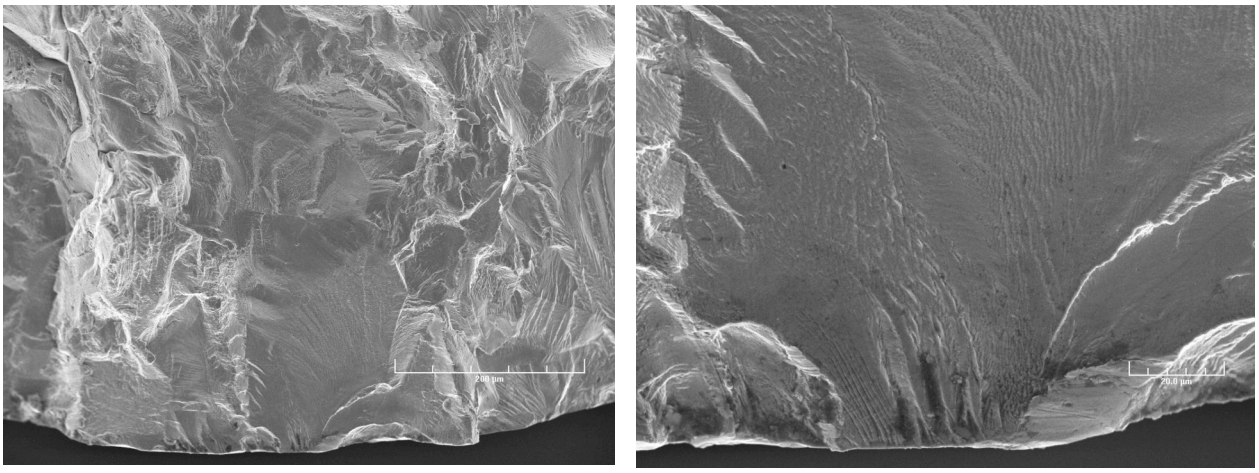

(e) (f)

Figure 8. Photomicrographs showing sites of crack initiation on fracture surfaces of Type 304 SS specimens tested in air: (a), (c), (e), low magnification; (b), (d), (f), high magnification.

Simulated BWR Environment

Heat 30956 mill annealed

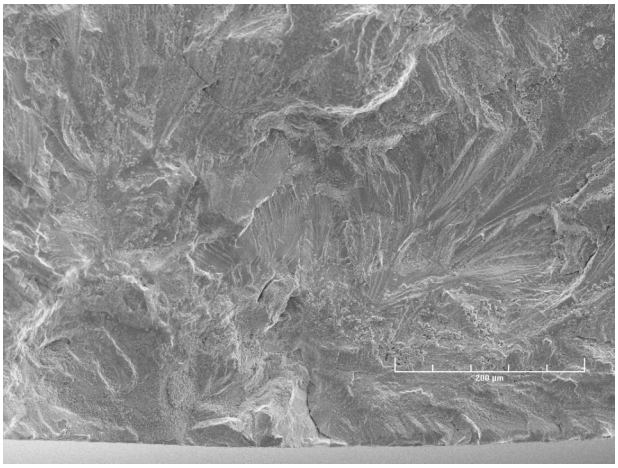

(a)

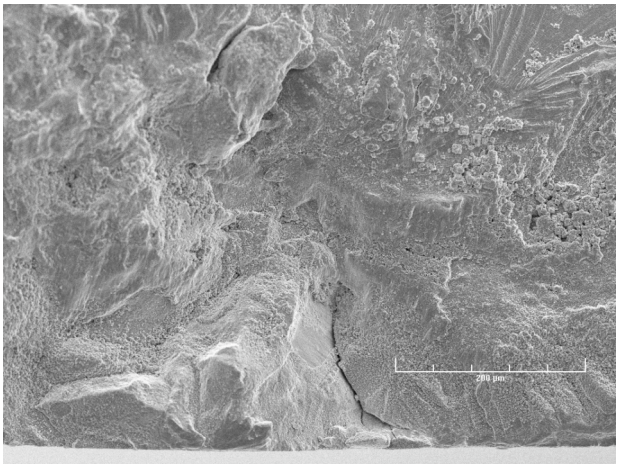

(b)

Heat 30956 mill annealed plus heat treated 0.67 h at 700°C

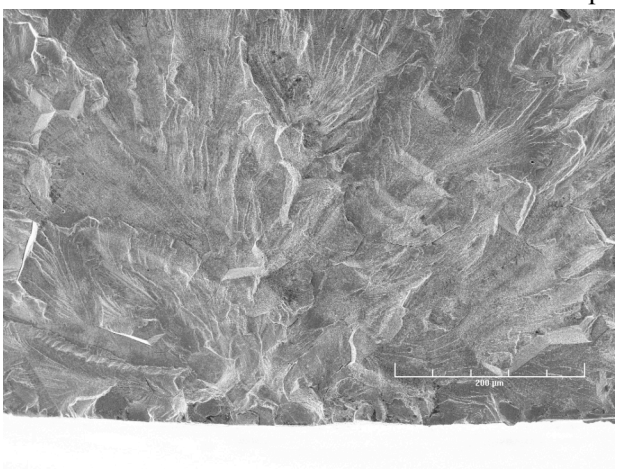

(c)

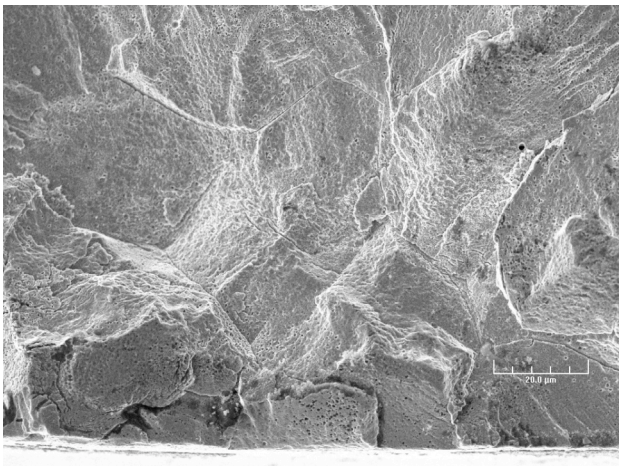

(d)

Heat 10285 mill annealed plus heat treated 24 h at 600°C

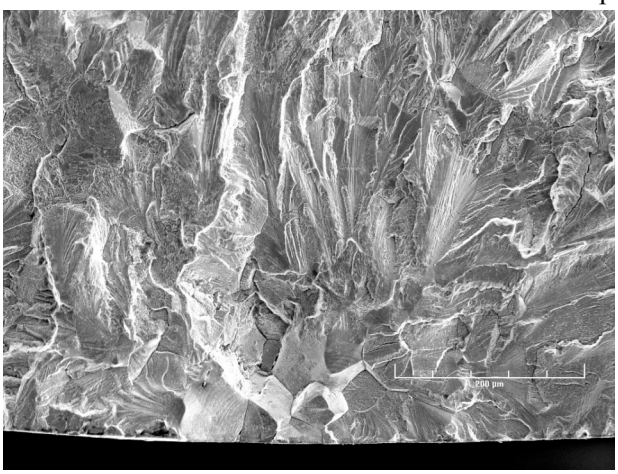

(e)

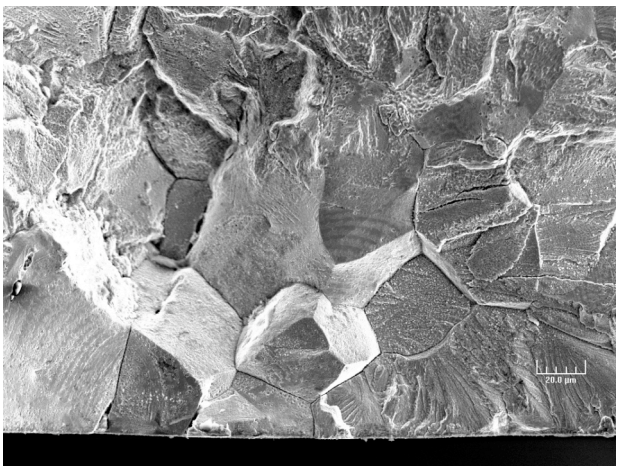

(f)

Heat 30956 mill annealed plus heat treated 24 h at 700°C

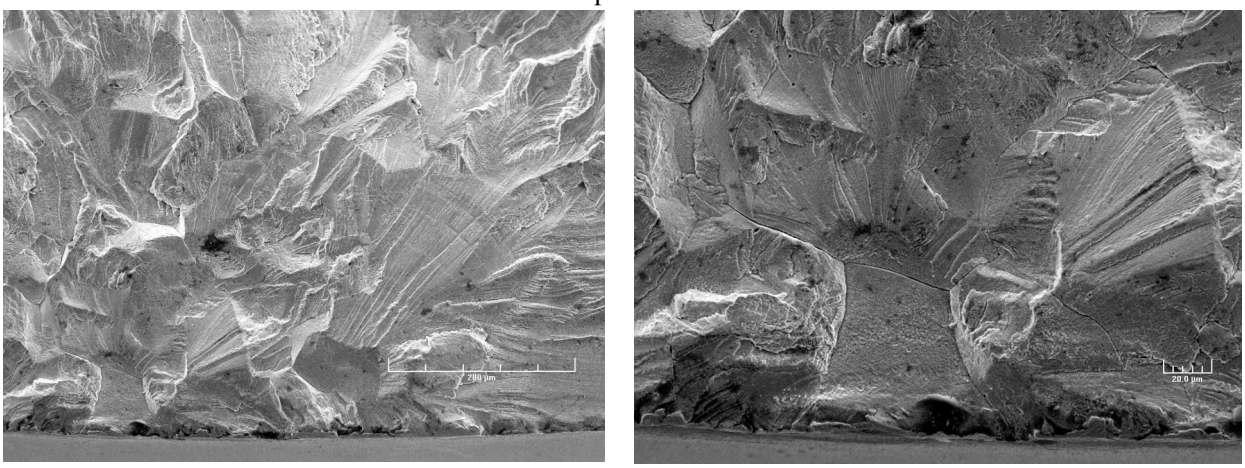

(g) (h)

Figure 9. Photomicrographs showing sites of crack initiation on fracture surfaces of Type 304 SS specimens tested in simulated BWR environment: (a), (c), (e), (g) low magnification; (b), (d), (f), (h) high magnification.

Simulated PWR Environment

Heat 30956 mill annealed

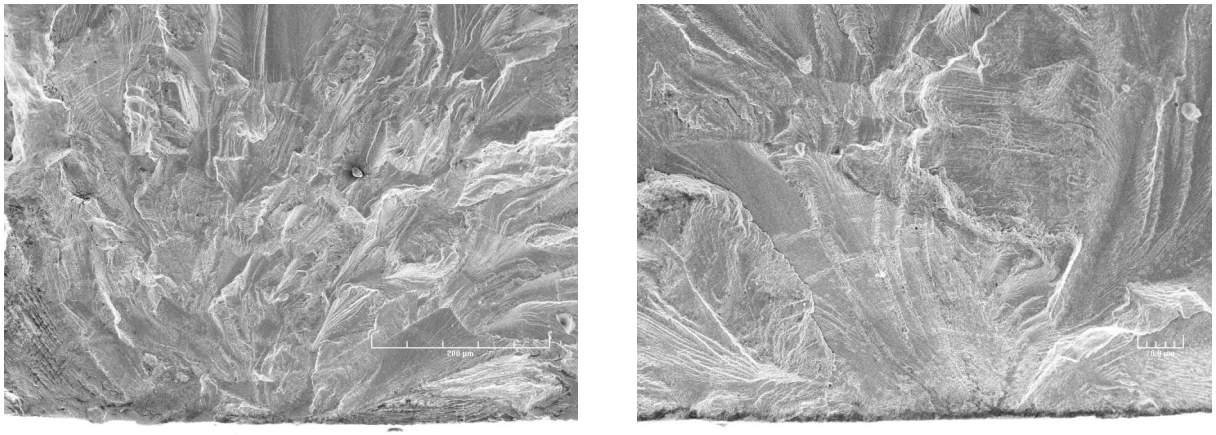

(a) (b)

Heat 30956 mill annealed plus 0.67 h at 700°C

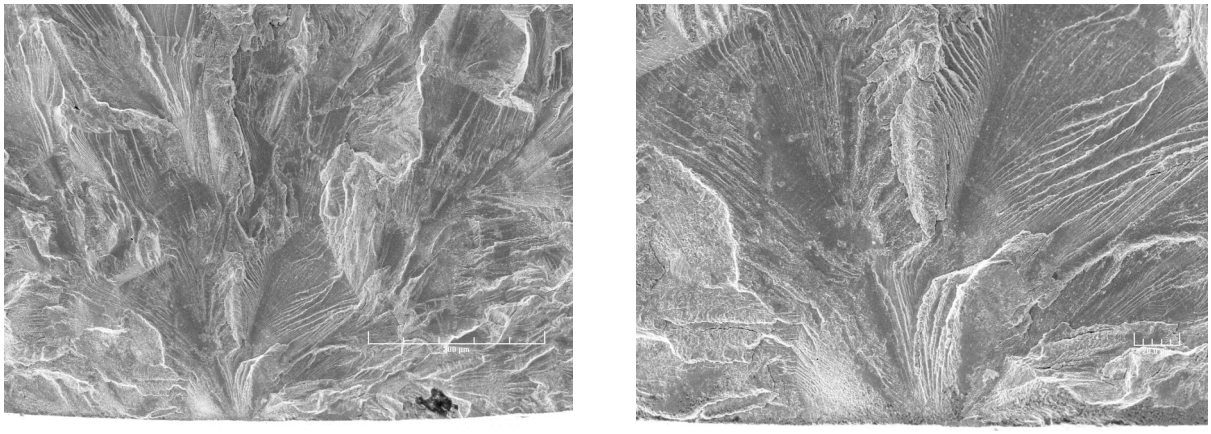

(c) (d)

Heat 10285 mill annealed plus 24 h at 600°C

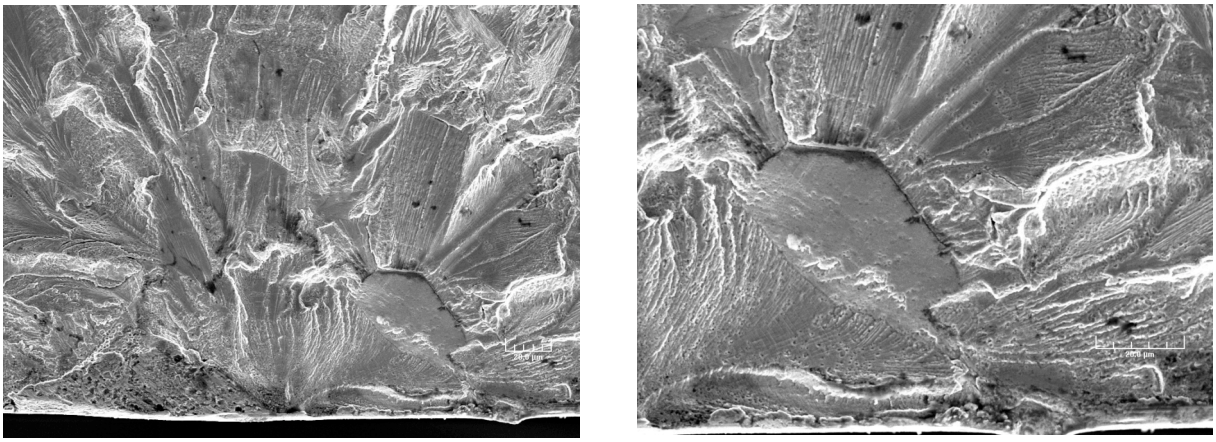

(e) (f)

Heat 30956 mill annealed plus 24 h at 700°C

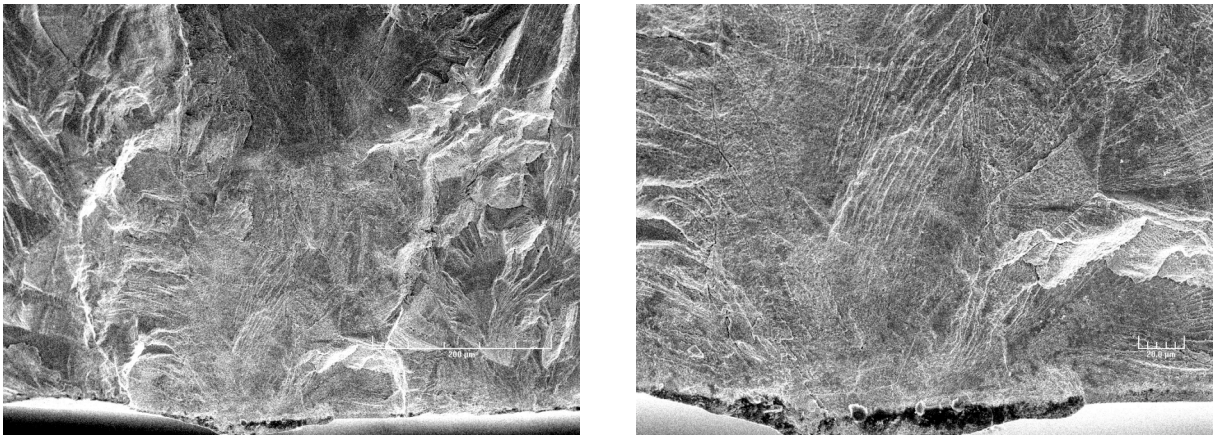

(g) (h)

Figure 10. Photomicrographs showing the sites of crack initiation on the fracture surfaces of Type 304 SS specimen tested in simulated PWR environment: (a), (c), (e), (g) low magnification; (b), (d), (f), (h) high magnification.

Simulated BWR environment

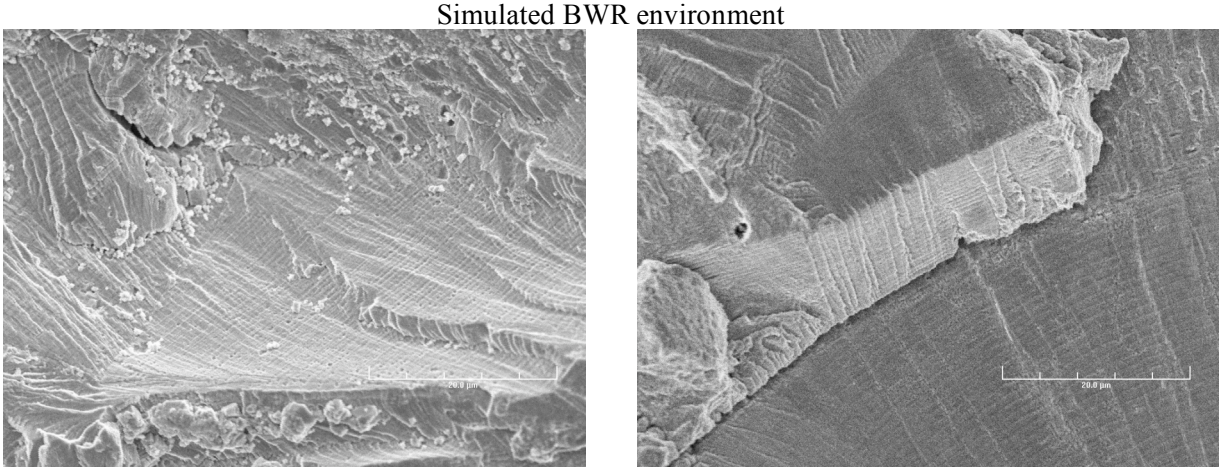

(a) (b)

Figure 11. (a) Low– and (b) high–magnification photomicrographs showing striations at select locations on fracture surfaces of MA specimen of Heat 30956 in simulated BWR environment.

Heat 30956 mill annealed plus 0.67 h at 700°C

Air Environment

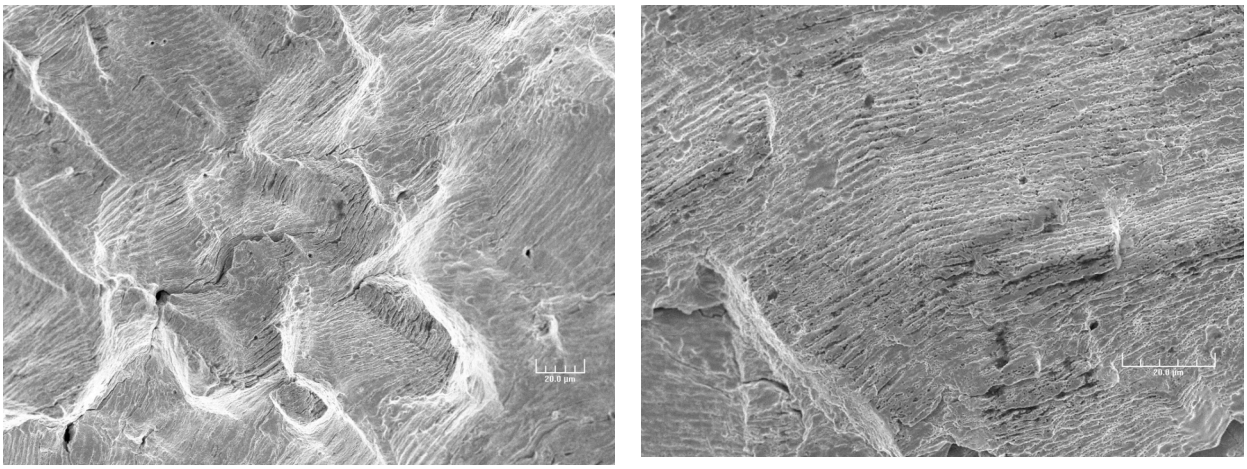

(a) (b)

Simulated BWR Environment

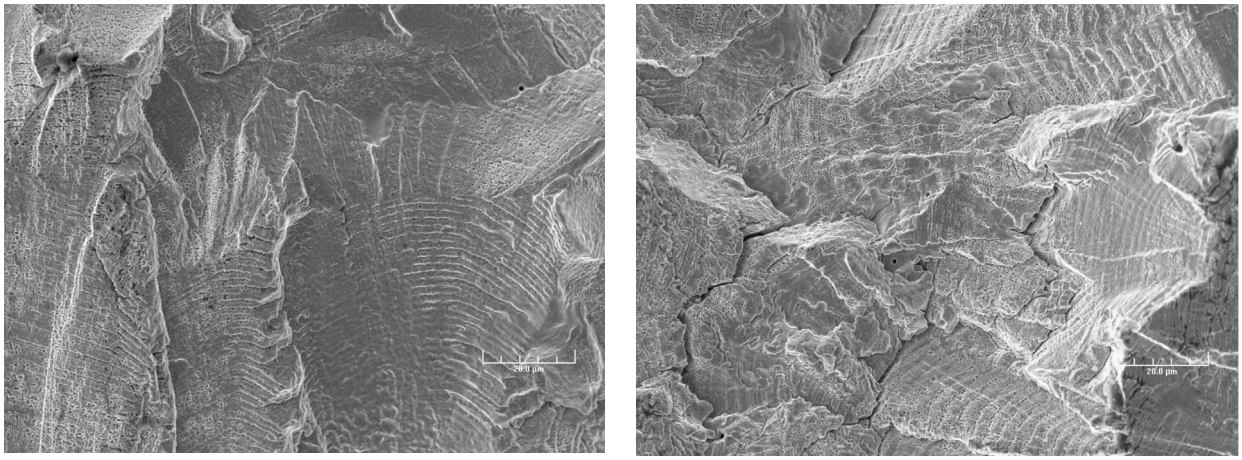

(c) (d)

Simulated PWR Environment

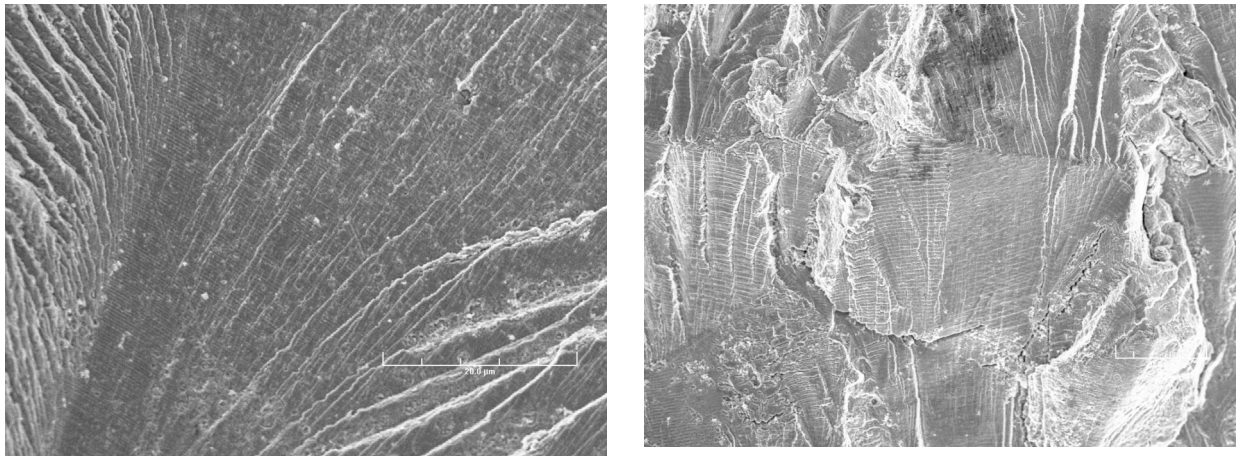

(e) (f)

Figure 12. Photomicrographs showing striations at select locations on fracture surfaces of MA specimens of Heat 30956 heat–treated for 0.67 h at 700°C in air, BWR, and PWR environments: (a), (c), (e) low magnification; (b), (d), (f) high–magnification.

Heat 10285 mill annealed plus 24 h at 600° C

Air Environment

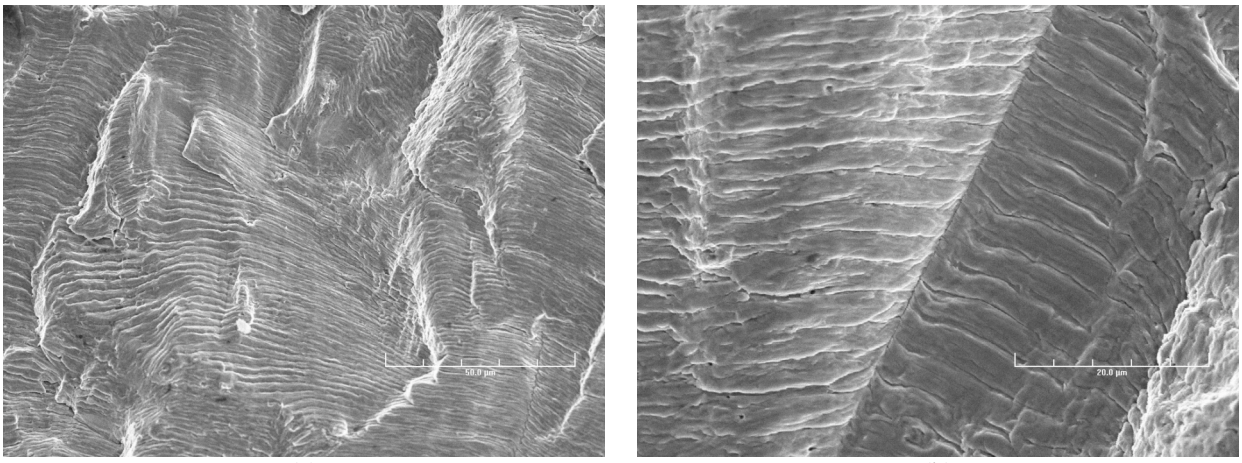

(a) (b)

Simulated BWR Environment

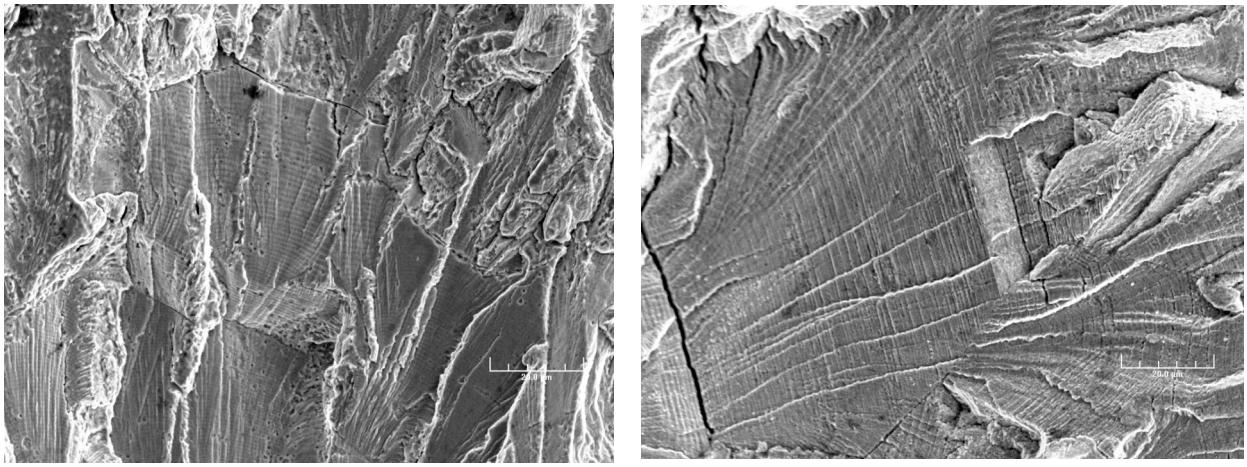

(c) (d)

Simulated PWR Environment

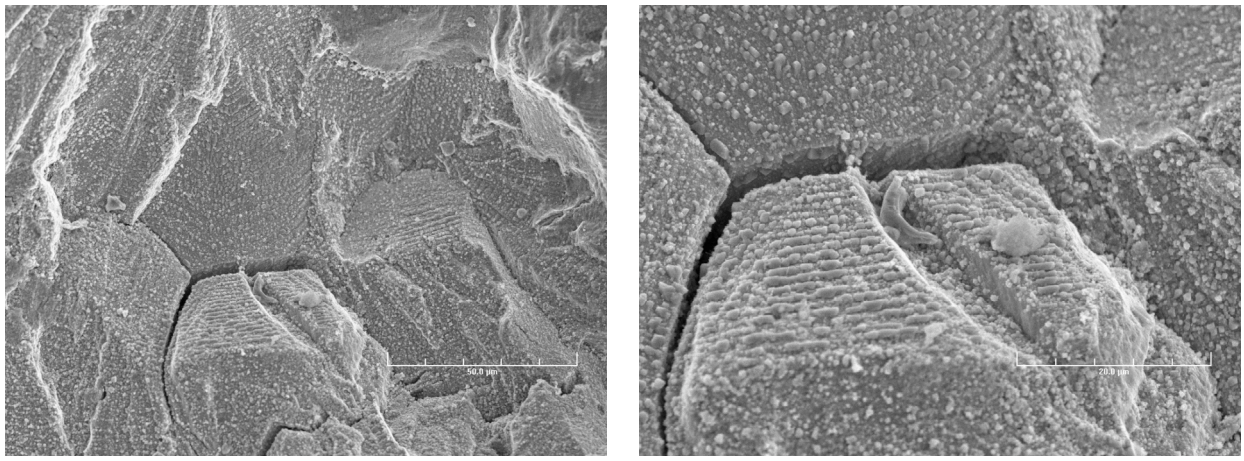

(e) (f)

Figure 13. Photomicrographs showing striations at select locations on fracture surfaces of MA specimens of Heat 10285 heat–treated for 24 h at 600°C in air, BWR, and PWR environments: (a), (c), (e) low magnification; (b), (d), (f) high–magnification.

Heat 30956 mill annealed plus 24 h at 700°C

Air Environment

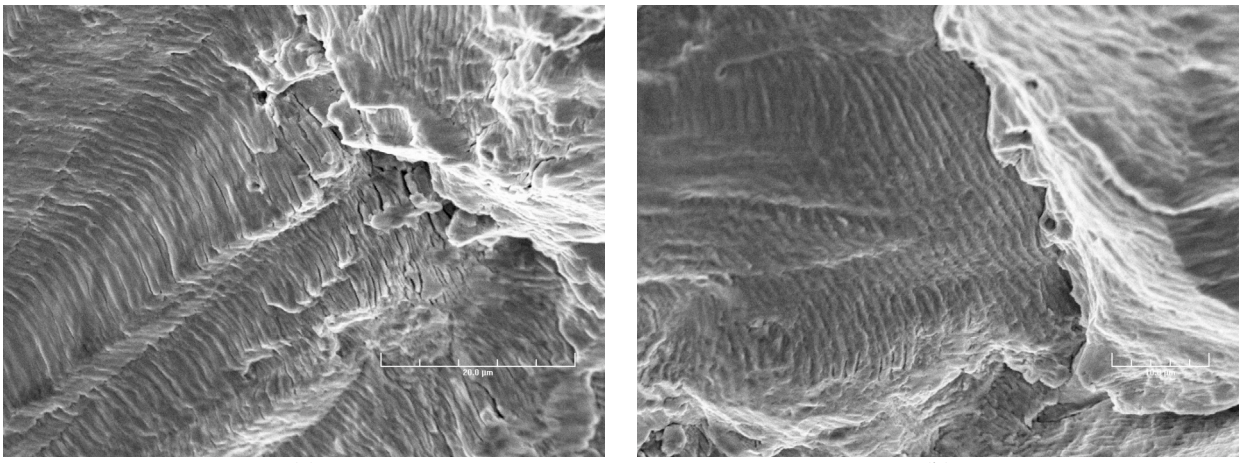

(a) (b)

Simulated BWR Environment

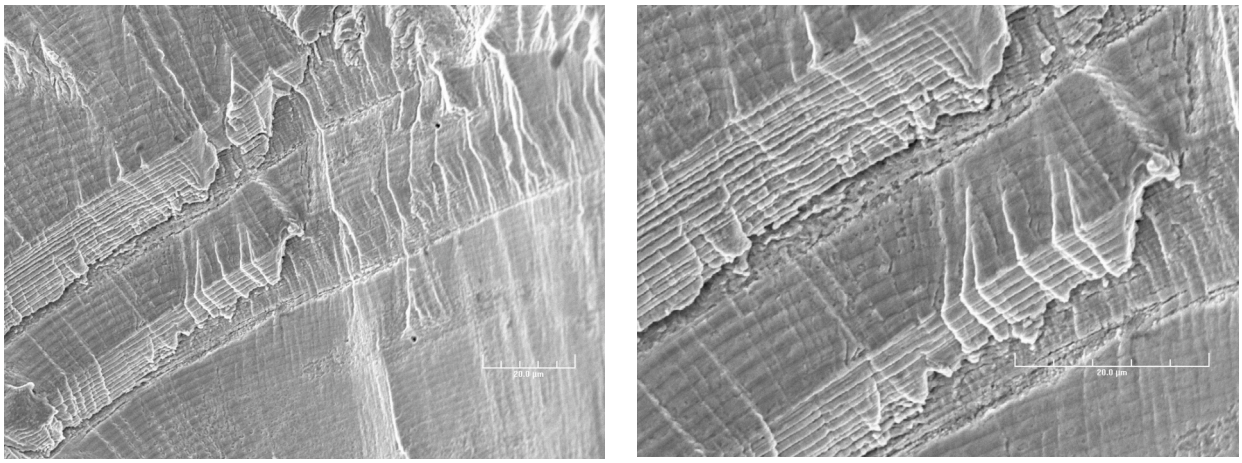

(c) (d)

Simulated PWR Environment

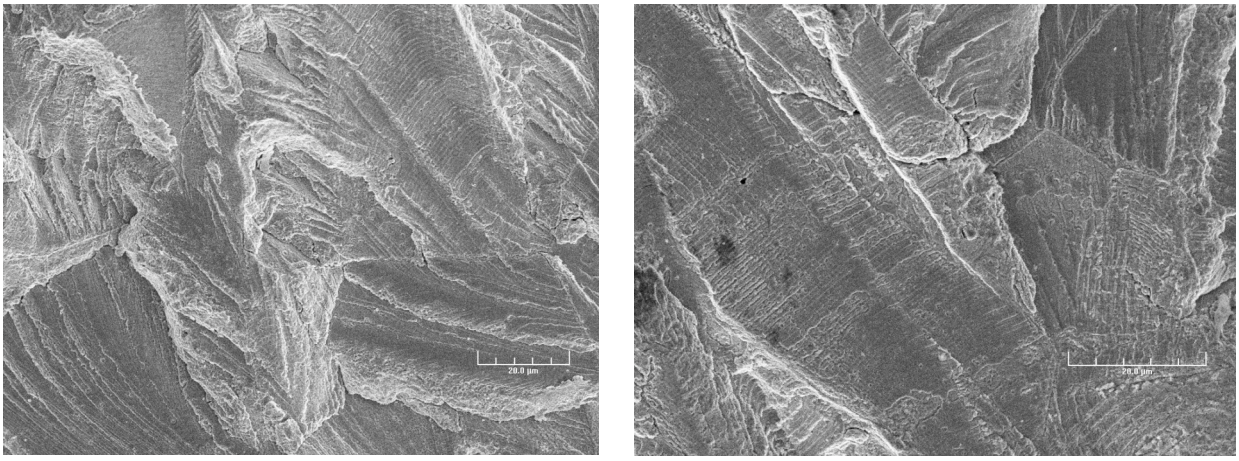

(e) (f)

Figure 14. Photomicrographs showing striations at select locations on fracture surfaces of MA specimens of Heat 30956 heat–treated for 24 h at 700°C in air, BWR, and PWR environments: (a), (c), (e) low magnification; (b), (d), (f) high–magnification.

Photomicrographs of the crack morphology of Type 304 SS under all test and environmental conditions are presented in Fig. 15. In all cases, the tensile axis is vertical, parallel to the plane of each picture. In general, for air tests the cracks are more likely to be oblique, approaching 45° with respect to the tensile axis. By contrast, the cracks that form in either BWR or PWR environments tend to be perpendicular to the tensile axis.

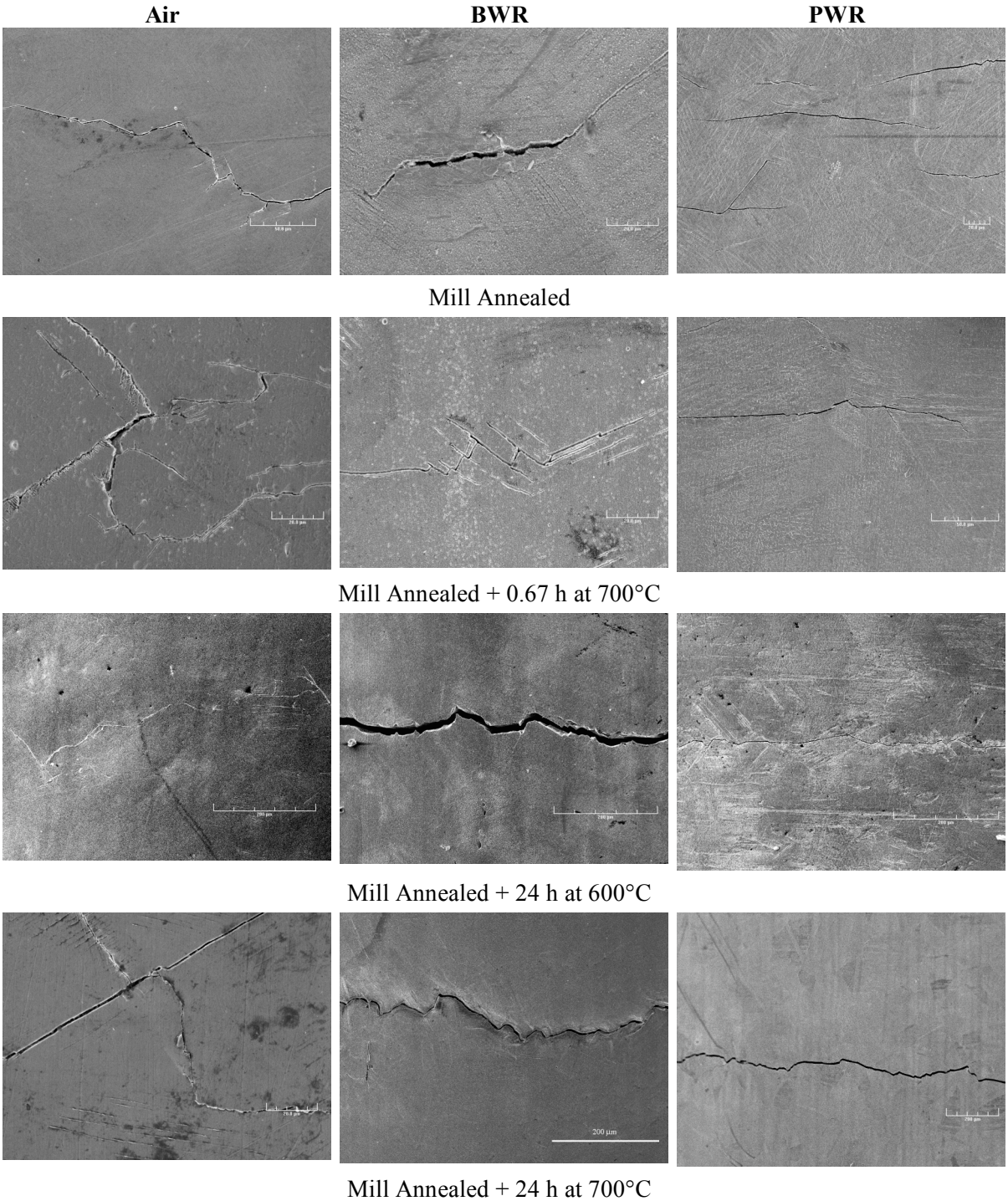

Figure 15. Photomicrographs of the crack morphology of Type 304 SS under all test and environmental conditions.

The metallographic evaluations of the fatigue test specimens may be summarized as follows. In air, cracking was initiated as TG, oblique with respect to the tensile axis. In BWR environments, cracking was initiated as IG, normal to the tensile axis. By contrast, in PWR environments cracking was initiated as TG, but still normal to the tensile axis. Cracking propagated as TG irrespective of the environment.

The crack and fracture morphology in Type 316NG SS specimens (Heat D432804) from earlier tests was also evaluated for comparison. Figure 16 shows, at low and high magnification, crack initiation sites on the fracture surfaces of Type 316NG specimens tested in air. Note that the cracks were initiated and propagated in the TG mode, most likely along crystallographic planes, leaving behind highly angular, cleavage–like or stepped surface features. Figures 16c and d show striations on some highly angular facets.

In a high–DO BWR environment, Fig. 17a–c, cracking was also initiated and propagated in TG mode, with riverlike patterns on the facets. Within 200 μm of the initiation site, fatigue striations were observed on some facets (Figs. 17b and c). Similarly, for specimens tested in a low–DO PWR environment (Fig. 17d), crack initiation and crack propagation are TG, with cleavage–like fracture facets

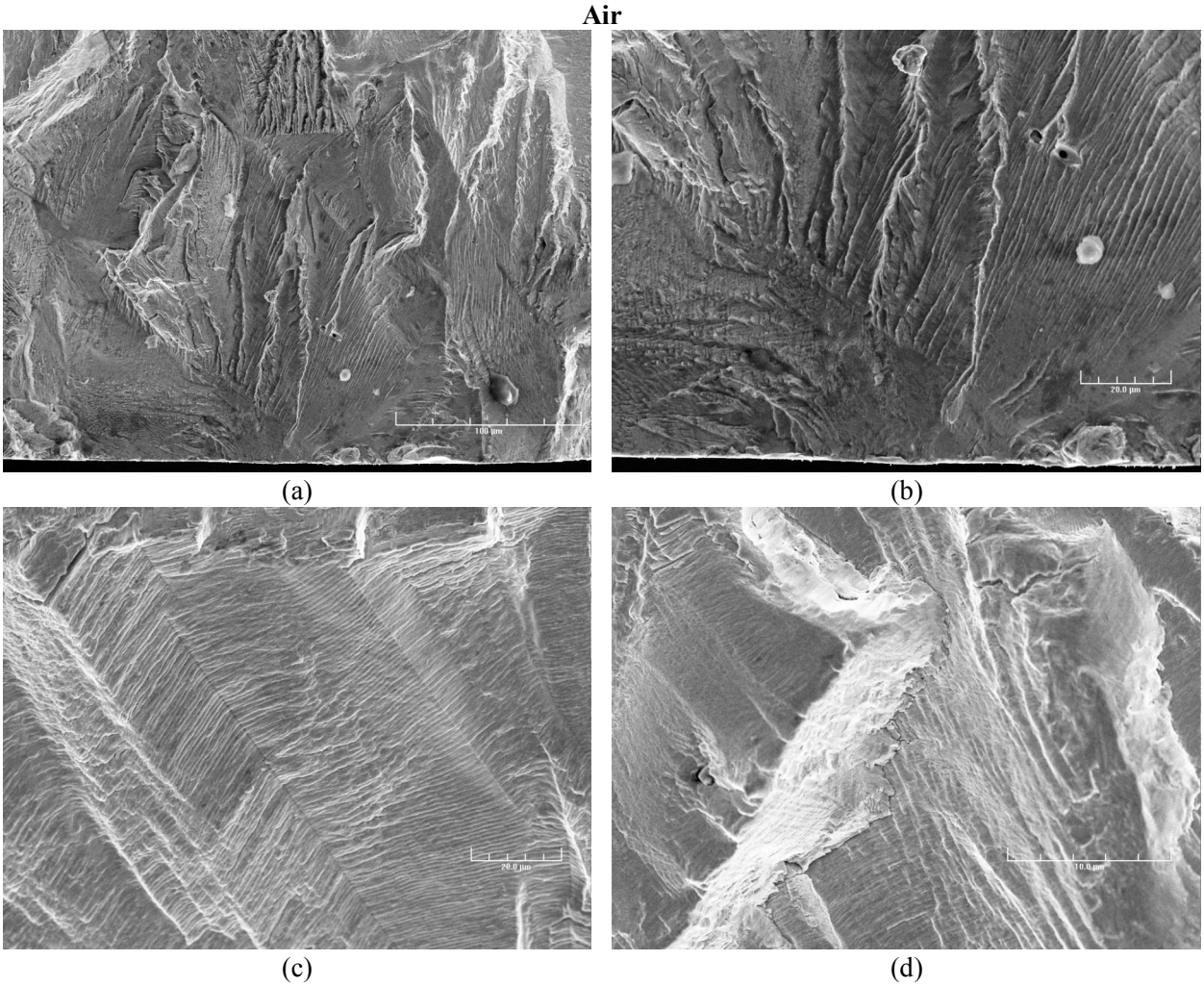

Figure 16. Photomicrographs showing crack initiation site at (a) low and (b) high magnification, and (c,d) striations at select locations in Type 316NG SS tested in air.

that exhibit river patterns. The higher magnification photomicrographs (at a location seen in Fig. 17d) show fatigue striations within 200 μm of the initiation site. Evidence of rubbing due to repeated contact between the two mating surfaces can also be observed in Fig. 17f.

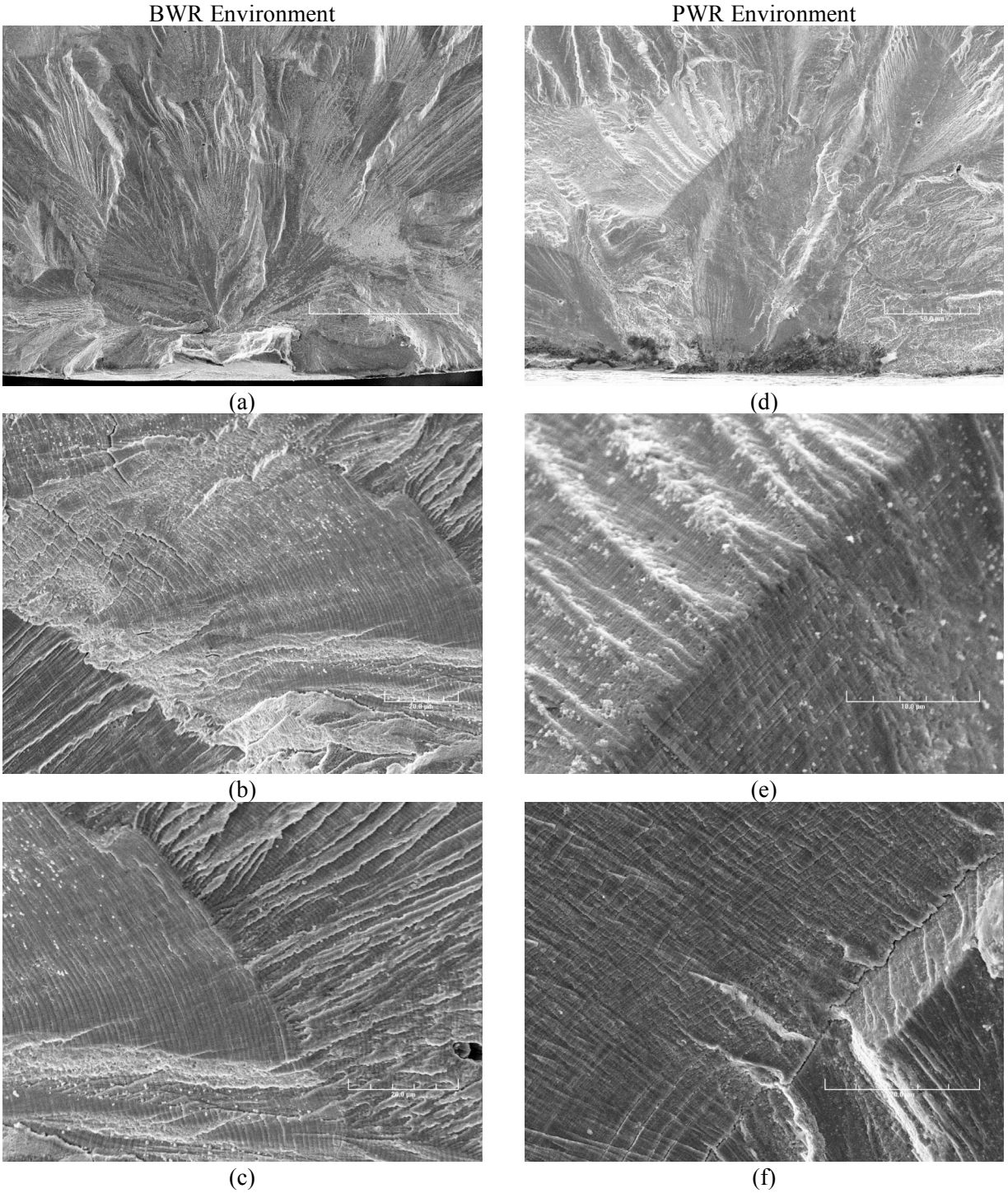

Figure 17. Photomicrographs showing crack initiation site and striations at select locations in Type 316NG SS tested in (a–c) BWR and (d–f) PWR environment.

Figure 18 presents photomicrographs that show the crack morphology in Type 316NG SS in three environments. In all cases, the tensile axis is vertical, parallel to the plane of each picture. The general appearance is that, for air tests, the cracks are more likely to be oblique, approaching 45° with respect to the tensile axis. By contrast, the cracks that formed in the BWR environment appeared mixed, both oblique and normal to the tensile direction, while the cracks that formed in the PWR environment appeared mostly perpendicular to the tensile axis.

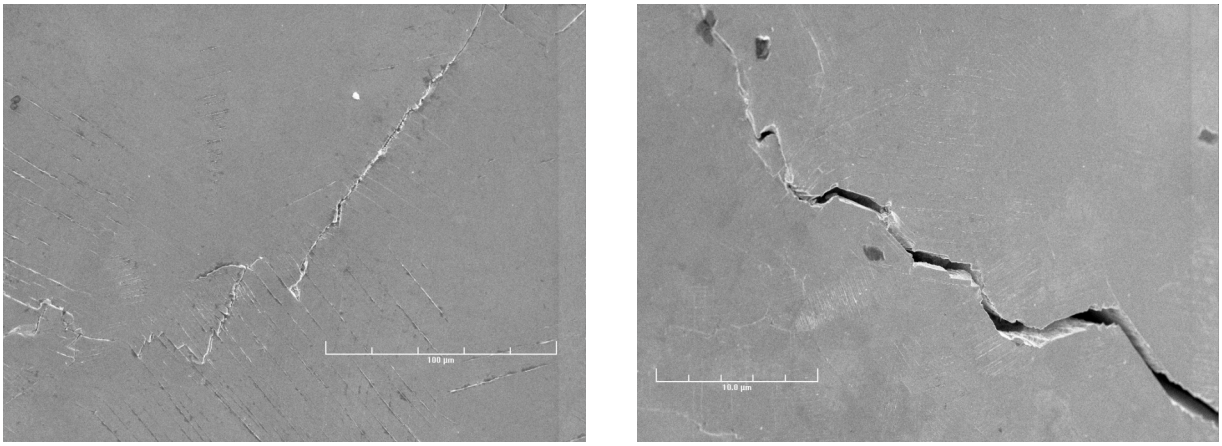

Air

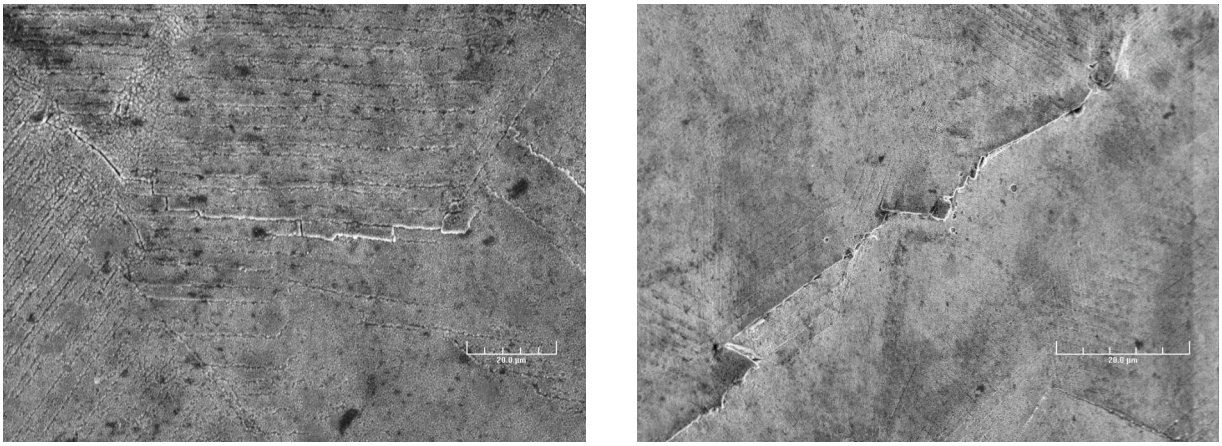

BWR Environment

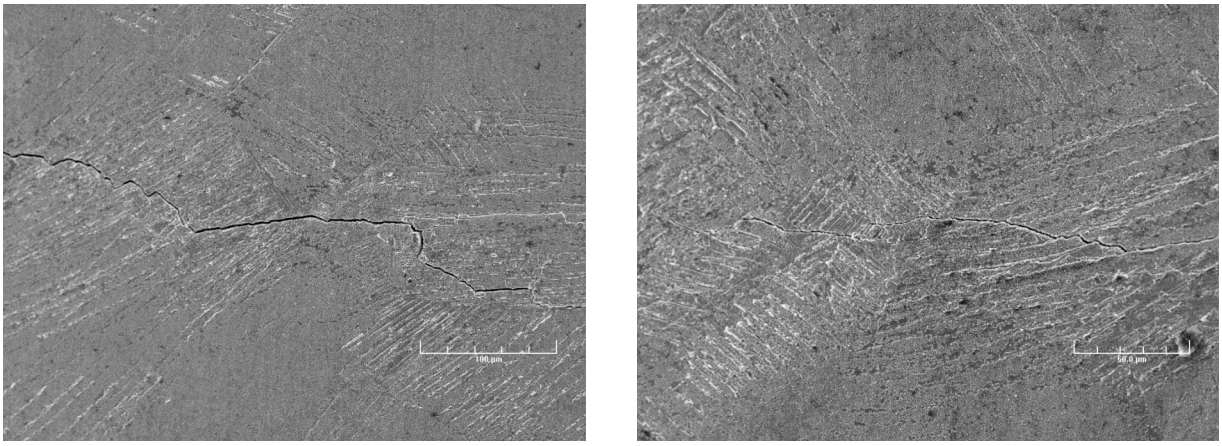

PWR Environment

Figure 18. Photomicrographs showing the morphology of lateral cracks formed in Type 316NG SS in three test environments.

3 Irradiation–Assisted Stress Corrosion Cracking of Austenitic Stainless Steel in BWRs

The susceptibility of austenitic SSs and their welds to IASCC as a function of the fluence level, water chemistry, material chemistry, welding process, and fabrication history is being evaluated. Crack growth rate (CGR) tests and slow strain rate tests (SSRTs) are being conducted on model SSs, irradiated at ≈288°C in a helium environment in the Halden boiling heavy water reactor, to investigate the effects of material chemistry and irradiation level on the susceptibility of SSs to IASCC. Crack growth tests will be conducted on irradiated specimens of submerged arc (SA) and shielded metal arc (SMA) welds of Types 304 and 304L SS to establish the effects of fluence level, material chemistry, and welding process on IASCC. Models and codes developed under CIR and from industry sources will be benchmarked and used in conjunction with this work. However, for crack–growth rate models for irradiated materials it is anticipated that relatively few data will be available because of the expense and difficulty of testing. Additional testing on nonirradiated materials will be performed to provide "limiting cases" against which the models can be tested. These tests will seek to determine the effects of Cr level in the steel and cold work on CGRs in austenitic SSs in LWR environments.

During this reporting period the results obtained in the present study from SSRT tests on irradiated austenitic SS alloys have been compared with data available in the literature. The IASCC–susceptible or –resistant behavior of austenitic SSs is represented in terms of a two–dimensional map of bulk S and C contents of the steels. Also, CGR data in BWR environments at 289°C are presented for (a) Heat C3 of Type 304L SS irradiated to 0.3 x 10^{21} n/cm^2 (0.45 dpa) and (b) nonirradiated SS weld HAZ specimens from the Grand Gulf (GG) reactor core shroud H5 weld and a laboratory–prepared weld.

3.1 Slow-Strain-Rate-Tensile Test of Model Austenitic Stainless Steels Irradiated in the Halden Reactor (H. M. Chung, R. V. Strain, and R. W. Clark)

3.1.1 Introduction

Failures of some BWR and PWR core internal components have been observed after accumulation of fast neutron fluences higher than ≈0.5 x 10^{21} n/cm^2 (E >1 MeV) (≈0.7 dpa) in BWRs and at fluences approximately an order of magnitude higher in PWRs. The general pattern of the observed failures indicates that as nuclear plants age and fluence increases, various nonsensitized austenitic stainless steels (SSs) become susceptible to intergranular (IG) failure. Failure of welded components (such as core shrouds fabricated from Type 304 or 304L SS) has also been observed in many BWRs, usually at fluence levels significantly lower than the threshold fluence for the solution-annealed base-metal components.

Although most failed components can be replaced, some safety–significant structural components (e.g., the BWR top guide, core shroud, and core plate) would be very difficult or costly to replace. Therefore, the structural integrity of these components has been a subject of concern, and extensive research has been conducted to gain an understanding of this type of degradation, which is commonly known as irradiation-assisted stress corrosion cracking (IASCC).[14–41]

Irradiation produces profound effects on local coolant water chemistry and component microstructure. Neutron irradiation causes alteration of microchemistry, microstructure, and mechanical properties of the core internal components, which are usually fabricated from ASTM Types 304, 304L, 316, or 348 SS. It produces defects, defect clusters, and defect-impurity complexes in grain matrices and

alters the dislocation and dislocation loop structures, leading to radiation-induced hardening, and in many cases, flow localization via dislocation channeling. It also leads to changes in the stability of second–phase precipitates and the local alloy chemistry near grain boundaries, precipitates, and defect clusters. Grain–boundary microchemistry significantly different from bulk composition can be produced in association with not only radiation–induced segregation, but also thermally driven equilibrium and nonequilibrium segregation of alloying and impurity elements.

Irradiation–induced grain–boundary depletion of Cr has been considered for many years to be the primary metallurgical process that leads to IASCC in BWRs. One of the most important factors that seem to support the Cr–depletion mechanism is the observation that the dependence on water chemistry (i.e., oxidizing potential) of intergranular stress corrosion cracking (IGSCC) of nonirradiated thermally sensitized material and of IASCC of BWR–irradiated solution–annealed material is similar.[14,17,18] Many investigators have also suggested that radiation–induced segregation of ASTM–specified impurities such as Si and P and other minor impurities not specified in the ASTM specification[21–36] has a role in the IASCC process. However, the exact mechanism of IASCC still remains unknown.

In general, IASCC is characterized by strong heat-to-heat variation in susceptibility, even among materials of virtually identical chemical compositions. This suggests that the traditional interpretation based on the role of grain-boundary Cr depletion alone may not completely explain the IASCC mechanism. An irradiation test program is being conducted to investigate systematically the effects of alloying and impurity elements (Cr, Ni, Si, P, S, Mn, C, N, and O) on the susceptibility of austenitic stainless steels to IASCC at several fluence levels.

In previous studies, SSRT tests and fractographic analysis were conducted on model austenitic SS alloys irradiated at 289°C to a "low-fluence" level of ≈0.3 x 10^{21} n/cm^2 (E > 1 MeV) (≈0.43 dpa), "medium-fluence" level of ≈0.9 x 10^{21} n/cm^2 (E > 1 MeV) (≈1.3 dpa),[41,42] and a "high-fluence" level of ≈2.0 x 10^{21} n/cm^2 (E > 1 MeV) (≈3.0 dpa).[43] Ten of the 11 heats were austenitic SS, and one was austenitic-ferritic SS containing ≈3 vol.% ferrite of globular shape. This report presents a comparison of the results with data available in the literature. The IASCC–resistant or –susceptible behavior of austenitic SSs is represented in terms of a two–dimensional map of bulk S and C contents of the steels.

3.1.2 Representation of IASCC-Resistant or –Susceptible Behavior of 304- and 316-Type Steels in Sulfur-Carbon Map

Typical in-service cracking of BWR core internal components occurs at >2 dpa and is characterized by a virtually full IG fracture surface, sometimes accompanied by a small amount of TG fracture surface. In this respect, the IASCC behavior of SSs at ≈3 dpa is more relevant than that at ≈1.3 dpa. The IASCC–resistant or –susceptible behavior at ≈ 3 dpa is largely determined by the bulk concentrations of S and C. Similar analysis was performed for data reported in the literature.[17–20,25–38] Virtually all literature data have been reported after 1987. The two-dimensional map of bulk S and C contents in Figs. 19 and 20 show the range in which 304– or 316–type steels are either resistant or susceptible to IASCC. The figure also includes similar data reported in the literature since 1987. The only data missing from the figure are those obtained for BWR internals for which S and C contents are not available, e.g., an IASCC-resistant 304 SS control blade sheath reported in Ref. 40 and an IASCC-susceptible 304L SS dry tube reported by Shen and Chang.[44]

In constructing the maps in Figs. 19 or 20, we assumed that a heat susceptible at <2.5 dpa is equally or more susceptible at ≥3 dpa under otherwise similar conditions. We also assumed that a heat susceptible at a DO concentration of <0.4 ppm is more susceptible at a DO concentration of ≥8 ppm

under otherwise identical conditions. Note that, in these figures, the plotted ranges of S and C contents extend beyond the AISI limits specified for Type 304 and 316 SS, i.e., maximum S = 0.030 wt.% and maximum C = 0.08 wt.%.

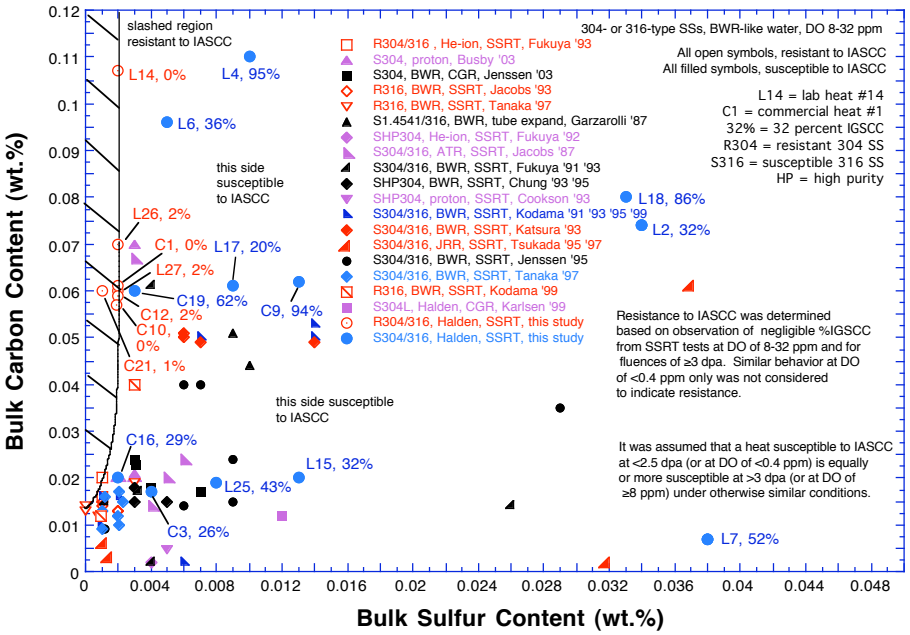

Figure 19. Range of bulk S and C contents in which 304- or 316-type steels are resistant or susceptible to IASCC in BWR-like oxidizing water.

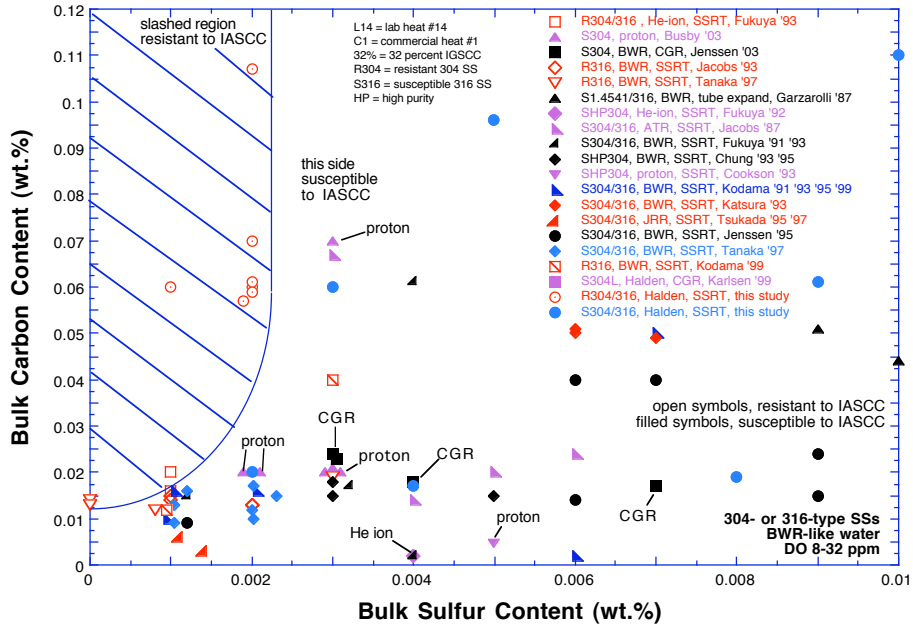

Figure 20. Expanded view of low-S portion of Fig. 19 showing data in detail.

In Figs. 19 and 20, data obtained on neutron-, ion-, or proton-irradiated steels from SSRT, CGR, or tube-expansion tests are shown for comparison with those obtained by SSRT in this investigation. As shown in Fig. 20, the results obtained on He–ion–irradiated steels by Fukuya et al.[25] and proton–irradiated steels by Cookson et al.[28] and Busby et al.[37] are also consistent with the IASCC–susceptible range shown in the S–C map. The earlier efforts by the latter group of investigators focused on "ultra-high-purity" (UHP) heats. However, their "UHP" heats contained either insufficiently low concentrations of S, insufficiently high concentrations of C, or both, to render the steel resistant to IASCC. Figure 20 also includes the results of CGR tests reported by Karlsen and Hauso[38] and Jenssen et al.,[35] in which IG crack propagation was confirmed by SEM fractography.

In Fig. 21, which is similar to Fig. 19, data points for four susceptible heats tested after irradiation to 1.3 dpa (i.e., Heats L22, L11, L13, and L8) are also included. It was assumed that the four heats are also susceptible to IASCC at 3 dpa, although they were not tested at this damage level.

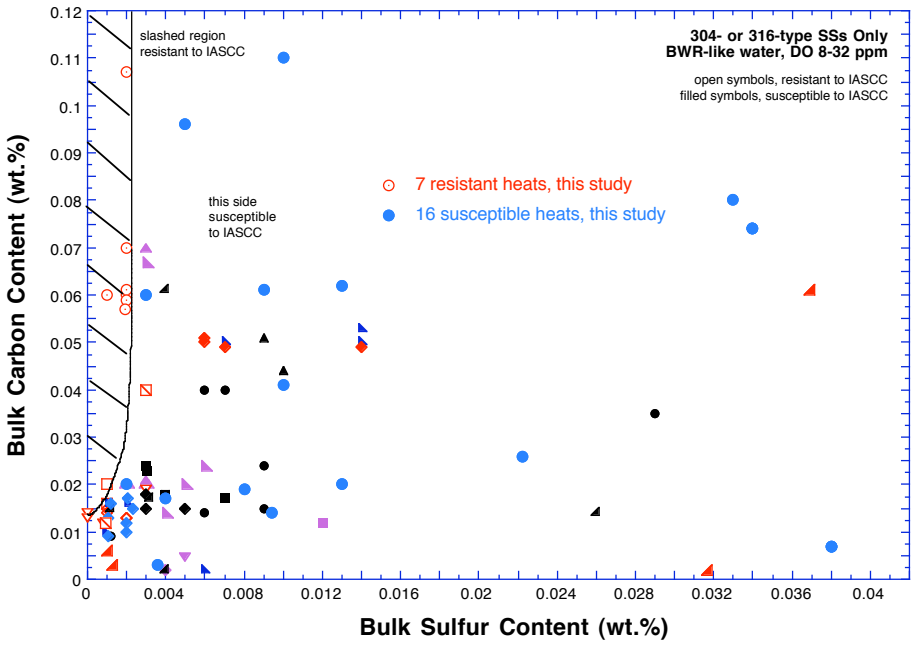

Figure 21. Range of bulk S and C contents in which 304– or 316–type steels are resistant or susceptible to IASCC, including four susceptible heats tested at 1.3 dpa in this study.

3.1.3 Grain-Boundary Segregation of Sulfur and Carbon

In the consideration of the importance of the roles of S and C in IASCC, the behavior of grain-boundary segregation of the two elements was characterized by Auger electron spectroscopy (AES). Similar analysis by advanced analytical electron microscopy (AAEM) is difficult or impractical for an ordinary grain boundary in an irradiated steel, although S-rich thin films on a crack-tip grain boundary can be detected.[45,46] Auger electron spectroscopy is probably the only practical technique that can characterize adequately the profile and degree of grain-boundary segregation of S and C in an irradiated steel.

The materials selected for the AES analysis were taken from BWR neutron absorber tubes. The absorber tubes were fabricated from two commercial heats of Type 304 SS (Heats A and B) and were

irradiated to 2.0 x 10^{21} n/cm^2 (E > 1 MeV) (≈3 dpa) during service in a BWR. The behavior of grain-boundary segregation in such material was considered most relevant to BWR IASCC. The neutron absorber tubes were susceptible to field cracking. Unfortunately, neither documented chemical composition of the absorber tubes nor the archive, unirradiated ingots could be found.

Needle-like specimens were prepared from the selected BWR neutron absorber tubes. After cathodically charging with hydrogen at ≈50°C in a solution that contained 100–mg/L $NaAsO_2$ dissolved in 0.1–N H_2SO_4, the needle-like specimen was fractured in a 23°C vacuum in a scanning Auger electron microscope (SAM). In-situ analysis was performed in a JEOL JAMP–10 SAM equipped with automated Ar-sputtering and depth-profiling devices. Four to six ductile fracture surfaces and 12–15 IG fracture surface locations were selected for spot analysis in each specimen. Sulfur and C signals from the selected surfaces were then recorded and compared.

After each spot analysis, a depth-profile analysis was performed on a selected IG fracture surface. The procedure for automated depth-profiling analysis has been described elsewhere.[23,27] Progressive sputtering of the intergranular surfaces with Ar ions and acquisition of the Auger electron signals in the ultra-high vacuum environment of the SAM were controlled by computer.

An example of an IG fracture surface, produced at 23°C in the H-charged specimens from an absorber tube (304 SS Heat B), is shown in Fig. 22. The IG fracture surfaces reveal numerous deformation steps and a precipitate (diameter ≈15 μm) denoted with the number "6". Spots denoted with numbers "5" and "20" were selected for acquisition of Auger electron signals. The results of spot analyses obtained for Tubes A-1 and B are shown in Figs. 23 and 24, respectively. In Fig. 23a, the peak heights of Auger electrons of S obtained from four ductile fracture surfaces are presented with their counterparts from 12 IG fracture surfaces in Tube A-1. The S intensities from the IG fracture surfaces are significantly higher than their counterparts from ductile-fracture surfaces (i.e., spots not on a grain boundary). This behavior shows that S segregated significantly to grain boundaries (i.e., IG fracture surface) in Tube A-1. Similar results for C are also plotted in Fig. 23b, which shows that C segregated significantly to grain boundaries in the same tube. Essentially the same behavior was observed for S and C segregation in Tube B; see Fig. 24.

A careful examination of Figs. 23 and 24 reveals that some spots that contain high concentrations of S also contain high concentration of C, e.g., intergranular Spot 16, Tube A-1, and intergranular Spot

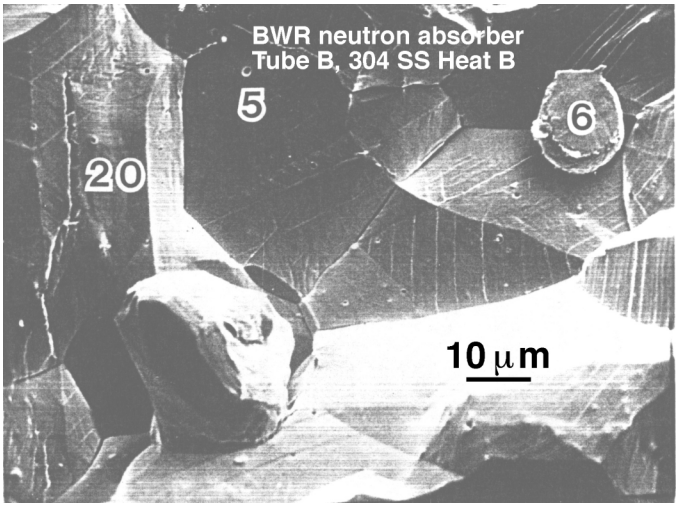

Figure 22. High-magnification fractograph of H-charged BWR neutron absorber tube, 304 SS, Heat B, ≈3 dpa; fracture was produced at 23°C in ultra-high vacuum environment in a scanning Auger electron microscope.

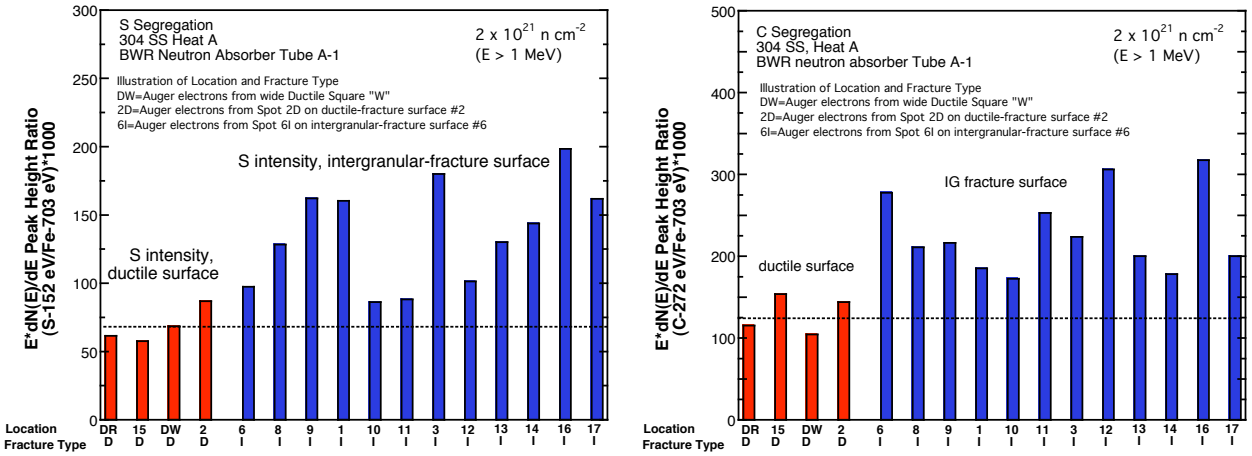

(a) (b)

Figure 23. Summary of AES analysis of grain-boundary segregation of S (a) and C (b) in BWR neutron absorber tube fabricated from Type 304 SS Heat A and irradiated to 3 dpa: S and C peak heights from ductile (denoted "D") and IG (denoted "I") fracture surfaces are compared.

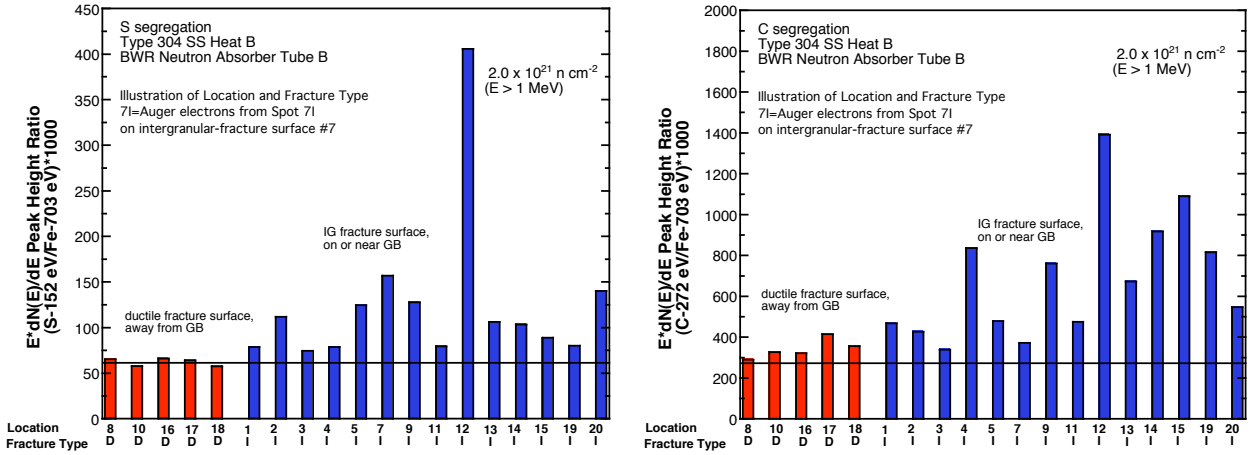

(a) (b)

Figure 24. Summary of AES analysis of grain-boundary segregation of S (a) and C (b) in BWR neutron absorber tube fabricated from Type 304 SS Heat B and irradiated to 3 dpa: S and C peak heights from ductile (denoted "D") and IG (denoted "I") fracture surfaces are compared.

12, Tube B. However, whether C segregates preferentially to a grain-boundary region that contains a high concentration of S, or vice versa, is not conclusive. This behavior could not be conclusively determined by AES in this investigation; it needs further study by a more direct technique such as the field-emission atom-probe technique.

Figure 25 shows the results of depth-profile analysis for the two tubes fabricated from 304 SS Heats A-1 and B. The figure confirms significant grain-boundary segregation of S in Tubes A-1 and B and C segregation in Tube B.

The results in Figs. 22–25, however, do not clarify whether the grain-boundary segregation of S or C occurred via a thermal process (during fabrication), an irradiation-induced process, or both. The former

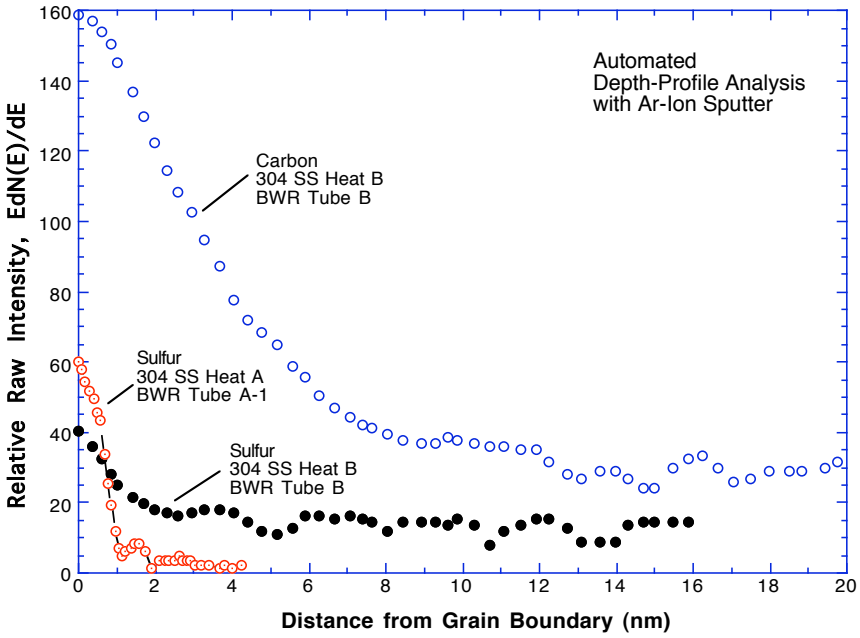

Figure 25. Result of AES depth-profiling analysis of grain-boundary segregation of S and C in BWR neutron absorber tubes fabricated from Type 304 SS Heats A and B and irradiated to ≈3 dpa.

type of segregation is expected to be significantly influenced by several steps during fabrication, e.g., ingot cooling, inter-rolling annealing and cooling, final annealing, and quenching. Thermal segregation is also influenced by plate thickness.

Results of AES analysis of grain-boundary segregation of S have been reported by Jacobs et al.[47] for fuel-cladding-like tubes that were irradiated in a BWR. A tube fabricated from a commercial heat of Type 348 SS was irradiated to 1.5 x 10^{21} n·cm^{-2} (E > 1 MeV), and a tube fabricated from a high-purity heat of Type 348 SS was irradiated to 3.4 x 10^{21} n·cm^{-2} (E > 1 MeV). Results of spot analyses, similar to those of Figs. 23 and 24, showed significant grain–boundary segregation of S in both tubes. Depth-profiling analysis similar to that of Fig. 25 was, however, not reported from their investigation.

Andresen and Briant reported on the thermal segregation of S in grain boundaries for unirradiated UHP austenitic SS doped with S.[48] They concluded that S plays an important role in producing the IG crack path in thermally sensitized non-irradiated steels. Because S atoms are thermally segregated on grain boundaries, more S ions are released into water from the grain boundary than from the grain matrix, and it was thought that an IG crack path is promoted in steels that contain high concentrations of S. Thus, the authors essentially viewed the role of S as accelerating corrosive attack (i.e., dissolution of grain boundary metal) of a Cr-depleted grain boundary, exacerbated by S ions released into the crack tip water. According to this model, as long as grain boundaries are significantly depleted of Cr, the production of an IGSCC path is predicted, even in a steel free of S.

However, a similar model of the role of S does not appear to explain our results on IASCC susceptibility of irradiated steels. One difficulty is how to explain the observation that IASCC susceptibility becomes negligible when S concentration is very low even though Cr depletion is

significant at ≈3 dpa. Another difficulty is how to explain the trend that the S effect is strongly influenced by fluence at >0.003 wt.% S, e.g., in 304- and 316-type steels.

3.1.4 Analysis of Solubility of Carbon in Sulfides

The results in Figs. 19–21 indicate that, when S concentration in 304– or 316–type steel is ≤0.002 wt.%, a high concentration of C (>0.03 wt.%) promotes a decrease of the susceptibility to IASCC. When S concentration exceeds ≈0.003 wt.%, such a "beneficial" effect of high C concentration appears to be insignificant or absent. This observation suggests that some kind of synergism occurs between S and C, and that the effect of such synergism is significant only at sufficiently low concentrations of S (<0.002 wt.%).

With respect to the above observation, our attention was focused on the composition and properties of Ni– and S–rich thin films that were observed on grain boundaries under three situations: at crack–tip grain boundaries in an nonirradiated thermally sensitized crack–growth specimen tested in sulfated BWR–like water (304 SS), reported by Dumbill;[49] at crack-tip grain boundaries in a field–failed BWR top guide and a PWR baffle bolt (Type 304 SS), reported by Thomas and Bruemmer;[45,46] and at ordinary grain boundaries of S-doped Ni specimens that failed during SSRT tests in air at 23°C, reported by Heuer et al.[50] The latter investigators showed that S–doped Ni specimens lose their tensile strength when the grain-boundary concentration of S exceeds ≈15 at.%, which causes an IG failure. Then, it was thought in our study that, if C is dissolved in a Ni_xS_y–type film in a significant amount, the mechanical properties of such a film are likely to be altered significantly. Accordingly, available information and data were evaluated to determine if C is soluble in sulfides.

The AES signal from the precipitate denoted with number "6" in Fig. 22 is shown in Fig. 26. The AES signal indicates that the precipitate is a CuS-type that contains a significant amount of C. Similar data are shown in Figs. 27 and 28 for two more CuS-type precipitates that were present in the same specimen.

The only direct evidence of significant solubility of C in Ni sulfide could be observed from the data reported by Dumbill.[49] The data obtained by field-emission-gun advanced analytical electron microscopy

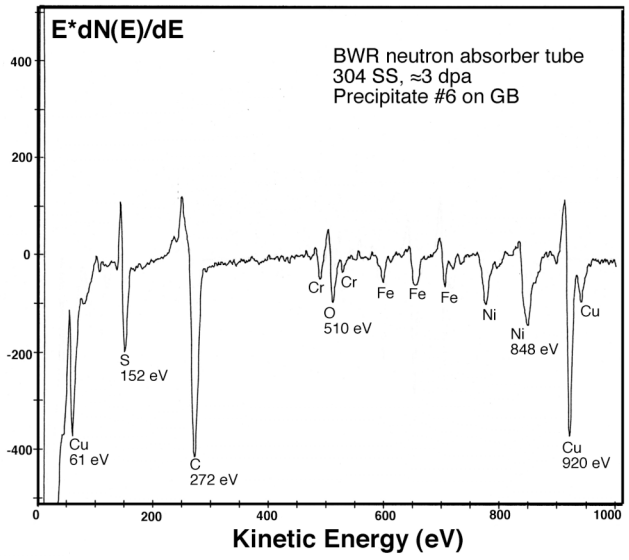

Figure 26.
AES signal showing high concentrations of Cu, S, and C in CuS-type precipitate denoted with number "6" in Fig. 22.

(FEG-AAEM) show X-ray intensities of Ni, S, and C contained in a Ni- and S-rich thin film that was observed at an intergranular crack in a thermally sensitized, unirradiated Type 304 SS. The FEG-AAEM X-ray spectra strongly indicate that C can be dissolved in significant amounts in Ni- and S-rich thin films at ≈290°C. Unfortunately, similar data were not reported for the field-cracked (irradiated) steels examined by Thomas and Bruemmer.[45,46] However, irradiation is not expected to significantly decrease the solubility of C in the Ni- and S-rich thin films or islands that they observed.

Based on the information described above, it is predicted that C atoms compete with S atoms to become incorporated in the unit cell of NiS-type sulfides under BWR conditions. The degree of such C incorporation, which replaces part of the S atoms in the sulfide, is predicted to be more pronounced for a higher concentration of C at the grain boundary, i.e., for a high C content in the steel and for a higher degree of grain-boundary segregation of C.

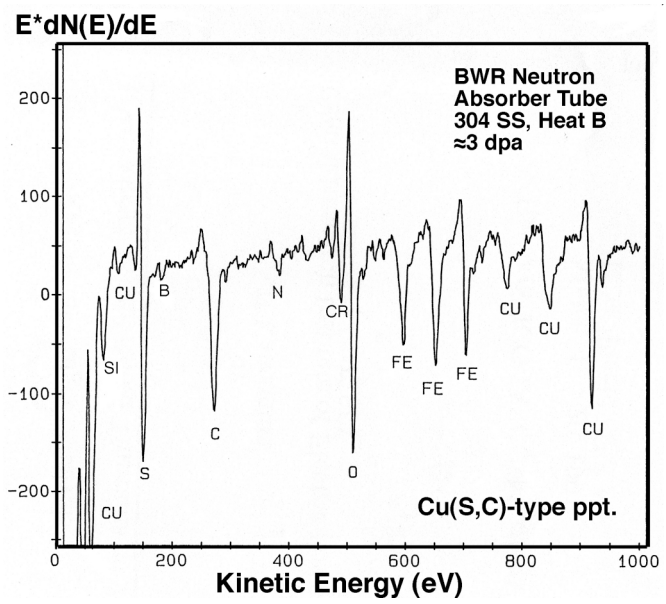

Figure 27.
AES signal showing a high concentration of C in CuS-type precipitate in BWR neutron absorber tube, 304 SS, Heat B, ≈3 dpa.

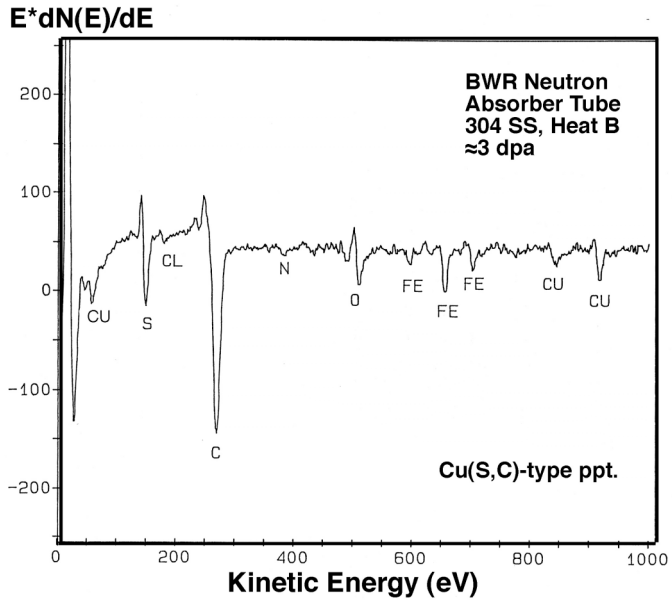

Figure 28.
AES signal showing a high concentration of C in another CuS-type precipitate in BWR neutron absorber tube, 304 SS, Heat B, ≈3 dpa.

3.2 Crack Growth Rate Test of Austenitic Stainless Steels Irradiated in the Halden Reactor (E. E. Gruber and O. K. Chopra)

3.2.1 Introduction

Austenitic stainless steels (SSs) are used extensively as structural alloys in reactor pressure vessel internal components because of their high strength, ductility, and fracture toughness. However, exposure to neutron irradiation for extended periods changes the microstructure and degrades the fracture properties of these steels. Irradiation leads to a significant increase in yield strength and a reduction in ductility and fracture resistance of austenitic SSs.[51–54] Radiation can exacerbate the corrosion fatigue and stress corrosion cracking (SCC) behavior of SSs[51,55,56] by affecting the material microchemistry, e.g., radiation–induced segregation; material microstructure, e.g., radiation hardening; and water chemistry, e.g., radiolysis.

The factors that influence SCC susceptibility of materials include neutron fluence, cold work, corrosion potential, water purity, temperature, and loading. The effects of neutron fluence on irradiation assisted stress corrosion cracking (IASCC) of austenitic SSs have been investigated for BWR control blade sheaths[57–59] and laboratory tests on BWR–irradiated material;[55,60–62] the extent of intergranular SCC increases with fluence. Although a threshold fluence level of 5×10^{20} n/cm^2 (E >1 MeV) (≈0.75 dpa) has been proposed for austenitic SSs in BWR environments based on early experimental results, intergranular cracking has been seen at fluences as low as $\approx 2 \times 10^{20}$ n/cm^2 (E >1 MeV) (≈0.3 dpa).[55,63] The results also show the beneficial effect of reducing the corrosion potential of the environment,[64,65] which suggests that the threshold fluence for IASCC is higher under low potential conditions such as BWR hydrogen water chemistry (HWC) or PWR primary water chemistry. However, low corrosion potential does not provide immunity to IASCC if the fluence is high enough, e.g., intergranular SCC has been observed in cold-worked, irradiated SS baffle bolts in PWRs.

A program is being conducted at Argonne National Laboratory (ANL) on irradiated SSs, to support the regulatory request to understand better the safety issues attendant to the cracking of BWR internals such as core shrouds. The susceptibility of austenitic SSs to IASCC is being evaluated as a function of the fluence level, material composition, and water chemistry. Crack growth rate (CGR) tests are being conducted on Type 304 and 316 SS base metal and weld heat affected zones (HAZ) irradiated to fluence levels up to 2.0×10^{21} n/cm^2 (E > 1 MeV) (3.0 dpa) at ≈288°C. The CGR tests are conducted in normal water chemistry (NWC) and hydrogen water chemistry (HWC) BWR environments at ≈289°C.

Crack growth tests have been completed on Type 304L and 316L SS (Heats C3 and C16, respectively) irradiated to a fluence level of 0.9 and 2.0×10^{21} n/cm^2 (E > 1 MeV). The results indicate significant enhancement of CGRs for irradiated steels in the NWC BWR environment.[66] Crack growth rates a factor of ≈5 higher than the disposition curve proposed in NUREG–0313[67] for sensitized austenitic SSs in water with 8 ppm dissolved oxygen (DO) have been observed. The CGRs of Type 304L SS irradiated to 0.9 and 2.0×10^{21} n/cm^2 (1.35 and 3.0 dpa) and of Type 316L SS irradiated to 2.0×10^{21} n/cm^2 (3 dpa) were comparable.

The results also indicated that in low–DO BWR environments, the CGRs of the irradiated steels decreased by an order of magnitude in some tests, e.g., Type 304L SS irradiated to 0.9×10^{21} n/cm^2 and Type 316L SS irradiated to 2×10^{21} n/cm^2. As noted previously, the benefit of low DO appears to decrease with increasing fluence. A threshold of about 5×10^{21} n/cm^2 has been suggested.[55,63] However, the beneficial effect of decreased DO was not observed in a test on Type 304L SS irradiated to

2 x 10^{21} n/cm^2, although this different behavior may be associated with the loss of constraint in the specimen due to the high applied–load.[66]

This section presents experimental CGR data concerning BWR environments at 289°C for Heat C3 of Type 304L SS irradiated to 0.3 x 10^{21} n/cm^2 (0.45 dpa). Baseline data have also been obtained on nonirradiated SS weld HAZ specimens obtained from Type 304L SS weld from the Grand Gulf (GG) reactor core shroud and a Type 304 SS laboratory–prepared weld.

3.2.2 Experimental

3.2.2.1 Specimen Geometry and Materials

The CGR tests were performed at ≈289°C on 1/4–T compact tension (CT) specimens in simulated BWR environments in accordance with ASTM E–647, "Standard Test Method for Measurement of Fatigue Crack Growth Rates", and ASTM E–1681, "Standard Test Method for Determining a Threshold Stress Intensity Factor for Environment–Assisted Cracking of Metallic Materials under Constant Load." The configuration of the specimens is shown in Fig. 29. Crack extensions were determined by DC potential measurements. The composition of Type 304L Heat C3 is presented in Table 3, and the tensile yield and ultimate stresses for the steel irradiated to three fluence levels and in the nonirradiated condition[41,42] are given in Table 4.

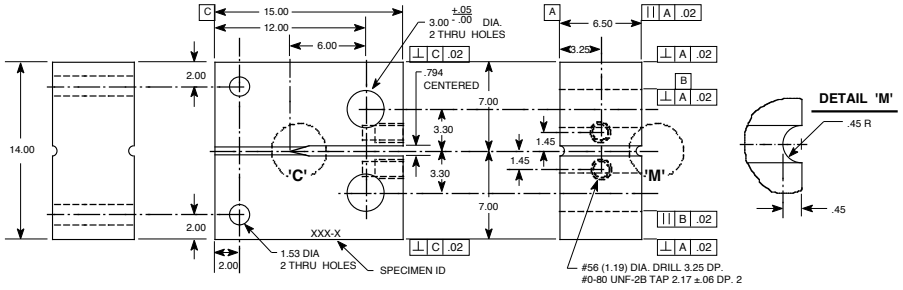

Figure 29. Configuration of compact–tension specimen for this study (dimensions in mm)

Table 3. Composition (wt.%) of Heat C3 of Type 304L stainless steel irradiated in the Halden reactor

ID[a]	Heat ID	Analysis	Ni	Si	P	S	Mn	C	N	Cr	Mo	O[b]
C3	PNL-C-6	Vendor	8.91	0.46	0.019	0.004	1.81	0.016	0.083	18.55	–	–
		ANL	9.10	0.45	0.020	0.003	1.86	0.024	0.074	18.93	–	144

[a]First letters "C" denotes commercial heat.
[b]In wppm.

Table 4. Tensile properties (MPa) of irradiated Heat C3 of Type 304L stainless steel at 288°C

			Fluence (E > 1 MeV)					
	Nonirradiated		0.3 x 10^{21} n/cm^2		0.9 x 10^{21} n/cm^2		2.0 x 10^{21} n/cm^2	
Steel Type (Heat)	Yield	Ultimate	Yield	Ultimate	Yield	Ultimate	Yield	Ultimate
304 SS (C3)	(154)[a]	(433)[a]	338	491	632	668	796	826

[a]Estimated value.

The HAZ specimens were obtained from the H5 core–shroud weld of the cancelled GG reactor and a shielded metal arc (SMA) weld prepared from a 30–mm plate of Type 304 SS (Heat 10285). The GG weld was fabricated from an SA 240 Type 304L hot–rolled plate using a double–V joint design. This

plate had been welded by submerged arc (SA) method and ER308L filler metal. The SMA weld was prepared in the laboratory by welding two 70 x 178 mm (2.75 x 7.0 in.) pieces of 30 -mm thick (1.18 -in. thick) plate. The weld had a single V-joint design and was produced by 31 weld passes using E308 filler metal. Passes 1–5 were produced with 3.2 -mm (0.125 -in.) filler metal rod and 178 -mm/min (7 -ipm) travel speed, and passes 6–31 were produced with 4.0 -mm (0.156 -in.) filler metal rod and 216 -mm/min (8.5 -ipm) travel speed. Between passes the weld surfaces were cleaned by wire brush and grinding and rinsed with de–mineralized water or alcohol. The composition of Type 304 SSs used in the present study is presented in Table 5. The specimens were machined from 9.5–mm thick slices of the weld; some slices were thermally treated for 24 h at 500°C before machining. For all specimens, the machined notch was located in the HAZ of the weld. Each slice was etched, and the specimen orientation and notch location relative to the weld was clearly identified, Fig. 30.

Table 5. Composition (wt.%) of Type 304 stainless steels investigated

Steel Type	Heat ID	Analysis	Ni	Si	P	S	Mn	C	N	Cr	Mo	O
304	10285	Vendor	8.40	0.51	0.032	0.006	1.64	0.058	–	18.25	0.41	–
		ANL	8.45	0.60	0.015	0.007	1.90	0.070	0.084	18.56	0.51	0.013
304L	GG Top Shell	ANL	9.05	0.53	0.027	0.016	1.84	0.013	0.064	18.23	0.44	0.010
	GG Bottom Shell	ANL	8.95	0.55	0.023	0.008	1.80	0.015	0.067	18.62	0.31	0.014

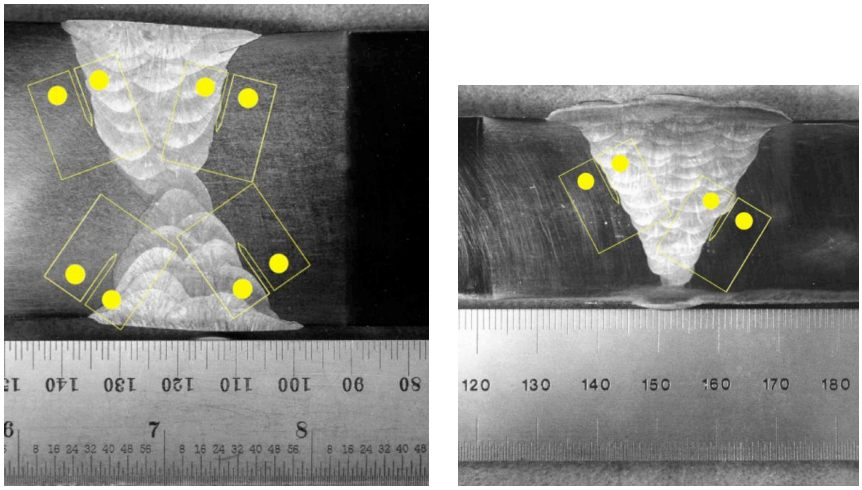

(a) (b)

Figure 30. Orientation of the 1/4–T CT specimens from the (a) Grand Gulf H5 SA weld HAZ and (b) laboratory–prepared SMA weld HAZ.

The microstructures of the base metal and as–welded HAZ of Type 304L SS from the GG top and bottom shells and Heat 10285 of Type 304 SS are shown in Figs. 31–36. The base metal of all the SSs contains stringers of ferrite, e.g., Figs. 31, 33, and 35; Heat 10285 appears to have the most amount of ferrite and the GG bottom shell the least amount. The grain sizes for the GG top and bottom shell materials are comparable and are larger than those for Heat 10285, e.g., the grain size in the HAZ region of the GG shell is ≈110 µm and that of Heat 10285 is ≈80 µm. In all welds, the fusion line extends into the base metal along the ferrite stringers, e.g., Figs. 32, 34, and 36. In other words, the ferrite stringers intersecting the fusion line appear to have melted and re–solidified during the welding process.

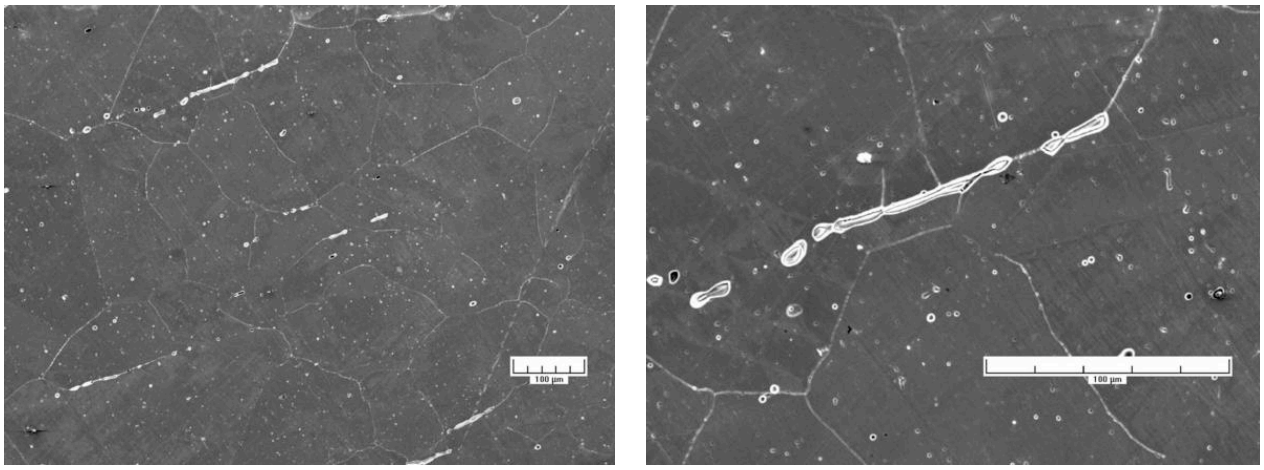

(a) (b)

Figure 31. (a) Low- and (b) high–magnification photomicrographs of the structure of the Type 304L base metal from the top shell of the H5 weld of the Grand Gulf core shroud.

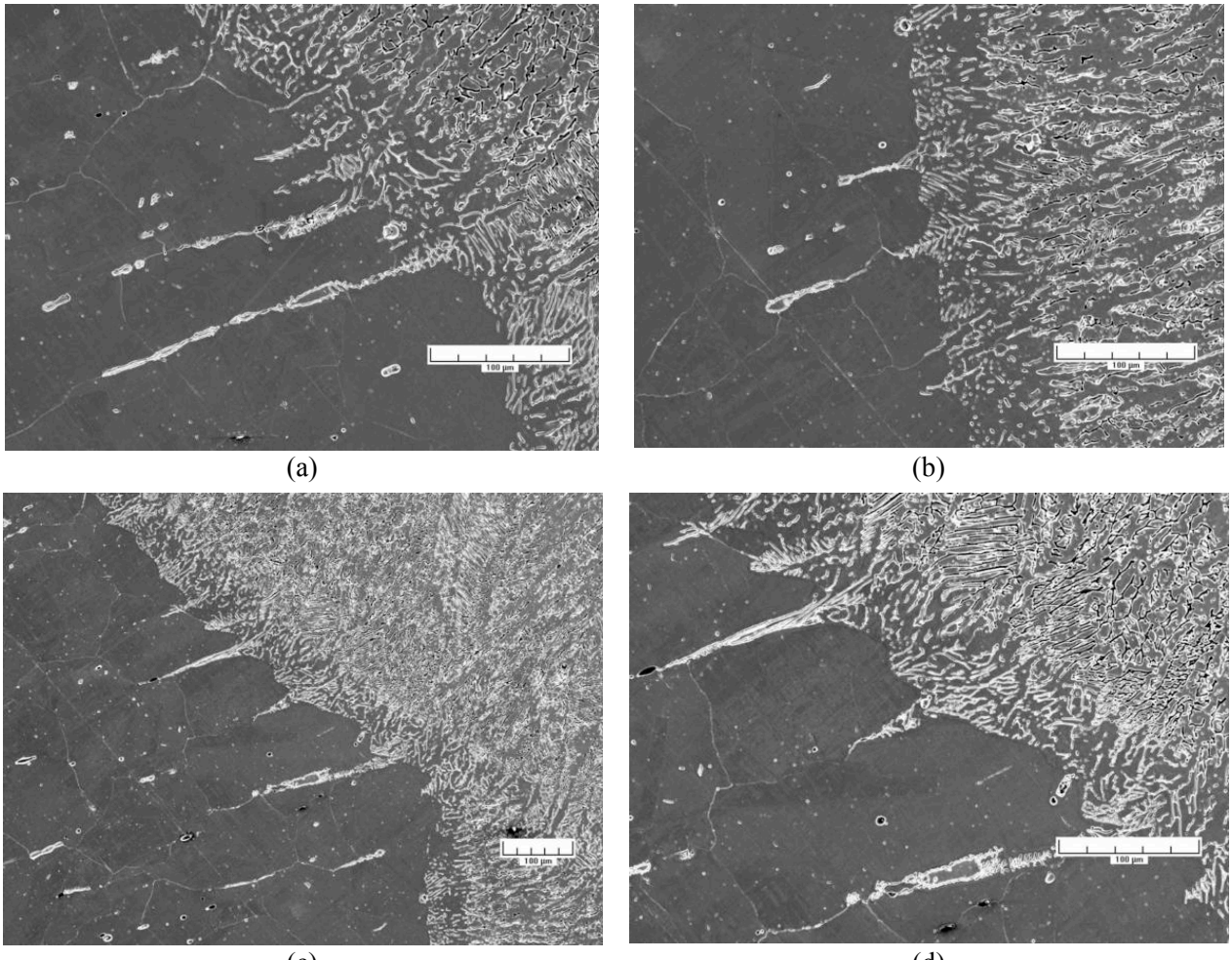

(a) (b)

(c) (d)

Figure 32. Micrographs of the interface between the weld metal and top shell of the H5 weld of the Grand Gulf core shroud.

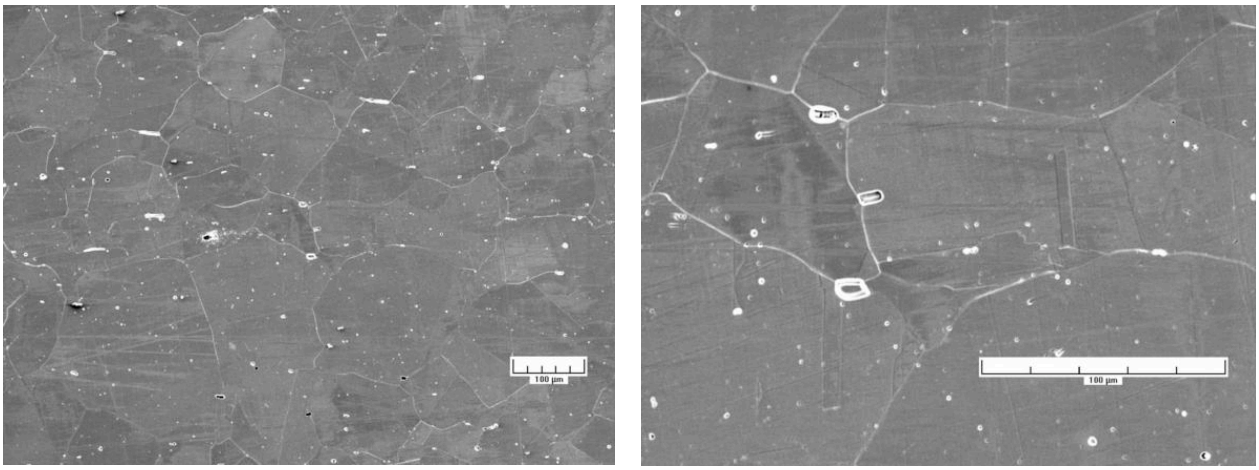

(a) (b)

Figure 33. (a) Low- and (b) high–magnification photomicrographs of the structure of the Type 304L base metal from the bottom shell of the H5 weld of the Grand Gulf core shroud.

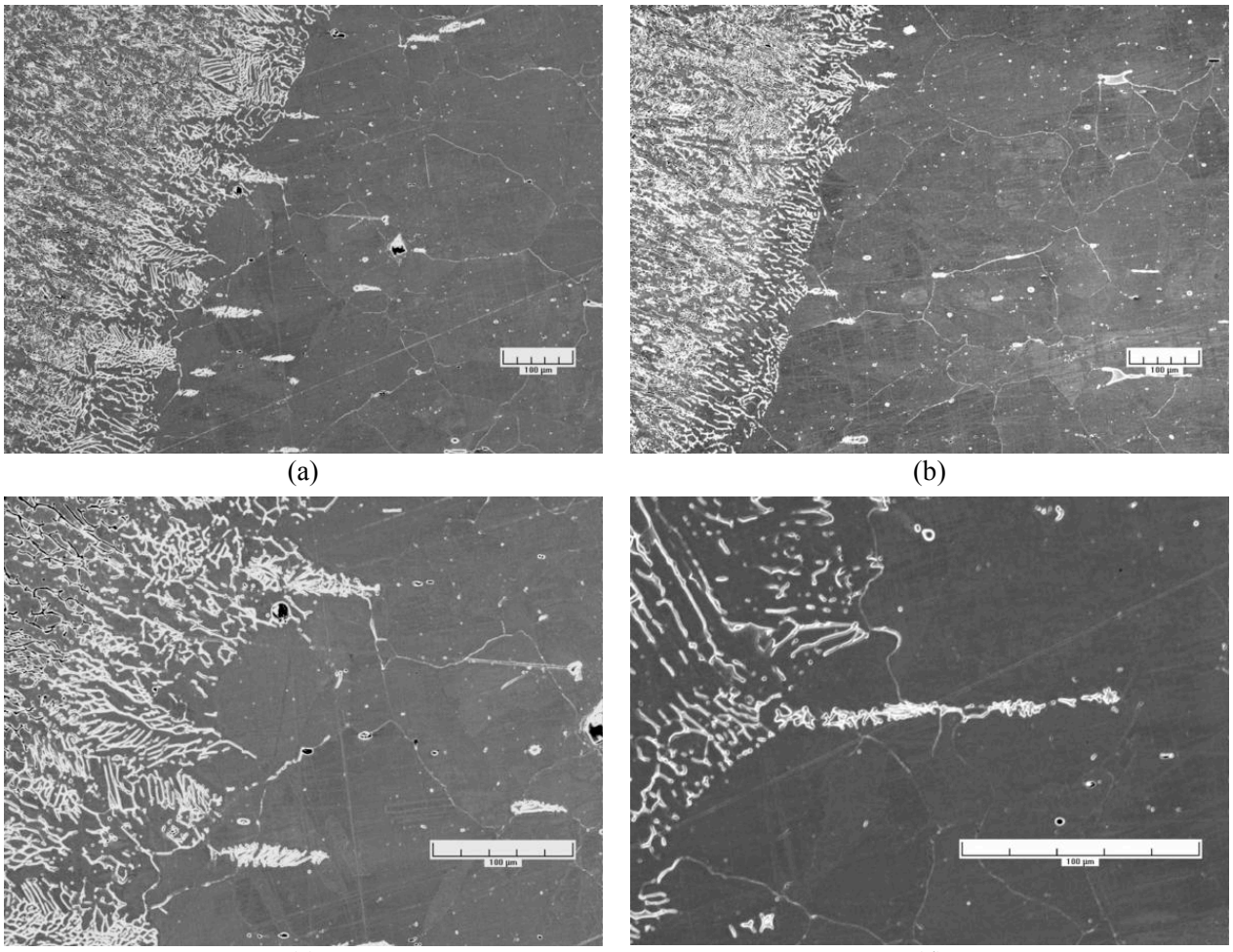

(a) (b)

(c) (d)

Figure 34. Micrographs of the interface between the weld metal and bottom shell of the H5 weld of the Grand Gulf core shroud.

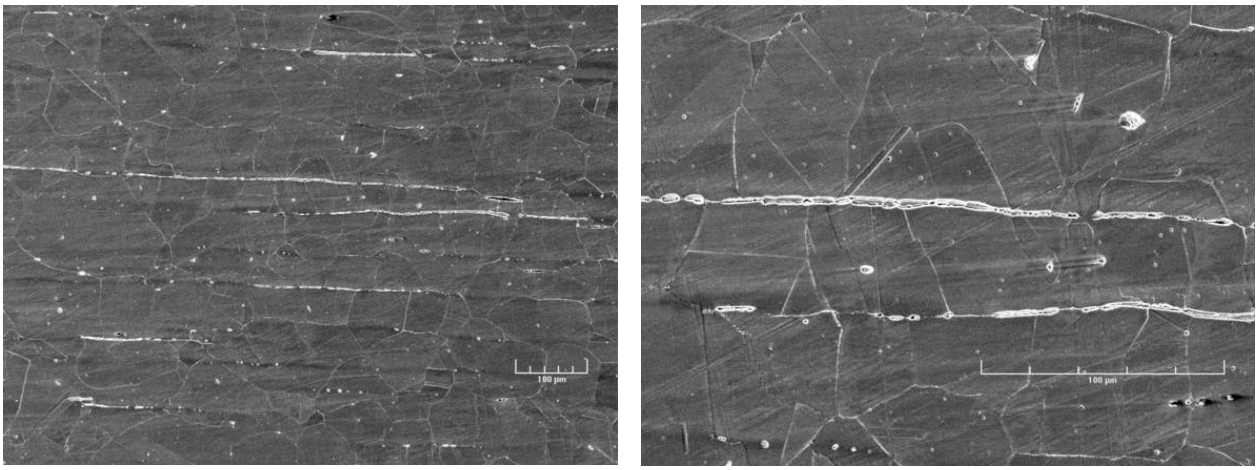

(a) (b)

Figure 35. (a) Low- and (b) high–magnification photomicrographs of the structure of Heat 10285 of the Type 304 base metal from the top shell of the H5 weld of the Grand Gulf core shroud.

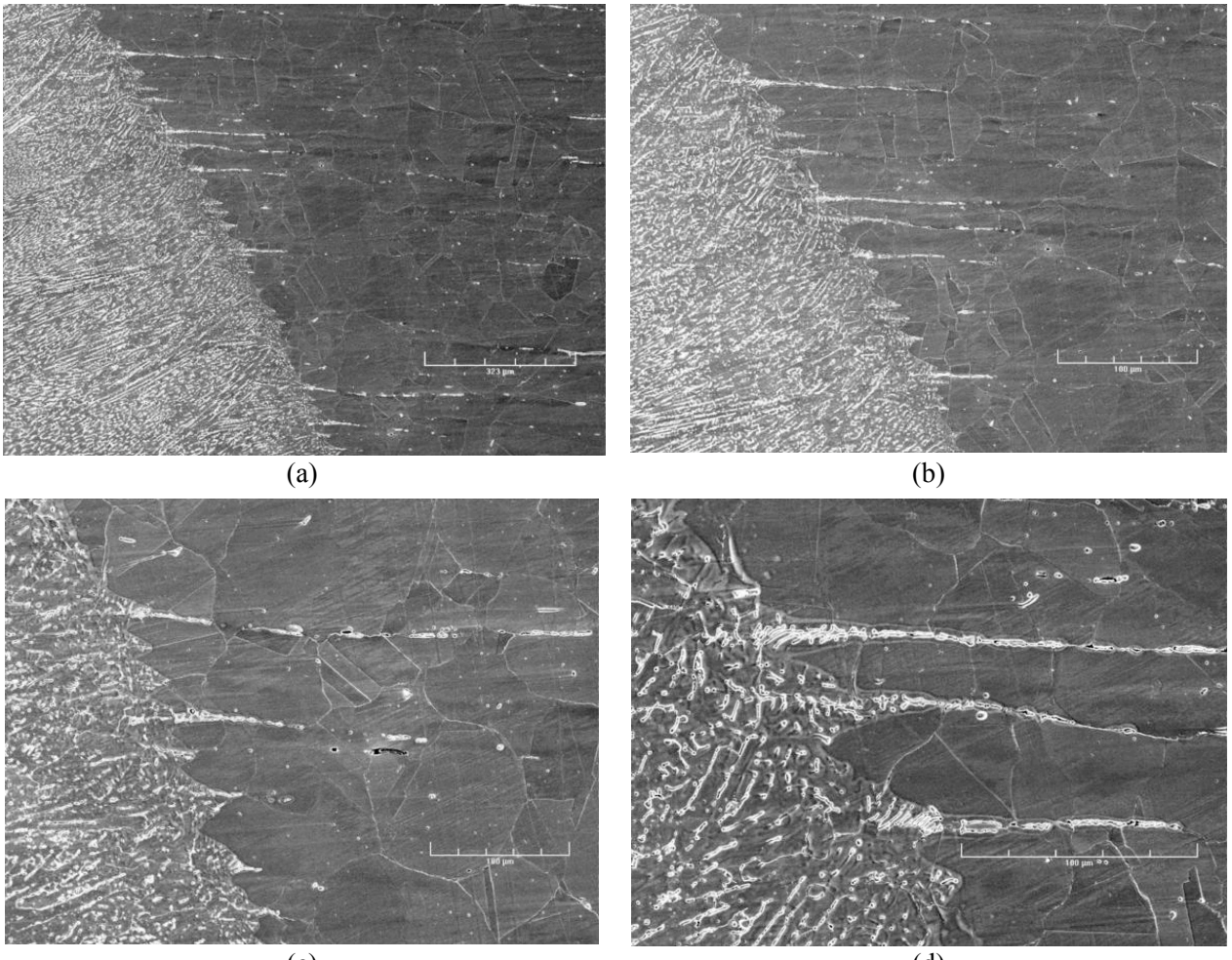

(a) (b)

(c) (d)

Figure 36. Micrographs of the interface between the weld metal and base metal.

The tensile properties of the GG core–shroud shell and Heat 10285, in the mill–annealed condition and after sensitization at 600°C for 10.5 h, are listed in Table 6. The tests were conducted on cylindrical specimens, 5.1 -mm diameter and 20.3 -mm gauge length, in air at 289°C and 0.008 %/s strain rate. The sensitization heat treatment has little effect on the tensile strength of the GG steel, whereas the strength of Heat 10285 is decreased. The tensile properties of the sensitized material are used to determine the K/size criterion for nonirradiated HAZ specimens, both in the as–welded and as–welded plus thermally treated conditions.

Table 6. Tensile properties of the austenitic stainless steels irradiated in the Halden reactor

		Nonirradiated	
Steel Type	Material Condition	Yield (MPa)	Ultimate (MPa)
304 SS Heat 10285	Mill annealed	196	508
	MA + 10.5 h at 600°C	156	501
304L SS GG Core Shroud	Mill annealed	158	411
	MA + 10.5 h at 600°C	159	425

3.2.2.2 Test Procedure

The facility for conducting the tests is designed for in–cell testing, with the hydraulic actuator, test load train, autoclave, and furnace mounted on top of a portable wheeled cart that can be easily rolled into the cell. A detailed description of the facility is presented elsewhere.[68] The CGR tests were performed in accordance with ASTM E–647, "Standard Test Method for Measurement of Fatigue Crack Growth Rates", and ASTM E–1681, "Standard Test Method for Determining a Threshold Stress Intensity Factor for Environment–Assisted Cracking of Metallic Materials under Constant Load."

The CGR tests were started in high–purity water that contained 250–500 ppb DO (i.e., NWC BWR environment). The electrochemical potentials (ECPs) of a Pt electrode and a SS sample located at the exit of the autoclave were monitored continuously during the test; the water DO level and conductivity were determined periodically. After data were obtained for high–DO water, the DO level in the feedwater was decreased to <30 ppb by sparging it with pure N_2 or N_2 + 5% H_2. Because of the very low water flow rates, several days were required for the environmental conditions to stabilize for the in–cell tests. In general, the changes in ECP of the SS sample were slower than in the ECP of the Pt electrode. Because of the higher flow rates the changes in water chemistry for the out–of–cell tests were significantly faster.

All specimens were fatigue precracked in the test environment at load ratio R = 0.2–0.3, frequency of 1–5 Hz, and maximum stress intensity factor $K_{max} \approx 15$ MPa $m^{1/2}$. After 0.3–0.5 mm crack extension, a prescribed loading sequence was followed to facilitate the transition of a TG fatigue crack to a IG stress corrosion crack. To achieve this transition, R was increased incrementally to 0.7, and the loading waveform changed to a slow/fast sawtooth with rise times of 30–1000 s. The loading history was then changed to a trapezoidal waveform, R = 0.7, hold period at peak of 1 or 2 h, and unload/reload period of 24 s to measure SCC growth rates. For some specimens, CGRs were also obtained under constant load. During individual test periods, K_{max} was maintained approximately constant by periodic load shedding (less than 2% decrease in load at any given time).

Under cyclic loading, the CGR (m/s) can be expressed as the superposition of the rate in air (i.e., mechanical fatigue) and the rates due to corrosion fatigue and SCC, given as

$$\dot{a}_{env} = \dot{a}_{air} + \dot{a}_{cf} + \dot{a}_{SCC} . \quad (2)$$

The CGRs in air, $\dot{a}_{air}$ (m/s), were determined from the correlations developed by James and Jones;[69] it is expressed as

$$\dot{a}_{air} = C_{SS}\, S(R)\, \Delta K^{3.3}/T_R\,, \tag{3}$$

where R is the load ratio (K_{min}/K_{max}), ΔK is $K_{max} - K_{min}$ in MPa $m^{1/2}$, T_R is the rise time (s) of the loading waveform, and the function S(R) is expressed in terms of the load ratio R as follows:

$$\begin{aligned} S(R) &= 1.0 && R < 0 \\ S(R) &= 1.0 + 1.8R && 0 < R < 0.79 \\ S(R) &= -43.35 + 57.97R && 0.79 < R < 1.0. \end{aligned} \tag{4}$$

Also, the function C_{SS} is given by a third–order polynomial of temperature T (°C), expressed as

$$C_{SS} = 1.9142 \times 10^{-12} + 6.7911 \times 10^{-15}\, T - 1.6638 \times 10^{-17}\, T^2 + 3.9616 \times 10^{-20}\, T^3. \tag{5}$$

Environmental effects on fatigue crack growth of nonirradiated austenitic SSs have been investigated by Shack and Kassner.[70] In the absence of any significant contribution of SCC to growth rate, the CGRs in water with ≈0.3 ppm DO are best represented by the expression

$$\dot{a}_{env} = \dot{a}_{air} + 4.5 \times 10^{-5}\, (\dot{a}_{air})^{0.5}, \tag{6}$$

and in water with ≈8 ppm DO by the expression

$$\dot{a}_{env} = \dot{a}_{air} + 1.5 \times 10^{-4}\, (\dot{a}_{air})^{0.5}. \tag{7}$$

The CGR (m/s) under SCC conditions is represented by the correlation given in the U.S. NRC report NUREG–0313, Rev. 2,[67]

$$\dot{a}_{SCC} = A\, (K)^{2.161}, \tag{8}$$

where K is the stress intensity factor (MPa $m^{0.5}$), and the magnitude of constant A depends on the water chemistry and composition and structure of the steel. A value of 2.1 x 10^{-13} has been proposed in NUREG–0313 for sensitized SS in water chemistries with 8 ppm DO. The magnitude of constant A will be smaller in low–DO environments, such as HWC BWR or PWR environments.

During crack growth tests in high–temperature water, environmental enhancement of CGRs typically does not occur from the start of the test. Under more rapid cyclic loading, the crack growth is dominated by mechanical fatigue. The CGRs during precracking and initial periods of cyclic loading in these tests were primarily due to mechanical fatigue. For tests under increasing rise times, the crack growth rates first decrease as shown by the curve denoted "Precracking" in Fig. 37, then jump to new, higher, growth rates for loading conditions that would lead to CGRs below 5 x 10^{-10} m/s in air. For K_{max} values of 15–18 MPa $m^{1/2}$, this means that environmental enhancement occurs for load ratios $R \geq 0.5$ and rise times ≥ 30 s.

After the test the final crack size was marked by fatigue cycling in air at room temperature. The specimens were then fractured, and the fracture surface of both halves of the specimen was photographed with a telephoto lens through the hot cell window. The fracture surfaces of the out–of–cell test specimens

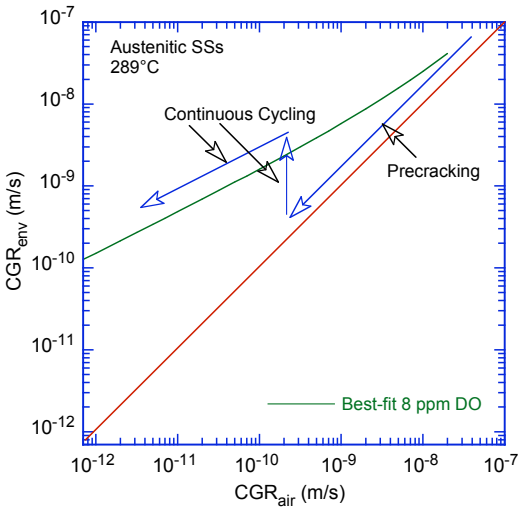

Figure 37.
Plot of CGR in water vs. the CGR in air showing environmental enhancement of growth rates in high purity water at 289°C.

were examined by scanning electron microscopy (SEM). The final crack length of each half of the fractured specimen was determined from the optical or SEM photograph by the 9/8 averaging technique: nine measurements were taken across the width of the specimen at equal intervals, the two near–surface measurements were averaged and the resultant value was averaged with the remaining seven measurements. The results were used to correct the experimental crack length measurements, e.g., the crack extensions determined from the DC potential drop method were proportionately scaled to match the final optically measured crack length.

The CGR test results were validated in accordance with the specimen size criteria of ASTM E 1681 and E 647. These criteria require that the plastic zone at the tip of a fatigue crack be small relative to the specimen geometry. The ASTM specifications for specimen K/size criteria are intended to ensure applicability and transferability of the cracking behavior of a component or specimen of a given thickness under a specific loading condition to a crack associated with a different geometry, thickness, and loading condition. For constant load tests, ASTM E 1681 requires that

$$B_{eff} \text{ and } (W-a) \geq 2.5\,(K/\sigma_{ys})^2, \tag{9}$$

and for cyclic loading ASTM 647 requires that

$$(W-a) \geq (4/\pi)\,(K/\sigma_{ys})^2, \tag{10}$$

where W the specimen length, a is the crack length, K is the applied stress intensity factor, and σ_{ys} is the yield stress of the material. The effective thickness B_{eff} of side–grooved specimen is calculated as the root mean square of the full and reduced thicknesses, i.e., $(B \cdot B_N)^{0.5}$. In high–temperature water, because the primary mechanism for crack growth during continuous cycling is not mechanical fatigue, Eq. 9 is the more appropriate criterion, but Eq. 10 may give acceptable results. For high–strain hardening materials, i.e., materials with an ultimate to yield stress ratio $(\sigma_{ult}/\sigma_{ys}) \geq 1.3$, both criteria allow the use of the flow stress defined as $\sigma_f = (\sigma_{ult} + \sigma_{ys})/2$ rather than the yield stress.

The K/size criteria were developed for materials that show work hardening and, therefore, may not be valid for materials irradiated to fluence levels where, on a local level, they do not strain harden. This lack of strain hardening, or strain softening, is most dramatic when dislocation channeling occurs but may also occur at lower fluences. For moderate to highly irradiated material, use of an effective yield stress,

defined as the average of the nonirradiated and irradiated yield stresses, has been suggested;[71] this discounts the irradiation–induced increase in yield stress by a factor of 2. In the present study, an effective flow stress was used to determine the valid K_{max} for SS weld HAZ specimens and Heat C3 specimen irradiated to a fluence level of 0.3 x 10^{21} n/cm^2.

3.2.3 Crack Growth Rates of Irradiated Stainless Steels in BWR Environments

3.2.3.1 Specimen C3–A of Type 304L SS (Heat C3), Test CGRI-12

A crack growth test has been completed on Heat C3 of Type 304L SS irradiated to 0.3 x 10^{21} n/cm^2. The environmental and loading conditions, experimental CGRs, allowed K_{max} from the K/size criterion in Eq. 9, and the deviation of applied K_{max} from the allowed value are given in Table 7. The test was started in a high–DO environment (≈300 ppb DO in effluent), and the water flow rate was ≈10 mL/min. The ECPs of Pt and SS electrodes in the effluent stream were monitored continuously.

Precracking was carried out at R = 0.3 and K_{max} = 13–14 MPa m$^{1/2}$. After ≈0.3 mm crack advance, R was increased incrementally to 0.7, and the waveform was changed from triangular to saw-tooth with rise times of 12–500 s. The changes in crack length and K_{max} with time during various test periods are shown in Figs. 38. For this specimen, crack growth could not be maintained for loading conditions with high values of R and relatively low K_{max}. For example, at K_{max} = 14 MPa m$^{1/2}$ increasing R from 0.3 to 0.5 essentially stopped crack growth (Fig. 38a). Changing R back to the earlier value did not restore crack growth; K_{max} had to be increased to start crack growth. To promote environmentally enhanced crack growth, the rise time for the cyclic loading at R = 0.3 was increased from 0.5 to 300 s before increasing R (Fig. 38b). For R = 0.7, crack growth occurred only at K_{max} greater than 17 MPa m$^{1/2}$.

Table 7. Crack growth results for Specimen C3–A of Type 304 SS[a] in high–purity water at 289°C

Test Period	Test Time, h	ECP[b] mV (SHE) Pt	ECP[b] mV (SHE) Steel	O_2 Conc.,[b] ppb	Load Ratio	Rise Time, s	Down Time, s	Hold Time, s	K_{max}, MPa·m$^{1/2}$	ΔK, MPa·m$^{1/2}$	Growth Rate, m/s	K_{max} from Eq. 13, MPa m$^{1/2}$	Deviation in K_{max}, %
Pre	55	226	167	300	0.31	0.5	0.5	0	12.9	8.9	2.94E-09	18.4	-30
1	165	212	166	300	0.30	0.5	0.5	0	14.0	9.8	8.37E-09	17.9	-22
2a	189	221	169	300	0.50	5	5	0	13.9	6.9	negligible	17.9	-23
2b	193	211	169	300	0.50	0.5	0.5	0	13.8	6.9	negligible	17.9	-23
2c	214	209	161	300	0.30	0.5	0.5	0	13.9	9.7	negligible	17.9	-23
2d	219	211	163	300	0.30	0.5	0.5	0	15.0	10.5	1.48E-08	17.7	-15
3	364	218	171	300	0.30	1	1	0	15.9	11.1	1.39E-08	17.5	-9
4	380	218	171	300	0.30	30	4	0	16.0	11.2	1.33E-09	17.4	-8
5	404	219	177	300	0.29	300	4	0	15.9	11.3	3.29E-10	17.4	-8
6	479	204	173	300	0.48	300	4	0	15.7	8.2	4.75E-11	17.4	-10
7	596	235	187	300	0.70	12	12	0	15.7	4.7	negligible	17.4	-10
8	670	228	188	300	0.70	12	12	0	17.6	5.3	6.23E-11	17.3	2
9	717	231	186	300	0.70	12	12	3600	17.8	–	–	17.3	3
10	910	234	197	300	0.70	500	12	3600	17.9	–	8.65E-11	17.2	4
11	1080	232	200	300	0.70	500	12	3600	22.0	–	1.11E-10	17.1	29
12	1175	226	203	300	0.70	500	1	9500	22.3	–	1.28E-10	17.0	31

[a]Heat C3, irradiated to 0.3 x 10^{21} n/cm^2.
[b]Represents values in the effluent. Conductivity was 0.07 and 0.3–0.45 μS/cm in feedwater and effluent, respectively. Feedwater pH at room temperature was 6.5.

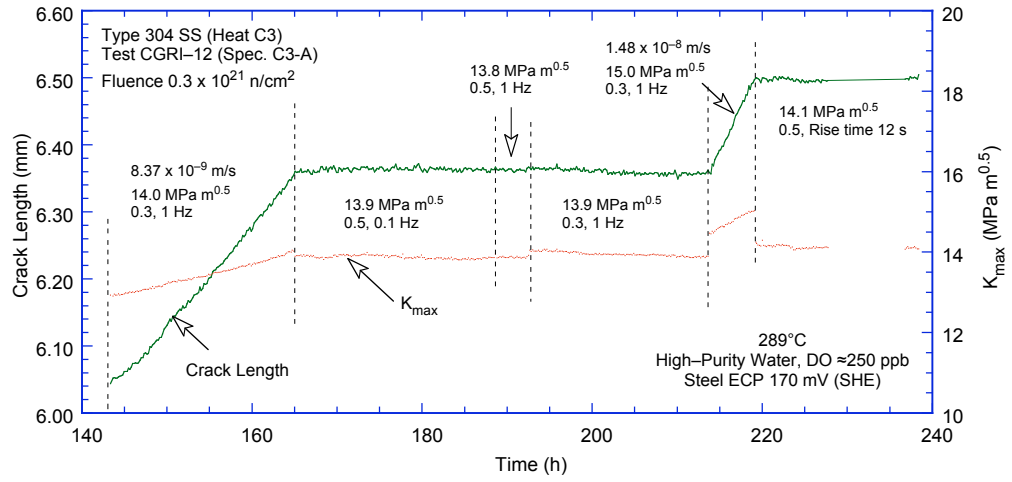

(a)

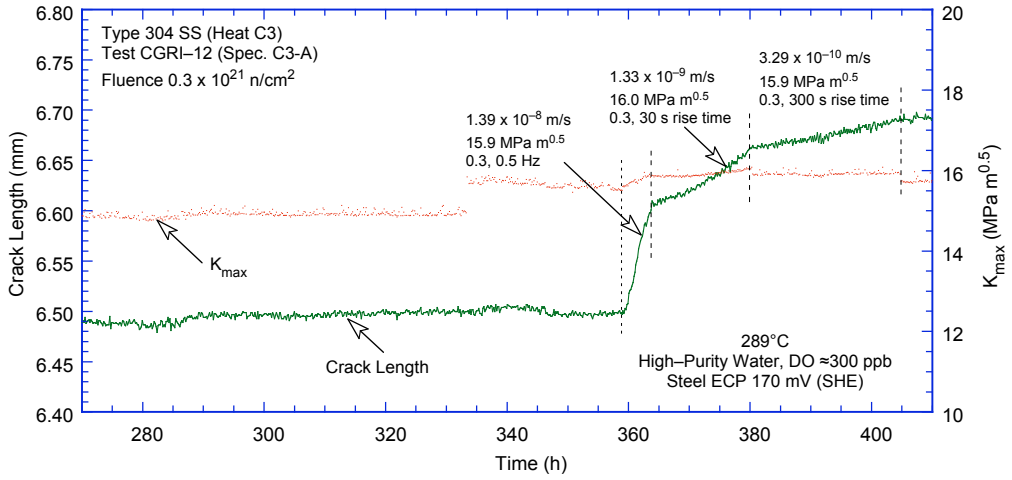

(b)

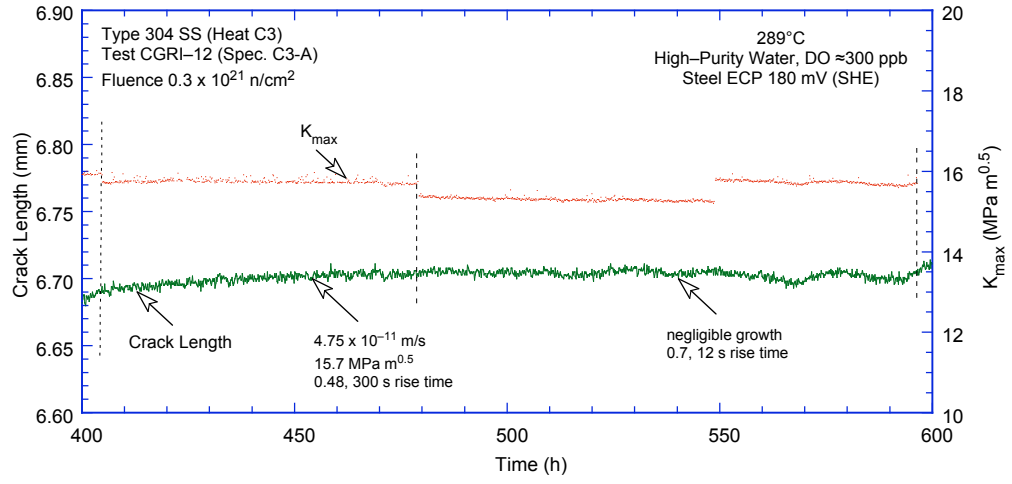

(c)

Figure 38. Crack length vs. time plots for irradiated Type 316 SS (Heat C16) in high–purity water at 289°C during test periods (a) 1–2, (b) 3–5, (c) 6–7, (d) 8–10, and (e) 11–12.

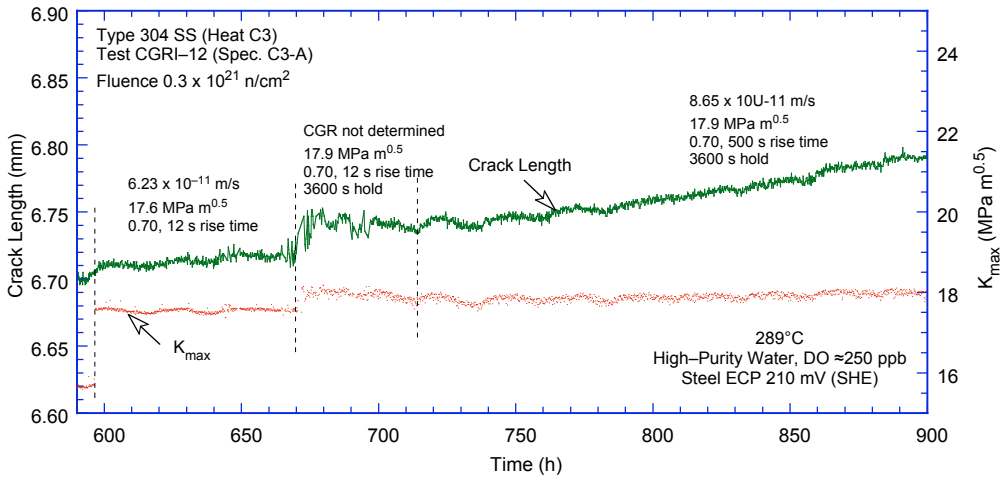

(d)

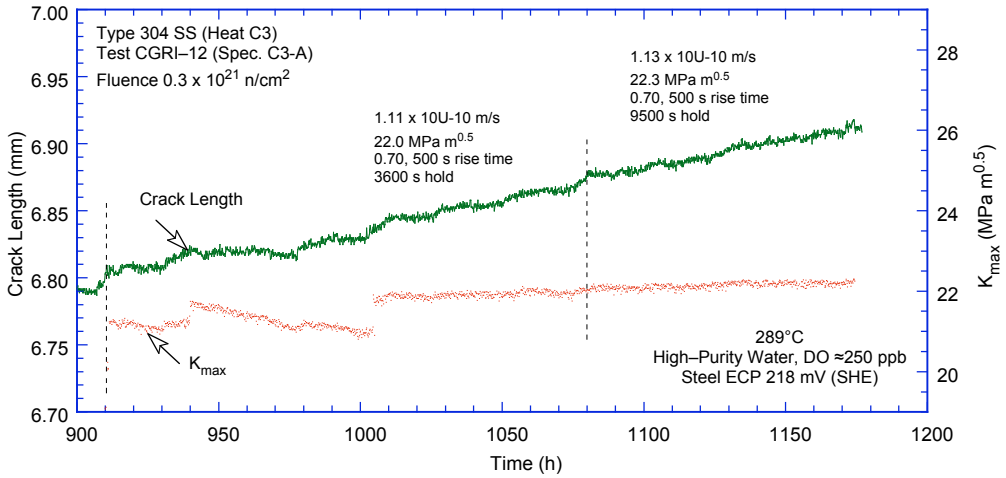

(e)

Figure 38. (Cont'd)

Crack growth rates could not be measured during test period 9 because of significant variations in the autoclave temperature, which resulted in large fluctuations in the DC potential measurements (Fig. 38d). Also, during test period 11 (Fig. 38e), applied K_{max} gradually decreased from the desired value of 22 to 20.5 MPa $m^{1/2}$ over a 50–h period because of a faulty back–pressure regulator. Specimen C3–A irradiated to 0.3 x 10^{21} n/cm^2 showed very little environmental enhancement of CGRs both under continuous cycling and SCC conditions. There was no change in CGR when the hold time was increased from 3600 to 9500 s (Fig. 38e, test periods 11 and 12).

A photomicrograph of the fracture surface of both halves of the test specimen is shown in Fig. 39. The final crack length, determined from the photograph, showed very good agreement with the value estimated from the DC potential measurement. Also, the results in Table 7 indicate that for specimen C3–A, loading conditions for all test periods, except 11 and 12, satisfied the K/size criterion of Eq. 9.

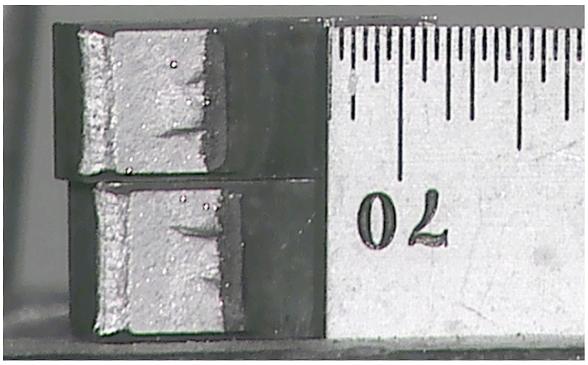

Figure 39.
Photomicrograph of the fracture surface of Specimen C3–A.

3.2.3.2 Irradiated Austenitic SSs under Continuous Cycling

For continuous cyclic loading, the experimental CGRs for specimen C3-A and other specimens of irradiated Heats C3 and C16 in BWR environments are compared in Fig. 40 with the CGRs predicted for austenitic SSs in air under the same loading conditions. The curves in the figure are calculated from the Shack/Kassner model for nonirradiated austenitic SSs in high–purity water with either 8 or 0.2 ppm DO (Eqs. 6 and 7, respectively) and are included to provide a comparison with the irradiated CGR data.

The results for SSs irradiated to 0.9 or 2.0 x 10^{21} n/cm^2 (1.35 or 3.0 dpa) indicate significant enhancement of the CGRs in high–DO water under cyclic loading with long rise times. The CGRs for Heat C3 irradiated to either 0.9 or 2.0 x 10^{21} n/cm^2 (open circles and triangles) and for Heat C16 irradiated to 2.0 x 10^{21} n/cm^2 (solid triangles) are comparable. For these irradiation conditions, the CGRs in water with ≈ 300 ppb DO are slightly higher than the rates predicted by the Shack/Kassner model for nonirradiated austenitic SSs in high–purity water with 8 ppm DO (Fig. 40a).

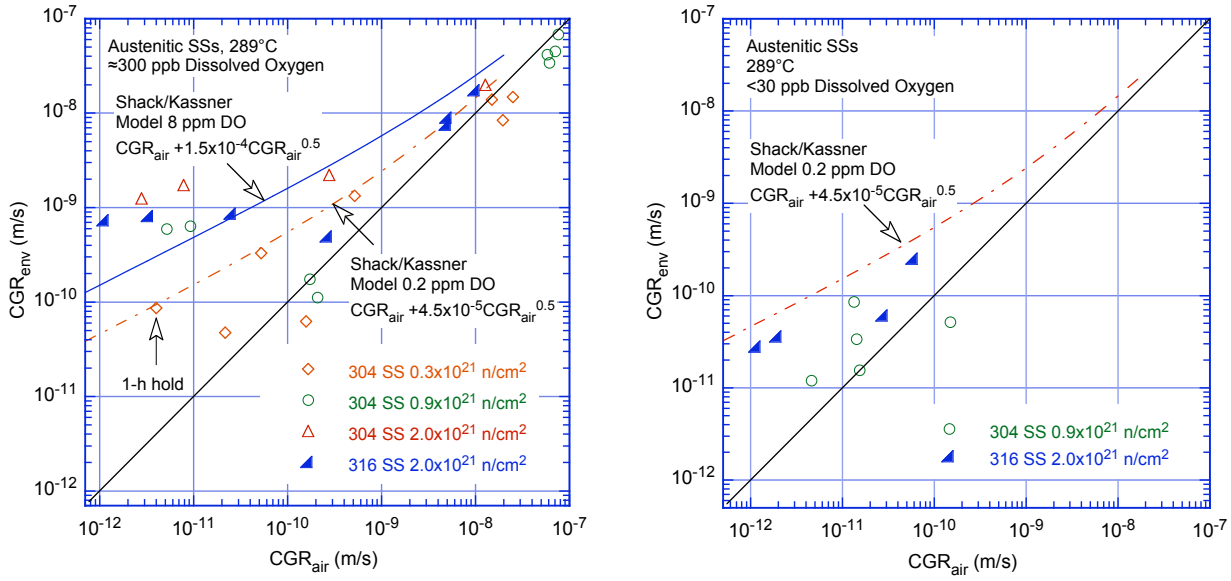

(a) (b)

Figure 40. CGR data for irradiated austenitic SSs under continuous cycling at 289°C in high–purity water with (a) ≈300 ppb and (b) <30 ppb dissolved oxygen.

Heat C3 irradiated to 0.3 x 10^{21} n/cm^2 (0.45 dpa) shows less environmental enhancement of CGRs in high–DO water (open diamonds in Fig. 40a); the CGRs in water with ≈ 300 ppb DO are best represented by the Shack/Kassner model for nonirradiated austenitic SSs in high–purity water with 0.2 ppm DO.

For continuous cyclic loading, decreasing the DO level has a beneficial effect on CGRs, e.g., decreasing the DO from ≈300 ppb DO to <30 ppb DO results in a factor of 25 decrease in the CGR. The growth rates are slightly lower for the irradiated steels in water with <30 ppb DO than for nonirradiated austenitic SSs in high–purity water with 0.2 ppm DO (Fig. 40b). The CGR data in the low–DO environment were not obtained for specimen C3-A because the relatively low CGRs expected for the material would have required long test durations. Based on other test results, the benefit of reduced DO is expected for Heat C3 irradiated to 0.3 x 10^{21} n/cm^2. The CGR data in low–DO environment was also not obtained for specimen C3–C irradiated to 2 x 10^{21} n/cm^2.

3.2.3.3 CGRs of Irradiated Austenitic SSs under Trapezoidal Waveform with Long Hold Periods

The experimental CGRs for irradiated Heats C3 and C16 obtained with a trapezoidal waveform (i.e., constant load with periodic partial unloading) in high– and low–DO water are plotted in Fig. 41. In high–DO water, the CGRs of Types 304L and 316L SS (Heats C3 and C16) irradiated to either 0.9 or 2.0 x 10^{21} n/cm^2 are a factor of ≈5 higher than the disposition curve for sensitized SSs in water with 8 ppm DO given in NUREG–0313.[67] The growth rates for the two steels at the same fluence level, as well as those for Heat C3 irradiated to 0.9 and 2.0 x 10^{21} n/cm^2 fluence levels, are comparable. In high–DO water, the CGRs for Type 304L Heat C3 irradiated to 0.3 x 10^{21} n/cm^2 are below the disposition curve for sensitized SSs in water with 8 ppm DO given in NUREG–0313.

The results also indicate a benefit from a low–DO environment. For Heat C3 irradiated to 0.9 x 10^{21} n/cm^2 and Heat C16 irradiated to 2.0 x 10^{21} n/cm^2 (circles and right triangles in Fig. 41), the CGRs decreased more than an order of magnitude when the DO level was decreased from ≈300 to <30 ppb. No benefit of low–DO environment was observed for Heat C3 irradiated to 2.0 x 10^{21} n/cm^2 (solid isosceles triangles in Fig. 41). However, the applied K_{max} for the test period in low–DO water was

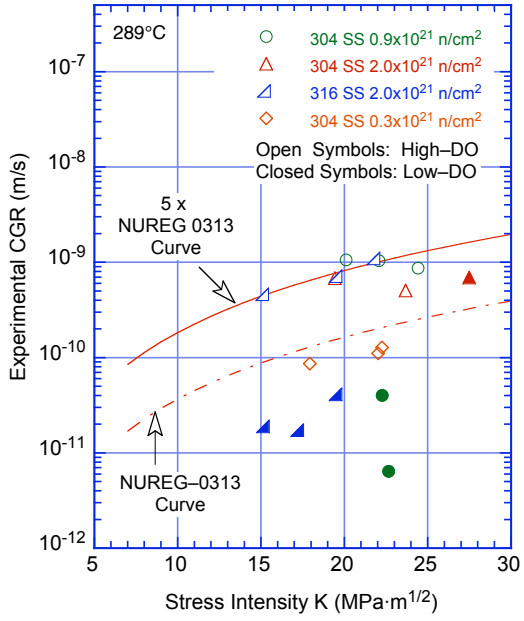

Figure 41.
CGR data under constant load with periodic partial unloads for irradiated austenitic SSs in high–purity water at 289°C.

44% greater than the allowable value based on the K/size criterion in Eq. 9. A detailed metallographic examination of the fracture surface of the specimen will be performed to validate the test results.

3.2.4 Crack Growth Tests on Nonirradiated Stainless Steel Weld HAZ Specimens

This section presents the results of crack growth tests in the BWR environment on nonirradiated 1/4–T CT specimens of Type 304L GG core shroud H5 weld HAZ and Type 304 laboratory–prepared weld HAZ. The GG weld HAZ specimens were from the bottom shell of the H5 weld and were in the as–welded condition (GG5B–A) and the as–welded plus thermally treated condition (GG3B–A–TT). The Type 304 SS laboratory prepared weld HAZ specimen was in the as–welded plus thermally treated condition (853B–A–TT).

3.2.4.1 Specimen GG5B–A of the HAZ from Grand Gulf Core Shroud H5 SA Weld, Test CGR–10

The environmental and loading conditions, experimental CGRs, allowed values of K_{max} from the K/size criterion, and the deviation of applied K_{max} from the allowed value are given in Table 8. The changes in the crack length and K_{max} with time during the various test periods are shown in Fig. 39. The test was started in high–DO water (≈580 ppb DO in effluent) and a flow rate of 140 mL/min. Because of a faulty reference electrode, the ECPs of the Pt and SS electrodes in the effluent could not be monitored during the test. The water conductivity was monitored continuously.

Precracking was initiated at R = 0.23, K_{max} ≈15 MPa $m^{1/2}$, and a triangular waveform. After ≈0.6 mm crack advance, R was increased incrementally to 0.7, and the waveform changed to a slow/fast sawtooth with a rise time of 30 s; in all cases the fast rate (time to unload) was 2 s. During the initial 300–h test period (i.e., precracking and test periods 1–2b in Table 8), no environmental enhancement was observed in the measured growth rates. Also, decreasing the flow rate from 140 to 35 mL/min had little or no effect on the CGRs, although the conductivity increased from 0.08 to 0.12 µS/cm.

Table 8. Crack growth results for Specimen GG5B–A[a] of Type 304L HAZ in high–purity water at 289°C

Test Period[b]	Test Time, h	Flow Rate, cc/min	Cond.,[c] µS/cm	O_2 Conc.,[c] ppb	R Load Ratio	Rise Time, s	Down Time, s	Hold Time, s	K_{max}, MPa·$m^{1/2}$	ΔK, MPa·$m^{1/2}$	Growth Rate, m/s	Allowed K_{max},[d] MPa·$m^{1/2}$	Deviation in K_{max},[d] %
Pre a	97	140	0.07	580	0.23	0.25	0.25	0	16.7	12.9	7.57E-08	19.3	-13
Pre b	98	140	0.07	580	0.23	0.25	0.25	0	15.0	11.5	3.42E-08	19.1	-22
Pre c	114	140	0.08	590	0.23	7.5	7.5	0	14.2	11.0	3.59E-10	19.1	-25
Pre d	120	140	0.07	590	0.23	0.50	0.50	0	15.7	12.1	3.40E-08	18.7	-16
1	143	140	0.08	485	0.52	30	2	0	15.5	7.4	5.85E-11	18.6	-17
2a	259	30	0.12	440	0.71	30	2	0	17.0	4.9	negligible	18.6	-9
2b	306	35	0.14	450	0.71	30	2	0	17.0	4.9	1.52E-11	18.6	-9
2c*	337	35	0.14	464	0.72	30	2	0	20.6	5.8	3.15E-10	18.6	11
3*	407	35	0.14	460	0.71	300	2	0	20.8	6.0	1.81E-10	18.5	13
4*	455	35	0.13	500	0.71	1,000	2	0	20.9	6.1	1.26E-10	18.5	13
5	572	35	0.13	500	0.71	12	12	3600	21.1	–	6.01E-11	18.4	14
6	646	105	0.08	500	0.71	12	12	3600	26.5	–	1.72E-10	18.3	45
7	692	105	0.07	500	0.71	12	12	3600	26.9	–	1.55E-10	18.2	47
8	767	105	0.07	500	0.71	1,000	2	0	27.4	7.9	3.18E-10	18.1	51

[a]Nonirradiated Grand Gulf H5 SA weld bottom shell HAZ, as–welded condition.
[b]An asterisk indicates environmental enhancement of growth rates under cyclic loading.
[c]Represents values in the effluent.
[d]Based on flow stress.

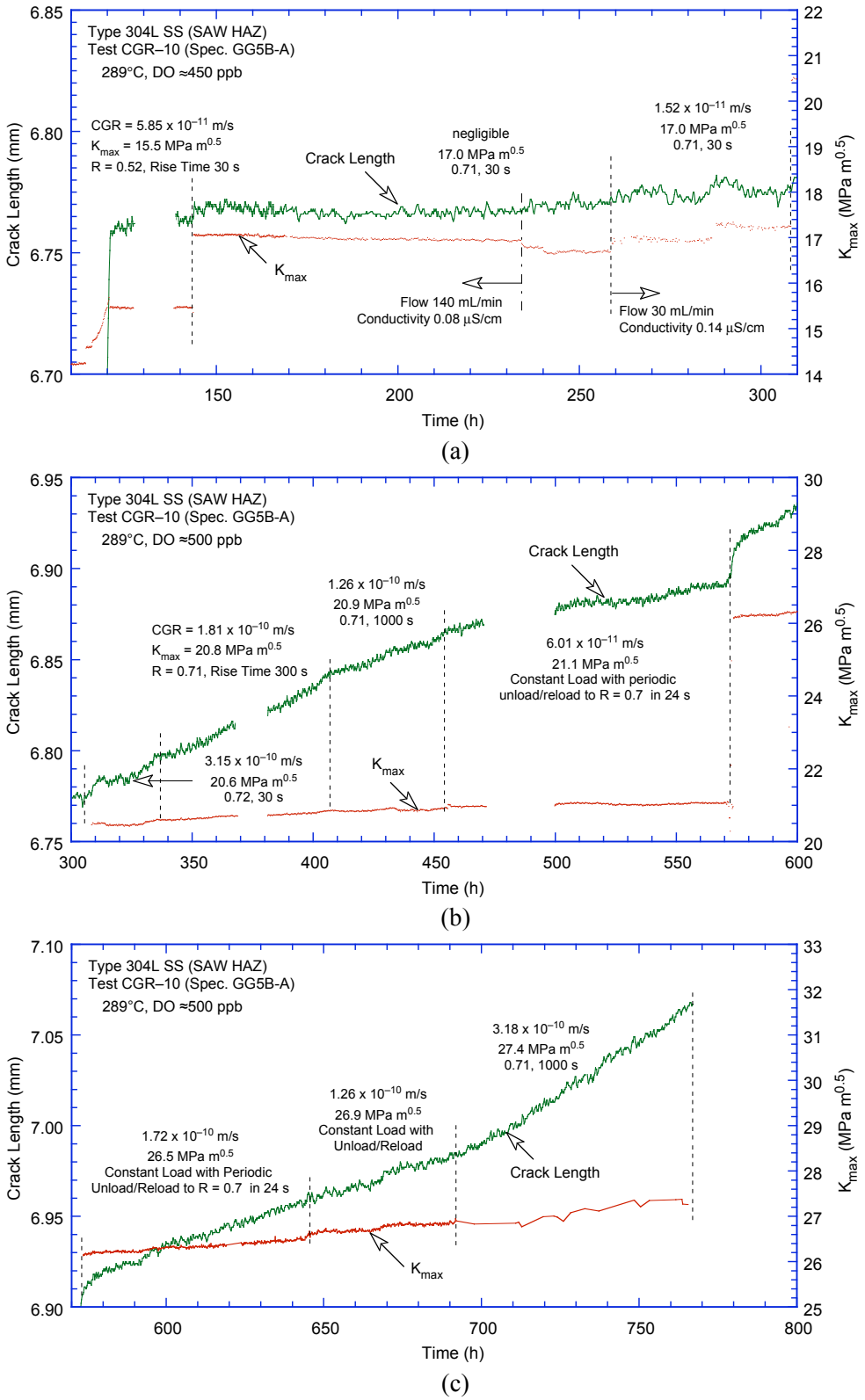

Figure 42. Crack length vs. time plots for nonirradiated HAZ specimen of Grand Gulf Type 304L bottom shell H5 weld in high–purity water at 289°C during test periods (a) precracking–3, (b) 4-6, and (c) 7–8.

After ≈310 h, K_{max} was increased to ≈20 MPa $m^{1/2}$, and the rise time was increased to 300 s and then 1000 s. Under these conditions, environmental enhancement of CGRs occurred. After ≈450 h the loading waveform was changed to trapezoidal waveform with 3600 s hold period and 12–s unload and reload periods. For Specimen GG5B–A, the experimental K_{max} values were generally higher (≈13% higher during test periods 2c–5 and over 45–50% higher during periods 6–8) than the allowed K_{max} based on flow stress and Eq. 9.

Photomicrographs of the fracture surface of the two halves of the broken specimen are shown in Fig. 43. A relatively straight crack front is evident. The crack lengths were measured by both optical and scanning electron microscopy. The results showed very good agreement with the values estimated from the DC potential measurements; the difference in measured and estimated values was <5%.

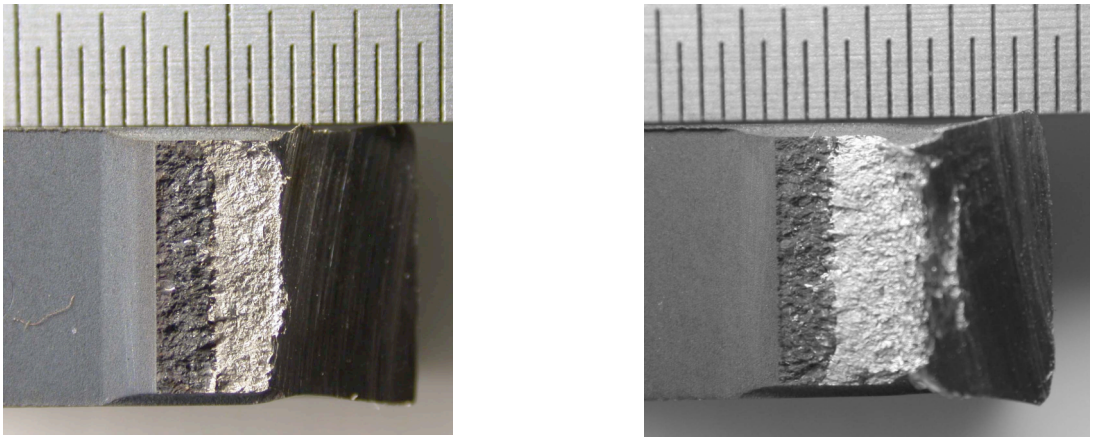

(a) (b)

Figure 43. Photomicrograph of the fracture surface of Specimen GG5B–A.

After the test both halves of the fractured specimen were then cleaned chemically to remove the surface oxide film, and the fracture surface was examined by SEM. A micrograph of the fracture surface for Specimen GG5B–A is shown in Fig 44. Micrographs showing a slice of the entire crack advance during the test and typical fracture morphology at select locations on the surface are given in Fig. 45. With minor variations, a predominantly transgranular (TG) fracture morphology appears for the entire test. Most of the TG facets show a well–defined river pattern (Fig 45a). Also, a TG fracture with river pattern is observed from room–temperature cycling after the test (Fig. 45d) to mark the final crack front.

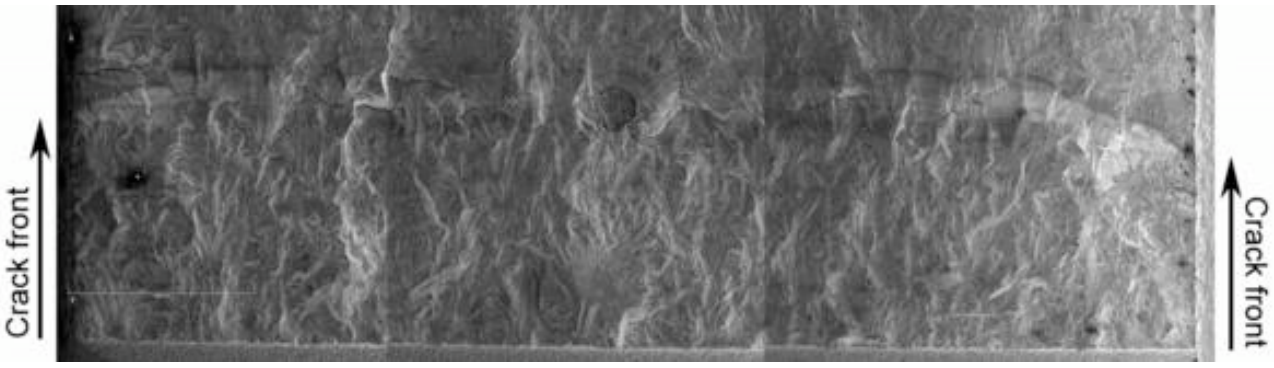

Figure 44. Micrograph of the fracture surface of Specimen GG5B–A tested in high–DO water at 289°C.

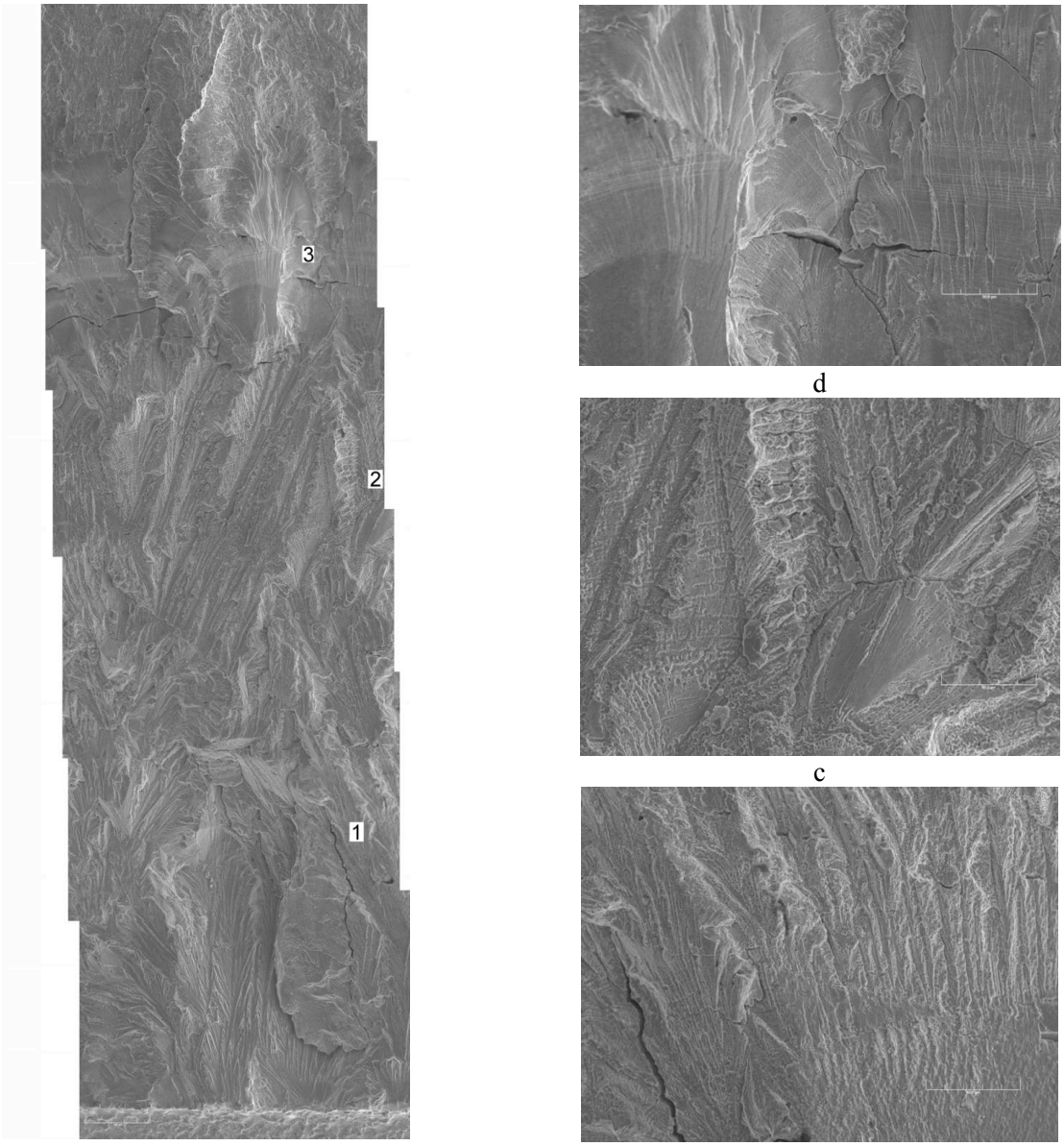

Figure 45. Micrographs showing (a) slice of the entire length of fracture surface, and (b), (c), and (d) high magnification micrographs of the fracture surface at locations 1, 2, and 3, respectively.

3.2.4.2 Specimen 85–3A–TT of the HAZ from Laboratory–Prepared SMA Weld, Test CGR-11

The environmental and loading conditions, experimental CGRs, allowed values of K_{max} from the K/size criterion, and deviation of applied K_{max} from the allowed value are given in Table 9. The test was started in a high–DO environment (e.g., effluent DO level of ≈600 ppb); the water flow rate was maintained constant at ≈105 mL/min during the test. The effluent water conductivity and ECPs of a Pt and SS electrode were monitored continuously; the values are listed in the table. The effluent DO level was measured periodically.

Table 9. Crack growth results for Specimen 85–3A–TT[a] of nonirradiated Type 304 SS SMA weld HAZ in high–purity water at 289°C

Test Period[b]	Test Time, h	Cond.,[c] µS/cm	ECP[c] mV (SHE) Pt	ECP[c] mV (SHE) Steel	R Load Ratio	Rise Time, s	Down Time, s	Hold Time, s	K_{max}, MPa·m$^{1/2}$	ΔK, MPa·m$^{1/2}$	Growth Rate, m/s	Allowed K_{max}, MPa m$^{1/2}$	Deviation in K_{max},[d] %
Pre a	144	0.10	183	27	0.21	0.50	0.50	0	16.13	12.74	5.46E-08	15.7	3
Pre b	148	0.08	182	32	0.21	0.50	0.50	0	15.01	11.86	5.00E-08	15.4	-2
1	166	0.07	182	32	0.51	30	2	0	14.64	7.18	5.61E-11	15.3	-5
2	190	0.07	184	41	0.51	30	2	0	16.73	8.20	5.50E-10	15.3	9
3	215	0.07	182	45	0.71	30	2	0	16.90	4.90	3.16E-11	15.3	11
4*	264	0.07	184	60	0.71	30	2	0	19.82	5.75	8.85E-10	15.1	32
5a*	298	0.07	188	68	0.71	300	2	0	19.80	5.74	2.75E-10	15.0	32
5b*	338	0.07	187	79	0.71	300	2	0	20.24	5.87	7.91E-10	14.8	36
6*	384	0.07	188	87	0.70	1000	2	0	20.51	6.15	4.57E-10	14.7	39
7	478	0.07	192	106	0.70	12	12	3600	21.15	0.00	6.60E-10	14.4	47
8	646	0.14	-482	-633	0.70	12	12	3600	21.37	0.00	9.13E-11	14.3	49
9	862	0.12	-477	-621	0.70	12	12	3600	24.96	0.00	4.29E-11	14.2	76

[a]Grand Gulf H5 SA weld bottom shell HAZ, nonirradiated.
[b]An asterisk indicates environmental enhancement of growth rates under cyclic loading.
[c]Represents values in the effluent. Water flow rate was maintained at ≈105 mL/min; the DO level in the effluent was ≈600 ppb during the high–DO test and <40 ppb during the low–DO test.
[d]Based on flow stress.

Precracking was initiated at R ≈0.2, K_{max} ≈14 MPa m$^{1/2}$, and a triangular waveform. After ≈0.4 mm crack advance, R was increased incrementally to 0.7, and the waveform was changed to a slow/fast sawtooth with rise times of 30–1000 s; in all cases time to unload was 2 s. The constant load tests were conducted using a trapezoidal waveform with R = 0.7, 1–h hold period at peak load, and 12–s unload and reload periods. During each test period, the maximum stress intensity factor was maintained approximately constant by periodic load shedding (less than 2% decrease in load at any given time).

After ≈480 h, the DO level in the feedwater was decreased from ≈600 ppb to <40 ppb by sparging the feedwater tank with pure N_2. Changes in crack length and ECP of Pt and SS electrodes during the transient period are shown in Fig. 46. For this test, because the flow rate was higher than the rate used for the in–cell tests, changes in the environment were significantly fast. However, the changes in the steel ECP were slower compared with the Pt ECP, e.g., the ECP decreased below –400 mV (SHE) within 10 h

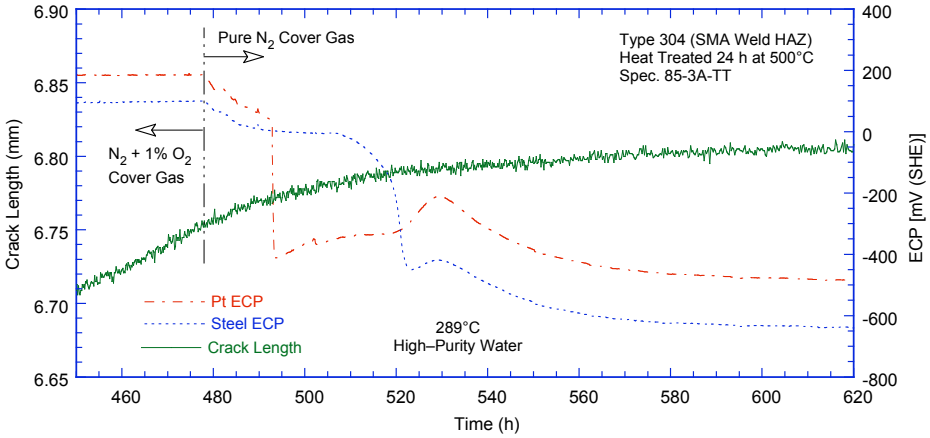

Figure 46. Change in crack length and ECP of Pt and SS electrodes during test periods 5–6 and the intermediate transition period.

for the Pt electrode and 40 h for the steel electrode. A slight increase in ECP values of both Pt and steel electrode at ≈530 h was due to an increase in the effluent DO level.

After the test, the final crack front was marked by fatigue cycling in air at room temperature. A detailed metallographic evaluation of the specimen was performed to examine the fracture surface and fracture plane morphologies. A 1–mm–thick slice of the entire CT specimen was cut off, and the remainder of the specimen was pulled apart. Photomicrographs of the fracture surface of the two halves of the broken specimen are shown in Fig. 47, and a composite micrograph of the cross section of the specimen is shown in Fig. 48. The crack lengths were measured by both optical and scanning–electron microscopy. The actual final crack extension was ≈40% greater than the value determined from the DC potential measurements. Crack extensions estimated from the DC potential drop method were scaled proportionately; the corrected values of K_{max} and growth rates are listed in Table. 9.

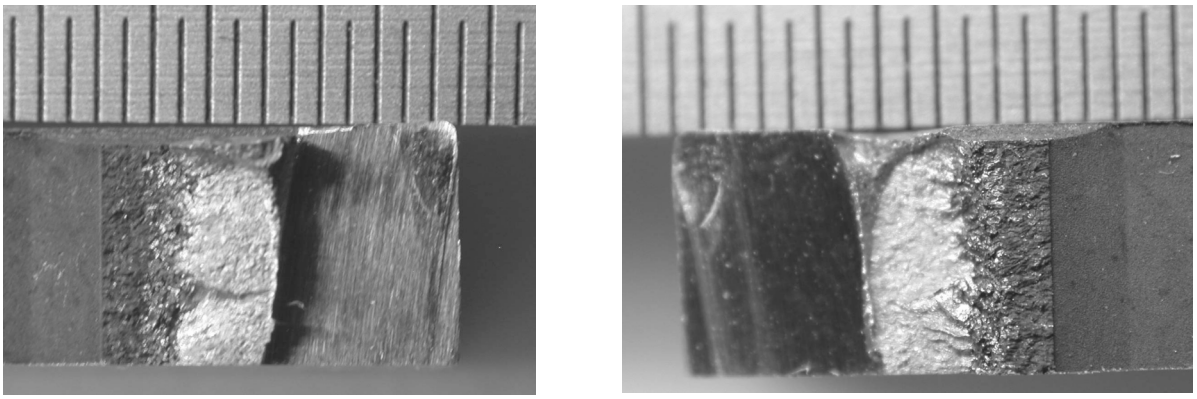

(a) (b)

Figure 47. Photomicrographs of the fracture surfaces of the two halves of Specimen 85–3A-TT.

The changes in crack length and K_{max} with time during the test periods are shown in Fig. 49. For this specimen, significant environmental enhancement occurred after ≈210 h when K_{max} was increased from ≈17 to 20 MPa $m^{0.5}$ (Fig. 49b). Also, the results in Table 9 indicate that the loading conditions from precracking up to test period 3 satisfy the K/size criterion and are ≈34% higher than the allowed value for periods 4–6, 48% higher for period 7 and 8, and 76% higher for period 9.

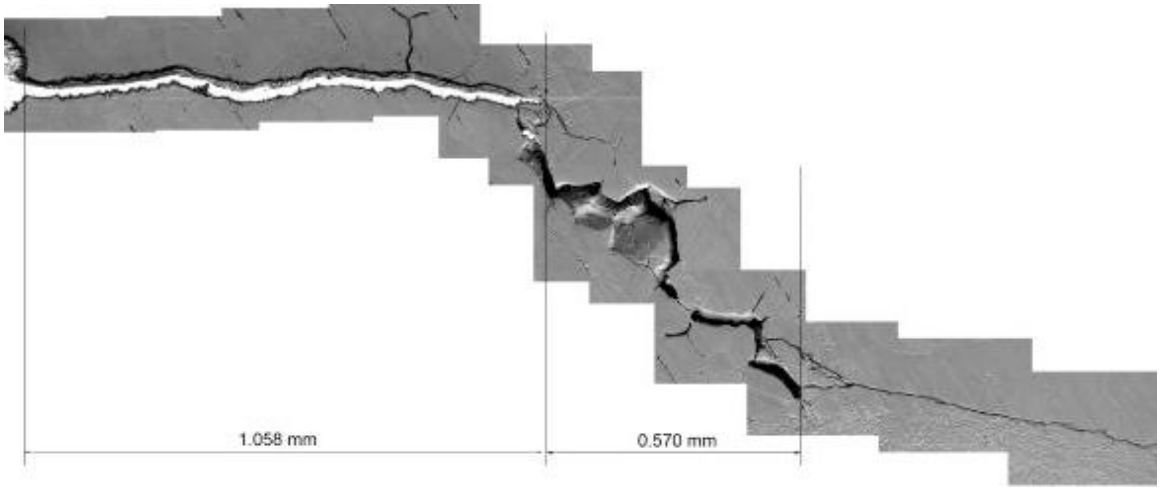

Figure 48. Micrograph of the cross section of Specimen 85-3A-TT showing the fracture plane profile.

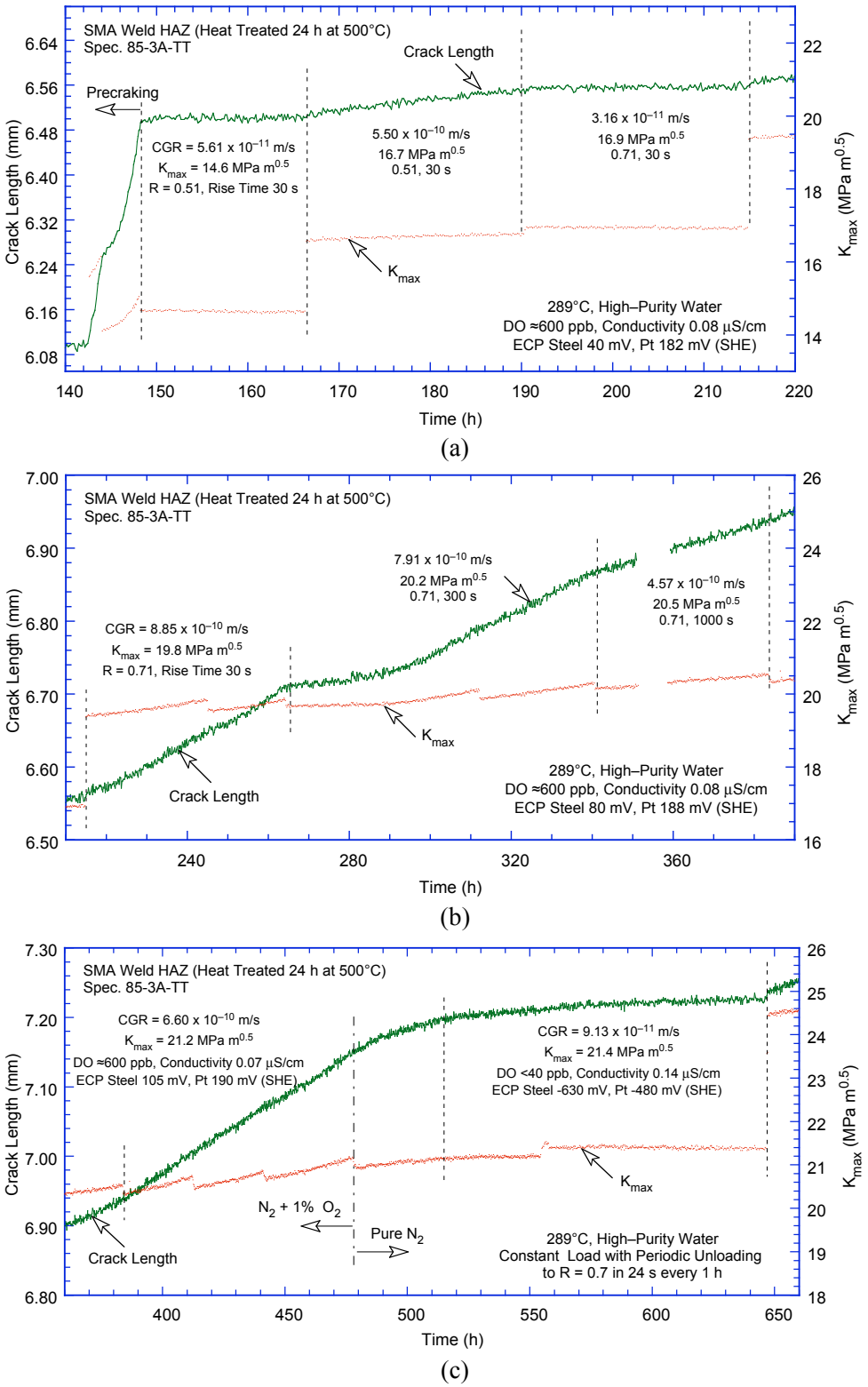

Figure 49. Crack length vs. time plots for nonirradiated HAZ specimen of Grand Gulf Type 304L bottom shell H5 weld HAZ in high–purity water at 289°C during test periods (a) 1–3, (b) 4-6, (c) 7–8, and (d) 9.

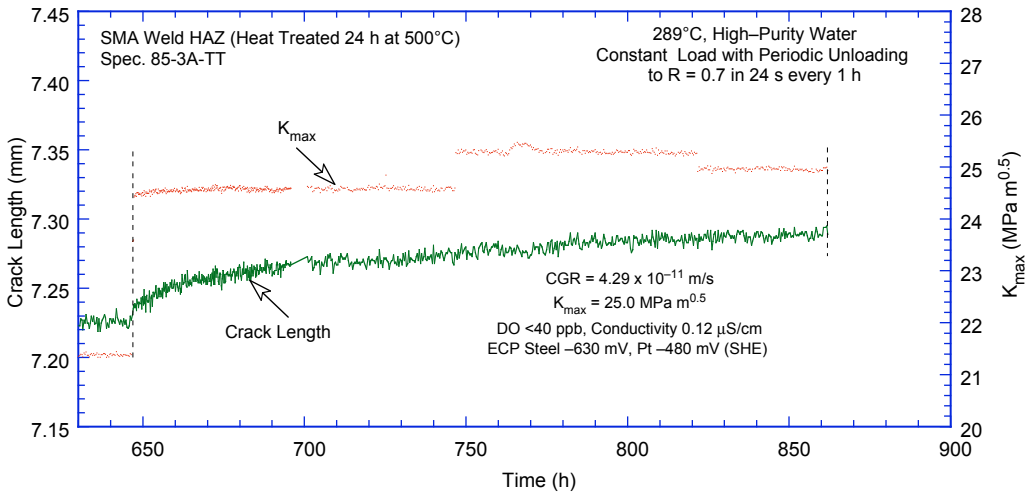

(d)

Figure 49. (Contd.)

The fracture plane orientation shown in Fig. 48 suggests that the applied K_{max} during the last few test periods may have exceeded the K/size criterion. The fracture plane is initially normal to the stress axis, but for the last ≈0.6 mm crack extension it is at 45° to the stress axis. The change in the fracture plane orientation occurred at an average crack extension of 1.16 mm; actual values varied ≈1.0–1.25 mm across the thickness of the specimen. Also, the fracture surface morphology is predominantly TG along the plane normal to the stress axis and completely IG along the plane 45° to the stress axis. A micrograph of the fracture surface for Specimen 85–3A-TT is shown in Fig 50.

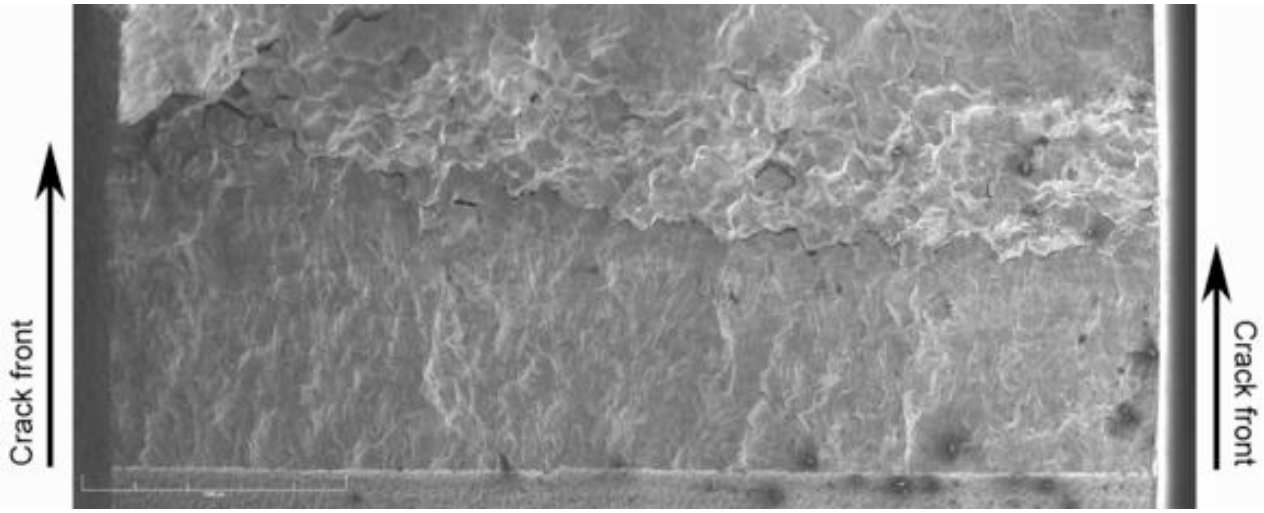

Figure 50. Micrograph of the fracture surface of Specimen 85-3A-TT tested in high–DO water at 289°C.

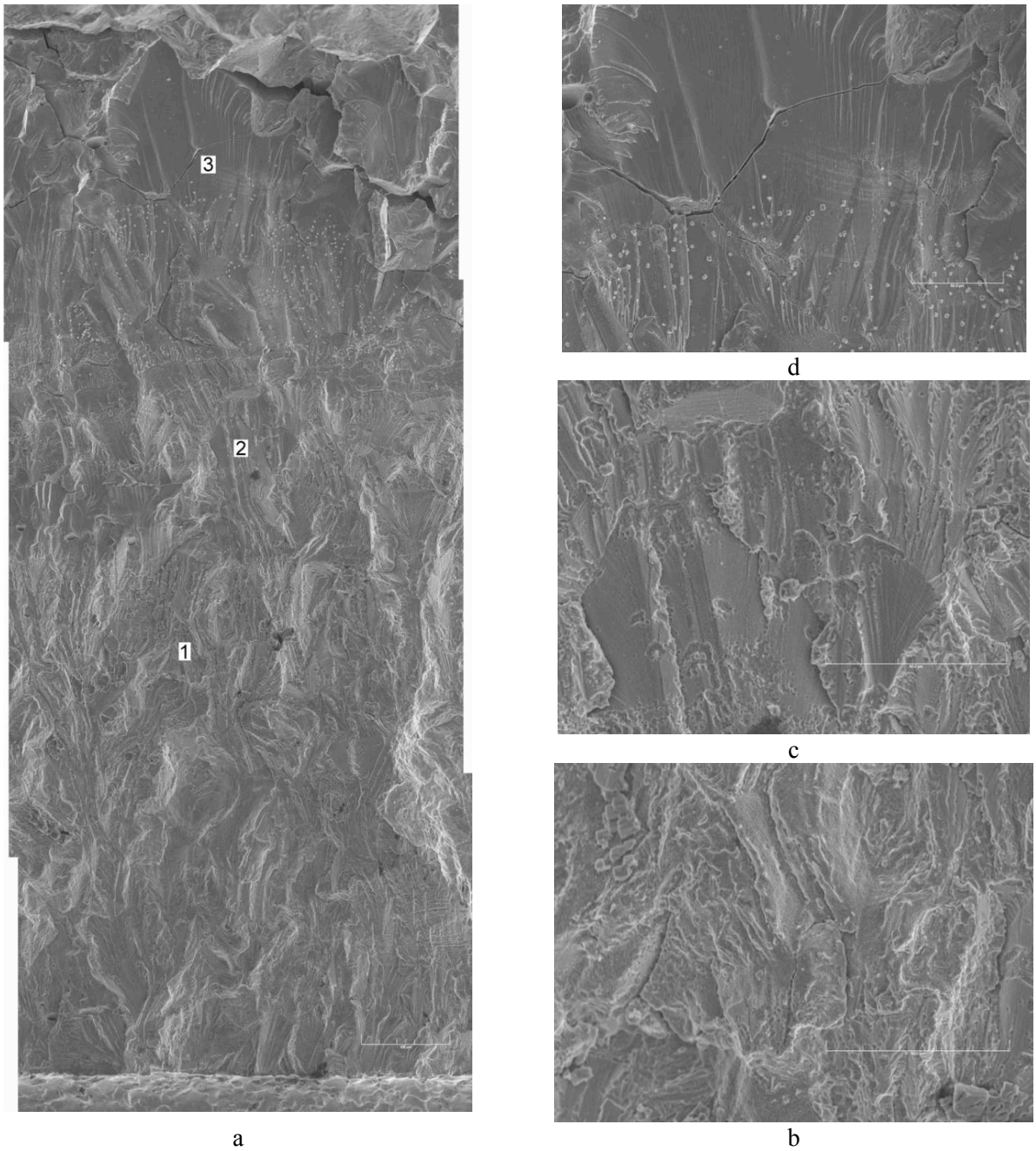

Figure 51. Micrograph showing (a) slice of the fracture surface that was perpendicular to the stress axis, and (b), (c), and (d) high-magnification micrographs of the fracture surface at locations 1, 2, and 3, respectively.

Micrographs showing a slice of the fracture surface that was normal to the stress axis and the typical fracture morphology at select locations on the surface are given in Fig. 51. The specimen was cleaned chemically to remove the surface oxide film. The fracture surface that is normal to the stress axis exhibits a predominantly TG fracture morphology, and most of the TG facets show a well–defined river pattern (Fig. 51c, d). A narrow region of IG fracture is observed before the fracture plane orientation changed along the plane 45° to the stress axis. Typical fracture morphologies along the change in the fracture plane orientation and before and after the change are shown in Fig. 52.

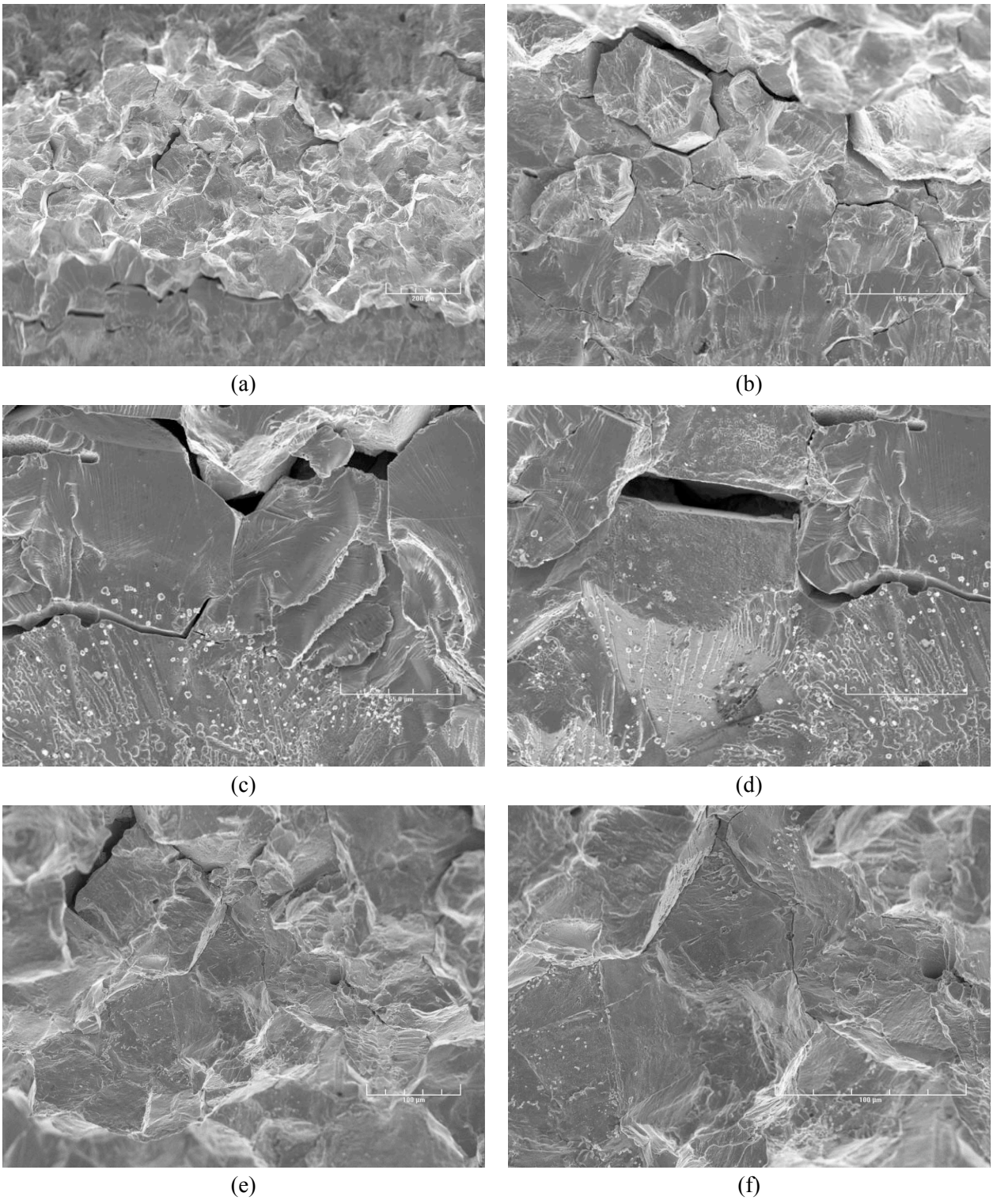

Figure 52. Typical fracture morphologies (a, b) along the change in the fracture plane direction and (c, d) before and (e, f) after the change in direction.

3.2.4.3 Specimen GG3B–A–TT of the HAZ from Grand Gulf Core Shroud H5 SA Weld, Test CGR-14

The environmental and loading conditions, experimental CGRs, allowable values of K_{max} by the K/size criterion, and the deviation of applied K_{max} from the allowable value are given in Table 10. During most test periods, K_{max} was maintained approximately constant by periodic load shedding. The test was started in high–DO water (≈400 ppb DO in effluent) and water flow rate of ≈100 mL/min. The effluent water conductivity and ECPs of a Pt and SS electrode were monitored continuously; the values are listed in the table. The effluent DO level was measured periodically.

Table 10. Crack growth results for Specimen GG3B–A–TT[a] of Type 304L HAZ in high–purity water at 289°C

Test Period[b]	Test Time, h	Cond.,[c] µS/cm	ECP[c] mV (SHE) Pt	ECP[c] mV (SHE) Steel	R Load Ratio	Rise Time, s	Down Time, s	Hold Time, s	K_{max}, MPa·m$^{1/2}$	ΔK, MPa·m$^{1/2}$	Growth Rate, m/s	Allowed K_{max}, MPa m$^{1/2}$	Deviation in K_{max},[d] %
Pre a	120	0.10	181	20	0.31	0.5	0.5	0	14.32	9.88	7.71E-09	14.4	-1
Pre b	143	0.09	185	25	0.31	5	5	0	14.41	9.95	5.91E-09	14.3	1
Pre c	238	0.08	192	36	0.51	1	1	0	15.02	7.36	1.34E-09	13.9	8
1a*	275	0.07	192	40	0.71	12	2	0	15.95	4.63	8.66E-10	13.9	15
1b*	305	0.07	193	42	0.71	12	2	0	16.31	4.73	2.50E-09	13.7	19
2*	328	0.07	194	44	0.71	30	2	0	16.49	4.78	1.22E-09	13.5	22
3*	403	0.07	195	53	0.70	300	2	0	16.66	5.00	2.80E-10	13.4	24
4*	522	0.07	198	65	0.70	1,000	12	0	16.65	5.00	1.12E-10	13.4	24
5a	580	0.07	203	79	0.70	12	12	3600	16.37	4.91	4.34E-11	13.4	22
5b	765	0.14	202	87	0.70	12	12	3600	16.66	5.00	9.60E-12	13.2	27
6	1,000	0.07	155	42	0.70	500	12	3600	18.52	5.56	9.06E-12	13.1	41
7	1,094	0.07	155	47	0.70	500	12	3600	20.38	6.11	4.47E-12	13.1	55

[a]Nonirradiated Grand Gulf H5 SA weld bottom shell HAZ as–welded plus thermally treated for 24 h at 500°C.
[b]An asterisk indicates environmental enhancement of growth rates under cyclic loading.
[c]Represents values in the effluent. Water flow rate was ≈100 mL/min; the DO level in the effluent was ≈400 ppb.
[d]Based on flow stress.

Precracking was initiated at R ≈0.3, K_{max} ≈14 MPa m$^{1/2}$, and a triangular waveform. After ≈0.4 mm crack advance, R was increased incrementally to 0.7, and the waveform was changed to a slow/fast sawtooth with rise times of 12–1000 s; in all cases time to unload was 2 s. The constant load tests were conducted using a trapezoidal waveform with R = 0.7, 1–h hold period at peak load, and 12–s unload and reload periods. The test was interrupted twice, once at ≈240 h when the hydraulic pump tripped because of an increase in cooling water temperature, and again at 580 h when a power bump caused the hydraulic system to trip. Each time the test was restarted under the loading conditions prior to the interruption. The test conditions, e.g., crack length and growth rates, prior to the interruption were restored after the first restart but not the second restart. The specimen was accidentally overstrained during the second interruption; the crack length increased by ≈0.13 mm after the restart, and the growth rate was a factor of ≈5 lower. To help restore the higher growth rates, a 500–s rise time was added to the loading cycle but with no success. The unusually low CGRs measured during test periods 5b–7 may have been influenced by the accidental overstrain.

After the test, the final crack front was marked by fatigue cycling in air at room temperature. A detailed metallographic evaluation of the specimen was performed to examine the fracture surface and fracture plane morphologies. A 1–mm–thick slice of the entire CT specimen was cut off, and the remainder of the specimen was pulled apart. Composite micrographs of the cross section of the specimen and the fracture surface of the specimen are shown in Figs. 53 and 54, respectively.

In Specimen GG3B–A–TT, fracture seems to have occurred along two planes. These two fracture planes overlap in the specimen cross section shown in Fig. 53. Also, note that the crack extension represented by the noncorroded fine cracks on the right occurred during fatigue cycling at room temperature to mark the final crack front. The final crack extension as measured by SEM was ≈30% greater than the value determined from the DC potential measurements. Crack extensions estimated from the DC potential drop method were scaled proportionately; the corrected values of K_{max} and growth rates are listed in Table 10.

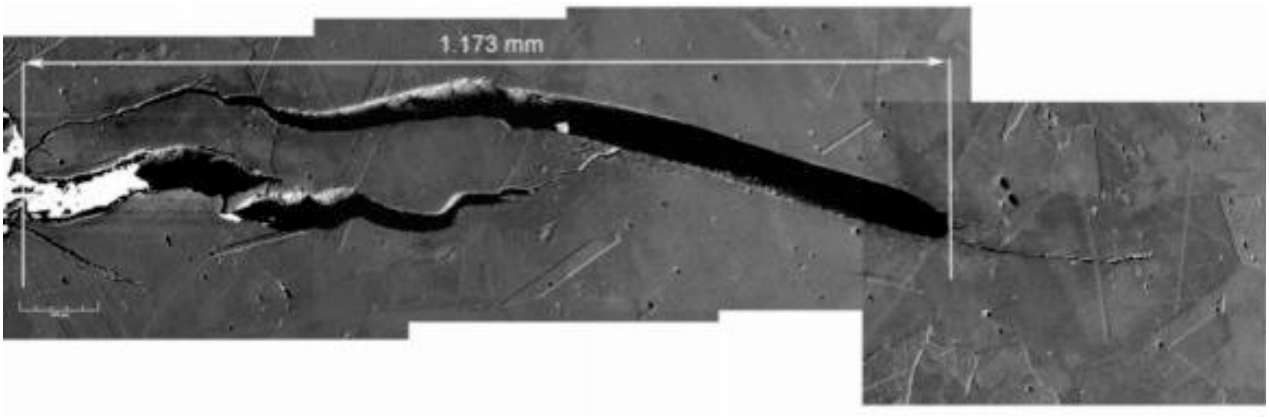

Figure 53. Micrograph of the cross section of Specimen GG3B-A-TT showing the fracture plane profile.

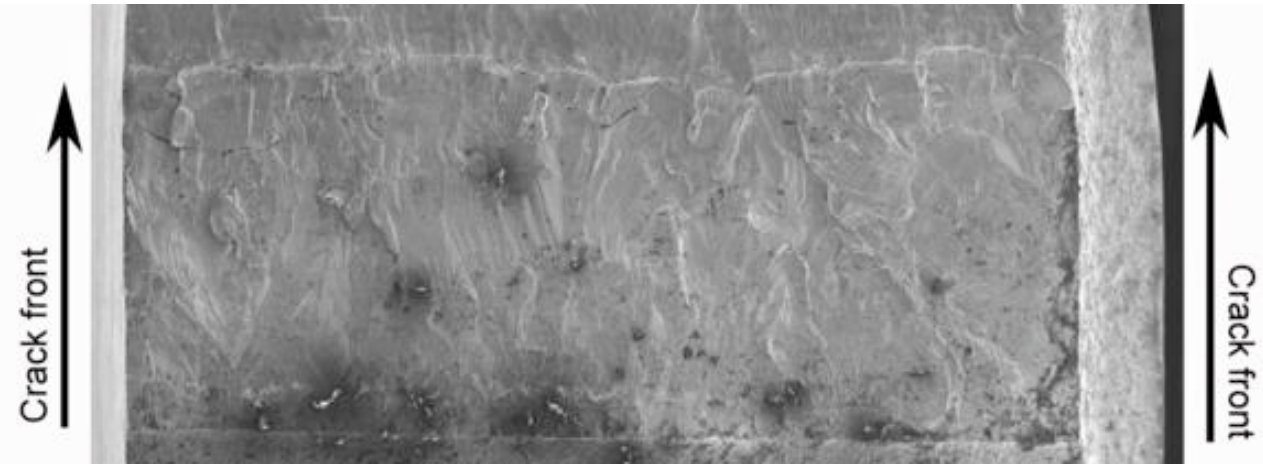

Figure 54. Micrograph of the fracture surface of Specimen GG3B-A-TT tested in high–DO water at 289°C.

The changes in crack length and K_{max} with time during the various test periods are shown in Figs. 55. For this specimen, significant environmental enhancement occurred after ≈270 h when R was increased from 0.5 to 0.7 (Fig. 55b). Also, the results in Table 9 indicate that for this specimen, the K values during precracking and up to test period 5 were 15–27% higher than the K/size criterion of Eq. 9, and 40–55% higher than the allowed value for periods 6 and 7.

Micrographs showing a slice of the entire crack extension and typical fracture morphology at select locations on the surface are given in Fig. 56. This specimen was not cleaned chemically to remove the surface oxide film. Once again, a predominantly TG fracture morphology is evident for the entire crack extension. Most of the TG facets show a well–defined river pattern.

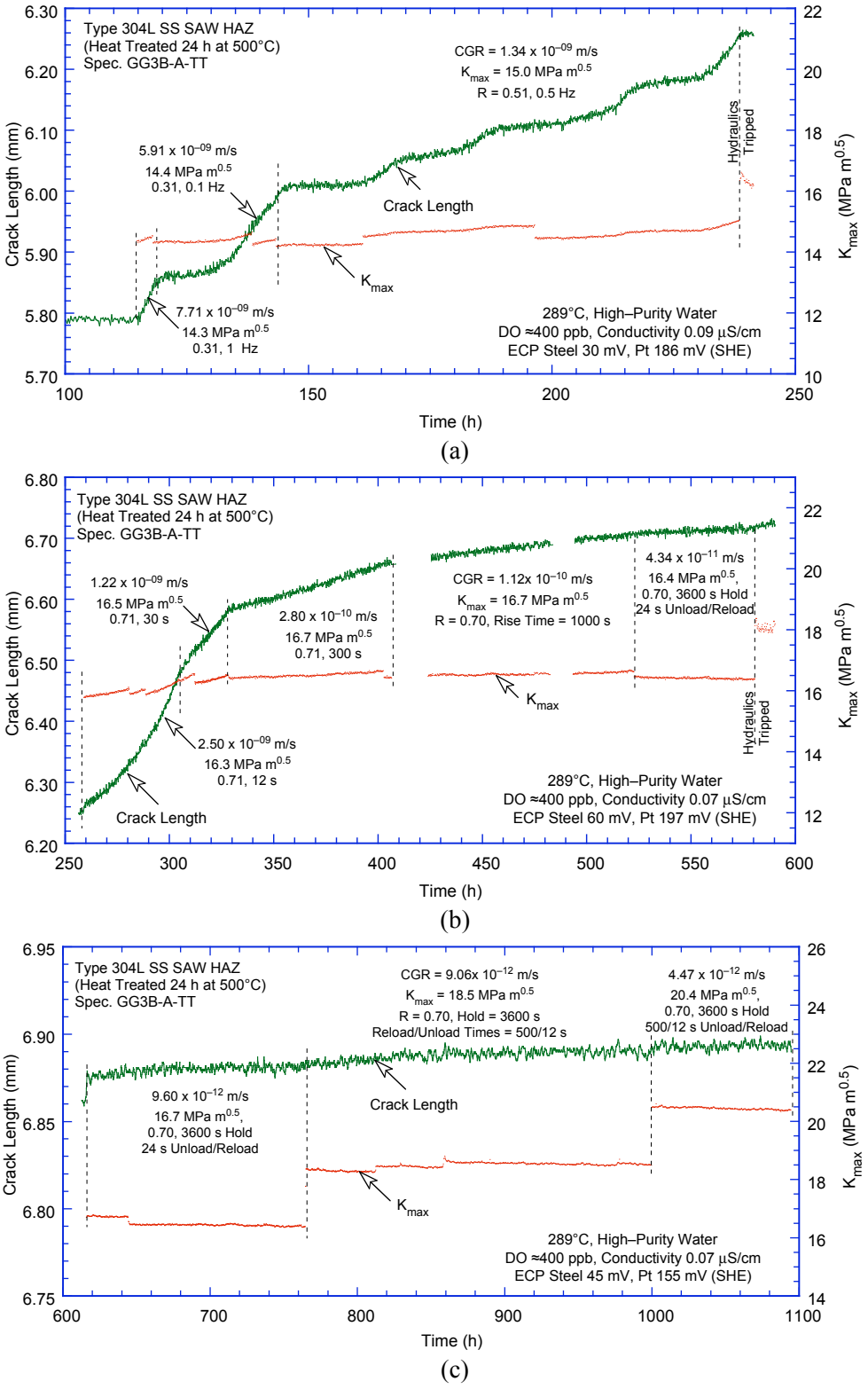

Figure 55. Crack length vs. time plots for nonirradiated thermally treated Type 304L bottom shell HAZ from the Grand Gulf H5 SA weld in high–purity water at 289°C during test periods (a) precracking, (b) 1-5, and (c) 5–7.

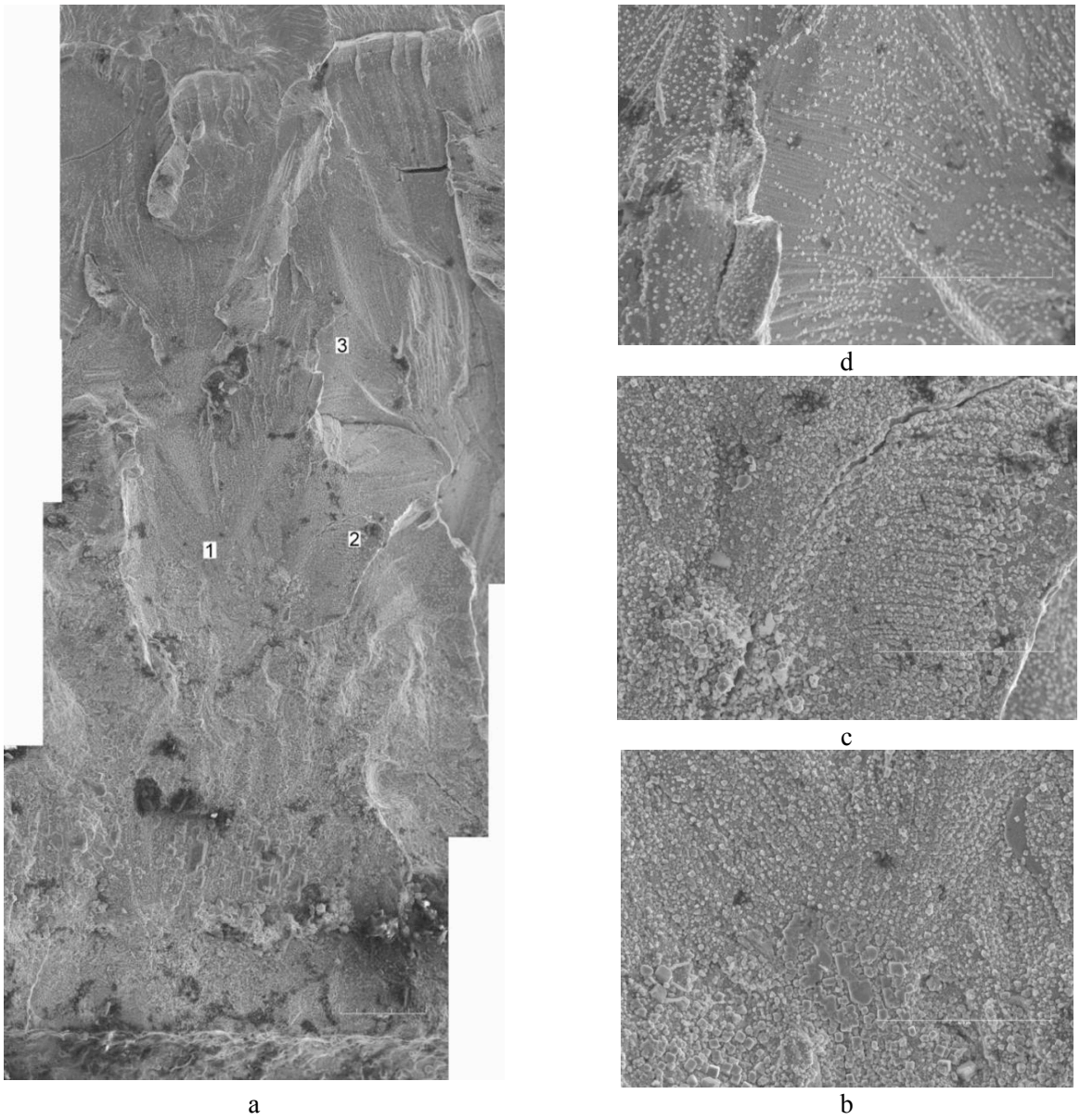

Figure 56. Micrographs showing (a) slice of the entire length of the fracture surface and (b), (c), and (d) high-magnification micrographs of the fracture surface at locations 1, 2, and 3, respectively.

3.2.4.4 Austenitic SS Weld HAZ under Continuous Cycling

For continuous cyclic loading, the experimental CGRs for nonirradiated SS weld HAZ specimens in high–DO environment and those predicted in air for the same loading conditions are plotted in Fig. 57. The uppermost curve represents the Shack/Kassner model for nonirradiated austenitic SSs in high–purity water with 8 ppm DO (Eq. 7). The CGRs in air $\dot{a}_{air}$ (m/s) were determined from the correlations developed by James and Jones,[69] e.g., Eqs. 3–5.

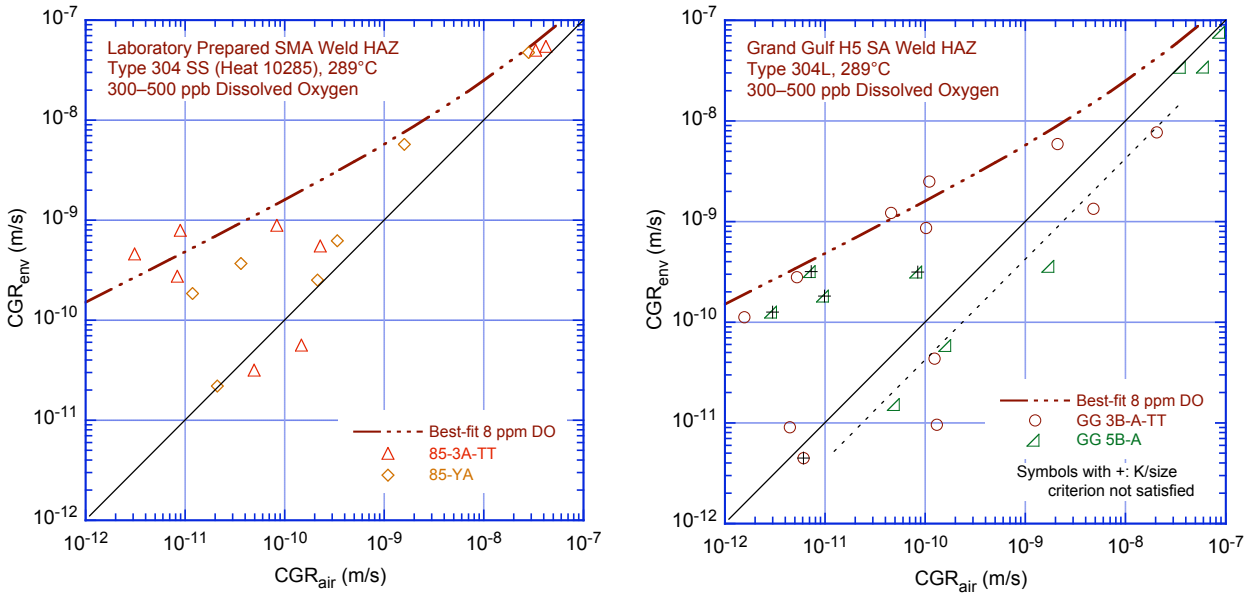

(a) (b)

Figure 57. CGR data for nonirradiated specimens of (a) laboratory–prepared Type 304 SS SMA weld HAZ and (b) Type 304L SA weld HAZ from the Grand Gulf core shroud under continuous cycling at 289°C in high–purity water with 300–500 ppb dissolved oxygen

In these figures, the data points that lie along the diagonal represent predominantly mechanical fatigue, and those that lie close to the Shack/Kassner model indicate environmentally enhanced crack growth. For both irradiated and nonirradiated specimens, enhancement of CGR did not occur readily when the load ratio and rise time were increased. For example, a large number of data points lie along the diagonal in Fig. 57, particularly for the GG Type 304L weld HAZ. The applied K_{max} had to be increased to observe enhanced growth rates.

The results indicate that under mechanical fatigue loading (i.e., no environmental enhancement), the CGRs for the GG Type 304L SA weld HAZ are lower than those for the Type 304 SMA weld HAZ, e.g., the CGRs for the laboratory–prepared Type 304 weld HAZ (Fig. 57a) show good agreement with the predicted values, while those for the GG weld HAZ are a factor of ≈2 lower (dashed line in Fig. 57b). Also, under this type of loading thermal treatment of the material for 24 h at 500° has little or no effect on growth rates.

In the high–DO NWC BWR environment (the environmentally enhanced condition), the CGRs of the laboratory–prepared Type 304 SS SMA weld HAZ (Fig. 57a) and those of the GG Type 304L SA weld HAZ (Fig. 57b) are comparable. For both GG and laboratory–prepared weld HAZ, the growth rates of the as–welded plus thermally–treated condition (triangles in Fig. 57a and circles in Fig. 57b) are marginally higher than those of the as–welded condition (diamonds in Fig. 57a and right–angle triangles in Fig. 57b). The results for GG weld HAZ are in good agreement with the growth rates obtained by Andresen et al.[72] for GG Type 304L weld HAZ in high–DO water (2000 ppb DO) at 288°C. For example, Andresen obtained a CGR of 3.4×10^{-10} m/s at R = 0.7, K_{max} = 27.4 MPa $m^{1/2}$, and triangular waveform with 500 -s rise time.

Metallographic examination of the fractured specimens indicates that under environmentally enhanced growth conditions (i.e., the data points that lie close to the Shack/Kassner model), an IG fracture morphology is observed for the laboratory–prepared Type 304 SS weld HAZ (Figs. 51 and 52).

Transgranular fracture morphology is observed under conditions that show little or no environmental enhancement (i.e., data points that lie close to the diagonal in Fig. 57a) and are predominantly due to mechanical fatigue. The fracture morphology of GG Type 304L HAZ seems to differ from that for Type 304 SMA weld HAZ. For example, in the GG HAZ, a TG fracture morphology with a well–defined river pattern is observed under all loading conditions, even where growth is environmentally enhanced (Figs. 45 and 56). IG fracture morphologies are usually observed in cold–worked SSs, whether initially annealed or sensitized.[72–74] Because of the residual strain associated with the welding process, the observed TG fracture morphology would not be expected in SS weld HAZ, especially for a case in which the environment enhancement is substantial. The reasons for this unexpected behavior are unclear.

3.2.4.5 Austenitic SS Weld HAZ under Constant Load or Cycling with Long Hold Periods

For CGR tests under constant load or using a trapezoidal waveform with long hold periods (i.e., constant load with periodic partial unloading), the experimental CGRs for nonirradiated SS weld HAZ specimens in the high–DO environment are shown in Fig. 58. The results are consistent with the data obtained under continuous cyclic loading. For nonirradiated Type 304L SA weld HAZ, the CGRs of both as–welded (right angle triangles in Fig. 58) and as–welded plus thermally treated (circles in Fig. 58) material are below the NUREG–0313 curve for sensitized SSs in water with 8 ppm DO. Limited data for the Type 304 SS SMA weld HAZ indicate that the CGRs for nonirradiated HAZ (open triangle in Fig. 58) are higher than those for Type 304L weld HAZ and are above the NUREG–0313 curve. A beneficial effect of reducing the corrosion potential of the environment was observed for the SMA weld HAZ. The fracture morphology is different for the two materials, e.g., TG fracture for the Type 304L SA weld HAZ and IG fracture for the Type 304 SMA weld HAZ.

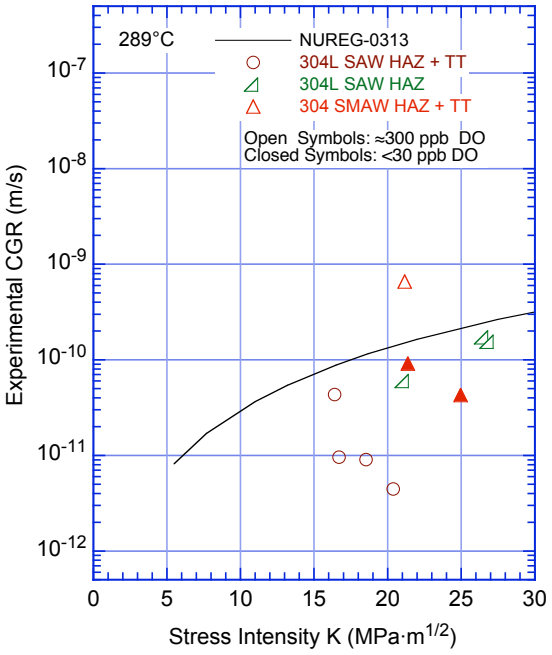

Figure 58.
CGR data under constant load with or without periodic partial unloads for nonirradiated SS weld HAZ specimens in high–purity water at 289°C.

4 Evaluation of Causes and Mechanisms of Irradiation-Assisted Cracking of Austenitic Stainless Steel in PWRs (H. M. Chung and W. K. Soppet)

4.1 Introduction

Field failures have been reported in various PWR core internal components fabricated from austenitic SSs, such as baffle bolts, control rod cladding, pins, keys, and bolts. Many of the failed components were fabricated from cold-worked materials of Type 316, 347, and 304 SS. Typically, failures of PWR core internals are intergranular (IG) and are observed at neutron-damage levels approximately a few orders of magnitude higher (i.e., >10 dpa) than the threshold damage level of BWR core internals (i.e., ≈0.7 dpa). At this time, the database and mechanistic understanding of PWR core internals are very limited, and it is not clear if the failures should be classified as IASCC or irradiation-assisted cracking (IAC).

The objectives in this task are to evaluate the susceptibility of austenitic SS core internals to IAC in PWRs as a function of the fluence, water chemistry, material chemistry, and cold work. The program will focus on the following: (a) evaluation of the effects of PWR-like high fluence on susceptibility to IASCC, (b) neutron irradiation embrittlement, e.g., loss of fracture toughness, (c) void swelling behavior in austenitic SSs, (d) effect of cold work and solution anneal, (e) fracture toughness and SCC behavior of cast duplex SSs at high fluence, and (f) effectiveness of mitigative measures, such as optimization of ferrite content, grain-boundary engineering, and minimization of S concentration. Tests will be conducted on austenitic SS specimens irradiated in the BOR–60 reactor in Russia.

4.2 Irradiation of Austenitic Stainless Steels in the BOR-60 Reactor

An experiment has been initiated to irradiate specimens of various types of materials and geometry under PWR-like conditions. The irradiation experiment is being conducted jointly in cooperation with the Cooperative Irradiation-Assisted Stress Corrosion Cracking Research (CIR) Program. Irradiation of the specimens is performed in the BOR-60 Reactor, a sodium-cooled breeder reactor located in the Research Institute of Atomic Reactors (RIAR), Dimitrovgrad, Ulyansk Region, Russian Federation.

In the first part of the irradiation campaign, specimens were irradiated to ≈5 and ≈10 dpa in Irradiation Cycle BORIS-6 in flowing sodium maintained at 322.1-322.6°C. Further irradiation of specimens to ≈40 dpa in Irradiation Cycle BORIS-7 continued in the second part of the campaign. After irradiation in BORIS–6, 48 tensile specimens (contained in 12 bundles) and 166 disk specimens (contained in 4 capsules) were discharged. Each bundle contains 4 tensile specimens, and the disk capsules contain 23-56 disk specimens. The specimens have been transported to the Westinghouse hot cell through Studsvik. Westinghouse is performing the work to separate and repackage ANL specimens from the CIR specimens. The ANL specimens are expected in August 2004.

4.3 Representation of IASCC–Ressistant or –Susceptible Behavior of Types 304 and 316 Stainless Steel in Sulfur–Carbon Map

Tests performed on materials irradiated in the Halden BWR reactor give some insight into potential mechanisms for IASCC that is also relevant to PWRs. After exposure to the conditions of the SSRT test in BWR water, susceptibility to IG cracking in inert environment was determined by rapid bending in air at 23°C. Similar tests were also performed on hydrogen–charged specimens in vacuum. Both types of

bend fracture exhibited similar characteristics, suggesting that in both cases the failures occurred due to hydrogen-induced IG failure. However, steels that showed high susceptibility to IGSCC in 289°C water exhibited low susceptibility to IG cracking in the tests at 23°C air or vacuum, and vice versa. This finding indicates that although IG cracking in 23°C is dominated by H–induced embrittlement of ordinary grain boundaries, other processes control IASCC in 289°C water.

On the basis of this investigation, and studies on binary Ni–S and crack-tip microstructural characteristics of LWR core internal components reported in the literature, an initial IASCC model based on a crack–tip grain–boundary process that involves S has been proposed. In this model, several processes play a key role: i.e., grain-boundary segregation of Ni and S, formation of grain-boundary oxide in front of the crack tip, formation of Ni– and S–rich thin films, and islands between the oxide and metal matrix, and disorder–induced melting or amorphization of the Ni–S thin films and islands at sufficiently high concentration of S.

Figure 59 is a two–dimensional map as a function of bulk S and C concentration[20–22,39,75–76] that shows the regimes in which austenitic SSs are found to be resistant or susceptible to IASCC in the PWR environment. The trends in Fig. 59 are similar to those observed earlier in the S–C map that shows the IASCC–resistant or –susceptible regimes under BWR oxidizing conditions (Fig. 21).

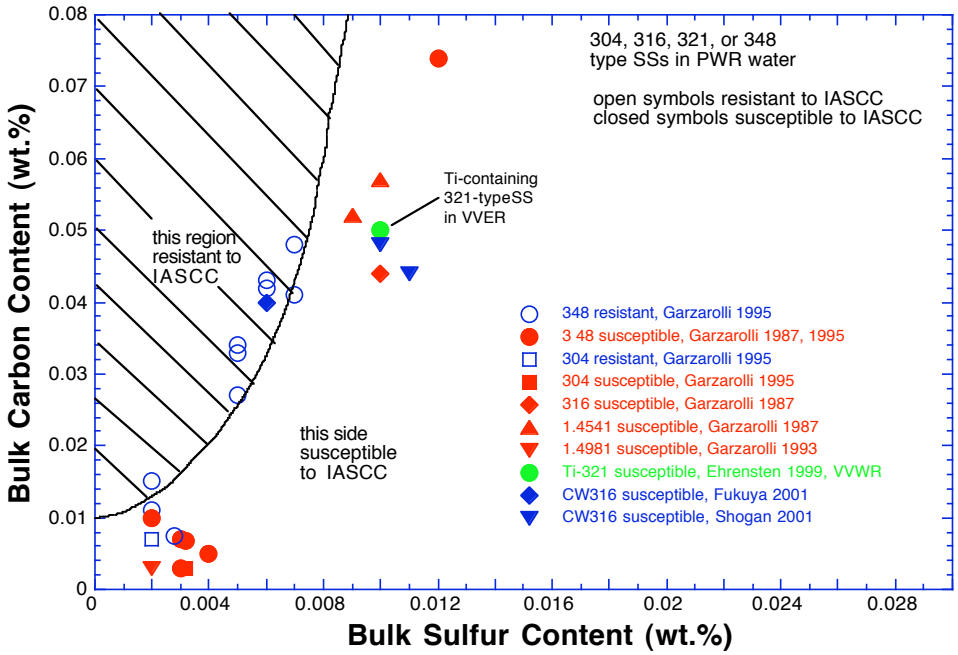

Figure 59. Representation of IASCC resistance or susceptibility of austenitic stainless steels as function of bulk S and C contents. Data obtained from PWR– or VVER—irradiated specimens in PWR, VVER, or PWR–like water reported in 1987–2004.

The beneficial effect of C can be explained based on the postulation that C atoms are dissolved in significant amount within the Ni– and S–rich thin film (thickness ≈3–8 nm) that was observed in some studies at the boundary between the steel matrix and Fe–Cr spinel oxide at a crack–tip grain boundary. In an initial model described in a previous annual report, it was assumed that such a Ni– and S–rich thin film loses metallic strength when the S content in the film exceeds a threshold level. Such loss of metallic strength is attributed to severe localization of free electrons in the Ni– and S–rich film when S content exceeds the threshold level. Without free electrons, the film no longer exhibits metallic behavior. A

simple consideration suggests that C atoms can easily occupy the same octahedral sites in the unit cell of Ni sulfide that are normally occupied by S atoms. That is, when C concentration is high near the Ni– and S–rich thin film produced at the crack–tip grain boundary, S and C atoms compete to occupy the same octahedral sites of the unit cell of the film. Under such a situation, C dissolved in the film is expected to suppress the deleterious effect of S, which reduces the number of free electrons in the film.

The above model is plausible only if the solubility of C in Ni sulfide is significant. Therefore, to provide an insight helpful to understand the behavior of C dissolution in Ni sulfide, data from previous analysis of BWR neutron absorber tubes by Auger electron spectroscopy (AES) are being examined. Because AES is sensitive to C and S signals, it can detect small amounts of C atoms that may be contained in a sulfide precipitate.

5 Cracking of Nickel Alloys and Welds (B. Alexandreanu, O. K. Chopra, and W. J. Shack)

5.1 Introduction

This part of the study consists primarily of establishing CGRs under constant and cyclic loading and evaluating Ni alloys and weld metals metallographically to develop comprehensive and statistically significant analyses that could be used to determine the dependence of the SCC of these materials on alloy composition, microstructure, water chemistry, temperature, and other factors. The Ni–base alloys used as construction material in light water reactors (LWRs) have experienced stress corrosion cracking (SCC). Primary–water SCC of Alloy 600 steam generator tubes in pressurized water reactors (PWRs) has been studied intensively.[77–79] Stress corrosion cracking has also occurred in Ni alloys used in applications such as instrument nozzles and heater thermal sleeves in the pressurizer[80] and penetrations for the control–rod drive mechanism (CRDM) in the reactor vessel closure heads.[81] In the fall of 1991, a leak was discovered in the pressure vessel head penetration at the Bugey 3 plant in France. Metallurgical evaluations indicated that the leak was caused by primary water SCC.[82] The main crack had initiated in Alloy 600 base metal and propagated into the Alloy 182 weld metal. Subsequent inspections of CRDM penetrations in domestic and foreign PWRs identified a small number of penetrations (<5% of the penetrations inspected) with axial cracks. None of the cracks were through–wall, and until recently, no more leaks occurred in pressure vessel head penetrations.

Leaks from axial through–wall cracks were identified at Oconee unit 1 in November 2000 and Arkansas Nuclear One unit 1 in February 2001.[83] During the next 15 months, inspections at Oconee units 2 and 3 and follow-up inspection at unit 1 identified both axial and circumferential cracks in reactor vessel head penetrations.[84] The presence of circumferential cracks, in particular, raised concerns regarding structural integrity.[85,86] Also, in October 2000, significant boron deposits were discovered in the vicinity and on the Loop "A" outlet nozzle–to–pipe weld at the V. C. Summer plant.[87] Ultrasonic inspection of the pipe revealed an axial crack in the dissimilar metal weld at the top of the pipe. Earlier in 2000, two shallow axial flaws were found in the outlet nozzle–to–safe–end weld of Ringhals unit 3, and four axial indications were found in the same region of Ringhals unit 4, in Sweden.[88] Cracks have also been found in pressure vessel head penetrations at North Anna unit 2[89] and Davis-Besse nuclear power plant[90] and, more recently, in the bottom–mounted instrumentation nozzles at South Texas unit 1.[91,92]

Long–term operating experience indicates that although wrought Ni–base Alloy 600 is susceptible to SCC, until recently, the weld metal Alloys 82 and 182 used with Alloy 600 had not shown environmentally assisted cracking. However, laboratory tests indicate that in PWR coolant environments, the SCC susceptibility of Alloy 182 may be greater than Alloy 600 and that of Alloy 82 may be comparable to Alloy 600. This apparent inconsistency between field and laboratory experience has been an issue that needs further investigation.

A program is being conducted at ANL to evaluate the resistance of Ni alloys and their welds to environmentally assisted cracking in simulated LWR coolant environments. The existing CGR data for Ni–alloys under cyclic and constant loads have also been analyzed to establish the effects of key parameters on CGRs; the results are presented elsewhere.[93–97] The fatigue crack growth data in air were analyzed to develop correlations for estimating the fatigue CGRs of Alloy 600 and 690 as a function of stress intensity factor range ΔK, load ratio R, and temperature.[98] The results indicate that in air, the CGRs of these materials are relatively insensitive to changes in frequency. The CGR (m/cycle) of Alloy 600 in air is best expressed as

$$da/dN = C_{A600} (1 - 0.82\ R)^{-2.2} (\Delta K)^{4.1}, \quad (11)$$

where ΔK is in $MPa \cdot m^{1/2}$, and the constant C_{A600} is given by a third-order polynomial of temperature T (°C) expressed as

$$C_{A600} = 4.835 \times 10^{-14} + (1.622 \times 10^{-16})T - (1.490 \times 10^{-18})T^2 + (4.355 \times 10^{-21})T^3. \quad (12)$$

In high–DO water, the CGRs of Alloy 600 show frequency–dependent enhancement under cyclic loading conditions. The environmental enhancement of growth rates does not appear to depend strongly on the material condition. In contrast, environmental enhancement of CGRs of Alloy 600 in low–DO water does seem to be strongly dependent on material conditions. In the literature[99–104] such variability has been attributed to parameters such as yield strength and grain boundary coverage of carbides, although the evidence for this dependence has been best demonstrated for steam generator tubing, rather than thicker structural materials.

In the earlier ANL work, correlations were developed to estimate the enhancement of CGRs in LWR environments relative to the CGRs in air under the same loading conditions. The best–fit curve for Alloy 600, either in the solution annealed (SA) condition or SA plus thermally treated condition, in ≈300 ppb DO water is given by the expression[95]

$$CGR_{env} = CGR_{air} + 4.4 \times 10^{-7} (CGR_{air})^{0.33}. \quad (13)$$

This section of the report presents CGR results for Alloy 600 from round robin tests and for Alloy 182 shielded metal arc (SMA) weld metal in simulated PWR environments at 320°C. The results have been compared with the existing CGR data for Ni–alloy welds to determine the relative susceptibility of the specific Ni–alloy weld to environmentally enhanced cracking under a variety of loading conditions. Detailed metallographic examinations of the material to characterize the microstructure of the weld metal are presented.

5.2 Experimental

5.2.1 Material and Specimen Design

Crack growth rate tests have been conducted on Alloy 182 weld metal samples in simulated PWR environments at 320°C in accordance with ASTM Designation E 647, "Standard Test Method for Measurement of Fatigue Crack Growth Rates." The tests were performed on 1–T compact tension (CT) specimens; the configuration of the CT specimen is shown in Fig. 60. Crack extensions were determined by the reversing DC potential drop technique. 14

The weld was prepared by welding two 152 x 305 mm (6 x 12 in.) pieces of 38–mm thick (1.5–in. thick) plate. The weld had a double "J" joint design and was produced by 48 weld passes. Root passes 1–5 were produced by gas tungsten arc (GTA) welding with Alloy 82 filler/electrode, and the other passes by shielded metal arc (SMA) process with Alloy 182 filler. The chemical compositions of the base and weld metals are given in Table 11. A schematic of the joint design and various passes is shown in Fig. 61 and the welding conditions for each weld pass are listed in Table 12. During welding the maximum inter–pass temperature was ≈120°C (250°F), and the weld surfaces were cleaned by use of a wire brush and grinding and by rinsing with de–mineralized water or alcohol. The orientation of the Alloy 182 SMA weld–metal specimen is shown in Fig. 62.

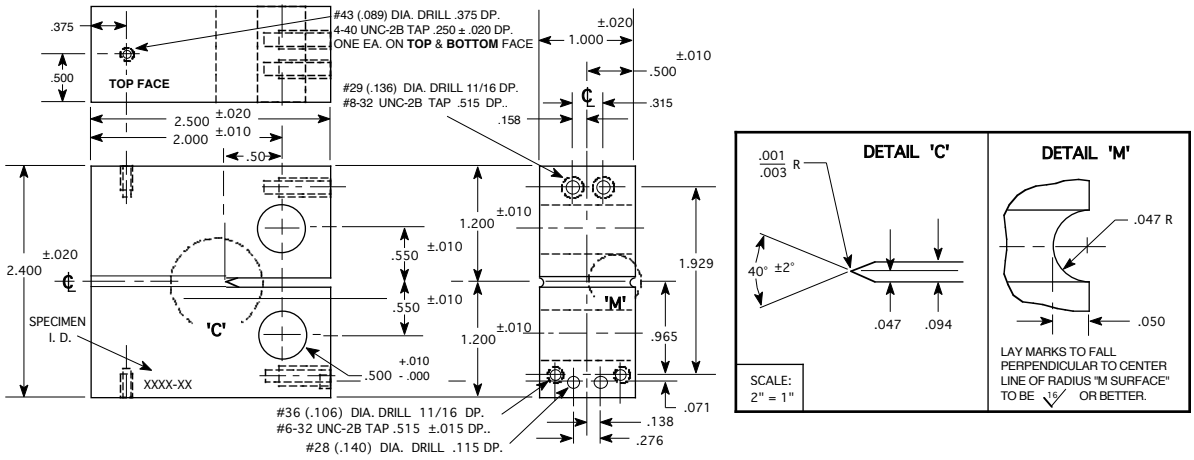

Figure 60. Configuration of compact-tension specimen used for this study (dimensions are in inches).

Table 11. Chemical composition (wt.%) of Alloy 600 base metal and Inconel 182 and 82 weld metals

Alloy ID (Heat)	Analysis	C	Mn	Fe	S	P	Si	Cu	Ni	Cr	Ti	Nb	Co
Alloy 600													
(NX1310)	Vendor	0.07	0.22	7.39	0.002	0.006	0.12	0.05	76.00	15.55	0.24	0.07	0.058
	ANL	0.07	0.22	7.73	0.001	–	0.18	0.06	75.34	–	–	–	–
Alloy 182	Spec.	0.10	5.0–	6.0–	0.015		1.0	0.5		13.0–	1.0	1.0–	0.12 max
		max	9.5	10.0	max	–	max	max	Bal	17.0	max	2.5	
	ANL	0.05	6.97	6.82	0.005	0.008	0.56	0.01	69.22	–	–	1.70	–
Alloy 82	Spec.	0.10	2.5–	3.0	0.015		0.5	0.5	67.00	18.0–	0.75	2.0–	0.75 max
		max	3.5	max	max	–	max	max	min	22.0	max	3.0	

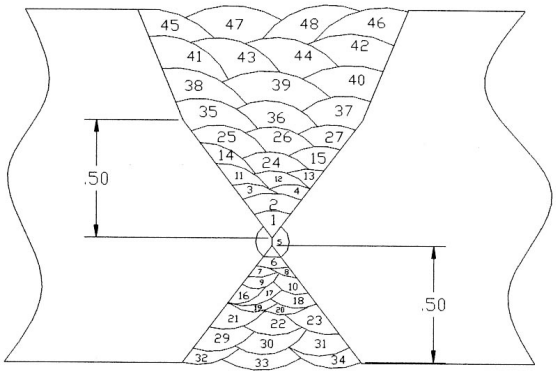

Figure 61. Schematic of the weld joint design and weld passes (dimensions are in inches).

Table 12. Welding process and conditions for various weld passes

Weld Pass	Process	Filler Metal	Filler/Electrode Size	Current (A)	Voltage (V)	Travel Speed (in./min.)
1 – 5	GTA	Alloy 82	3/32	185 – 215	21 – 22	2 – 4
6 – 10	SMA	Alloy 182	3/32	140 – 155	24 – 26	6 – 7
11 –27	SMA	Alloy 182	1/8	155 – 170	25 – 27	6 – 7
28 – 48	SMA	Alloy 182	5/32	170 – 180	26 – 28	6 – 7

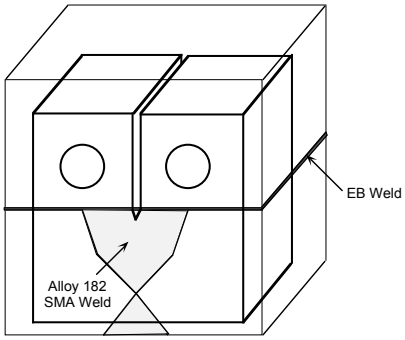

Figure 62. Orientation of the CT specimen from the Alloy 182 SMA weld

5.2.2 Test Facility

The CGR tests were conducted with an MTS™ closed-loop electro–hydraulic material test system equipped with a Type 316 SS autoclave supplied with the test water solution from a feedwater tank. The simulated PWR feedwater contains less than 10 ppb DO, 2 ppm Li, 1000 ppm B, and ≈2 ppm dissolved hydrogen (≈23 cm^3/kg). It is prepared from the building deionized water by first passing this water through a local filtration system that includes a carbon filter, an Organex–Q filter, two ion exchangers, and a 0.2–mm capsule filter. The DO in the deionized water is reduced to <10 ppb by bubbling/sparging a mixture of N_2 + 5% H_2 through the water. A vacuum may be applied to the feedwater tank at the vent port, to speed deoxygenation. The PWR water is prepared by dissolving boric acid and lithium hydroxide in 20 L of deionized water before adding the solution to the supply tank. The hydrogen gas pressure of the feedwater tank was maintained at 34 kPa. The dissolved hydrogen in water was calculated from the tank hydrogen pressure and temperature.

Water samples are taken periodically to measure pH, resistivity, and DO concentration both upstream and downstream from the autoclave. An Orbisphere meter and CHEMetrics™ ampules are used to measure the DO concentrations in the supply and effluent water. The redox and open–circuit corrosion potentials were monitored at the autoclave outlet by measuring the ECPs of platinum and an Alloy 600 electrode, respectively, against a 0.1–M KCl/AgCl/Ag external (cold) reference electrode.

5.2.3 Test Procedure

The CGR tests were conducted in the load–control mode using a triangular, sawtooth, or trapezoidal waveform with load ratio R of 0.3–0.7. The CT specimens were fatigue precracked in the test environment at temperature and load ratio R = 0.3, frequency of ≈1 Hz, and maximum stress intensity factor K_{max} of 20–25 MPa·$m^{1/2}$. After ≈0.5–mm crack extension, R was increased incrementally to 0.7, and the loading waveform changed to a slow/fast sawtooth with rise times of 30–1000 s. The SCC growth rates were determined using a trapezoidal waveform with R = 0.5 or 0.7, 12–1000 s rise time, 3600–s hold period at peak, and 12 -s unload time. This loading sequence is considered to result in reproducible CGRs.[105] During individual test periods, K_{max} was maintained approximately constant by periodic load shedding (less than 2% decrease in load at any given time).

Crack extensions were monitored by the reversing DC potential difference method. The current leads were attached to the holes on the top and bottom surfaces of the specimen (Fig. 60) and the potential leads were welded on the front face of the specimen across the machined notch but on diagonal ends. Also, to compensate for the effects of changes in resistivity of the material with time, an Alloy 600

internal reference bar was installed near the test specimen. The CT specimen and reference bar were connected in series, and the DC potential across the specimen as well as the reference bar was monitored continuously during the test. The results for the reference bar were used to normalize potential drop measurements for the CT test specimen. The stress intensity factor range ΔK was calculated as follows:

$$\Delta K = \frac{\Delta P}{\left(B B_N W\right)^{1/2}} \frac{\left(2+\frac{a}{W}\right)}{\left(1-\frac{a}{W}\right)^{3/2}} f\left(\frac{a}{W}\right), \tag{15}$$

$$\Delta P = P_{max} - P_{min} \qquad \text{for } R > 0, \tag{16}$$

$$f\left(\frac{a}{W}\right) = 0.886 + 4.64\left(\frac{a}{W}\right) - 13.32\left(\frac{a}{W}\right)^2 + 14.72\left(\frac{a}{W}\right)^3 - 5.6\left(\frac{a}{W}\right)^4, \tag{17}$$

where P_{max} and P_{min} are maximum and minimum applied load, a is crack length, W is the specimen width, and the effective thickness $B_{eff} = (B\ B_N)^{0.5}$. The applied K for the tests was in accordance with the specimen size criteria of ASTM E 1681 and E 647. These criteria are intended to ensure applicability and transferability of the cracking behavior of a component or specimen of a given thickness under a specific loading condition to a crack associated with a different geometry, thickness, and loading condition. The K/size criteria require that the plastic zone at the tip of a crack is small relative to the specimen geometry. For constant load tests, ASTM E 1681 requires that

$$B_{eff} \text{ and } (W-a) \geq 2.5\ (K/\sigma_{ys})^2, \tag{18}$$

and for cyclic loading ASTM 647 requires that

$$(W-a) \geq (4/\pi)\ (K/\sigma_{ys})^2, \tag{19}$$

where K is the applied stress intensity factor, and σ_{ys} is the yield stress of the material. For high–strain hardening materials, i.e., materials with an ultimate-to-yield stress ratio $(\sigma_{ult}/\sigma_{ys}) \geq 1.3$, both criteria allow the use of the flow stress defined as $\sigma_f = (\sigma_{ult} + \sigma_{ys})/2$ rather than the yield stress.

After the test the specimen was fractured in liquid nitrogen, and the fracture surfaces were examined by optical or electron microscopy to measure the final crack length using the 9/8 averaging technique; the two near–surface measurements were averaged, and the resultant value was averaged with the remaining seven measurements. The number of measurements was increased for irregular crack fronts.

5.2.4 Material Characterization

5.2.4.1 Alloy 600 for the Round Robin Specimen

This section presents the results of the metallographical characterization conducted on the alloy used in the round robin test. The alloy coupons used were cut to examine the microstructure on both the

plane of the crack and the plane normal to the plane of the crack. These coupons were first mechanically polished with 1–μm diamond paste, then electrochemically etched in either a 5% nital solution at 5 V to show grain boundaries, or a 70% phosphoric acid solution at 5 V to show the carbides.

Figure 63 shows the microstructure on the plane normal to that of the crack. The micrographs were taken from the same area, after the nital etch (Figs 63a, b) and after the phosphoric acid etch (Figs. 63c,d). Both etchants revealed a mictostructure with a grain size of approximately 35 μm, with a good intergranular and matrix carbide coverage. Titanium-rich precipitates were also observed, e.g. those shown in the upper center of Figs. 63c, d.

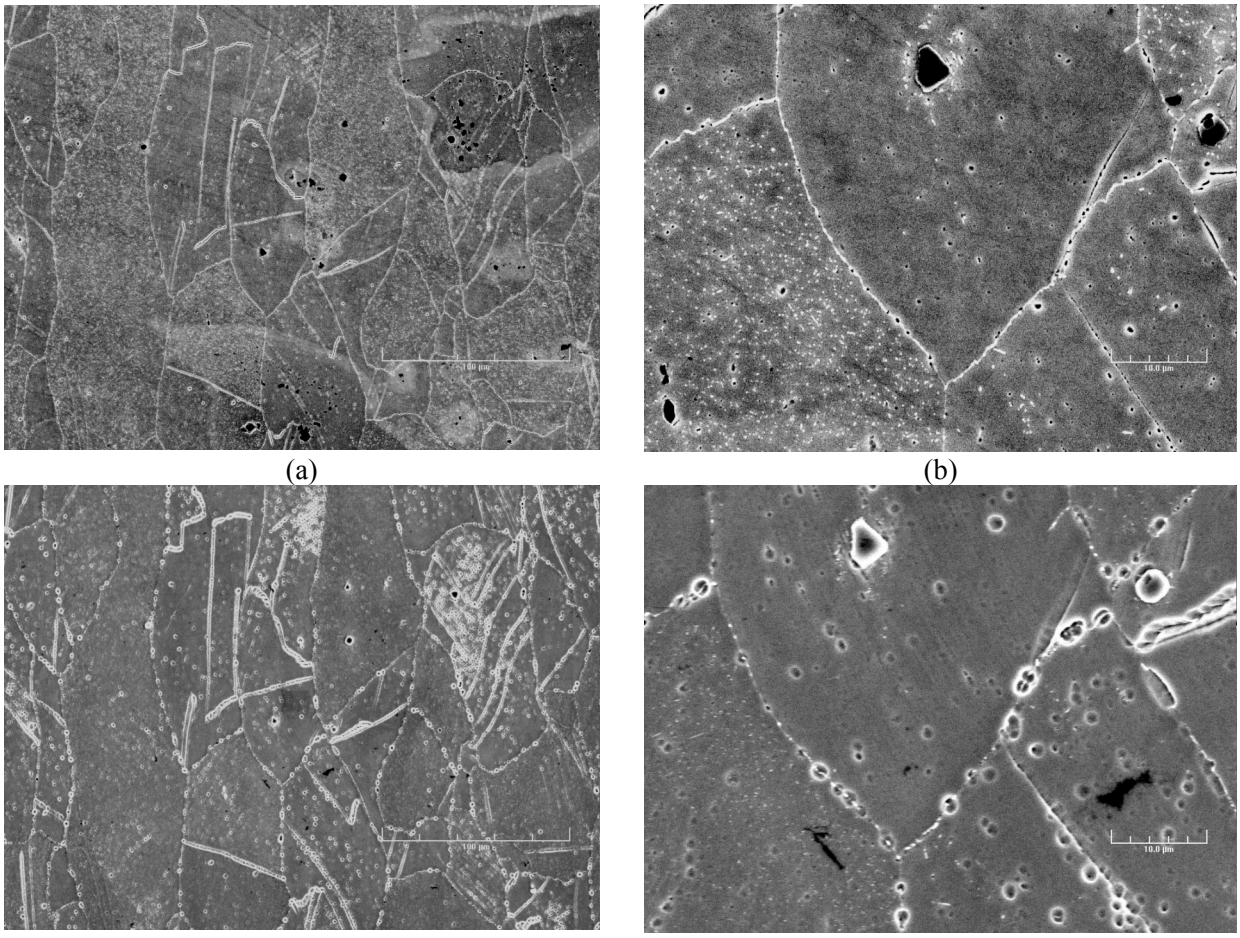

(a) (b)

(c) (d)

Figure 63. Microstructure of the round robin Alloy 600 etched with (a, b) nital and (c, d) phosphoric acid solution.

Figure 64 shows two magnifications of the microstructure on the plane parallel to that of the crack following a phosphoric acid etch. We observe that the etchant attacked different grains in different manners, suggesting the presence of matrix precipitates in some grains and the absence of precipitates in others.

In support of the previous observation, Figs. 65a,b show the microstructure of the round robin alloy, and Figs. 65c,d show the microstructure of a similar Alloy 600 used previously in our laboratory (CT31-01). Unlike the round robin alloy, the laboratory heat has an uniform distribution of carbides both

on the grain boundaries and in the matrix, with carbides on the grain boundaries being, as expected, larger in size than those in the matrix.

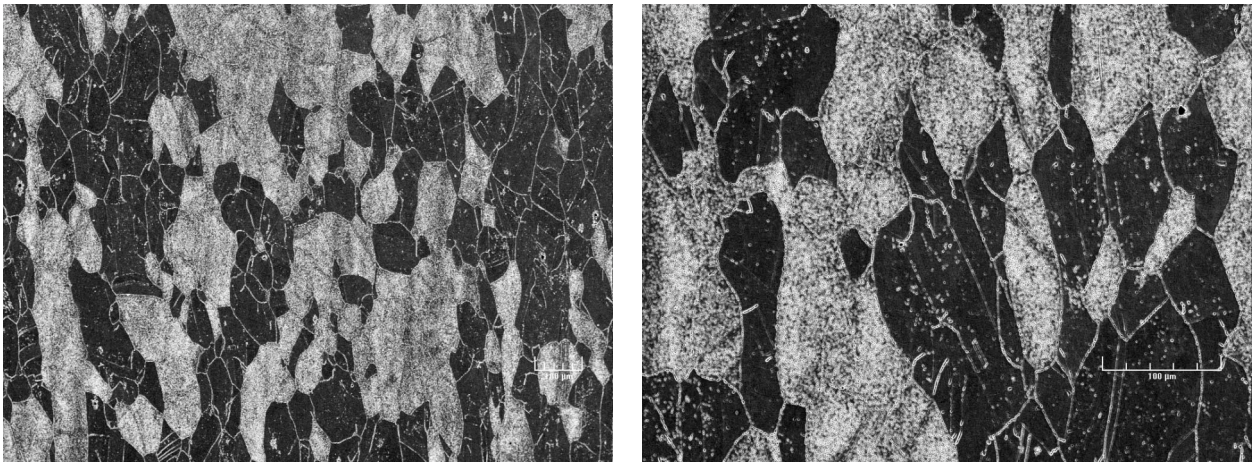

(a) (b)

Figure 64. Microstructure of the round robin alloy in the plane of the crack at two magnifications.

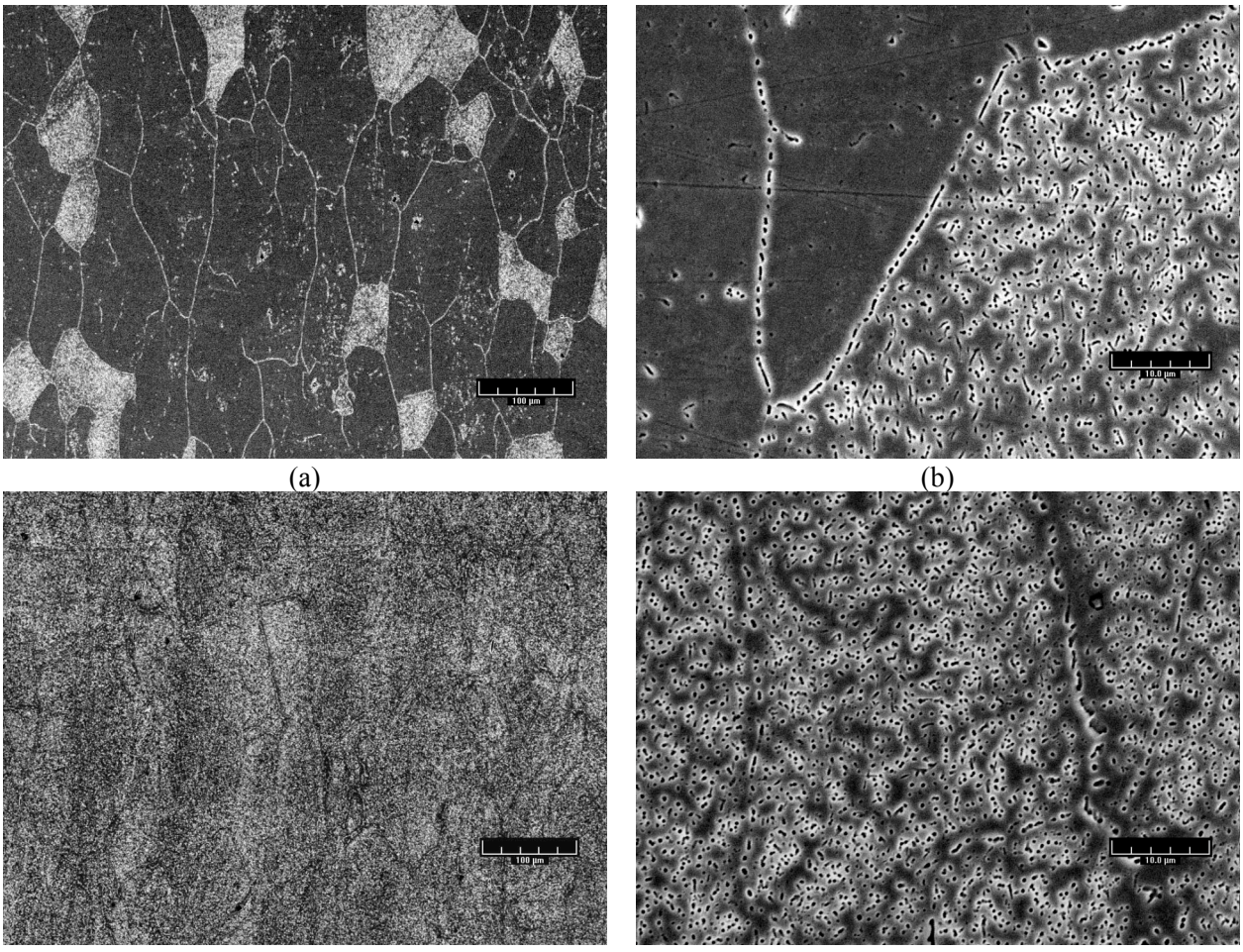

(a) (b)

(c) (d)

Figure 65. Microstructure of the round robin alloy in the plane of the crack at two magnifications (a,b) and that of a different heat of Alloy 600, used previously in our experiments (c, d).

5.2.4.2 Double–J Weld

The microstructures of Ni–alloy weld metals such as Alloy 182 and 82 are similar to those of wrought Alloys 600 and 690. Under certain thermal treatments, Cr–rich carbides can precipitate at both interdendrite and intradendrite grain boundaries.[106] Chromium depletion also occurs at the boundaries that are covered with such carbides. The precipitate phases are predominantly $M_{23}C_6$ and Ti–rich MC carbide. During the welding process, only the $M_{23}C_6$ carbide precipitates because of the rapid cooling of the weld metal from fusion temperature. Nucleation of M_7C_3 carbides requires long periods at relatively high temperatures, whereas nucleation of $M_{23}C_6$ is quite rapid and cannot be avoided even during water quenching from solution treatment temperatures. The matrix also contains a uniform dispersion of spherical γ' phase (Ni_3Ti).

The greater susceptibility of Alloy 182 to SCC than Alloy 82 has been attributed to differences in Cr depletion observed in the two alloys because of differences in their composition. Alloy 182 contains higher concentrations of C and Fe and a lower concentration of Cr, all of which enhance Cr depletion during carbide precipitation.

Weld Microstructure

A metallographic examination was performed to characterize the microstructure of the weld. For this purpose, three 1 cm × 2 cm rectangular pieces, designated 1, 2, and 3, were cut from the Alloy 182 weld (Fig. 66). The thickness of all three samples was 0.5 cm. Sample 3 was further cut in half to enable the examination of both surfaces A and B, normal to the plane of Fig. 66.

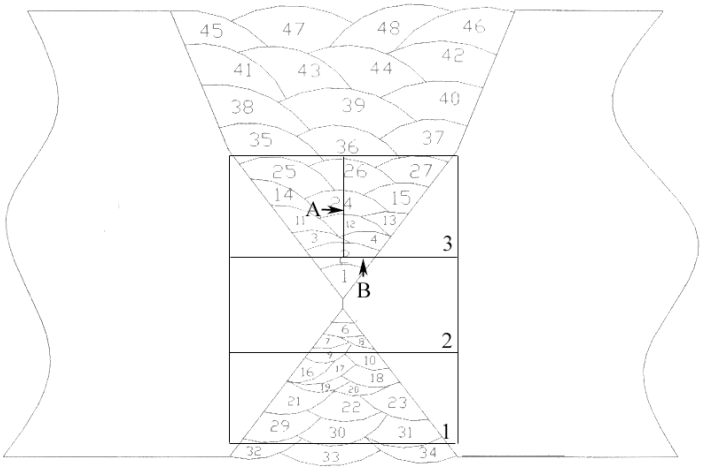

Figure 66. Schematic showing the locations of the three samples cut from the weld.

All samples were mechanically polished through 1–μm diamond paste, followed by electrolytic etching in a 70% H_3PO_4 and water solution at 5 V. The samples were then examined in a JEOL JSM-6400 SEM. Figure 67a shows the entire span of the weld microstructure on Sample 1 (the picture shown here was rotated by 90° with respect to the schematic shown in Fig. 66 to fit on the page). The elongated grains with dendritic features are easily discernible from the regular microstructure of Alloy 600 (upper-left and bottom-left corners). This difference is also visible in Fig. 67b. Figures 67c and 67d also show the dendritic microstructure in the weld. Large variations in grain size were evident between the different passes.

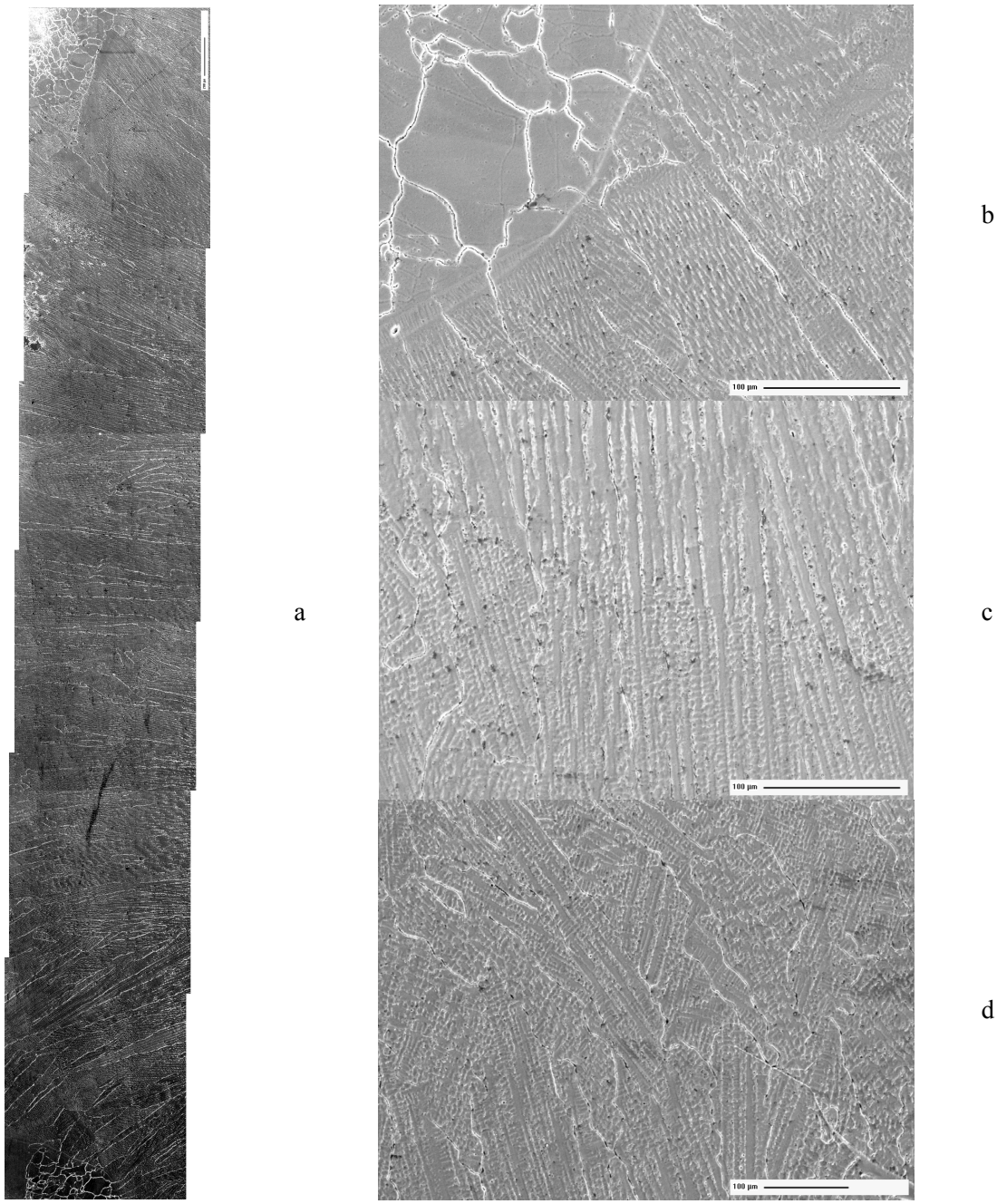

Figure 67. (a) Weld microstructure from Sample 1 (rotated 90° with respect to Fig. 9); (b) transition area between the weld and Alloy 600; and (c,d) dendritic microstructure in the weld.

Figure 68 focuses on the transition area between the weld and the base material, i.e., the HAZ. A larger grain size than that of the base material is observed in the immediate vicinity of the well in both Figs. 68a and 68b. These micrographs were obtained from two different, opposite locations on Sample 1. A dendritic microstructure was observed on the 3A plane (Fig. 66), and examples are shown in Fig. 69. The picture shown in Fig. 69a was taken at a location where the grain is still visible; however, internal dendritic features are apparent. Figure 69b was obtained at a weld pass, showing the different structures of the two weld layers.

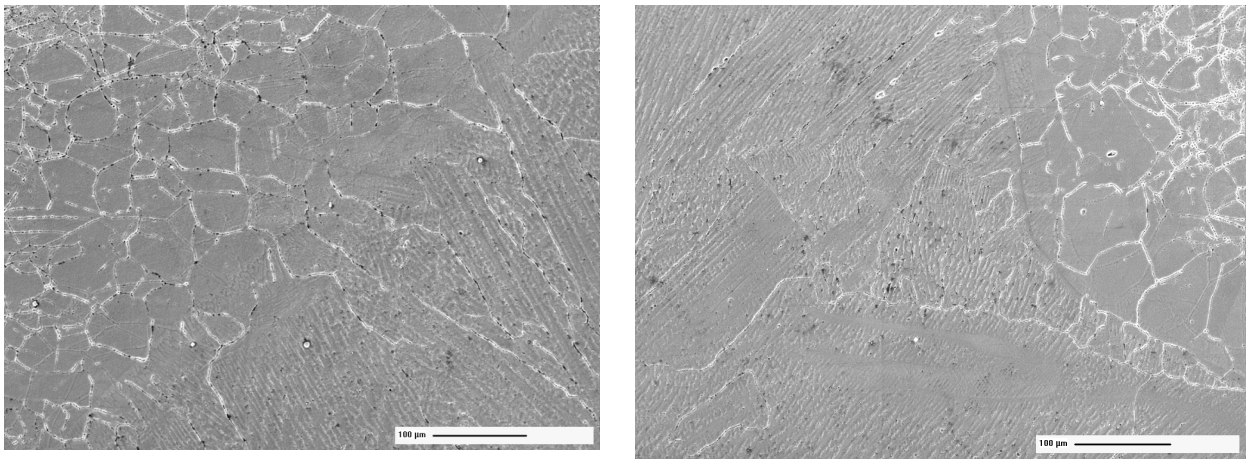

(a) (b)

Figure 68. Large grain microstructure in the HAZ at two opposite positions (a and b).

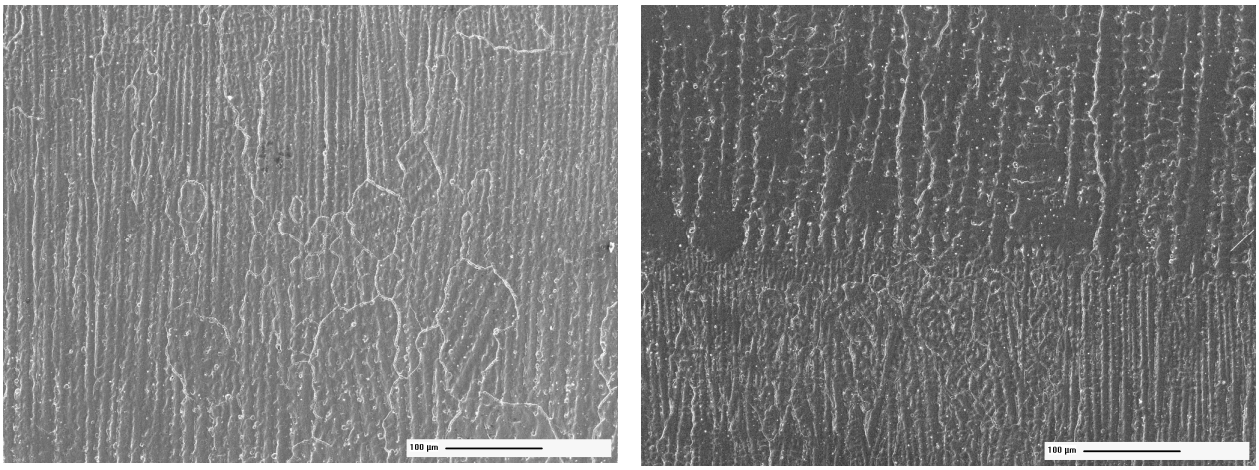

(a) (b)

Figure 69. (a) Dendritic microstructure on sample 3A, and (b) at a weld pass.

Figures 70a and b are micrographs obtained on the 3B plane at weld passes. Figure 70c and d are higher magnification micrographs obtained at locations in Figs. 70a and b, respectively. The grain as well as the dendritic microstructure are visible; however, as expected, the grains are more regular and the dendrites are perpendicular to the plane of observation.

Figure 71a is another example of microstructure obtained on the 3B plane at a weld pass. Fig. 71b is a higher magnification micrograph obtained at a location in Fig. 71a. From the manner in which the phosphoric acid attacked the grain boundaries, it appears that grain boundary precipitates were present. Additional precipitates or particles are also observed in both grain boundaries and matrix which have not been attacked by the phosphoric–acid etch.

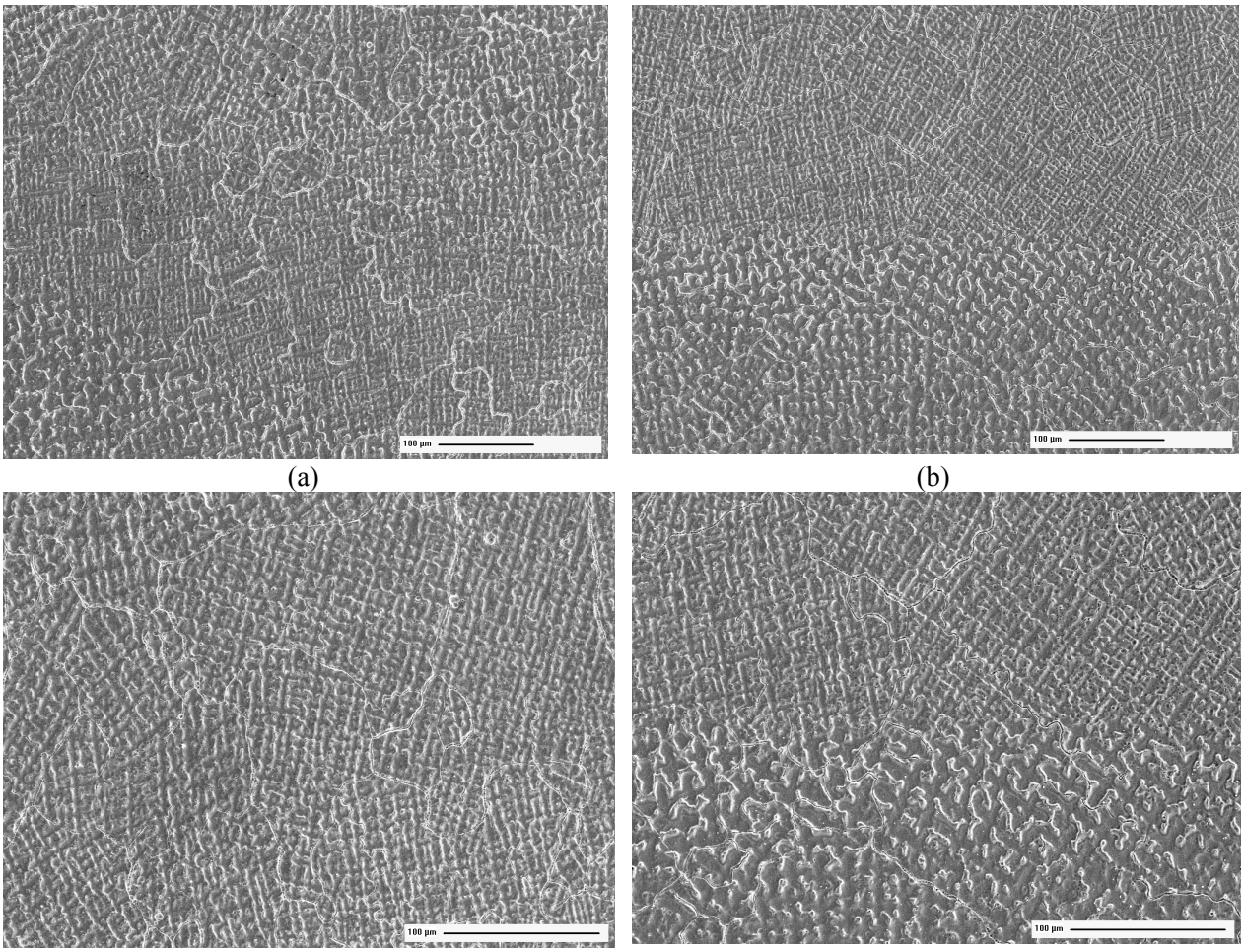

(a) (b)

(c) (d)

Figure 70. Examples of dendritic microstructure at a weld passes on sample 3B (a,b) and high magnification micrographs at the respective locations (c,d).

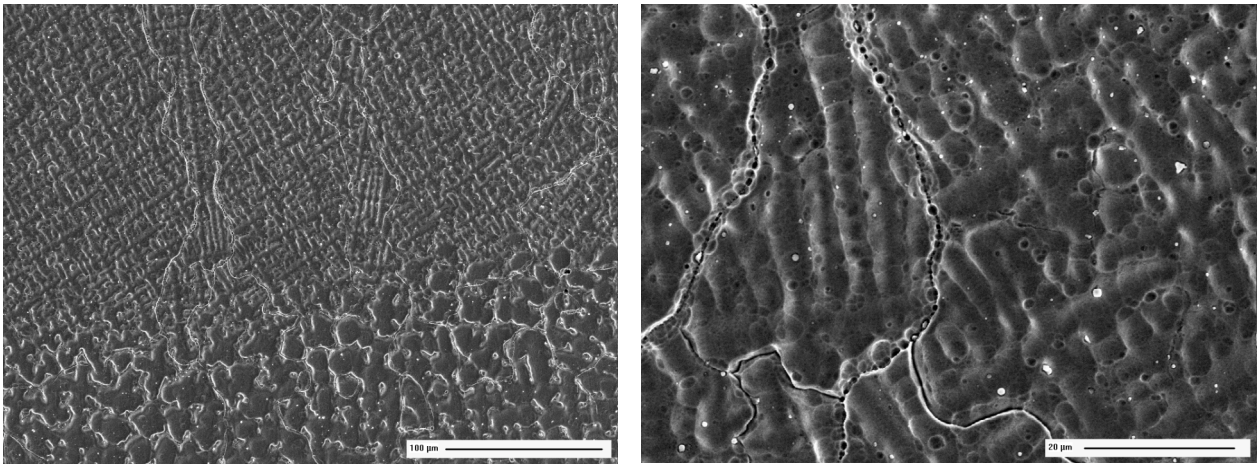

(a) (b)

Figure 71. (a) Dendritic mictostructure on sample 3B and (b) high magnification of a region from (a).

Examination of weld by SEM/EDX

Sample 3A was analyzed by scanning electron microscopy and energy dispersive x–ray (SEM/EDX). This sample was mechanically polished with 1–μm diamond paste, followed by electrolytic etching in a 70% H_3PO_4 and water solution at 5 V. Figure 72a–d shows the microstructure observed on the surface of sample 3A, at several magnifications. The elongated grains with dendritic features observed previously can be seen in all micrographs, as well as large variations in grain size between the different passes (Figs. 72a and d).

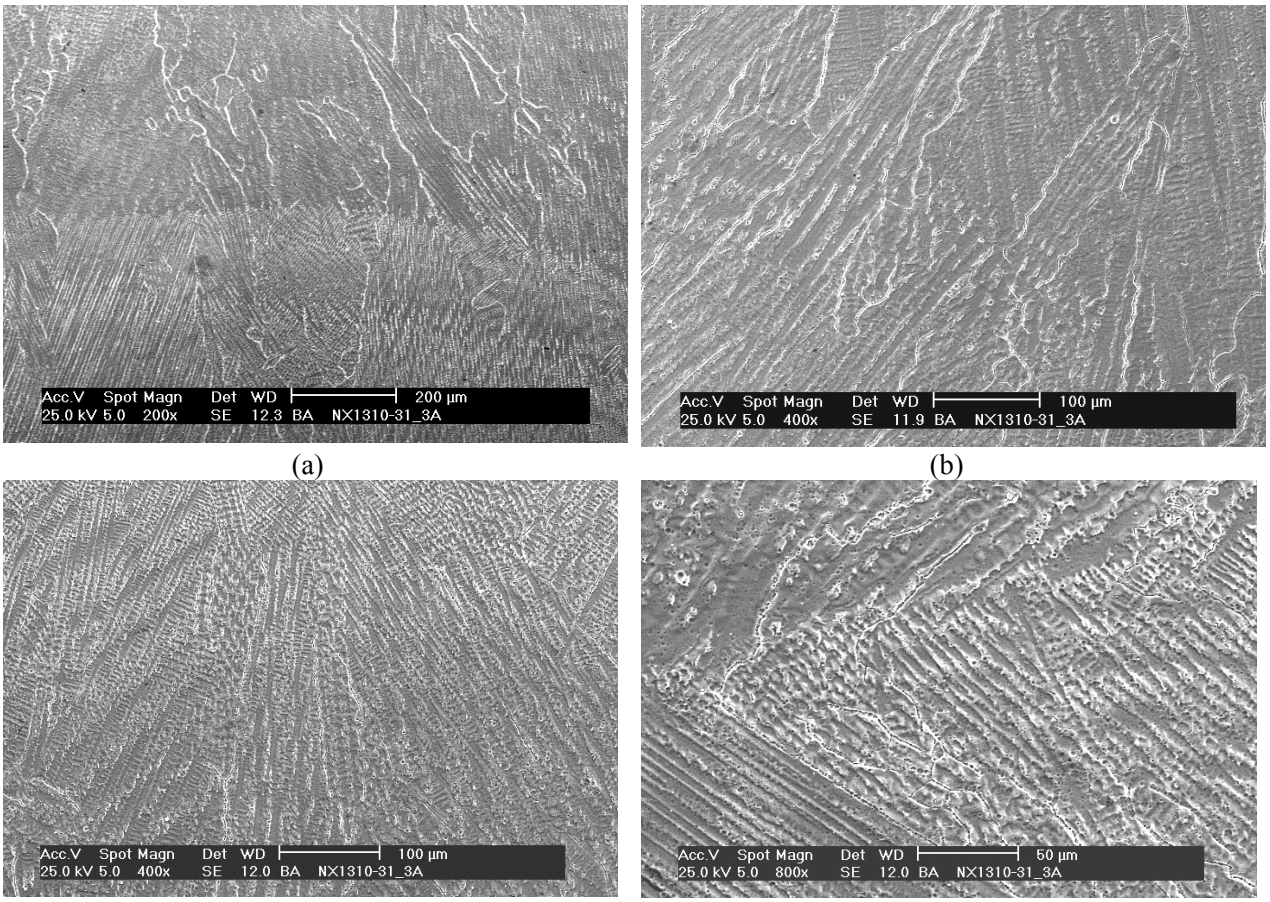

Figure 72. Dendritic microstructure observed on the surface of sample 3A at (a) 200×, (b,c) 200×, and (d) 800× magnifications.

The objective of this part of the analysis was to investigate the nature of both matrix and grain boundary precipitates. Figure 73a shows one of the matrix precipitates on the surface of sample 3A. In Fig. 73b the EDX spectra resulting from the bulk and the precipitate are shown. Comparison of the two spectra allows for the observation that both the Ti and O peaks are higher in the spectrum resulting from the precipitate, suggesting that the particle is TiO_2. The compositional results of the analysis are shown in Table 13, confirming that indeed the precipitates are TiO_2.

Table 13. Chemical compositions of the bulk material and matrix precipitate resulting from EDX analysis.

	Bulk		Matrix precipitate	
	wt. %	at. %	wt. %	at. %
C	1.53	6.56	1.66	3.63
O	**1.77**	**5.72**	**39.08**	**64.24**
Si	0.60	1.10	0.56	0.52
Ti	**0.48**	**0.52**	**50.15**	**27.54**
Cr	15.20	15.08	3.83	1.94
Fe	7.30	6.74	1.06	0.50
Ni	73.12	64.27	3.67	1.64
Total	100.00	100.00	100.00	100.00

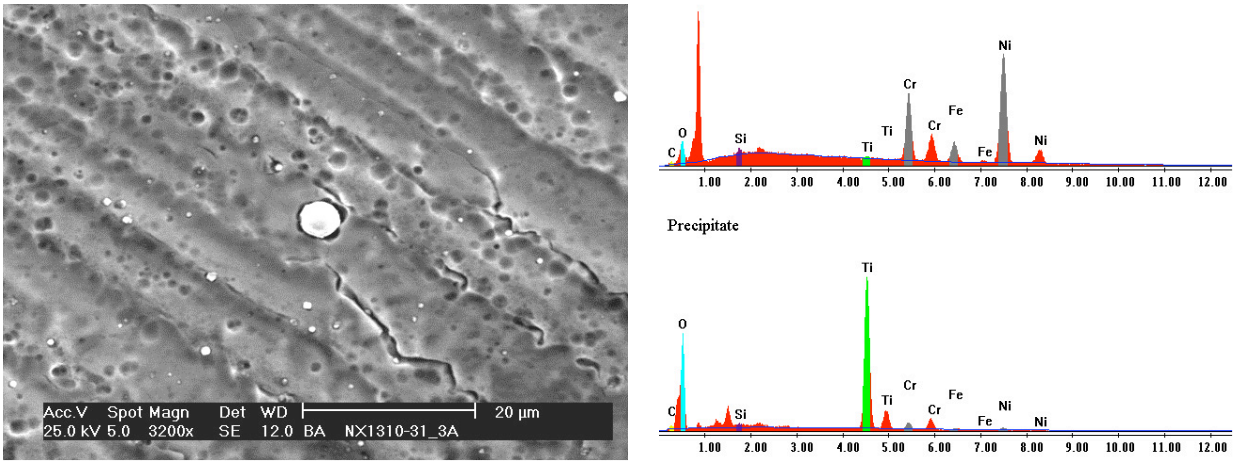

(a) (b)

Figure 73. (a) Micrograph showing one of the matrix precipitates observed on the surface of sample 3A and (b) EDX spectra resulting from the bulk and the precipitate shown in (a).

Next, the nature of the grain boundary precipitates was investigated. Figure 74a shows the microstructure on plane "A" (Fig. 66), while Fig. 74b is a higher magnification micrograph showing both matrix and grain boundary precipitates. In Fig. 74c EDX spectra resulting from the bulk and from the grain boundary precipitate are shown. The comparison of the two spectra as well as the quantitative results shown in Table 14 suggest that the grain boundary precipitate is TiO_2.

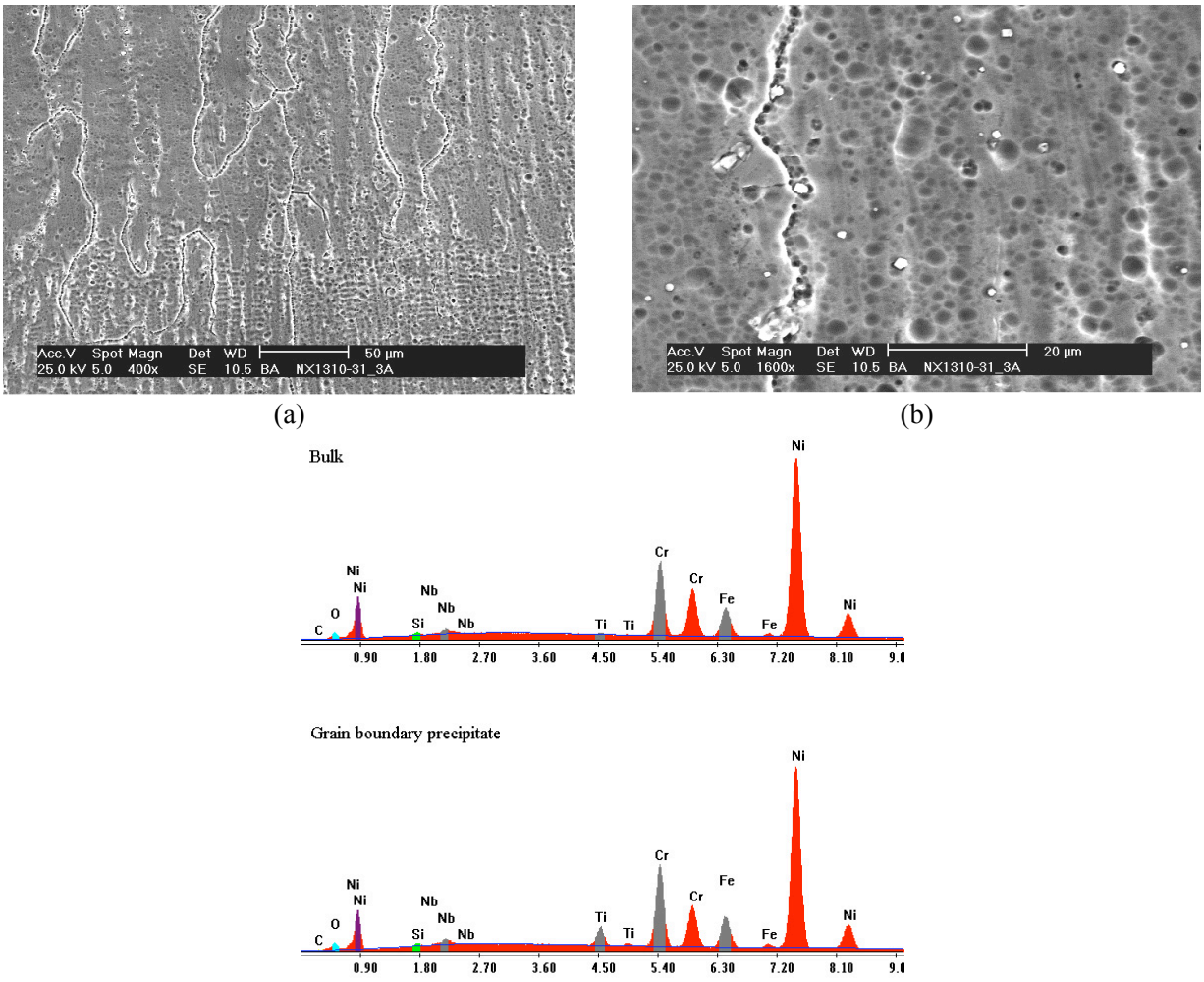

Figure 74. Micrographs showing (a) the microstructure on plane 3A, and (b) matrix and grain boundary precipitates, and (c) EDX spectra resulting from the bulk and from the grain boundary precipitate shown in (b).

Table 14. Chemical compositions of the bulk material and grain boundary precipitate resulting from EDX analysis.

	Bulk		GB precipitate	
	wt. %	at. %	wt. %	at. %
C	1.34	5.82	1.65	6.99
O	**1.94**	**6.33**	**2.25**	**7.18**
Si	0.75	1.39	0.62	1.13
Nb	2.14	1.20	2.26	1.24
Ti	**0.30**	**0.32**	**2.70**	**2.87**
Cr	14.23	14.26	14.73	14.44
Fe	7.27	6.78	7.41	6.76
Ni	72.03	63.90	68.38	59.38
Total	100.00	100.00	100.00	100.00

The microstructure on plane "A" (Fig. 66) was further examined in the Hitachi S-4700 field emission gun SEM, allowing a close inspection of the precipitates and grain boundary continuity across the HAZ. Figure 75 shows the microstructure observed on the surface of the weld sample, plane A, at increasing magnifications. The elongated grains with dendritic features observed previously can be seen in all micrographs, as well as the large variations in grain size between the different passes (Figs. 75a vs. 75b, c). In Fig. 75d, several matrix precipitates can be observed.

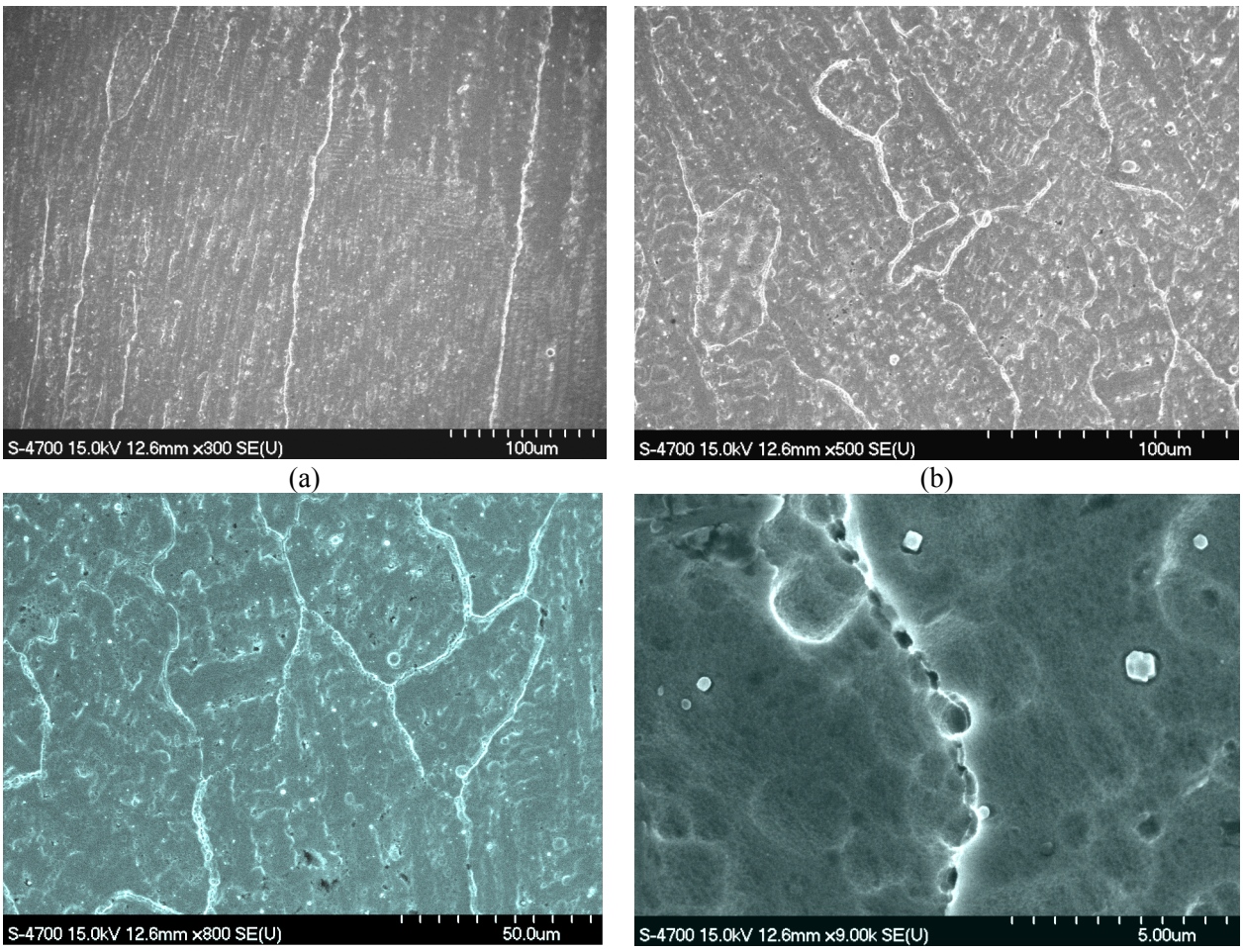

Figure 75. Dendritic microstructure observed on the surface of sample 3A at (a) 300×, (b) 500×, (c) 800×, and (d) 9,000× magnification.

The objective of this part of the analysis was to image at high magnification the precipitates present in the weld and HAZ. Figures 76a, c, e is a series of high magnification micrographs showing Ti–rich precipitates in the weld material, in both matrix and grain boundaries. Figures 76 b, d, f are maps showing the topography at the locations where the high magnification micrographs were taken.

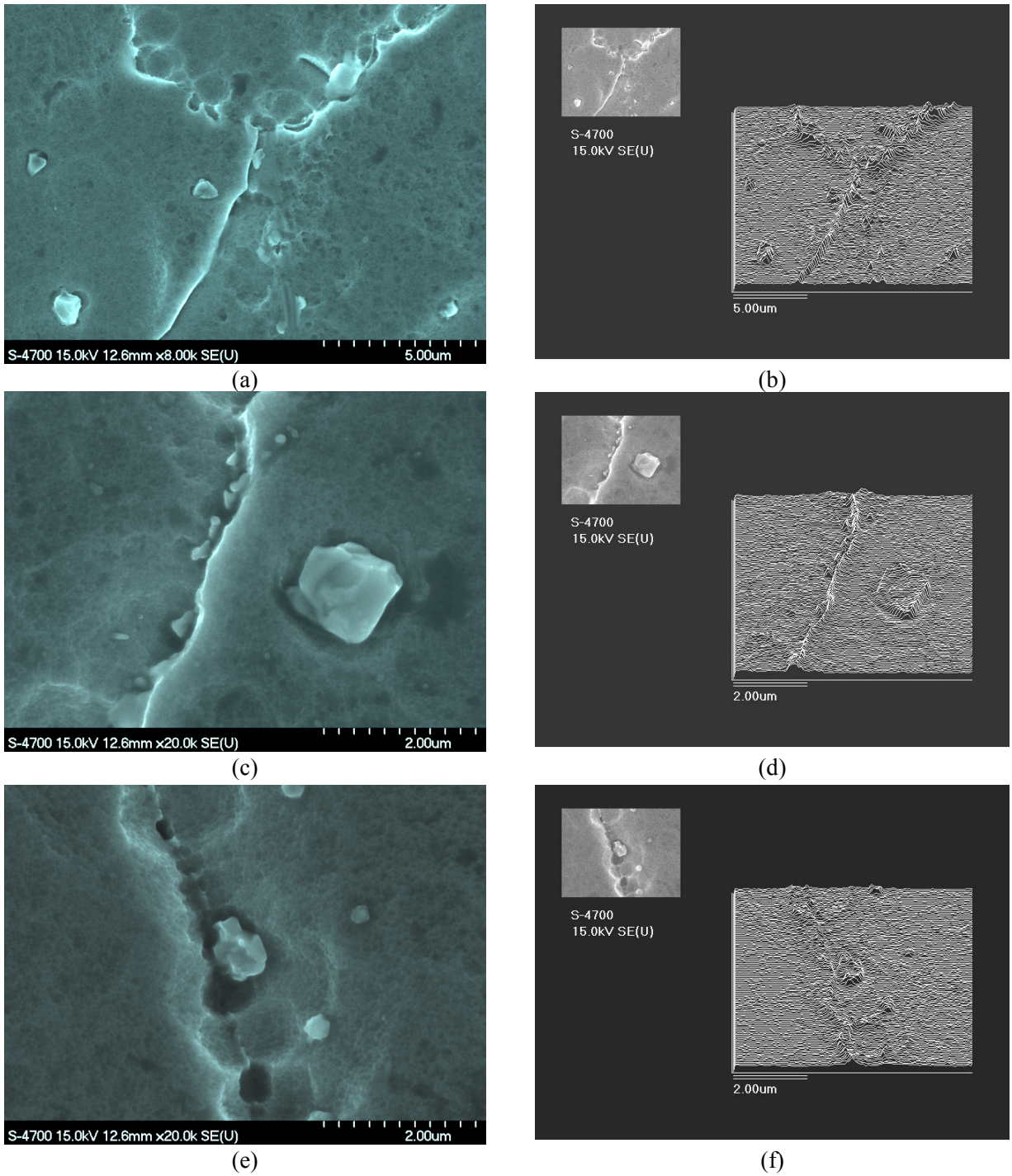

Figure 76. Micrographs showing Ti-rich precipitates in the weld material (a,c,e), and maps showing the topography at the locations where the high magnification micrographs were taken (b,d,f).

Further, the heat–affected zone (HAZ) was investigated. Figures 77a, c show areas on the HAZ where the dendritic microstructure (lower left) is replaced by the large grains of the HAZ. Figures 77b, d are high magnification micrographs of the precipitates observed in Figs. 77a and 77c, respectively. Figure 77 also shows that the random, high–angle boundaries from the weld extend into the HAZ.

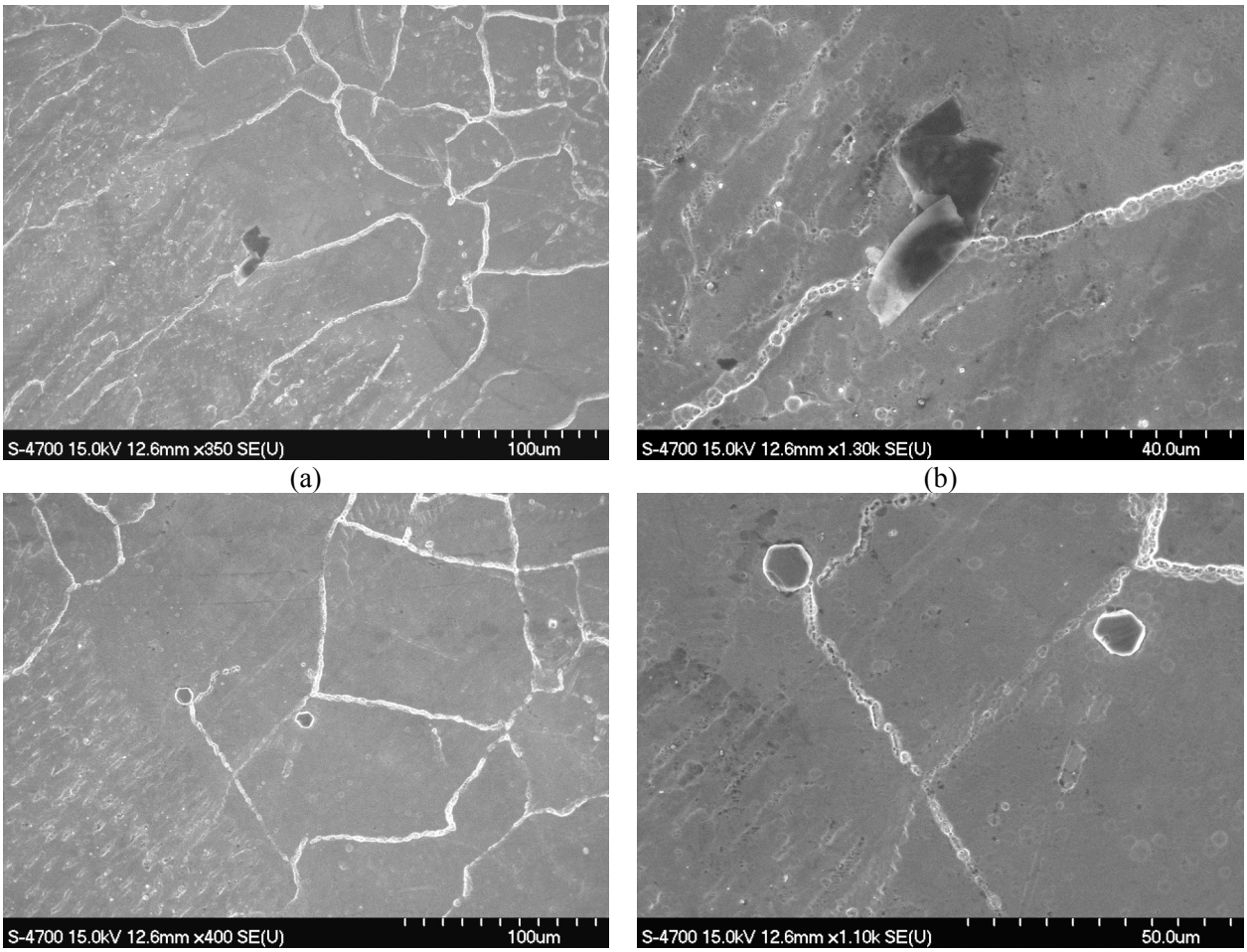

Figure 77. Micrographs showing the heat affected zone (a,c), and high magnification micrographs showing precipitates in the heat affected zone (b,d).

Examination of Weld specimens by Orientation Imaging Microscopy

Orientation imaging microscopy (OIM) is a diffraction-based technique by which maps of the crystal structure of a material can be obtained, thereby providing both the orientations of the crystals (grains) and the types of grain boundaries present. The interest to apply the OIM technique to the current weld samples was driven by two features (that OIM can analyze) that have been shown to strongly influence the intergranular stress corrosion cracking behavior of austenitic alloys in high temperature aqueous environments: the grain boundary character distribution (i.e., the proportions of boundaries in special orientation relationships), and the amount and location of residual stress.

For the preliminary OIM analysis reported here, specimen 3B was first mechanically polished with 1–μm diamond paste on both surface and plane "B" (see Fig. 66), and electro-polished in a perchloric acid (10%) and methanol solution at –50°C. Repeated double polishing cycles of 5 s at 40 V provided the best surface finish.

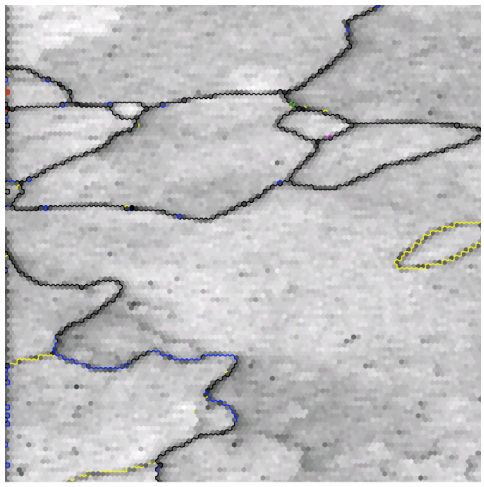

(a)

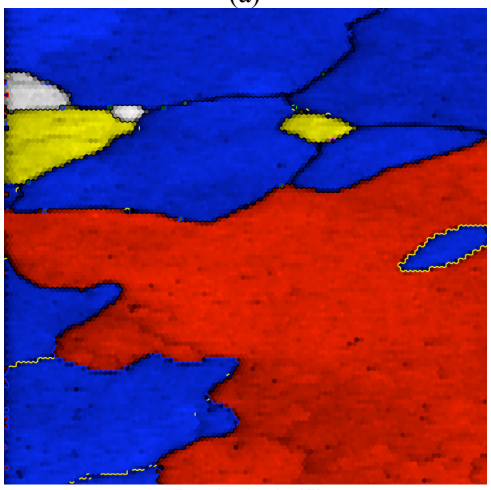

(b)

Gray Scale Map Type: Image Quality
24.8...82.8 (24.8...82.8)

Color Coded Map Type: Crystal Direction

Direction	Min	Max	Total Fraction	Partition Fraction
<1 0 0>|||[0 0 1]	0°	15°	0.465	0.465
<0 1 1>|||[0 0 1]	0°	15°	0.036	0.036
<1 1 1>|||[0 0 1]	0°	15°	0.000	0.000
<1 1 2>|||[0 0 1]	0°	15°	0.000	0.000
<1 1 4>|||[0 0 1]	0°	15°	0.488	0.488

Boundaries: Rotation Angle

Min	Max	Fraction
15°	180°	0.883

Boundaries: CSL

Sigma	Tolerance	Fraction	Volume	MDF Value
1	15.00	0.117	0.0228	5.14
3	8.66	0.005	0.0176	0.26
5	6.71	0.006	0.0123	0.50
7	5.67	0.000	0.0099	0.00
11	4.52	0.005	0.0075	0.72
13a	4.16	0.001	0.0029	0.26
13b	4.16	0.012	0.0039	2.96
15	3.87	0.097	0.0094	10.29
17a	3.64	0.006	0.0020	3.15
17b	3.64	0.006	0.0039	1.58
19a	3.44	0.005	0.0033	1.63
19b	3.44	0.000	0.0022	0.00
21a	3.27	0.000	0.0019	0.00
21b	3.27	0.000	0.0057	0.00
23	3.13	0.000	0.0050	0.00
25a	3.00	0.000	0.0011	0.00
25b	3.00	0.000	0.0044	0.00
9	5.00	0.002	0.0102	0.15
27a	2.89	0.002	0.0020	1.18
27b	2.89	0.000	0.0039	0.00
summary	-	0.264	0.1317	2.01

*For statistics - any point pair with misorientation exceeding 2° is considered a boundary

(c)

Figure 78. (a) OIM map of the weld, on plane “B”, sample 3B; (b) the same OIM map showing the orientation of each grain; and (c) legends for crystal directions and the resulting grain boundary character distribution.

Figure 78a shows an OIM map resulting from the weld, plane B. In this analysis, the grain boundaries were classified according to the coincident site lattice model as low angle boundaries (LAB, $\Sigma=1$), coincident site lattice boundaries (CSLB, $3\leq\Sigma<29$), or high angle boundaries (HAB, $\Sigma\geq29$). Cracking would be expected along the high angle boundaries, identified as such, with black color in the OIM map. Also shown (Fig. 78b) is a map indicating the crystal directions parallel (±15°) to the normal sample surface. First, we observe that the dendritic structure does not appear in the OIM maps, suggesting that the dendrites are coherent, and, therefore, very unlikely to crack. Second, little or no texture (Fig. 78b) is evident on this plane (“B” in Fig. 66). Third, the proportion of crack-resistant coincident site lattice boundaries (CSLBs) is very low (26%), as indicated by the data in Fig. 78c. For comparison, solution annealed Alloy 600 has a CSLB fraction of approximately 50%. If this last observation holds true for a larger area – where a statistically significant number of boundaries are analyzed – it in itself suggests a high degree of susceptibility of the weld.

Next, an area on the surface of sample 3B was mapped by OIM. The area included the weld, HAZ, and part of the Alloy 600, as shown in Fig. 79a. The resulting proportion of CSLBs was 35%. Although somewhat larger than in the previous example, this result was probably due to the inclusion of the area from Alloy 600 in the total count.

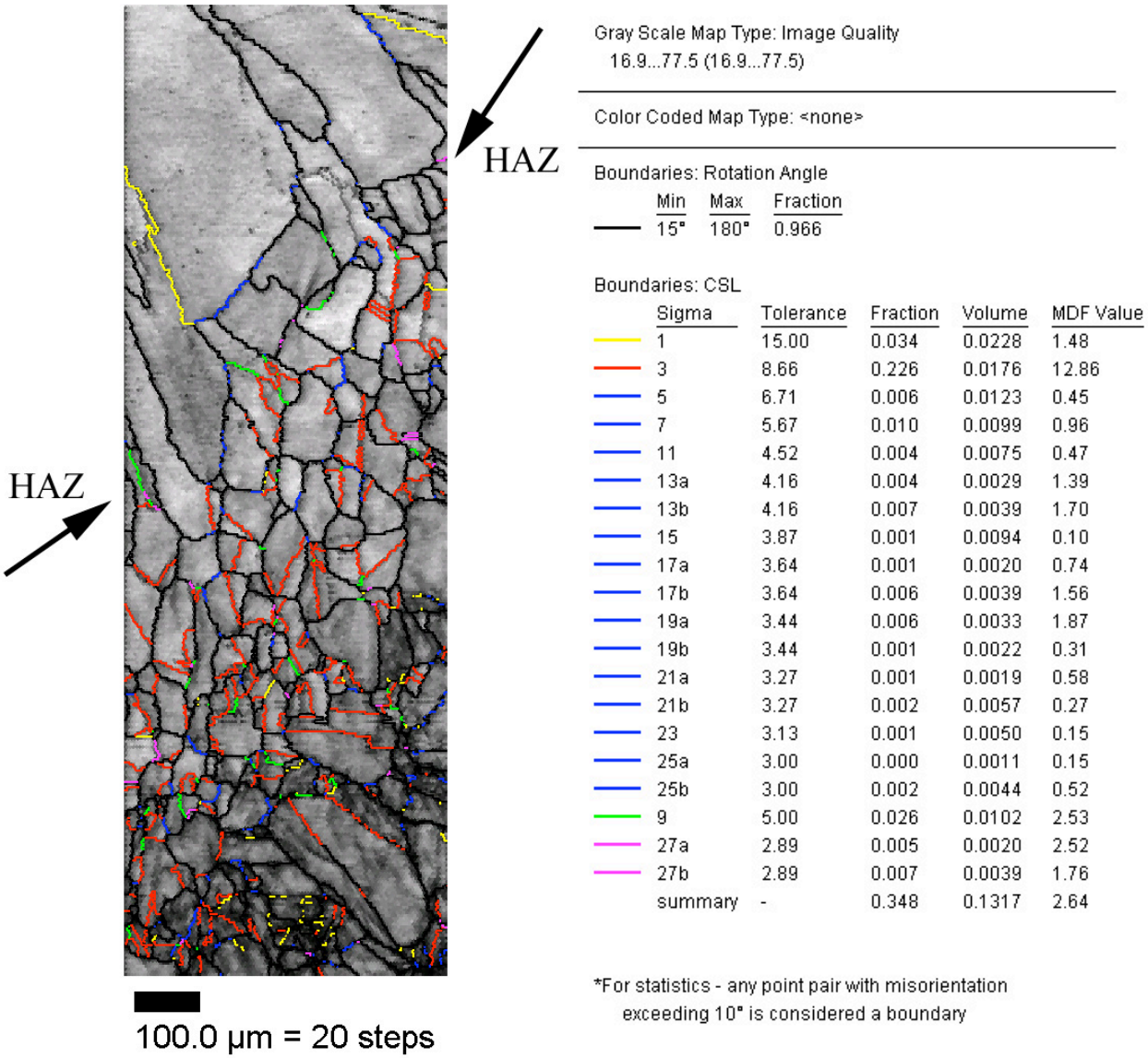

Figure 79. (a) OIM map on the surface of sample 3B and (b) the resulting grain boundary character distribution. The OIM map covers the weld (upper part), the HAZ (indicated by arrows), and Alloy 600 (lower part).

Figure 80a shows the same OIM map as Fig. 79a, but with the grain directions included. Again, no definitive conclusion can be drawn with respect to the presence or absence of a texture in the weld due to the small weld area analyzed. Nevertheless, we notice that, as in Fig. 78, the OIM did not distinguish the dendritic structure (SEM micrograph of Fig. 80b was included for comparison). Thus, it is very likely that the grain boundary character distribution will determine the cracking behavior of the weld.

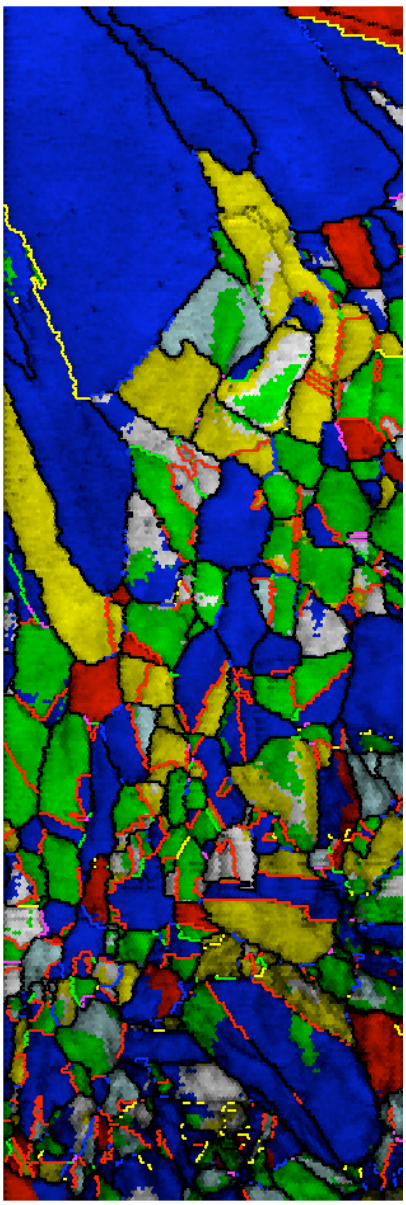

(a)

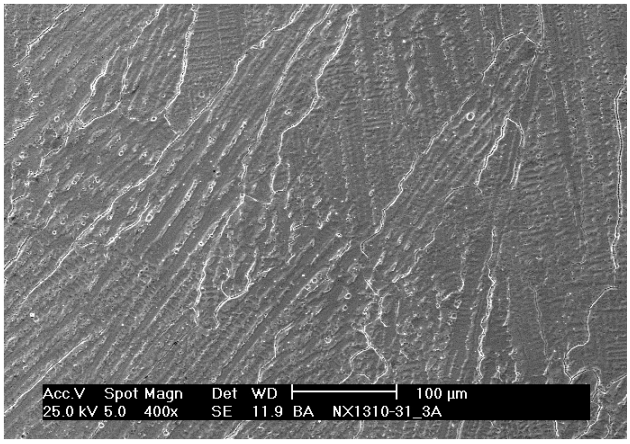

(b)

Color Coded Map Type: Crystal Direction

Direction	Min	Max
<1 0 0>||[0 0 1]	0°	15°
<0 1 1>||[0 0 1]	0°	15°
<1 1 1>||[0 0 1]	0°	15°
<1 1 2>||[0 0 1]	0°	15°
<1 1 4>||[0 0 1]	0°	15°

Figure 80. (a) The same OIM map as in Fig. 79a showing crystal directions and (b) SEM micrograph illustrating the dendritic microstructure of the weld.

In conclusion, the OIM analysis presented here has shown that the intragranular dendrites are coherent and are, therefore, expected to be resistant to cracking. In consequence, the grain boundary character distribution (along with residual deformation) that will likely determine the cracking behavior of the welds. The proportion of cracking-resistant CSL boundaries in the weld was found to be relatively small; however, a statistically significant population of boundaries needs to be analyzed to substantiate this last observation.

5.3 Results

5.3.1 Alloy 600 Round Robin Specimen

A CGR test was conducted on Alloy 600 round–robin specimen in simulated PWR environment at 320°C according to the testing protocol agreed upon by the CIR group. The round robin test protocol specifies a progression of loading conditions during the test, and are given in Table 15. The actual environmental and loading conditions and experimental CGRs for the test are given in Table 16; the changes in crack length and K_{max} with time during various test periods are shown in Fig. 81.

Table 15. Loading conditions for the Alloy 600 round-robin test

Step	K_{max}, MPa $m^{1/2}$	Load Ratio, R	Frequency	Crack Increment
1	25	0.3	1 Hz sine	0.5 mm
2	28	0.5	1 Hz sine	0.3 mm
3	30	0.6	1 Hz sine	0.3 mm
4	30	0.7	1 Hz sine	0.3 mm
5	30	0.7	0.1 Hz sine	0.2 mm
6	30	0.7	0.01 Hz sine	0.2 mm
7	30	0.7	0.001 Hz triangle	0.2 mm
8	30	0.7	0.001 Hz + 9 ks hold	0.1 mm
9	30	Constant load	Constant load	≥1 month

Table 16. Crack growth results for Alloy 600[a] round robin specimen RR-1 in PWR water[b] at 320°C

Test Period	Test Time, h	Conduc-tivity,[c] µS/cm	ECP A600/Pt, mV	R Load Ratio	Rise Time, s	Down Time, s	Hold Time, s	K_{max}, MPa·$m^{1/2}$	ΔK, MPa·$m^{1/2}$	CGR, m/s	CGR in Air, m/s	Crack Length, mm
1	146	25.7	-639/-660	0.3	0.5	0.5	0	24.8	17.4	2.01E-08	4.07E-08	20.619
1b	166	26.0		0.3	0.5	0.5	0	25.0	17.5	2.64E-08	4.23E-08	20.801
2	175	26.0		0.5	0.5	0.5	0	27.9	14.0	1.30E-08	2.85E-08	21.029
3	193	25.3		0.6	0.5	0.5	0	30.0	12.0	9.89E-09	2.13E-08	21.350
4	234	23.5		0.7	0.5	0.5	0	30.4	9.1	3.80E-09	1.02E-08	21.743
5	354	25.5	-670/-705	0.7	5	5	0	30.1	9.0	1.19E-09	9.83E-10	21.947
6	550	25.5		0.7	50	50	0	29.8	9.0	3.00E-10	9.44E-11	21.993
7a	642	26.3		0.7	500	500	0	29.6	8.9	2.55E-10	9.18E-12	22.124
7b	863	24.6	-666/-668	0.7	500	500	0	29.9	9.0	negligible	9.50E-12	22.108
3B	865	24.6		0.6	0.5	0.5	0	30.1	12.0	1.13E-07	2.16E-08	22.199
4B	871	27.4		0.7	0.5	0.5	0	30.1	9.0	1.45E-08	9.82E-09	22.385
5B	898	25.1		0.7	5	5	0	29.6	8.9	1.25E-09	9.19E-10	22.425
3C	904	25.1		0.6	0.5	0.5	0	30.0	12.0	1.90E-08	2.13E-08	22.501
4C	928	24.9		0.7	0.5	0.5	0	30.0	9.0	4.73E-09	9.63E-09	22.780
5C	1040	25.3		0.7	5	5	0	29.9	9.0	8.09E-10	9.55E-10	22.938
6C	1320	25.1	-658/-684	0.7	50	50	0	30.1	9.0	3.14E-10	9.72E-11	23.087
7C	1570	26.0		0.7	500	500	0	30.2	9.1	5.91E-10	9.86E-12	23.351

[a]Alloy 600 Heat 3110439 cold worked 30% (cross–rolled 15% per pass).
[b]Simulated PWR water with 2 ppm Li, 1100 ppm B, and 2 ppm dissolved hydrogen (≈23 cc/kg); O_2 concentration was always less than 10ppb.
[c]Represents values in the effluent; conductivity was ≈22.0 µS/cm in feedwater.

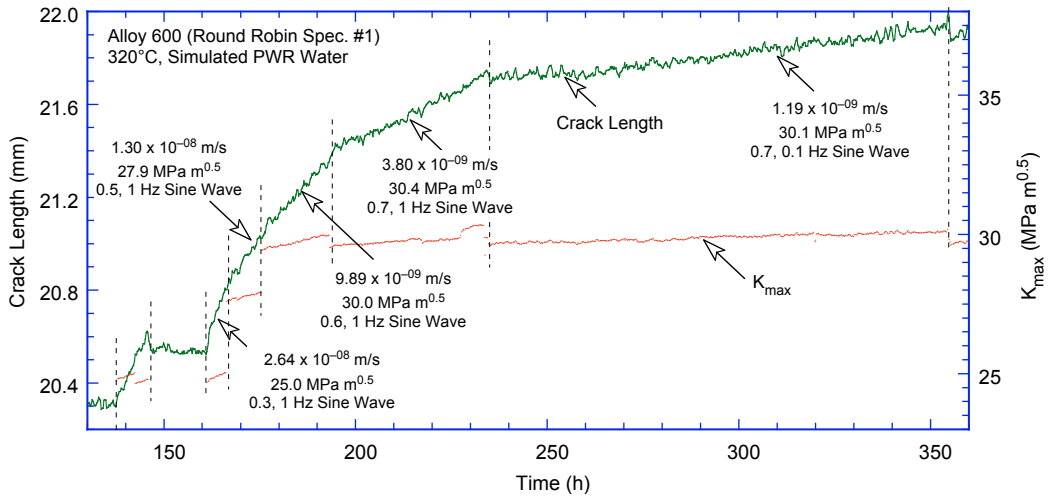

(a)

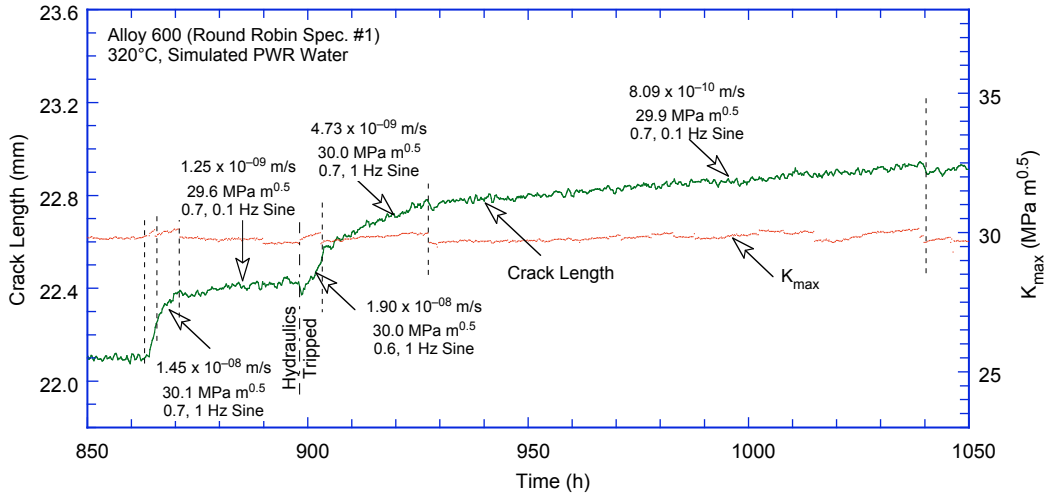

(b)

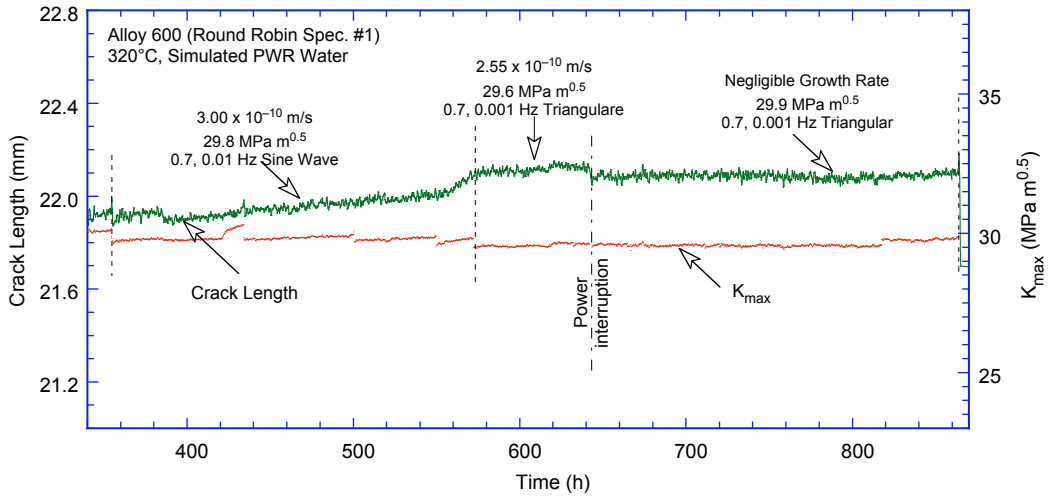

(c)

Figure 81. Crack length vs. time plot for Alloy 600 round-robin specimen RR-1 in simulated PWR environment at 320°C during periods (a) 1-5, (b) 3B-5C, (c) 6-7, and (d) 6C-7C.

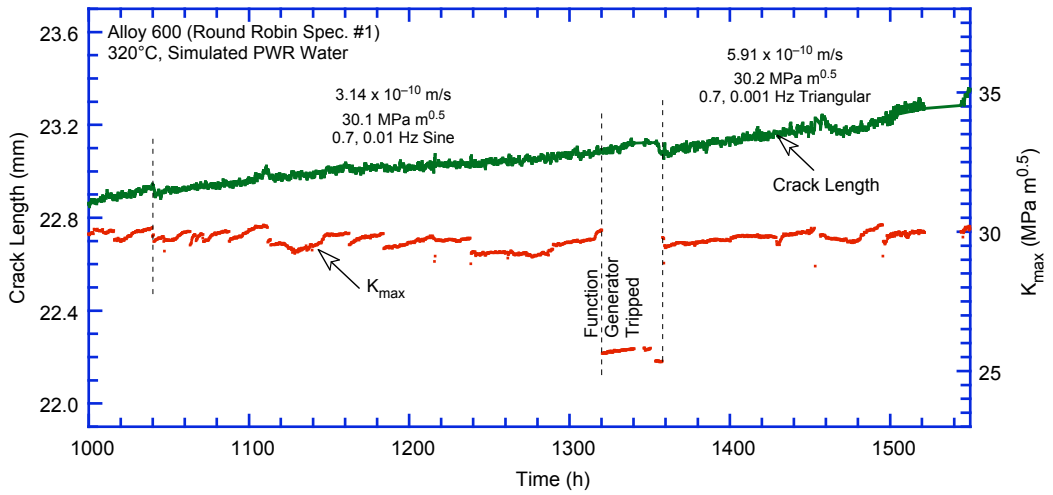

(d)

Figure 81. (Contd.)

The existing CGR data under cyclic loading indicate that in simulated PWR or low–DO water at 320°C only some heats of Alloy 600 show enhanced growth rates. For the heats that show environmental enhancement, the CGRs may be represented by the best–fit curve for Alloy 600 in high–purity water with 300 ppb DO at 289°C. The experimental CGRs from the present test and those predicted in air for the same loading conditions are plotted in Fig. 82. For high growth rates, the rates measured for the round robin specimen are a factor of ≈2 lower than those predicted in air. The difference, most likely, is due to the material condition; the round robin specimen was 30% cold worked, whereas the data in air are for annealed material. For low growth rates, the measured rates are higher than predicted in air.

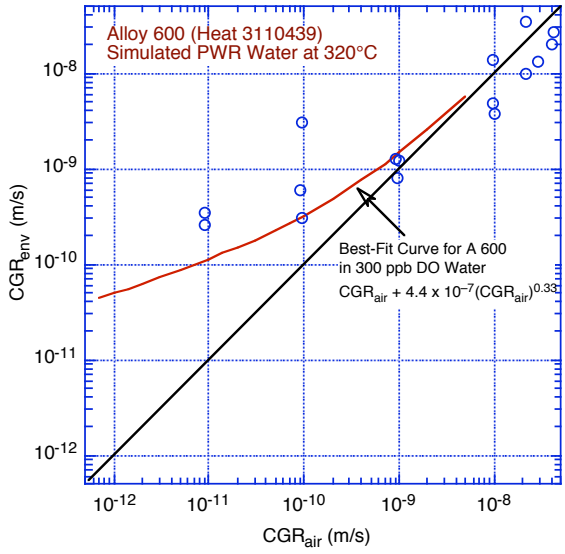

Figure 82.
CGR data for specimen RR-1 of the Alloy 600 round-robin test in simulated PWR environment at 320°C.

The test had to be stopped because of large pressure fluctuations and, finally, total flow blockage. The cause of flow blockage was identified to be $Al(OH)_3$ deposits. The source of Al in our system is the alumina insulators used for the DC potential and current leads. Because water is being recirculated without a purification system, the concentration of Al gradually builds up during operation, eventually leading to plugging of the cooler regions. The entire return line from the autoclave to the supply tank

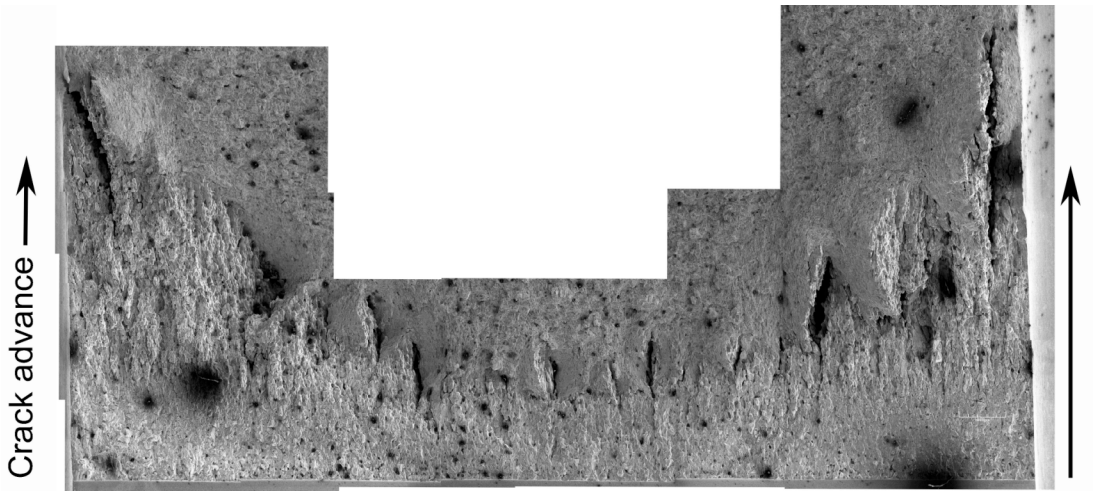

Figure 83. Entire crack surface of Alloy 600 round robin specimen RR-1 tested in PWR water at 320°C.

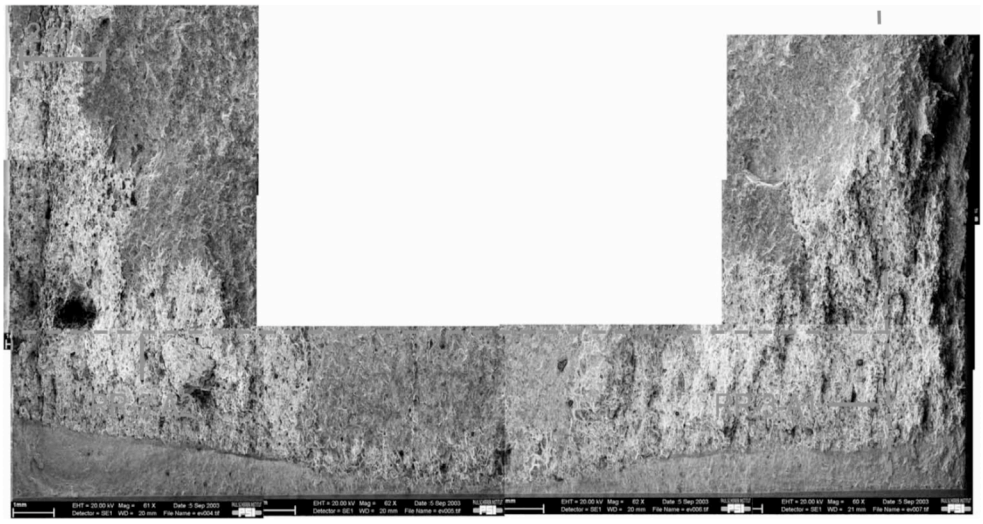

Figure 84. Entire crack surface of Alloy 600 round robin specimen RR-3 tested in PWR water at 320°C.

including the back–pressure regulator was either replaced or cleaned by back flushing. However, the water system was operated in a once–through mode to minimize the chance for the build–up of deposits.

The specimen was next fractured in preparation for metallographic examination. A photomicrograph of the broken half of the CT specimen is shown in Fig. 83. The crack front appears to be consistent with the observations in Switzerland; growth rates are significantly higher near the edge of the specimen than the center. For comparison, Fig. 84 shows the very similar fracture surface from round-robin specimen RR-3 reported by H. P. Seifert of Paul Sherrer Institute in Switzerland.* It is possible that since the round-robin specimens were fabricated from Heat 3110439 cold worked 30% (cross–rolled 15% per pass) the distribution of cold work may have not been uniform across the specimen thickness. The fracture mode is TG near the machine notch, followed by a transition region of highly angular, cleavage–like facets with "river" patterns, and changing to completely IG for most of the test. Also, finger–like regions of IG fracture extend ahead of the crack front near these secondary cracks.

* H. P. Seifert, Paul Scherrer Institute, Switzerland, private communication to O. K. Chopra, 2003.

Figure 85a shows a more detailed, selected portion of the crack surface. Figures 85b,c are high magnification micrographs showing the boxed areas in Fig. 85a. We observed a morphology with cleavage–like facets and broken planes early in the test (Fig. 85b), followed by an exclusively IG fracture mode (Fig. 85b). Secondary cracks, along a plane parallel to the direction of crack growth but perpendicular to the fracture plane, are visible in the IG fracture region.

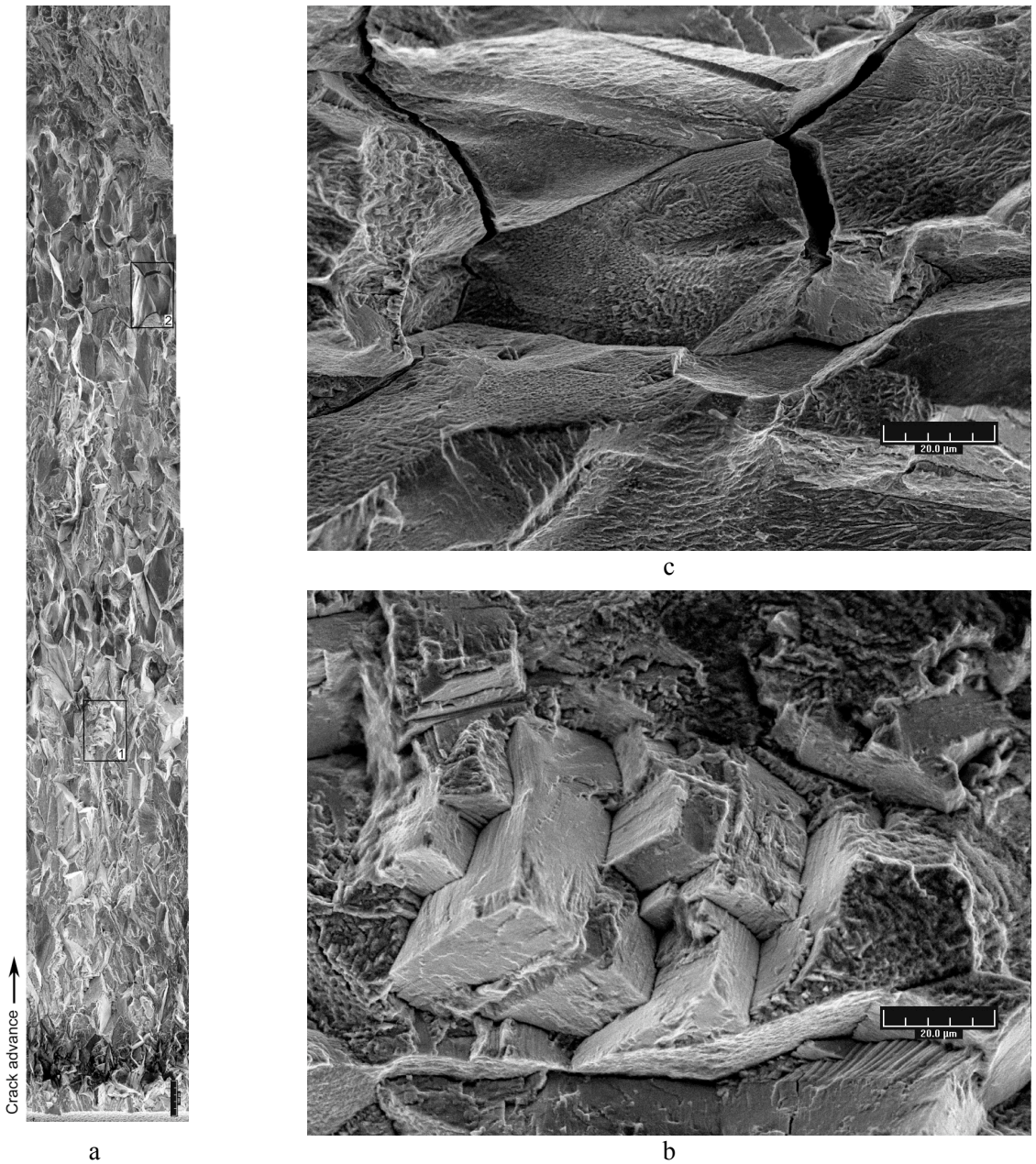

Figure 85. (a) Selected portion of the crack surface of Alloy 600 round robin specimen RR-1 tested in PWR water at 320°C showing the changes in fracture morphology, and (b,c) micrographs taken at the boxed positions 1 and 2, respectively, in (a).

5.3.2 Alloy 182 Double–J Weld Specimen

The CGR test on Specimen CT31–W01 (TS orientation) of Alloy 182 SMA weld was started in simulated PWR water at 320°C with the water system operating in the recirculating mode at a flow rate of ≈60 cc/min. The system was operated about a week for the environmental conditions to stabilize. The ECPs, measured at 289°C at the exit of the autoclave, of a Alloy 600 sample and Pt electrode were –686 and –690 mV (SHE), respectively; the water system was switched to the once–through mode during ECP measurements to prevent possible contamination of the test solution. The specimen was fatigue precracked at R = 0.3, K_{max} = 23 MPa $m^{1/2}$, triangular waveform, and 0.5 Hz frequency. After ≈0.3–mm extension, R was increased incrementally to 0.7, and the frequency decreased to 0.005 Hz. The experimental conditions and results for the test are given in Table 17; the changes in crack length and K_{max} with time during various test periods are shown in Fig. 86. Note that at 140, 250, 380, and 580 h, the DC potential measurements were not recorded for short periods extending 10–20 h.

The test was interrupted at 407 h and 593 h because of large fluctuations in the system pressure. The problem was identified to be caused by $Al(OH)_3$ deposits in the cooler regions of the water system. Alumina beads used to insulate the DC potential and current leads were the source for Al. In a recirculating system, the concentration of Al gradually builds up during operation, eventually leading to plugging. The entire return line from the autoclave to the supply feedwater tank including the back–pressure regulator, was replaced or cleaned by back flushing. The test was restarted under the loading conditions prior to the interruption but with the system operating in a once–through mode at a lower flow rate of ≈10 cc/min. In the case of both interruptions, the CGRs existing before the interruption were restored after restart.

After the test, the specimen was fractured in liquid nitrogen. A photomicrograph of the fracture surface of one-half of the specimen is shown in Fig. 87; the crack front is relatively straight. Average crack extension was determined by taking ≈20 measurements across the width of the specimen. The measured crack extension was 35% greater than the value determined from the DC potential measurements, most likely because of several unbroken ligaments on the fracture surface. Crack extensions determined from the DC potential method were scaled proportionately; the corrected data are given in Table 17.

Table 17. Crack growth data for specimen CT31-W01 TS of Alloy 182 SMA weld in PWR water[a] at 320°C

Test Period	Test Time, h	Conduc-tivity,[b] µS/cm	O_2 Conc.,[b] ppb	Load Ratio R	Rise Time, S	Down Time, s	Hold Time, s	K_{max}, MPa·$m^{1/2}$	ΔK, MPa·$m^{1/2}$	CGR_{env}, m/s	Estimated CGR_{air}, m/s	Crack Length, mm
1	25	25.0	<10	0.3	1	1	0	23.26	16.28	7.58E-08	1.56E-08	13.044
2	40	25.0	<10	0.3	10	10	0	24.19	16.93	2.32E-08	1.83E-09	13.783
3	90	25.0	<10	0.6	10	10	0	24.28	9.71	2.62E-09	4.48E-10	14.046
4a	135	25.3	<10	0.7	10	10	0	25.05	7.52	1.02E-09	2.31E-10	14.125
4b	281	25.3	<10	0.7	10	10	0	25.39	7.62	8.10E-10	2.44E-10	14.471
5	407	24.4	<10	0.7	100	100	0	25.57	7.67	1.64E-10	2.51E-11	14.503
6	498	23.9	<10	0.7	100	100	0	25.59	7.68	2.73E-10	2.52E-11	14.497
7	552	22.7	<10	0.7	500	500	0	25.57	7.67	negligible	5.02E-12	14.497
8	593	23.0	<10	0.7	1000	12	0	28.55	8.56	2.34E-10	3.94E-12	14.588
9	858	20.0	<10	0.7	1000	12	0	28.86	8.66	5.22E-11	4.12E-12	14.687
10	1214	20.5	<10	0.7	1000	12	3600	29.03	8.71	5.93E-11	4.22E-12	14.790

[a]Simulated PWR water with 2 ppm Li, 1100 ppm B, and 2 ppm dissolved hydrogen (≈23 cc/kg).
[b]Represents values in the effluent; conductivity was ≈21.5 µS/cm in feedwater.

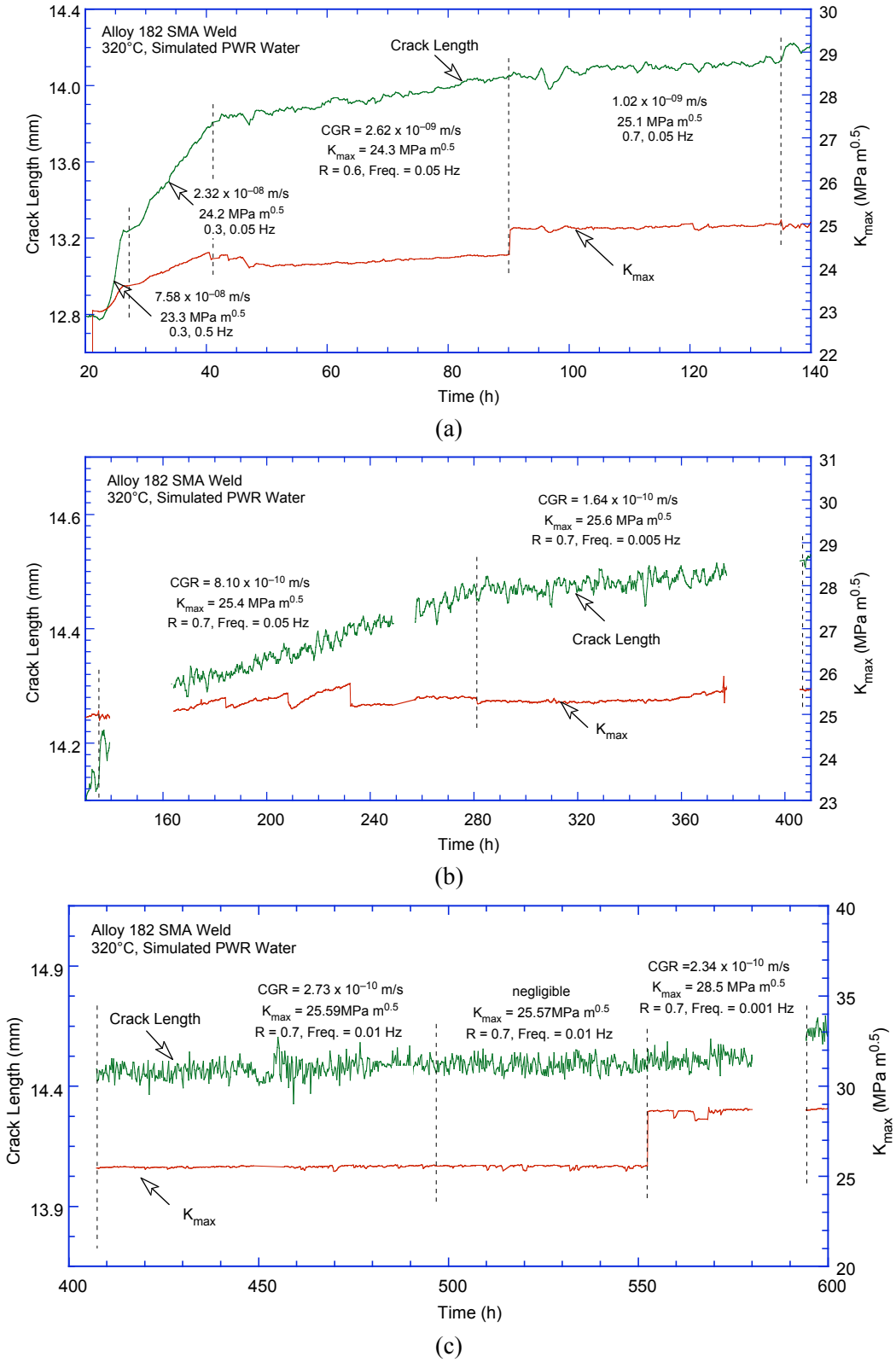

Figure 86. Crack length vs. time plot for Alloy 182 SMA weld–metal specimen in simulated PWR environment at 320°C during test periods (a) 1–4a, (b) 4b-5, (c) 6-8, (d) 9, and (e) 10.

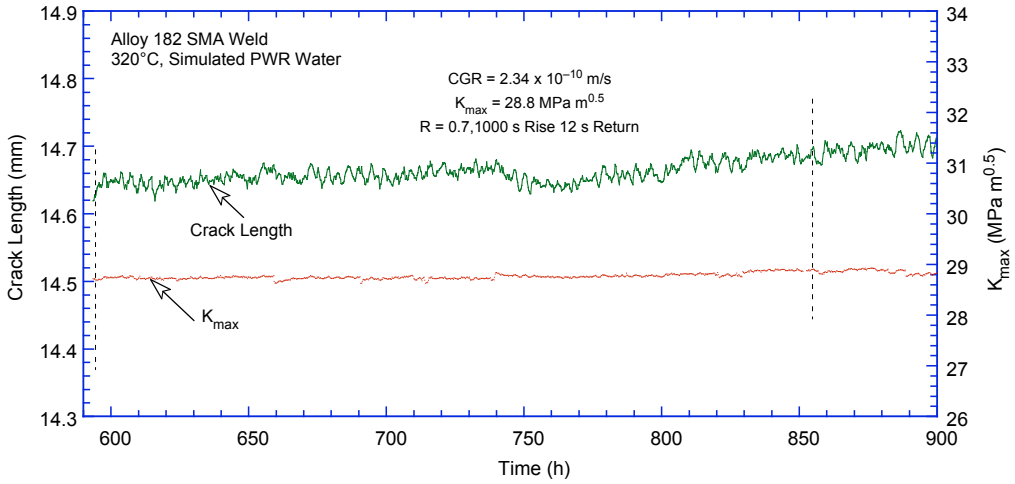

(d)

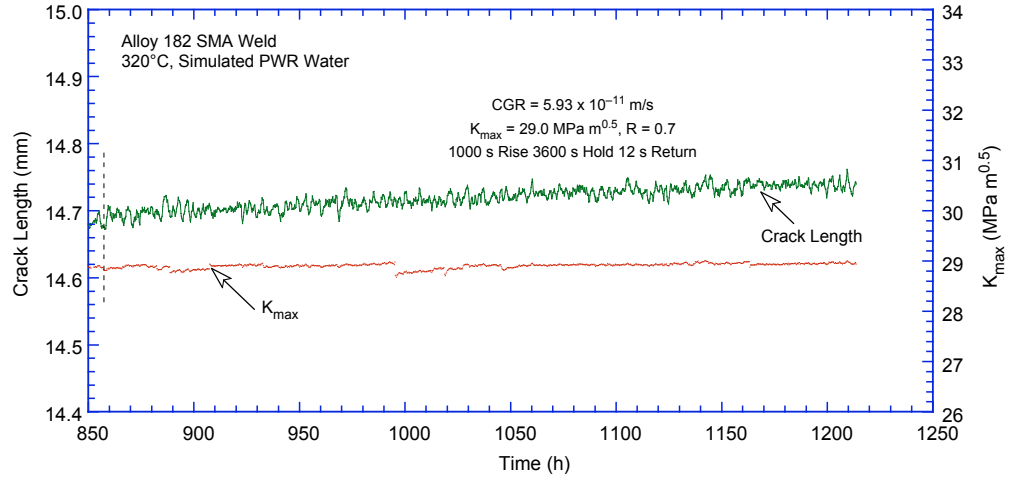

(e)

Figure 86. (Contd.)

To correlate different fracture modes with the test parameters (Table 17), the fracture surface of the specimen was also investigated by high magnification SEM. Figure 88a is a collage of micrographs showing the entire crack extension in a region corresponding to the boxed area of Fig. 87. High magnification micrographs of locations designated 3, 2, and 1 in Fig. 88a are shown in Figs. 88b, c, and d, respectively.

The results indicate that cracking initiated and progressed in a transgranular (TG) mode along the columnar grains and through the dendritic microstructure up to approximately 1300-1400 µm. At longer

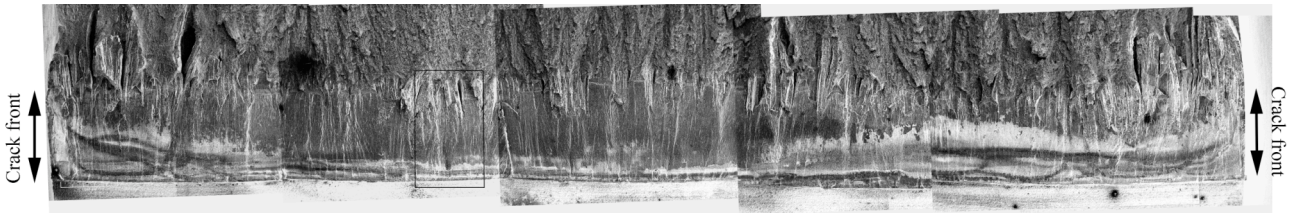

Figure 87. Photomicrograph of the fracture surface of specimen CT31-W01.

crack extensions, the fracture mode is predominantly intergranular (IG) with significant secondary IG cracks parallel to the direction of crack advance (Fig. 88a). A comparison with Table 17 indicates that the change to an IG fracture mode occurred during test period 5 when the rise time was increased from 10 to 100 s. Nevertheless, secondary IG cracks apparently are observed quite early during the test (Figs. 88a and d), but, as shown later in this section, there is evidence suggesting that the secondary IG cracking most likely occurred during the high rise–time test periods and extended back into the already cracked region. Figure 88c (location "2" in Fig. 88a) is a high magnification micrograph from the area corresponding to the high rise-time testing period, and shows the highly deformed facet of an IG crack. Further, close to the end of the crack front, Fig. 88b (location "3" in Fig. 88a) shows a TG stepped fracture surface.

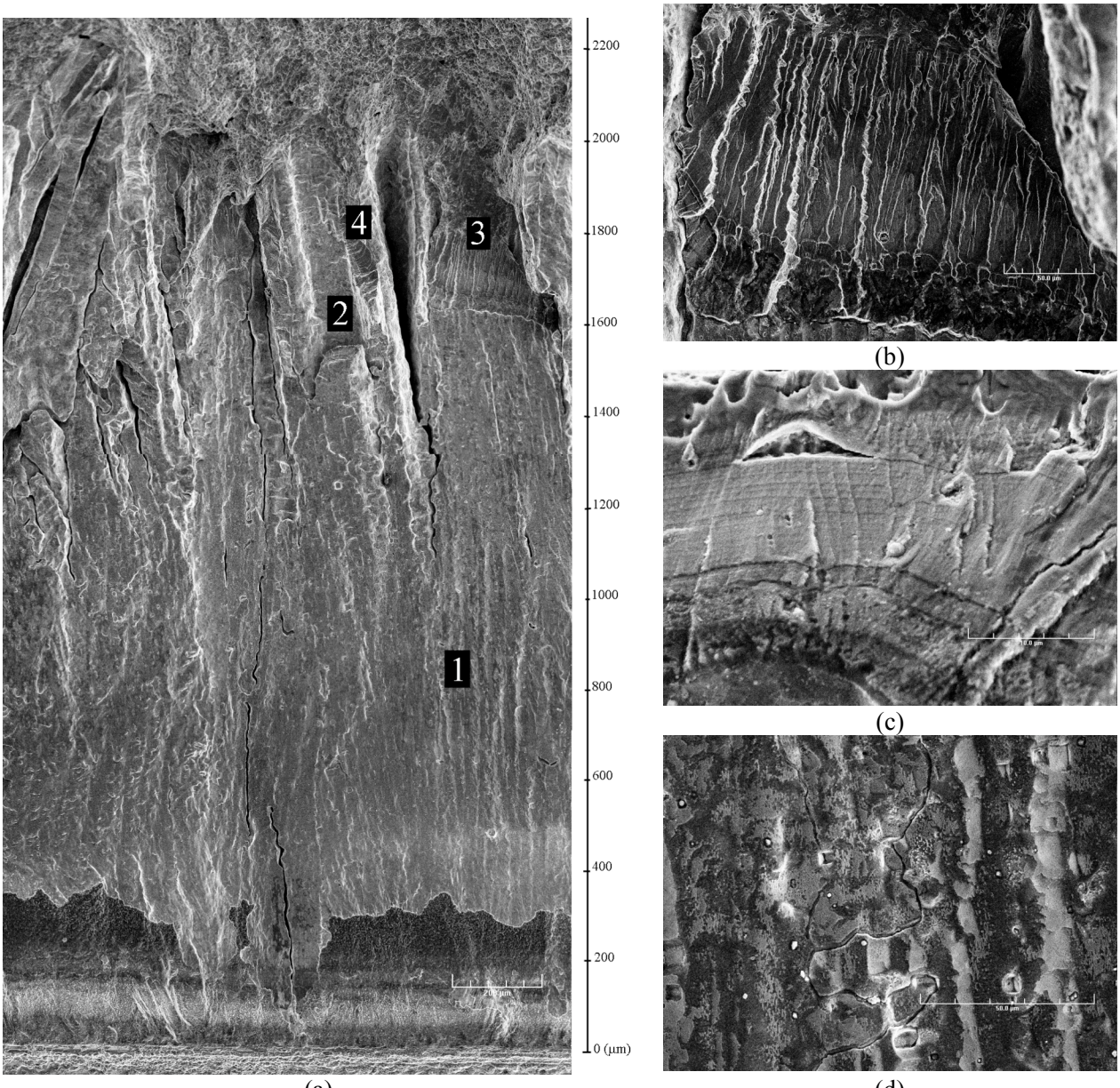

Figure 88. A higher magnification photomicrograph showing entire crack extension in a region in the center of the specimen.

The transition from a TG to an IG fracture mode is shown in Fig. 89a. The top–center brighter area of the figure shows IG cracks with the dendrites oriented perpendicular to the direction of crack advance, whereas the adjacent grain with the dendrites oriented parallel to the direction of crack advance shows TG fracture. The existing CGR data for Ni-alloy welds indicate that in PWR environments, the growth rates parallel to the columnar grain structure (T–S orientation) are generally a factor of two greater than those perpendicular to the columnar grain structure (T–L orientation). The present results suggest that this may not be true in all cases; the onset of IG cracking seems to have occurred sooner for the perpendicular grains.

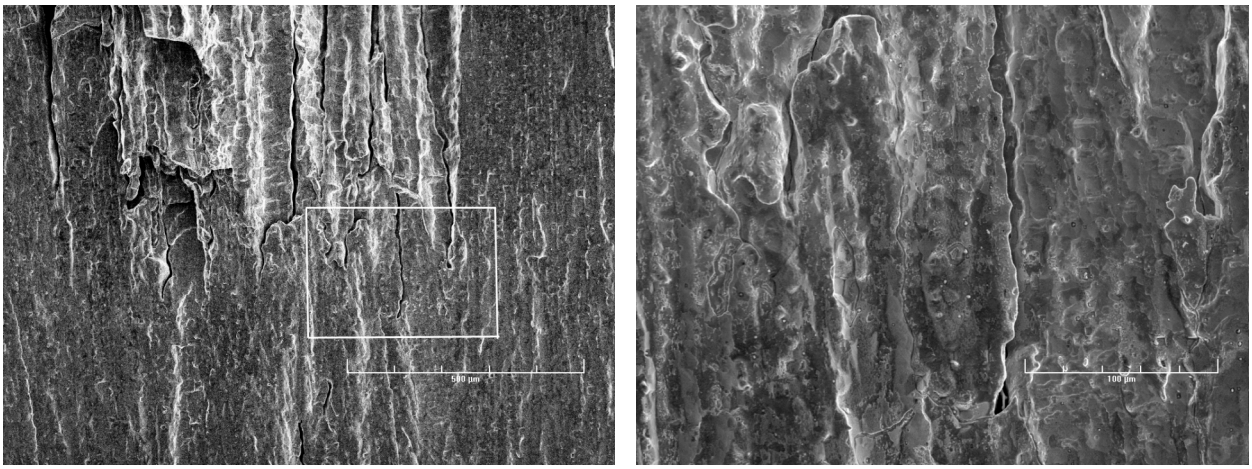

a b

Figure 89. (a) Transition from TG to IG fracture and (b) higher magnification micrograph of the boxed area showing the tip of a few cracks.

Another significant observation concerns the apparent formation of secondary IG cracks quite early during the test. A few examples are shown in the boxed area of Fig. 89a, and at higher magnification in Fig. 89b. The cracks seem to blunt in the TG region, suggesting that they had actually originated in the IG region and propagated back into the TG region. This behavior is substantiated further by additional micrographs in Fig. 90.

Figure 90a identifies an area in the TG region where IG cracks were observed (boxed area). A high magnification micrograph of the region is shown in Fig. 90b, where the two most prominent cracks are designated "1" and "2". The two cracks appear to shrink as they advance in the TG region, and furthermore, the tips appear blunt (Figs. 90c and d). Such observations lend further support to the hypothesis that the secondary IG cracks most likely originated in the IG region and propagated opposite to the direction of crack advance into the TG region.

The next two sets of micrographs focus on the region obtained near the end of the test during test periods with a hold time and/or a high rise–time. As mentioned earlier the crack extension measured after the test was ≈35% greater than that determined by the DC potential measurements. The present results indicate that the crack front might have advanced in a non–uniform manner, faster along some grain orientations, leaving behind more–resistant, unbroken ligaments, which in turn would cause the DC potential technique to underestimate the crack length. The first set of micrographs (Figs. 91) show two examples where ductile fracture is adjacent to IG cracking. The high magnification micrographs (Figs. 91 b, d) were obtained at the positions indicated by arrows in Figs. 91a and c. It thus appears likely that some IG crack fronts propagated independently of each other, and the unbroken ligament ruptured when the specimen was fractured in air.

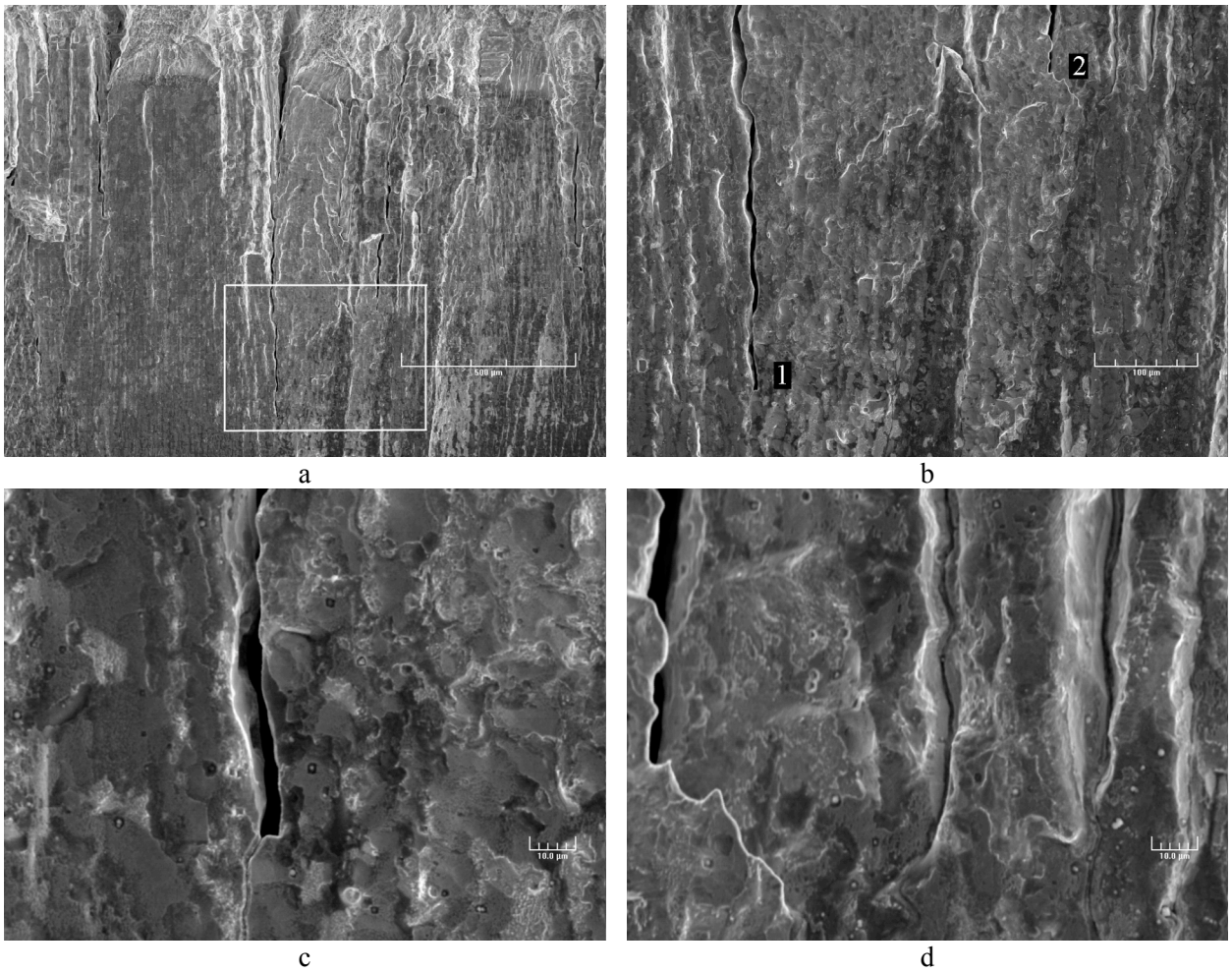

Figure 90. (a) Mixed TG and IG fracture modes, (b) high magnification micrograph of the boxed area, and (c,d) micrographs showing the crack tips at locations “1” and “2.”

By contrast, the second set of micrographs, Fig. 92, documents cases of various TG fracture morphologies observed in the last test region. These show examples of stepped TG (Figs. 92a, b) and quasi-cleavage with cleavage steps and crack arrest markings (Figs. 92c, d). These cases of TG in a test condition favoring IG are probably similar to those described in Fig. 91, i.e., grains of unfavorable orientation for crack advance situated between two faster propagating regions. High local stresses combined with the effect of the environment probably caused these grains to crack in a TG mode.

In summary, the examination of the fracture surface of the CT31-W01 specimen revealed that the fracture mode correlates well with the testing condition. Specifically, it was found that high rise times or long hold periods favor IG SSC. Also, IG cracking apparently advanced more readily along some grain orientations than others, resulting in a crack front with occasional unbroken ligaments and few regions of TG cracking.

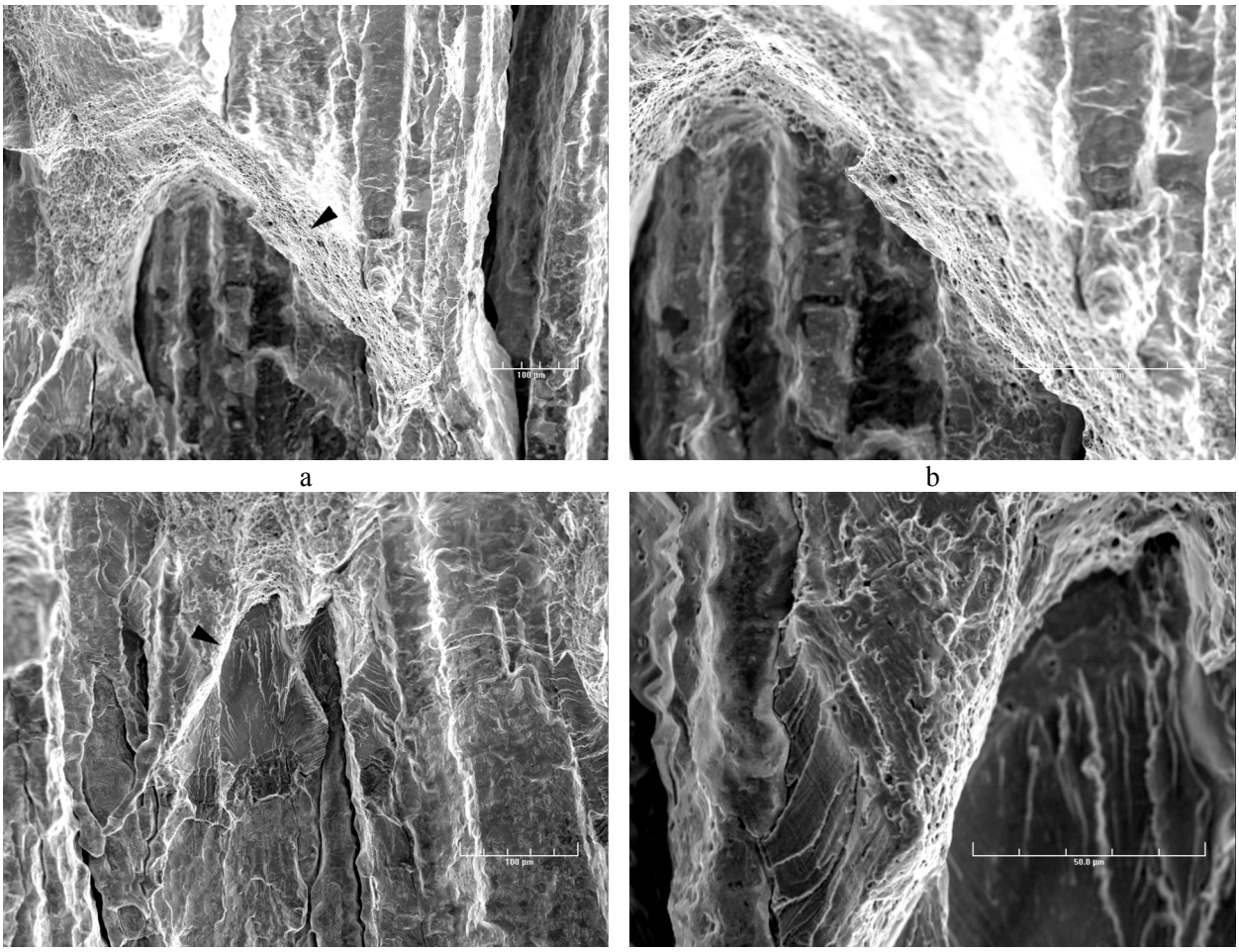

a b c d

Figure 91. (a,c) Photomicrographs detailing the fracture in a region during test periods with a hold time and/or a high rise time, and (b,d) high magnification micrographs of positions indicated by arrows.

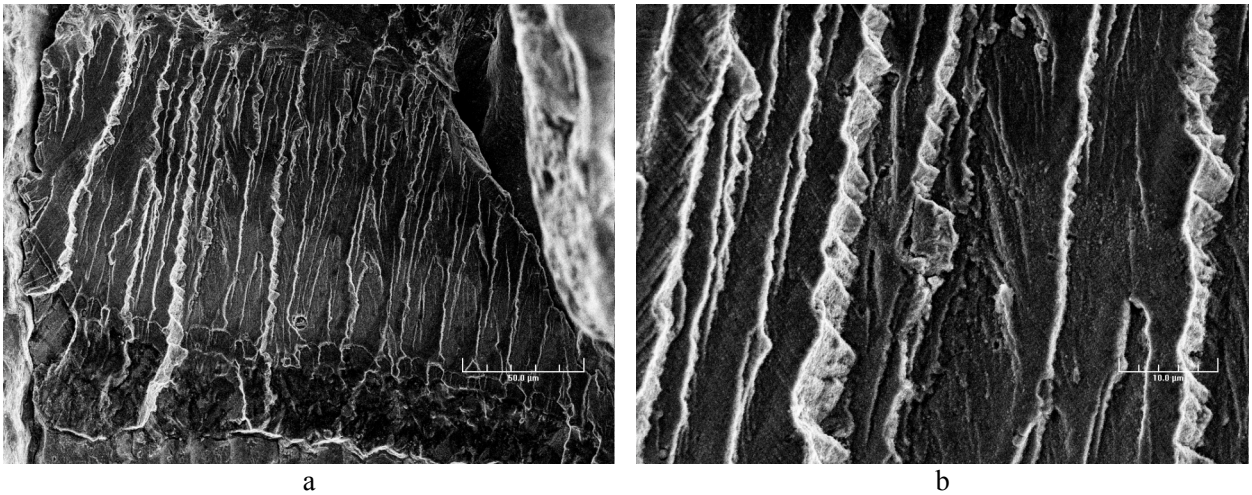

a b

Figure 92. (a,c) Photomicrographs detailing the fracture in a region during test periods with a hold time and/or a high rise time, and (b,d) high magnification micrographs.

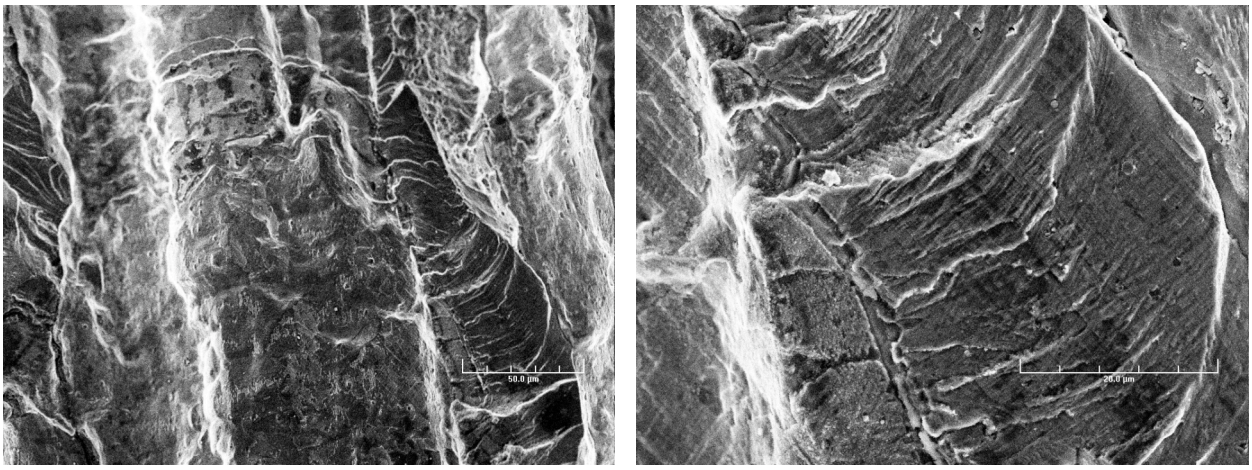

c d

Figure 92. (Continued)

The experimental CGRs obtained under cyclic loading and those predicted in air for Alloy 600 (i.e., calculated from Eq. 11) under the same loading conditions are plotted in Fig. 93. The results follow a line parallel to the diagonal in the figure, indicating little or no environmental enhancement of CGRs of Alloy 182 weld–metal in the PWR environment. In general, the CGRs for Alloy 182 are a factor of ≈5 higher than for Alloy 600 under the same loading conditions.

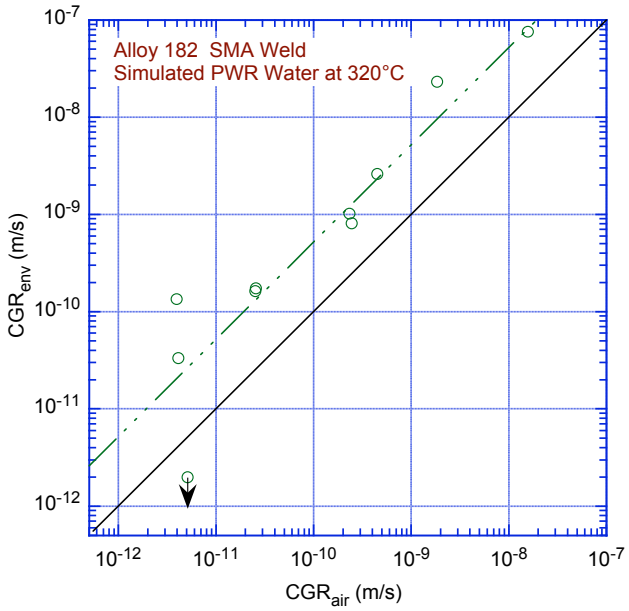

Figure 93.
CGR data for Alloy 182 SMA weld–metal specimen in simulated PWR environment at 320°C.

The experimental CGRs obtained with a trapezoidal waveform (i.e., essentially a constant load with periodic unload/reload) are compared with available CGR data for Ni–alloy welds[107–115] in Fig. 94. The CGR curve, based on the Scott model proposed in MRP–21 for Alloy 182[115] in the PWR environment at 325°C, is also plotted in the figure. The data were normalized to 325°C using the K dependency of the Scott model and an activation energy of 130 kJ/mole. The growth rate for the ANL weld is close to the average behavior for Alloy 600. Most of the existing data for Alloy 182 and 82 welds are between the Alloy 600 average curve and a factor of 10 above this curve.

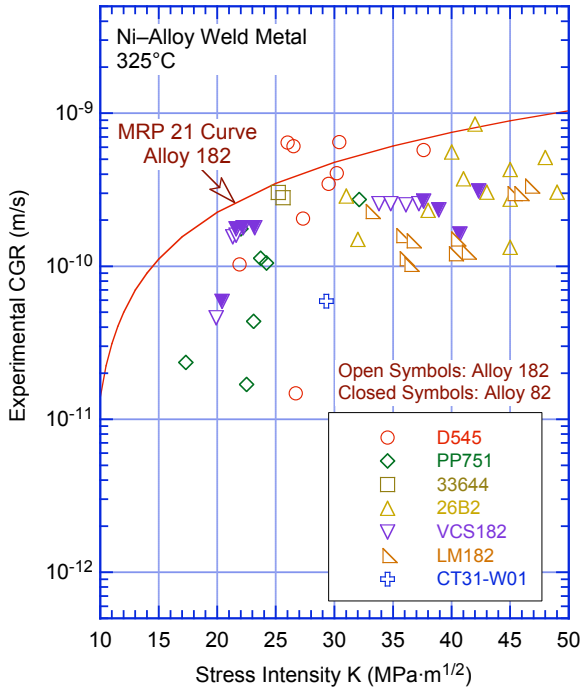

Figure 94.
Comparison of the SCC growth rate for the Argonne Alloy 182 weld with the available data for Alloy 182 and 82 welds in simulated PWR environment. All results normalized to 325°C using an activation energy of 130 kJ/mole.
Data from Refs. 107–115.

6 Summary

6.1 Environmental Effects on Fatigue ε–N Behavior

Fatigue tests have been conducted on two heats of Type 304 SS under various material conditions to determine the effect of heat treatment on fatigue crack initiation in these steels in air and LWR environments. A detailed metallographic examination of fatigue test specimens was performed, with special attention to crack morphology at the sites of initiation, the fracture surface, and the occurrence of striations.

The results indicate that heat treatment has little or no effect on the fatigue life of Type 304 SS in air and low–DO PWR environments. In a high–DO BWR environment, fatigue life is lower for sensitized SSs; life continues to decrease as the degree of sensitization is increased. The cyclic strain–hardening behavior of Type 304 SS under various heat treatment conditions is identical; only the fatigue life varies in different environments.

In air, irrespective of the degree of sensitization, the fracture mode for crack initiation (crack lengths up to ≈200 μm) and crack propagation (crack lengths >200 μm) is transgranular (TG), most likely along crystallographic planes, leaving behind relatively smooth facets. With increasing degree of sensitization, cleavage–like or stepped TG fracture, and occasionally ridge structures on the smooth surfaces were observed. In the BWR environment, the initial crack appeared intergranular (IG) for all heat–treatment conditions, implying a weakening of the grain boundaries. For all four conditions tested, the initial IG mode transformed within 200 μm into a TG mode with cleavage–like features. It appears, however, that the size of the IG portion of the crack surface increased with the degree of sensitization. By contrast, for all of the samples tested in PWR environments, the cracks initiated and propagated in a TG mode irrespective of the degree of sensitization. Prominent features of all fracture surfaces in the PWR case were highly angular, cleavage–like fracture facets that exhibited well–defined "river" patterns. Intergranular facets were rarely observed, but those that were found were mostly in the more heavily sensitized alloys.

Fatigue striations normal to the crack advance direction were clearly visible beyond ≈200 μm on the fracture surfaces for all material and environmental conditions. Striations were found on both the TG and IG facets of the samples tested in BWR conditions, or co-existing with the "river" patterns specific to the samples tested in the PWR environment. Evidence of extensive rubbing due to repeated contact between the two mating surfaces was also found.

The orientation of the cracks as they initiated at the specimen surface was also a function of the test environment. For air tests, cracks initiated obliquely, approaching 45°, with respect to the tensile axis. By contrast, for tests in either the BWR or PWR environment cracks tended to initiate perpendicular to the tensile axis. In all environments, the overall orientation of the crack became perpendicular to the tensile axis as the crack grew beyond the initiation stage.

6.2 Irradiation–Assisted Stress Corrosion Cracking of Austenitic Stainless Steel in BWRs

Slow-strain-rate tensile tests were conducted in high-purity 289°C water on steels irradiated to ≈0.43, 1.3, and 3.0 dpa in helium in the Halden Reactor. The bulk S content provided the best and the only good correlation with the susceptibility to IG SCC in 289°C water. Good resistance to IASCC was

observed in Type 304 and 316 steels that contain very low concentrations of S of ≈0.002 wt.% or less. The IASCC susceptibility of Type 304, 304L, 316, and 316L steels that contain >0.003 wt.% S increased drastically. Steels containing ≥0.008 wt.% were very susceptible at high fluence. These observations indicate that the deleterious effect of S plays a dominant role in the failure of core internal components at high fluence.

In contrast to Type 304 and 316 SSs, a low concentration of S of ≈0.001-0.002 wt.% does not necessarily render low-C Type 304L and 316L, or high-purity-grade steel resistant to IASCC. This finding indicates that a high concentration of C is beneficial in reducing the deleterious effect of S, and that the threshold S concentration to ensure good IASCC resistance is lower in a low-C steel than in a high-C steel.

A comparison of the results with data available in the literature is presented. The IASCC–resistant or –susceptible behavior of austenitic SSs in BWR-like oxidizing environment is represented in terms of a two–dimensional map of bulk S and C contents of the steels. To investigate the importance of the roles of S and C on IASCC, evidence of grain-boundary segregation was characterized by Auger electron spectroscopy on BWR neutron absorber tubes fabricated from two heats of Type 304 SS.

Crack growth tests have been performed in simulated BWR environments at ≈289°C on austenitic SS base metal and weld HAZ specimens irradiated up to 2.0×10^{21} n/cm^2 (3 dpa) at ≈288°C in a helium environment. The tests were conducted under cyclic loading with a slow/fast sawtooth waveform and long rise times or a trapezoidal waveform. The CGR data were obtained on Type 304L SS (Heat C3) irradiated to 0.3×10^{21} n/cm^2, nonirradiated Type 304L SS weld HAZ from the GG reactor core shroud, and a Type 304 SS SS laboratory–prepared weld.

Type 304L irradiated to 0.3×10^{21} n/cm^2 showed very little enhancement of CGRs in high–DO water. Under cyclic loading, the CGRs may be represented by the Shack/Kassner model for nonirradiated austenitic SSs in high–purity water with 0.2 ppm DO. Under constant load, the CGRs were below the NUREG–0313 disposition curve for sensitized SSs in water with 8 ppm DO.

The results for the weld HAZ material indicate that under loading conditions that resulted in predominantly mechanical fatigue (i.e., no environmental enhancement), experimental CGRs for the GG Type 304L weld HAZ are lower than those for the Type 304 SMA weld HAZ. The CGRs for Type 304 weld HAZ are consistent, and those for the GG weld HAZ are a factor of ≈2 lower than those predicted for austenitic SSs in air. In the high–DO BWR environment (i.e., with environmental enhancement), the cyclic CGRs of Type 304 SS SMA weld HAZ are comparable to those of the GG Type 304L SA weld HAZ. For either the GG or the laboratory–prepared weld HAZ, the growth rates of the thermally treated condition are marginally higher than those of the as–welded condition.

Under constant load, the CGRs of as–welded and as–welded plus thermally treated GG weld HAZ are comparable. For both conditions, the CGRs are a factor of ≈2 lower than the NUREG–0313 curve for sensitized SSs in water with 8 ppm DO. For the thermally treated condition, the CGR of the Type 304 SS weld HAZ is a factor of ≈10 higher than that for the Type 304L weld HAZ.

6.3 Irradiation–Assisted Cracking of Austenitic Stainless Steel in PWRs

A comprehensive irradiation experiment in the BOR-60 Reactor is underway to obtain a large number of tensile and disk specimens irradiated to 5, 10, and 40 dpa under PWR-like conditions at ≈325°C. Irradiation to ≈5 and ≈10 dpa has been completed. The specimens have been transported to

Westinghouse hot cell trough Studsvik. Westinghouse is performing the work to separate and repackage ANL specimens from the CIR and industry specimens. The ANL specimens are expected in August 2004.

Tests performed on the materials irradiated in the Halden BWR reactor may, however, give some insight into potential mechanisms for IASCC that is also relevant to PWRs. After exposure to the conditions of the SSRT test in BWR water, susceptibility to intergranular cracking in an inert environment was determined by rapid bending in air at 23°C. Similar tests were also performed on hydrogen-charged specimens in vacuum. Both types of bend fracture exhibited similar characteristics, suggesting that in both cases hydrogen-induced intergranular failure occurred. However, steels that showed high susceptibility to IGSCC in 289°C water exhibited low susceptibility to intergranular cracking in the tests at 23°C air or vacuum, and vice versa. This finding indicates that although intergranular cracking in 23°C is dominated by H-induced embrittlement of ordinary grain boundaries, other processes control IASCC in 289°C water.

On the basis of this investigation, and studies on binary Ni–S and crack-tip microstructural characteristics of LWR core internal components reported in the literature, an initial IASCC model based on a crack-tip grain-boundary process that involves S has been proposed. In this model, several factors play key roles: grain-boundary segregation of Ni and S, formation of grain-boundary oxide in front of crack tip, formation of Ni– and S–rich thin films, formation of islands between the oxide and metal matrix, and disorder–induced melting or amorphization of the Ni–S thin films and islands at sufficiently high concentration of S.

6.4 Cracking of Nickel Alloys and Welds

The resistance of Ni alloys to EAC in simulated LWR environments is being evaluated. Crack growth tests are being conducted to establish the effects of alloy chemistry, material heat treatment, cold work, temperature, load ratio R, stress intensity K, and DO level on the CGRs of Ni alloys. During this reporting period, CGR tests in simulated PWR environments at 320°C were completed on Alloy 600 from the round robin and Alloy 182 SMA weld metal. The results were compared with the existing CGR data for Ni–alloy welds to determine the relative susceptibility of the specific Ni–alloy weld to environmentally enhanced cracking under a variety of loading conditions. Detailed metallographic examinations to characterize the microstructure of the weld metal are presented.

A CGR test was conducted on a specimen of Alloy 182 SMA weld in TS orientation in simulated PWR water at 320°C. The experimental CGRs obtained under cyclic loading were found to be approximately a factor of 5 higher than for Alloy 600 under the same loading conditions; however, for this Alloy 182 weld metal, little or no environmental enhancement in PWR environment occured. The experimental CGRs obtained with a trapezoidal waveform (essentially a constant load with periodic unload/reload) were compared with the available CGR data from the literature and with the CGR curve based on the Scott model, proposed in PWRMRP–21 for Alloy 182. The growth rate for the specimen tested at ANL agreed well with the available data for welds and was found to be close to the average behavior of Alloy 600. The CGR test was complemented by an extensive examination of the fracture surface conducted with the objective of correlating the test parameters to the resultant fracture modes. The analysis has found that cracking initiated in a TG mode and transitioned to an IG mode during long rise time testing. This testing approach also resulted in an uniform, straight crack front. Another potentially important observation was that the fracture mode was affected by grain orientation. Specifically, IG cracking began more readily along grains having the dendrites parallel to the crack front than on grains having the dendrites perpendicular to the crack front. This orientation-dependent crack

growth was also the cause of the unbroken ligaments left behind, which in turn, caused the DC potential technique to underestimate the crack length.

A CGR test was conducted on an Alloy 600 round–robin specimen in the simulated PWR environment at 320°C according to the testing protocol agreed upon by the CIR group. The resultant CGR data under cyclic loading indicate that for high growth rates, the rates measured for the round robin specimen are a factor of ≈2 lower than those predicted in air. The difference, most likely, is due to the material condition; the round robin specimen was 30% cold worked, whereas the material tested air was annealed. For low growth rates, the measured CGR was higher than predicted. Surface examination revealed that the fracture mode was TG near the machine notch, followed by a transition region of highly angular, cleavage–like facets with "river" patterns, which changed to completely IG fracture for the remainder of the test. Also, the crack front was U-shaped, indicating that the crack growth rates were significantly higher near the edge of the specimen than the center. This last observation is consistent with that made by other round-robin participants from France and Switzerland, and suggests that the distribution of cold work was not uniform across the specimen thickness.

During the reporting period, an OIM analysis of the weld microstructure was also initiated. These initial results indicate that weld alloys contain relatively high proportions of cracking-susceptible random boundaries. In addition, OIM imaging revealed that the weld microstructure consists of clusters of grains sharing similar orientations. The implication of this finding is that weld alloys may contain a class of random boundaries that are be more resistant to cracking when separating grains of similar than different orientations.

References

1. Langer, B. F., "Design of Pressure Vessels for Low–Cycle Fatigue," ASME J. Basic Eng. 84, 389–402 (1962).

2. Criteria of Section III of the ASME Boiler and Pressure Vessel Code for Nuclear Vessels, The American Society of Mechanical Engineers, New York (1964).

3. Chopra, O. K., and W. J. Shack, "Effects of LWR Coolant Environments on Fatigue Design Curves of Carbon and Low–Alloy Steels," NUREG/CR–6583, ANL–97/18 (March 1998).

4. Chopra, O. K., and W. J. Shack, "Environmental Effects on Fatigue Crack Initiation in Piping and Pressure Vessel Steels," NUREG/CR–6717, ANL–00/27 (May 2001).

5. Chopra, O. K., and W. J. Shack, "Review of the Margins for ASME Code Design Curves – Effects of Surface Roughness and Material Variability," NUREG/CR–6815, ANL–02/39 (Sept. 2003).

6. Chopra, O. K., "Effects of LWR Coolant Environments on Fatigue Design Curves of Austenitic Stainless Steels," NUREG/CR–5704, ANL–98/31 (1999).

7. Chopra, O. K., "Mechanisms and Estimation of Fatigue Crack Initiation in Austenitic Stainless Steels in LWR Environments," NUREG/CR–6787, ANL–01/25 (Aug. 2002).

8. Park, J. Y., and W. J. Shack, "Intergranular Crack Propagation Rates in Sensitized Type 304 Stainless Steel in an Oxygenated Water Environment," ANL–83–93 (Dec. 1983).

9. Ruther, W. E., W. K. Soppet, and T. F. Kassner, "Evaluation of Environmental Corrective Actions," Materials Science and Technology Division Light–Water–Reactor Safety Research Program: Quarterly Progress Report, October–December 1983, NUREG/CR–3689 Vol. IV, ANL–83–85 Vol. IV, pp. 51–57 (Aug. 1984).

10. Kanasaki, H., R. Umehara, H. Mizuta, and T. Suyama, "Fatigue Lives of Stainless Steels in PWR Primary Water," Trans. 14th Intl. Conf. on Structural Mechanics in Reactor Technology (SMiRT 14), Lyon, France, pp. 473–483 (1997).

11. Tsutsumi, K., H. Kanasaki, T. Umakoshi, T. Nakamura, S. Urata, H. Mizuta, and S. Nomoto, "Fatigue Life Reduction in PWR Water Environment for Stainless Steels," in Assessment Methodologies for Preventing Failure: Service Experience and Environmental Considerations, PVP Vol. 410-2, R. Mohan, ed., American Society of Mechanical Engineers, New York, pp. 23–34, (2000).

12. Fujiwara, M., T. Endo, and H. Kanasaki, "Strain Rate Effects on the Low–Cycle Fatigue Strength of 304 Stainless Steel in High–Temperature Water Environment; Fatigue Life: Analysis and Prediction," in Proc. Intl. Conf. and Exposition on Fatigue, Corrosion Cracking, Fracture Mechanics, and Failure Analysis, ASM, Metals Park, OH, pp. 309–313 (1986).

13. Higuchi, M., and K. Iida, “Reduction in Low–Cycle Fatigue Life of Austenitic Stainless Steels in High–Temperature Water,” Pressure Vessel and Piping Codes and Standards, PVP Vol. 353, D. P. Jones, B. R. Newton, W. J. O'Donnell, R. Vecchio, G. A. Antaki, D. Bhavani, N. G. Cofie, and G. L. Hollinger, eds., American Society of Mechanical Engineers, New York, pp. 79–86 (1997).

14. Indig, M. E., J. L. Nelson, and G. P. Wozadlo, "Investigation of Protection Potential against IASCC," Proc. 5th Intl. Symp. on Environmental Degradation of Materials in Nuclear Power Systems – Water Reactors, D. Cubicciotti, E. P. Simonen, and R. Gold, eds., American Nuclear Society, LaGrange Park, IL, pp. 941-947 (1992).

15. Kanasaki, H., T. Okubo, I. Satoh, M. Koyama, T. R. Mager, and R. G. Lott, "Fatigue and Stress Corrosion Cracking Behavior of Irradiated Stainless Steels in PWR Primary Water," Proc. 5th Intl. Conf. on Nuclear Engineering, March 26-30, 1997, Nice, France.

16. Kasahara, S., K. Nakata, K. Fukuya, S. Shima, A. J. Jacobs, G. P. Wozadlo, and S. Suzuki, "The Effects of Minor Elements on IASCC Susceptibility in Austenitic Stainless Steels Irradiated with Neutrons," Proc. 6th Intl. Symp. on Environmental Degradation of Materials in Nuclear Power Systems - Water Reactors, R. E. Gold and E. P. Simonen, eds., The Minerals, Metals, and Materials Society, Warrendale, PA, pp. 615-623 (1993).

17. Kodama, M., S. Nishimura, J. Morisawa, S. Shima, S. Suzuki, and M. Yamamoto, "Effects of Fluence and Dissolved Oxygen on IASCC in Austenitic Stainless Steels," Proc. 5th Intl. Symp. on Environmental Degradation of Materials in Nuclear Power Systems – Water Reactors, D. Cubicciotti, E. P. Simonen, and R. Gold, eds., American Nuclear Society, LaGrange Park, IL, pp. 948-954 (1992).

18. Chung, H. M., W. E. Ruther, J. E. Sanecki, A. G. Hins, and T. F. Kassner, "Effects of Water Chemistry on Intergranular Cracking of Irradiated Austenitic Stainless Steels," Proc. 7th Intl. Symp. on Environmental Degradation of Materials in Nuclear Power Systems - Water Reactors, G. Airey et al., eds., NACE International, Houston, pp. 1133-1143 (1995).

19. Jacobs, A. J., G. P. Wozadlo, K. Nakata, T. Yoshida, and I. Masaoka, "Radiation Effects on the Stress Corrosion and Other Selected Properties of Type-304 and Type-316 Stainless Steels," Proc. 3rd Intl. Symp. Environmental Degradation of Materials in Nuclear Power Systems – Water Reactors, G. J. Theus and J. R. Weeks, eds., The Metallurgical Society, Warrendale, PA, pp. 673-680 (1988).

20. Garzarolli, F., D. Alter, P. Dewes, and J. L. Nelson, "Deformability of Austenitic Stainless Steels and Ni–Base Alloys," Proc. 3th Intl. Symp. on Environmental Degradation of Materials in Nuclear Power Systems - Water Reactors, G. J Theus and J. R. Weeks, eds., The Metallurgical Society, Warrendale, PA, pp. 657-664 (1988).

21. Garzarolli, F., P. Dewes, R. Hahn, and J. L. Nelson, "Deformability of High-Purity Stainless Steels and Ni–Base Alloys in the Core of a PWR," Proc. 6th Intl. Symp. on Environmental Degradation of Materials in Nuclear Power Systems - Water Reactors, R. E. Gold and E. P. Simonen, eds., The Minerals, Metals, and Materials Society, Warrendale, PA, pp. 607-613 (1993).

22. Fukuya, K., K. Fuji, M. Nakano, N. Nakajima, and M. Kodama, "Stress Corrosion Cracking on Cold-Worked Stainless Steels Irradiated to High Fluence," Proc. 10th Intl. Conf. on Environmental Degradation of Materials in Nuclear Power Systems - Water Reactors, August 5-9, 2001, Lake Tahoe, Nevada, G. S. Was and J. L. Nelson, eds., NACE International CD-ROM.

23. Chung, H. M., W. E. Ruther, J. E. Sanecki, and T. F. Kassner, "Grain-Boundary Microchemistry and Intergranular Cracking of Irradiated Austenitic Stainless Steels," Proc. 6th Intl. Symp. on Environmental Degradation of Materials in Nuclear Power Systems - Water Reactors, R. E. Gold, and E. P. Simonen, eds., The Minerals, Metals, and Materials Society, Warrendale, PA, pp. 511-519 (1993).

24. Kodama, M., R. Katsura, J. Morisawa, S. Nishimura, S. Suzuki, K. Asano, K. Fukuya, and K. Nakata, "IASCC Susceptibility of Austenitic Stainless Steels Irradiated to High Neutron Fluence," Proc. 6th Intl. Symp. on Environmental Degradation of Materials in Nuclear Power Systems - Water Reactors, R. E. Gold and E. P. Simonen, eds., The Minerals, Metals, and Materials Society, Warrendale, PA, pp. 583-588 (1993).

25. Fukuya, K., K. Nakata, and A. Horie, "An IASCC Study Using High Energy Ion Irradiation," Proc. 5th Intl. Symp. on Environmental Degradation of Materials in Nuclear Power Systems – Water Reactors, August 25-29, 1991, Monterey, CA, D. Cubicciotti, E. P. Simonen, and R. Gold, eds., American Nuclear Society, La Grange Park, IL, 814–820 (1992).

26. Fukuya, K., S. Shima, K. Nakata, S. Kasahara, A. J. Jacobs, G. P. Wozadlo, S. Suzuki, and M. Kitamura, "Mechanical Properties and IASCC Susceptibility in Irradiated Stainless Steels," Proc. 6th Intl. Symp. on Environmental Degradation of Materials in Nuclear Power Systems - Water Reactors, R. E. Gold, and E. P. Simonen, eds., The Minerals, Metals, and Materials Society, Warrendale, PA, pp. 565-572 (1993).

27. Chung, H. M., W. E. Ruther, J. E. Sanecki, A. G. Hins, and T. F. Kassner, "Stress Corrosion Cracking Susceptibility of Irradiated Type 304 Stainless Steels," Effects of Radiation on Materials: 16th Int. Symp., ASTM STP 1175, A. S. Kumar, D. S. Gelles, R. K. Nanstad, and T. A. Little, eds., American Society for Testing and Materials, Philadelphia, pp. 851-869 (1993).

28. Cookson, J. M., D. L. Damcott, G. S. Was, and P. L. Anderson, "The Role of Microchemical and Microstructural Effects in the IASCC of High-Purity Austenitic Stainless Steels," Proc. 6th Intl. Symp. on Environmental Degradation of Materials in Nuclear Power Systems - Water Reactors, R. E. Gold, and E. P. Simonen, eds., The Minerals, Metals, and Materials Society, Warrendale, PA, pp. 573-580 (1993).

29. Jacobs, A. J., G. P. Wozadlo, T. Okada, S. Kawano, K. Nakata, S. Kasahara, and S. Suzuki, "The Correlation of Grain Boundary Composition in Irradiated Stainless Steels with IASCC Resistance," Proc. 6th Intl. Symp. on Environmental Degradation of Materials in Nuclear Power Systems - Water Reactors, R. E. Gold and E. P. Simonen, eds., The Minerals, Metals, and Materials Society, Warrendale, PA, pp. 597-604 (1993).

30. Kodama, M., J. Morisawa, S. Nishimura, K. Asano, S. Shima, and K. Nakata, “Stress Corrosion Cracking and Intergranular Corrosion of Austenitic Stainless Steels Irradiated at 323 K,” J. Nucl. Mater., 212–215, 1509 (1994).

31. Tsukada, T., and Y. Miwa, "Stress Corrosion Cracking of Neutron Irradiated Stainless Steels," Proc. 7th Int. Symp. on Environmental Degradation of Materials in Nuclear Power Systems - Water Reactors, G. Airey et al., eds., NACE International, Houston, pp. 1009–1018 (1995).

32. Tsukada, T., Y. Miwa, H. Nakajima, and T. Kondo, "Effects of Minor Elements on IASCC of Type 316 Model Stainless Steels," Proc. 8th Int. Symp. on Environmental Degradation of Materials in Nuclear Power Systems - Water Reactors, Aug. 10-14, 1997, Amelia Island, FL, S. M. Bruemmer, ed., American Nuclear Society, La Grange Park, IL, pp. 795-802 (1997).

33. Katsura, S., Y. Ishiyama, N. Yokota, T. Kato, K. Nakata, K. Fukuya, H. Sakamoto, and K. Asano, "Post-Irradiation Annealing Effects of Austenitic SS in IASCC," Corrosion 98, NACE International, Houston, TX, Paper #0132 (1998).

34. Jenssen, A., and L. G. Ljungberg, "Irradiation-Assisted Stress Corrosion Cracking - Postirradiation CERT Tests of Stainless Steels in a BWR Test Loop," Proc. 7th Intl. Symp. on Environmental Degradation of Materials in Nuclear Power Systems - Water Reactors, G. Airey et al., eds., NACE International, Houston, pp. 1043–1052 (1995).

35. Jenssen, A., P. Efsing, K. Gott, and P.-O. Andersson, "Crack Growth Behavior of Irradiated Type 304L Stainless Steel in Simulated BWR Environment," in CD, Proc. 11th Intl. Conf. on Environmental Degradation of Materials in Nuclear Power Systems - Water Reactors, Stevenson, WA, Aug. 10-14, pp. 1015-1026 (2003).

36. Tanaka, Y., S. Suzuki, K. Fukuya, H. Sakamoto, M. Kodama, S. Nishimura, K. Nakata, and T. Kato, "IASCC Susceptibility of Type 304, 304L, and 316 Stainless Steels," Proc. 8th Int. Symp. on Environmental Degradation of Materials in Nuclear Power Systems - Water Reactors, S. M. Bruemmer, ed., American Nuclear Society, LaGrange Park, IL, pp. 803-811 (1997).

37. Busby, J. T., and G. S. Was, "Irradiation-Assisted Stress Corrosion Cracking in Model Austenitic Alloys with Solute Additions," in CD-ROM Proc. 11th Intl. Conf. on Environmental Degradation of Materials in Nuclear Power Systems - Water Reactors, Stevenson, WA, Aug. 10-14, pp. 995-1014 (2003).

38. Karlsen, T. M., and E. Hauso, "Qualification and Application of Instrumented Specimens for In-Core Studies on Cracking Behavior of Austenitic Stainless Steels," Proc. 9th Intl. Symp. on Environmental Degradation of Materials in Nuclear Power Systems - Water Reactors, August 1-5, 1999, Newport Beach, CA, S. Bruemmer, P. Ford, and G. Was, eds., The Metallurgical Society, Warrendale, PA, pp. 951-961 (1999).

39. Garzarolli, F., P. Dewes, R. Hahn, and J. L. Nelson, "In-Reactor Testing of IASCC Resistant Stainless Steels," Proc. 7th Intl. Symp. on Environmental Degradation of Materials in Nuclear Power Systems - Water Reactors, G. Airey et al., eds., NACE International, Houston, pp. 1055–1065 (1995).

40. Chung, H. M., W. E. Ruther, J. E. Sanecki, A. G. Hins, N. J. Zaluzec, and T. F. Kassner, "Irradiation–Assisted Stress Corrosion Cracking of Austenitic Stainless Steels: Recent Progress and New Approaches," J. Nucl. Mater. 239, 61 (1996).

41. Chung, H. M., R. V. Strain, and W. J. Shack, "Irradiation-Assisted Stress Corrosion Cracking of Model Austenitic Stainless Steel Alloys," in CD-ROM, Proc. 10th Intl. Conf. on Environmental Degradation of Materials in Nuclear Power Systems - Water Reactors, Lake Tahoe, NV (Aug. 2001).

42. Chung, H. M., R. V. Strain, and R. W. Clark, "Irradiation-Assisted Stress Corrosion Cracking of Austenitic Stainless Steel in BWRs," Environmentally Assisted Cracking in Light Water Reactors, NUREG/CR-4667, Vol. 32, ANL-02/33, Annual Report, Argonne National Laboratory, pp. 19-28 (June 2003).

43. Chung, H. M., R. V. Strain, and R. W. Clark, "Irradiation-Assisted Stress Corrosion Cracking of Austenitic Stainless Steel in BWRs," in Environmentally Assisted Cracking in Light Water Reactors, NUREG/CR-4667, Vol. 33, ANL-03/36, Annual Report, Argonne National Laboratory, pp. 21-33 (2005).

44. Shen, A.-T., and C. S. Chang, "IASCC Behavior of 304L Stainless Steel," in CD-ROM Proc. 11th Intl. Conf. on Environmental Degradation of Materials in Nuclear Power Systems - Water Reactors, Stevenson, WA, Aug. 10-14, pp. 986-994 (2003).

45. Thomas, L. and S. Bruemmer, "Analytical Transmission Microscopy (ATEM) Characterization of Stress Corrosion Cracks in LWR–Irradiated Austenitic Stainless Steel Components," EPRI–1003422, Electric Power Research Institute, Palo Alto, CA (May 2002).

46. Thomas, L. and S. Bruemmer, "Analytical Transmission Microscopy (ATEM) Characterization of Stress Corrosion Cracks in LWR–Irradiated Austenitic Stainless Steel Components," in CD–ROM Proc. 11th Intl. Conf. on Environmental Degradation of Materials in Nuclear Power Systems – Water Reactors, Stevenson, WA, Aug. 10–14, pp. 1049–1061 (2003).

47. Jacobs, A. J., R. E. Clausing, M. K. Miller, and C. Shepherd, "Influence of Grain Boundary Composition on the IASCC Susceptibility of Type 348 Stainless Steel," Proc. 4th Intl. Conf. on Environmental Degradation of Materials in Nuclear Power Systems – Water Reactors, Stevenson, WA, pp. 14–21 to 14–44.

48. Andresen, P. L., and C. L. Briant, "The Role of S, P, and N Segregation in Intergranular Environmental Cracking of Stainless Steels in High-Temperature Water," Proc. 3rd Intl. Symp. Environmental Degradation of Materials in Nuclear Power Systems – Water Reactors, G. J. Theus and J. R. Weeks, eds., The Metallurgical Society, Warrendale, PA, pp. 371-381 (1988).

49. Dumbill, S., "Examination of Stress Corrosion Crack Tip Microstructures in Stainless Steel," SKI Report 01:35, Swedish Nuclear Power Inspectorate (Sept. 2001).

50. Heuer, J. K., P. R. Okamoto, N. Q. Lam, and J. F. Stubbins, "Disorder–Induced Melting in Nickel: Implication to Intergranular Sulfur Embrittlement," J. Nucl. Mater., 301, 129–141 (2002).

51. Bruemmer, S. M., et al., "Critical Issue Reviews for the Understanding and Evaluation of Irradiation–Assisted Stress Corrosion Cracking," EPRI TR–107159, Electric Power Research Institute, Palo Alto, CA (1996).

52. Herrera, M. L., et al., "Evaluation of the Effects of Irradiation on the Fracture Toughness of BWR Internal Components," Proc. ASME/JSME 4th Intl. Conf. on Nucl. Eng. (ICONE–4) Vol. 5, A. S. Rao, R. M. Duffey, and D. Elias, eds., American Society of Mechanical Engineers, New York, pp. 245–251 (1996).

53. Mills, W. J., "Fracture Toughness of Type 304 and 316 Stainless Steels and their Welds," Intl. Mater. Rev. 42, 45–82 (1997).

54. Kanasaki, H., I. Satoh, M. Koyama, T. Okubo, T. R. Mager, and R. G. Lott, "Fatigue and Stress Corrosion Cracking Behaviors of Irradiated Stainless Steels in PWR Primary Water," Proc. 5th Intl. Conf. on Nuclear Engineering, ICONE5-2372, pp. 1–7 (1997).

55. Andresen, P. L., F. P. Ford, S. M. Murphy, and J. M. Perks, "State of Knowledge of Radiation Effects on Environmental Cracking in Light Water Reactor Core Materials," Proc. 4th Intl. Symp. on Environmental Degradation of Materials in Nuclear Power Systems – Water Reactors, NACE, pp. 1.83–1.121 (1990).

56. Jenssen, A., and L. G. Ljungberg, "Irradiation Assisted Stress Corrosion Cracking of Stainless Alloys in BWR Normal Water Chemistry and Hydrogen Water Chemistry," Proc. Sixth Intl. Symp. on Environmental Degradation of Materials in Nuclear Power Systems – Water Reactor, R. E. Gold and E. P. Simonen, eds., Minerals, Metals & Materials Society, pp. 547–553 (1993).

57. Brown, K. S., and G. M. Gordon, "Effects of BWR Coolant Chemistry on the Propensity for IGSCC Initiation and Growth in Creviced Reactor Internals Components," Proc. Third Intl. Symp. on Environmental Degradation of Materials in Nuclear Power Systems – Water Reactor, AIME, pp. 243–248 (1987).

58. Gordon, G. M., and K. S. Brown, "Dependence of Creviced BWR Component IGSCC Behavior on Coolant Chemistry," Proc. 4th Intl. Symp. on Environmental Degradation of Materials in Nuclear Power Systems – Water Reactor, Daniel Cubicciotti, ed., NACE, pp. 14.46–14.61 (1990).

59. Garzarolli, F., D. Alter, and P. Dewes, "Deformability of Austenitic Stainless Steels and Nickel–Base Alloys in the Core of a Boiling and a Pressurized Water Reactor," Proc. Intl. Symp. on Environmental Degradation of Materials in Nuclear Power Systems – Water Reactor, ANS, pp. 131–138 (1986).

60. Kodama, M., et al., "IASCC Susceptibility of Austenitic Stainless Steels Irradiated to High Neutron Fluence," Proc. Sixth Intl. Symp. on Environmental Degradation of Materials in Nuclear Power Systems – Water Reactor, R. E. Gold and E. P. Simonen, eds., Minerals, Metals & Materials Society, pp. 583–588 (1993).

61. Kodama, M., et al., "Effects of Fluence and Dissolved Oxygen on IASCC in Austenitic Stainless Steels," Proc. Fifth Intl. Symp. on Environmental Degradation of Materials in Nuclear Power Systems – Water Reactor, American Nuclear Society, pp. 948–954 (1991).

62. Clark, W. L., and A. J. Jacobs, "Effect of Radiation Environment on SCC of Austenitic Materials," Proc. First Intl. Symp. on Environmental Degradation of Materials in Nuclear Power Systems – Water Reactor, NACE, p. 451 (1983).

63. Andresen, P. L., and F. P. Ford, "Irradiation Assisted Stress Corrosion Cracking: From Modeling and Prediction of Laboratory & In–Core Response to Component Life Prediction," Corrosion/95, Paper No. 419, NACE, Houston TX (1995).

64. Jenssen, A., and L. G. Ljungberg, "Irradiation Assisted Stress Corrosion Cracking of Stainless Alloys in BWR Normal Water Chemistry and Hydrogen Water Chemistry," Proc. Sixth Intl. Symp. on Environmental Degradation of Materials in Nuclear Power Systems – Water Reactor, R. E. Gold and E. P. Simonen, eds., Minerals, Metals & Materials Society, pp. 547–553 (1993).

65. Jenssen, A., and L. G. Ljungberg, "Irradiation Assisted Stress Corrosion Cracking: Post Irradiation CERT Tests of Stainless Steels in a BWR Test Loop," Proc. Seventh Intl. Symp. on Environmental Degradation of Materials in Nuclear Power Systems – Water Reactor, G. Airey et al., eds., NACE, pp. 1043–1052 (1995).

66. Gruber, E. E., and O. K. Chopra, "Crack Growth Rate Test of Austenitic Stainless Steels Irradiated in the Halden Reactor," Environmentally Assisted Cracking in Light Water Reactors, Annual Report, January–December 2002, NUREG/CR–4667 Vol. 33, ANL–03/36, pp. 34-43 (2004).

67. Hazelton, W. S., and W. H. Koo, "Technical Report on Material Selection and Processing Guidelines for BWR Coolant Pressure Boundary Piping, Final Report," NUREG–0313, Rev. 2 (1988).

68. Gruber, E. E., and O. K. Chopra, "Fracture Toughness J," Environmentally Assisted Cracking in Light Water Reactors, Annual Report, January–December 2002, NUREG/CR–4667 Vol. 33, ANL–03/36, pp. 34-43, 2004.

69. James, L. A., and D. P. Jones, "Fatigue Crack Growth Correlation for Austenitic Stainless Steels in Air," Proc. Conf. on Predictive Capabilities in Environmentally–Assisted Cracking, PVP Vol. 99, R. Rungta, ed., American Society of Mechanical Engineers, New York, pp. 363–414 (1985).

70. Shack, W. J., and T. F. Kassner, "Review of Environmental Effects on Fatigue Crack Growth of Austenitic Stainless Steels," NUREG/CR–6176, ANL–94/1 (May 1994).

71. Andresen, P. L., "Similarity of Cold Work and Radiation Hardening in Enhancing Yield Strength and SCC Growth of Stainless Steel in Hot Water," Corrosion/02, Paper 02509, NACE (2002).

72. Andresen, P. L., T. M. Angeliu, W. R. Catlin, L. M. Young, and R. M. Horn, "Effect of Deformation on SCC of Unsensitized Stainless Steel," Corrosion/2000, Paper 00203, NACE (2000).

73. Angeliu, T. M., P. L. Andresen, E. Hall, J. A. Sutliff, and S. Sitzman, "Strain and Microstructure Characterization of Austenitic Stainless Steel Weld HAZs," Corrosion/2000, Paper 00186, NACE (2000).

74. Andresen, P. L., T. M. Angeliu, L. M. Young, W. R. Catlin, and R. M. Horn, "Mechanism and Kinetics of SCC in Stainless Steels," Proc. Tenth Intl. Symp. on Environmental Degradation of Materials in Nuclear Power Systems – Water Reactor, NACE (2001).

75. Shogan, R. P., and T. R. Mager, "Susceptibility of Type 316 Stainless Steel to Irradiated–Assisted Stress Corrosion Cracking in a PWR Environment," Proc. 10th Intl. Conf. on Environmental Degradation of Materials in Nuclear Power Systems - Water Reactors, G. S. Was and J. L. Nelson, eds., August 5-9, 2001, Lake Tahoe, Nevada, NACE International CD-ROM.

76. Ehrnsten, U., et al., "Intergranular Cracking of an Irradiated Ti-stabilized Austenitic Stainless Steel Spacer Grid Sleeve from a VVER-440 Reactor," Proc. Ninth Intl. Symp. on Environmental Degradation of Materials in Nuclear Power Systems - Water Reactors, Newport Beach, CA, S. Bruemmer, P. Ford, and G. Was, eds., The Metallurgical Society, Warrendale, PA, pp. 941-950 (1999).

77. Scott, P., "An Analysis of Primary Water Stress Corrosion Cracking in PWR Steam Generators," Proc. of the Specialists Meeting on Operating Experience with Steam Generators, Brussels, Belgium, pp. 5–6 (1991).

78. Cattant, F., "Lessons Learnt from the Examination of Tubes Pulled from Electricite de France Steam Generators," Nucl. Eng. Des. 168, 241–253 (1997).

79. Diercks, D. R., W. J. Shack, and J. Muscara, "Overview of Steam Generator Tube Degradation and Integrity Issues," Nucl. Eng. Des. 194, 19–30 (1999).

80. USNRC Information Notice No. 90–10, "Primary Water Stress Corrosion Cracking (PWSCC) of Inconel 600," Feb. 1990.

81. USNRC Generic Letter 97-01, "Degradation of Control Rod Drive Mechanism and Other Vessel Closure Head Penetrations," April 1, 1997.

82. Economou, J., A. Assice, F. Cattant, J. Salin, and M. Stindel, "NDE and Metallurgical Examination of Vessel Head Penetrations," 3rd Intl. Symp. of Fontevraud, Sept. 12–16, 1994.

83. Robinson, M. R., Duke Power Company, "Oconee Unit 1 and Unit 3 Reactor Vessel Head Leakage, Cracking of RV Head Penetrations due to Primary Water Stress Corrosion Cracking," presented at the NRC Meeting with the NEI EPRI Material Reliability Program Regarding CRDM Nozzle Crackling Issues, Rockville, MD, April 12, 2001.

84. Frye, C. R., T. Alley, M. L. Arey, Jr., and M. R. Robinson, "Cracking in Alloy 600/182 Reactor Vessel Head Penetrations," PVP–Vol. 437, Service Experience and Failure Assessment Applications ASME 2002, P. S. Lam, ed., American Society of Mechanical Engineers, New York, pp. 171–178 (2002).

85. USNRC Information Notice 2001–05, "Through–Wall Circumferential Cracking of Reactor Pressure Vessel Head Control Rod Driver Mechanism Penetration Nozzle at Oconee Nuclear Station, Unit 3," April 30, 2001.

86. USNRC Bulletin 2001–01, "Circumferential Cracking of Reactor Pressure Vessel Head Penetration Nozzles," Aug. 3, 2001.

87. USNRC Information Notice 2000–17, "Crack in Weld Area of Reactor Coolant System Hot Leg Piping at V. C. Summer," Oct. 18, 2000; Suppl. 1, Nov. 16, 2000; Suppl. 2, Feb. 28, 2001.

88. Jenssen, A., K. Norrgard, J. Lagerstrom, G. Embring, and D. Tice, "Assessment of Cracking in Dissimilar Metal Welds," Proc. of the Tenth Intl. Conf. on Environmental Degradation of Materials in Nuclear Power Systems-Water Reactors, NACE International, Houston, TX (2001).

89. Bennetch, J. I., G. E. Modzelewski, L. L. Spain, and G. V. Rao, "Root Cause Evaluation and Repair of Alloy 82/182 J–Groove Weld Cracking of Reactor Vessel Head Penetrations at North Anna Unit 2," PVP–Vol. 437, Service Experience and Failure Assessment Applications ASME 2002, P. S. Lam, ed., American Society of Mechanical Engineers, New York, pp. 179–185 (2002).

90. USNRC Information Notice 2002–11, "Recent Experience with Degradation of Reactor Pressure Vessel Head," March 12, 2002.

91. USNRC Information Notice 2003–11, "Leakage Found on Bottom–Mounted Instrumentation Nozzles," Aug. 13, 2003; Suppl. 1, Jan. 8, 2004.

92. USNRC Bulletin 2003–02, "Leakage from Reactor Pressure Vessel Lower Head Penetrations and Reactor Coolant Pressure Boundary Integrity," Aug. 21, 2003.

93. Ruther, W. E., W. K. Soppet, and T. F. Kassner, "Corrosion Fatigue of Alloys 600 and 690 in Simulated LWR Environments," NUREG/CR–6383, ANL–95/37 (April 1996).

94. Ruther, W. E., W. K. Soppet, and T. F. Kassner, "Environmentally Assisted Cracking of Alloys 600 and 690 in Simulated LWR Water," in Environmentally Assisted Cracking in Light Water Reactors, Semiannual Report, July 1997–December 1997, NUREG/CR–4667, Vol. 25, ANL–98/18, pp. 42–75 (Sept. 1998).

95. Ruther, W. E., W. K. Soppet, T. F. Kassner, and W. J. Shack, "Environmentally Assisted Cracking of Alloys 600 and 690 in Simulated LWR Water," in Environmentally Assisted Cracking in Light Water Reactors, Semiannual Report, January 1998–July 1998, NUREG/CR–4667, Vol. 26, ANL–98/18, pp. 25–32 (March 1999).

96. Ruther, W. E., W. K. Soppet, T. F. Kassner, and W. J. Shack, "Environmentally Assisted Cracking of Alloys 600 and 690 in Simulated LWR Water," in Environmentally Assisted Cracking in Light Water Reactors, Semiannual Report, July 1998–December 1998, NUREG/CR–4667, Vol. 27, ANL–99/11, pp. 45-54 (October 1999).

97. Soppet, W. K., O. K. Chopra, and W. J. Shack, "Environmentally Assisted Cracking of Alloys 600 and 690 in Simulated LWR Water," in Environmentally Assisted Cracking in Light Water Reactors, Semiannual Report, July 1999–December 1999, NUREG/CR–4667, Vol. 29, ANL–00/23, pp. 39-45 (November 2000).

98. Chopra, O. K., W. K. Soppet, and W. J. Shack, "Effects of Alloy Chemistry, Cold Work, and Water Chemistry on Corrosion Fatigue and Stress Corrosion Cracking of Nickel Alloys and Welds," NUREG/CR–6721, ANL–01/07 (April 2001).

99. Cassagne, T. B., and A. Gelpi, "Crack Growth Rate Measurements on Alloy 600 Steam Generator Tubes in Steam and Primary Water," Proc. of the Fifth Intl. Symp. on Environmental Degradation of Materials in Nuclear Power Systems-Water Reactors, American Nuclear Society, La Grange Park, IL, pp. 518–524 (1991).

100. Foster, J. P., W. H. Bamford, and R. S. Pathania, "Initial Results of Alloy 600 Crack Growth Rate Testing in a PWR Environment," Proc. of the Seventh Intl. Symp. on Environmental Degradation of Materials in Nuclear Power Systems-Water Reactors, NACE International, Houston, TX, pp. 25–39 (1995).

101. Magdowski, R., F. Vaillant, C. Amzallag, and M. O. Speidel, "Stress Corrosion Crack Growth Rates of Alloy 600 in Simulated PWR Coolant," Proc. of the 8th Intl. Symp. on Environmental Degradation of Materials in Nuclear Power Systems-Water Reactors, S. M. Bruemmer, ed., American Nuclear Society, La Grange Park, IL, pp. 333–338 (1997).

102. Le Hong, S., C. Amzallag, and A. Gelpi, "Modeling of Stress Corrosion Crack Initiation on Alloy 600 in Primary Water of PWRs," Proc. of the Ninth Intl. Symp. on Environmental Degradation of Materials in Nuclear Power Systems-Water Reactors, F. P. Ford, S. M. Bruemmer, and G. S. Was, eds., The Minerals, Metals, and Materials Society, Warrendale, PA, pp. 115–122 (1999).

103. Raquet, O., and G. Santarini, "Stress Corrosion Crack Propagation Rate of Alloy 600 in the Primary Water of PWR Influence of a Cold Worked Layer," Proc. of the Ninth Intl. Symp. on Environmental Degradation of Materials in Nuclear Power Systems-Water Reactors, F. P. Ford, S. M. Bruemmer, and G. S. Was, eds., The Minerals, Metals, and Materials Society, Warrendale, PA, pp. 207–213 (1999).

104. "Materials Reliability Program (MRP) Crack Growth Rates for Evaluating Primary Water Stress Corrosion Cracking (PWSCC) of Thick–Wall Alloy 600 Material", MRP–55, EPRI, Licensed Document, Electric Power Research Institute, Palo Alto (2002).

105. Andresen, P. L., and P. G. Campbell, "The Effects of Crack Closure in High–Temperature Water and its Role in Influencing Crack Growth Data," Proc. of the Fourth Intl. Symp. on Environmental Degradation of Materials in Nuclear Power Systems-Water Reactors, D. Cubicciotti, ed, NACE International, Houston, TX, pp. 4.86–4.111 (1990).

106. Briant, C. L., and E. L. Hall, "The Microstructural Causes of Intergranular Corrosion of Alloys 82 and 182," Corrosion, 43, 539–548 (1987).

107. Bamford, W. H., J. P. Foster, and R. S. Pathania, "An Investigation of Alloy 182 Stress Corrosion Cracking in Simulated PWR Environment", Proc. of the Ninth Intl. Symp. on Environmental Degradation of Materials in Nuclear Power Systems-Water Reactors, F. P. Ford, S. M. Bruemmer, and G. S. Was, eds., The Minerals, Metals, and Materials Society, Warrendale, PA, pp. 279–294 (1999).

108. Bamford, W. H., J. P. Foster, K. R. Hsu, L. Tunon–Sanur, and A. McIlree, "Alloy 182 Weld Crack Growth, and its Impact on Service–Induced Cracking in Operating PWR Plant Piping," Proc. Tenth Intl. Conf. on Environmental Degradation of Materials in Nuclear Power Systems-Water Reactors, NACE International, Houston, TX (2001).

109. Lindstrom, R., P. Lidar, and J. Lagerstrom, "Crack Growth of Alloy 182 in Simulated Primary Side PWR Environment," Proc. of the 8th Intl. Symp. on Environmental Degradation of Materials in Nuclear Power Systems-Water Reactors, S. M. Bruemmer, ed., American Nuclear Society, La Grange Park, IL, pp. 422–429 (1997).

110. Le Hong, S., J. M. Boursier, C. Amzallag, and J. Daret, "Measurement of Stress Corrosion Cracking Growth Rates in Weld Alloy 182 in Primary Water of PWR," Proc. Tenth Intl. Conf. on Environmental Degradation of Materials in Nuclear Power Systems-Water Reactors, NACE International, Houston, TX (2001).

111. Cassagne, T., D. Caron, J. Daret, and Y. Lefevre, "Stress Corrosion Crack Growth Rate Measurements in Alloys 600 and 182 in Primary Loops Under Constant Load," Proc. of the Ninth Intl. Symp. on Environmental Degradation of Materials in Nuclear Power Systems-Water Reactors, F. P. Ford, S. M. Bruemmer, and G. S. Was, eds., The Minerals, Metals, and Materials Society, Warrendale, PA, pp. 217-224 (1999).

112. Magdowski, R., and M. Speidel, "Stress Corrosion Crack Growth of Weld Material Alloy 182 in Simulated PWR Environments," Institute of Metallurgy, Swiss Federal Institute, Internal Report No. 226, Zurich (Jan. 2001).

113. Jacko, R. J., R. E. Gold, G. V. Rao, K. Koyama, and A. Kroes, "Results of Accelerated SCC Testing of Alloy 82, Alloy 182 and Alloy 52M Weld Metals," presented at Vessel Penetration Inspection, Crack Growth and Repair Conference, Oct. 2, 2003, Gaithersburg, MD (2003).

114. Attanasio, S., J. V. Mullen, J. W. Wuthrich, W. W. Wilkening, and D. S. Morton, "Stress Corrosion Crack Growth Rates (SCCGRs) for Alloy 182 and 82 Welds," presented at Vessel Penetration Inspection, Crack Growth and Repair Conference, Oct. 2, 2003, Gaithersburg, MD (2003).

115. Bamford, W. H., and J. Foster, "Crack Growth of Alloy 182 Weld Metal in PWR Environments," PWRMRP–21, Electric Power Research Institute, Palo Alto (June 2000).

NRC FORM 335
(9-2004)
NRCMD 3.7

U. S. NUCLEAR REGULATORY COMMISSION

BIBLIOGRAPHIC DATA SHEET

(See instructions on the reverse)

1. REPORT NUMBER

NUREG/CR–4667. Vol. 34
ANL—05/17

2. TITLE AND SUBTITLE

Environmentally Assisted Cracking in Light Water Reactors, Annual Report, January–December 2003

3. DATE REPORT PUBLISHED

MONTH	YEAR
	2005

4. FIN OR GRANT NUMBER

Y6388

5. AUTHOR(S)

B. Alexandreanu, O. K. Chopra, H. M. Chung, E. E. Gruber, and W. J. Shack

6. TYPE OF REPORT

Technical; Topical

7. PERIOD COVERED (Inclusive Dates)

8. PERFORMING ORGANIZATION – NAME AND ADDRESS *(If NRC, provide Division, Office or Region, U.S. Nuclear Regulatory Commission, and mailing address; if contractor, provide name and mailing address.)*

Argonne National Laboratory
9700 South Cass Avenue
Argonne, IL 60439

9. SPONSORING ORGANIZATION – NAME AND ADDRESS *(If NRC, type "Same as above": if contractor, provide NRC Division, Office or Region, U.S. Nuclear Regulatory Commission, and mailing address.)*

Division of Engineering Technology
Office of Nuclear Regulatory Research
U.S. Nuclear Regulatory Commission
Washington, DC 20555–0001

10. SUPPLEMENTARY NOTES

W. H. Cullen, Jr., and C. E. Moyer, NRC Project Managers

11. ABSTRACT (200 words or less)

This report summarizes work performed by Argonne National Laboratory on fatigue and environmentally assisted cracking (EAC) in light water reactors (LWRs) from January to December 2002. Topics that have been investigated include: (a) environmental effects on fatigue crack initiation in carbon and low–alloy steels and austenitic stainless steels (SSs), (b) irradiation–assisted stress corrosion cracking (IASCC) of austenitic SSs in BWRs, (c) evaluation of causes and mechanisms of irradiation-assisted cracking of austenitic SS in PWRs, and (d) cracking in Ni–alloys and welds. Fatigue tests have been conducted on two heats of Type 304 SS under various material conditions to determine the effect of heat treatment on fatigue crack initiation in these steels in air and LWR environments. Slow-strain-rate tensile tests have been completed in high-purity 289°C water on steels irradiated to ≈3 dpa. The bulk S content provided a good correlation with the susceptibility to intergranular SCC in 289°C water. Crack growth tests were performed in BWR environments on SSs irradiated to 0.3×10^{21} n/cm^2 and on nonirradiated SS weld heat affected zone specimens. The irradiated specimen of Heat C3 showed very little enhancement of CGRs in high–DO water. Crack growth tests were completed on a Alloy 600 round robin specimen and a Alloy 182 weld specimen in simulated PWR water at 320°C. Under cyclic loading, the CGRs for the weld specimen were a factor of ≈5 higher than for Alloy 600 under the same loading conditions; little or no environmental enhancement was observed.

12. KEY WORDS/DESCRIPTORS *(List words or phrases that will assist researchers in locating this report.)*

Fatigue Crack Initiation
Crack Growth Rate
Irradiation–Assisted Stress Corrosion Cracking
Radiation–Induced Segregation
Stress Corrosion Cracking
Nickel Alloys

13. AVAILABILITY STATEMENT

unlimited

14. SECURITY CLASSIFICATION

(This Page)
unclassified

(This Report)
unclassified

15. NUMBER OF PAGES

139

16.PRICE